

Estimation of Areal Soil Water Content
through
Microwave Remote Sensing

BLD 101111
LANDBOU UNIVERSITEIT
WAGeningen

Promotor: dr. ir. R. A. Feddes
hoogleraar in de bodemnatuurkunde, agrohydrologie
en het grondwaterbeheer

Co-promotor: dr. ir. D. H. Hoekman
universitair hoofddocent bij de leerstoelgroep,
bodemnatuurkunde, agrohydrologie en het grondwaterbeheer

STELLINGEN

1. Meetmethoden die een ruimtelijke meting vertegenwoordigen zoals bij remote sensing, kunnen niet goed gevalideerd worden met conventionele methoden.
Dit proefschrift.
2. Schattingen van bodemvocht op pixelbasis met actieve microgolf remote sensing introduceren een constante fout door speckle, die niet optreedt bij het schatten op veldbasis.
Dit proefschrift.
3. Assimilatie van microgolf helderheidstemperaturen of verstrooiingscoëfficiënten is effectiever dan de assimilatie van de daaruit afgeleide bodemvochtschattingen in hydrologische modellen.
Dit proefschrift.
4. Remote sensing technieken zijn een aanvulling op reeds bestaande technieken en niet een vervanging van deze technieken.
5. De politiek kent vaak veel gewicht aan bepaalde zaken toe, springt er vervolgens lichtvoetig mee om, om te constateren dat het toch te weinig massa heeft.
6. To expect science to give you answers to problems is absurd.
7. Werkwoorden in *stellingen* die een schijnbare *tegenstelling* aanduiden zoals lijken, schijnen e.d. zijn een contradictio in terminis.
8. In de rechtsstaat is gelijk hebben gratis, maar gelijk krijgen niet.
9. Moderne vogelbescherming: beter 10 vogels in de lucht dan 1 in de hand.
10. De wet op natuurbescherming, en met name de verboden daarin, als beleidsinstrument voor natuurbescherming is vrijwel zinloos als er geen alternatief voor het onwenselijke (te straffen) gedrag voor handen is.

Stellingen behorend bij het proefschrift *Estimation of Areal Water Content through Microwave Remote Sensing*. Peter J. van Oevelen, Wageningen, 1 november 2000.

NN 201,2878

Peter J. van Oevelen

Estimation of Areal Soil Water Content through Microwave Remote Sensing

Proefschrift

ter verkrijging van de graad van doctor
op gezag van de rector magnificus
dr. ir. L. Speelman,
van de Universiteit Wageningen,
in het openbaar te verdedigen
op woensdag 1 november, 2000
des namiddags om half twee in de aula.

gbs 658

The research in this dissertation was funded by the Netherlands Remote Sensing Board (BCRS) under contract numbers, NRSP-2/prj.4.2/AO-01 and NRSP-2/prj.4.2/AO-07 , by the European Community through NOPEX/FOREST-DYNAMO EV5V-CT94-0502. A field trip to the Little Washita River Watershed (Oklahoma-USA) in the framework of the SIR-C campaign was partly funded by the Netherlands Organization of Scientific Research (NWO).

Many of the satellite and airborne data used in this study has been made available through NASA-GSFC (Dr. E.T. Engman), ESA-ESTEC, USDA-Hydrology Laboratory (Dr. T. J. Jackson, Dr. T.J. Schmugge, Dr. J.T. Ritchie) or has been financed by the European Community.

A temporary stay at the Department of Civil and Environmental Engineering, University of California at Davis has been made possible by the financial support of the Wageningen Agricultural University, through a Fulbright scholarship (CIES-NACEE), and additional support by Prof. Dr. M.L. Kavvas

CIP-DATA KONINKLIJKE BIBLIOTHEEK, DEN HAAG

Van Oevelen, Peter J.

Estimation of areal soil water content through microwave remote sensing /
Peter J. van Oevelen

Doctoral thesis Wageningen University. - With ref. - With summary in Dutch
ISBN 90-5808-321-7

Subject headings: remote sensing / hydrology

Abstract

Van Oevelen, P.J., 2000. *Estimation of areal soil water content through microwave remote sensing*. Ph.D. thesis, Wageningen University, The Netherlands.

In this thesis the use of microwave remote sensing to estimate soil water content is investigated. A general framework is described which is applicable to both passive and active microwave remote sensing of soil water content. The various steps necessary to estimate areal soil water content are discussed through literature review, laboratory experimental results and results of extensive field experimental work. Even with the large amount of field data being available, no experiment provided all the necessary data to illustrate the framework completely for both passive and active techniques.

The framework developed is intended to be independent of the models used. In this way insight is gained in the dominating factors and problems associated with the use of remote sensing and not with specific models. Throughout the thesis both passive and active techniques are used and compared.

The passive techniques, mainly L-band and C-band, show better results that are more easily obtained at the cost of a relatively low spatial resolution. The standard error in the remotely sensed soil moisture estimates ($< 5\%$) even in the presence of low to moderate vegetation cover is often lower than that of the ground truth measurements. The launch of a space-borne L-band radiometer will make this technique useful for mesoscale and global scale hydrological and meteorological modelling.

The active techniques are severely hampered by vegetation and surface roughness effects, making soil water content estimation more cumbersome. Despite these drawbacks this technique is complementary to the passive technique because of the higher attainable spatial resolutions and the possible use of longer wave lengths (P-band). The latter enables estimation of soil water content under vegetation cover and over larger depths, about 30 cm for P-band, compared to for example about 5-10 cm depth for L-band. The standard error of soil moisture estimates in absence of vegetation is in general around 5%.

In this thesis the effects of vegetation have been excluded in the analysis. To operationalise remotely sensed soil moisture estimation it will be necessary to develop methods that can estimate soil water content when vegetation is present. Especially for active and space-borne passive techniques.

Direct comparison between a passive L-band radiometer and an active C-band radar showed consistent results over stationary heterogeneous areas, i.e. low vegetation cover and relatively homogeneous surface roughness characteristics.

The estimation of soil water content needs to be done from the perspective of the objective. This means that in the case of hydrological and meteorological modelling *assimilation of direct remotely sensed measurements such as brightness temperatures*

or backscattering coefficients can yield better results, e.g. better forecast, than incorporation of the remotely sensed soil water content. This depends strongly on the land surface parameterization and in particular the definition of soil water content in the models used.

Contents

List of symbols and conventions	v
1 Introduction	1
1.1 Remote sensing as a measurement tool	1
1.2 Problem definition	2
1.2.1 Temporal and spatial variability of soil moisture	2
1.3 A theoretical framework	3
1.3.1 Surface parameters, observed backscatter and microwave emission	4
1.3.2 Effects of vegetation	4
1.3.3 Effective soil water content	5
1.3.4 Soil moisture profile and sensing depth	6
1.3.5 The role of soil moisture in hydrological models	6
1.4 Thesis objective and outline	7
1.4.1 Thesis objective	7
1.4.2 Thesis outline	7
2 Dielectric properties of soils	9
2.1 Introduction	9
2.2 Theory of dielectrics	9
2.2.1 Description of the dielectric properties	9
2.2.2 Polarization and magnetization	10
2.3 Dielectric behaviour of various materials	14
2.3.1 Homogenous materials	14
2.3.2 Soil and other heterogeneous materials	17
2.3.3 Semi-empirical approaches	18
2.3.4 De Loor-Polder and Van Santen based formula	22
2.4 Effects of salinity and soil texture on soil dielectric properties	26
2.5 Conclusions	26
3 Microwave emission and scattering of bare soil and vegetated surfaces	29
3.1 Introduction	29
3.2 Coherent modelling approach	30
3.3 Radiative transfer approach	30
3.4 Microwave emission	33
3.4.1 Microwave emissivity	33

3.4.2	Emission models	34
3.5	Microwave scattering of bare soils	39
3.5.1	Microwave backscatter coefficient	39
3.5.2	Scattering theory from bare soil surfaces	41
3.5.3	A more general model: Integral Equation Method (IEM)	49
3.5.4	(Semi-)empirical approaches: The OSU model	50
3.6	Scattering from vegetated surfaces	53
3.7	Conclusions	53
4	Soil moisture estimation by inversion techniques	57
4.1	Introduction	57
4.2	Inversion of soil dielectric mixing model of Wang and Schmugge . . .	61
4.3	Inversion of microwave emission models using a simple radiative transfer approach	62
4.4	Inversion of microwave scattering models	66
4.4.1	The INVOSU model	66
4.4.2	The INVIEM model	67
4.5	Sensing-, skin- and penetration depth	68
4.6	Conclusions	70
5	Description of data sets	73
5.1	Introduction	73
5.2	EFEDA-Spain	73
5.2.1	Site Description	73
5.2.2	Remote sensing data collection	75
5.2.3	In situ data collection	76
5.3	HAPEX-Sahel	77
5.3.1	Site description	78
5.3.2	Ground truth data collection	80
5.3.3	Remote sensing data collection	85
5.4	Little Washita River Watershed	86
5.4.1	Site description	86
5.4.2	Washita'92	87
5.4.3	Ground truth data collection	87
5.4.4	Remote sensing data collection	88
5.4.5	Washita'94/SIR-C	89
5.4.6	Ground truth data collection	89
5.4.7	Remote sensing data collection	93
5.5	NOPEX/Forest-Dynamo	94
5.5.1	Site description general NOPEX area	94
5.5.2	Ground truth data collection	95
5.5.3	Remote sensing data collection	95
6	Application of remote sensing soil moisture estimation techniques	101
6.1	Introduction	101
6.2	Passive microwave remote sensing techniques	101

6.2.1	Push Broom Microwave Radiometer (PBMR) measurements during HAPEX-Sahel	101
6.2.2	ESTAR	104
6.2.3	Conclusions of passive microwave results	104
6.3	Active microwave remote sensing techniques	106
6.3.1	ERS-1	106
6.3.2	AIRSAR	110
6.3.3	EMISAR	117
6.3.4	Effect of surface roughness on soil moisture estimation	119
6.3.5	Conclusions of active microwave results	119
6.4	Assessment of soil moisture estimation performance	123
6.4.1	Introduction	123
6.4.2	Sensitivity analysis of soil moisture estimation of bare soil fields through Monte Carlo simulations	124
6.4.3	Consistency between passive and active microwave soil moisture estimates	131
6.4.4	Conclusions of soil moisture estimation performance	134
6.5	Conclusions	136
7	Remotely sensed soil moisture in hydrological models	141
7.1	Introduction	141
7.2	Data assimilation in mesoscale hydrological models: variational analysis	143
7.3	Assimilation of remotely sensed soil moisture in hydrological modelling	144
7.4	Outlook on applications and operationalisation of remotely sensed soil moisture	146
	Summary and conclusions	147
	Samenvatting en conclusies	157
A	Determination of dielectric properties of materials	167
A.1	Time domain reflectometry	167
A.2	Other methods	168
B	Platform and Sensor Description	171
B.1	Space-borne platforms and sensors	171
B.1.1	ERS	171
B.1.2	AMI-SAR	172
B.1.3	JERS	175
B.1.4	JERS-1 SAR	175
B.1.5	LANDSAT	177
B.1.6	LANDSAT TM	179
B.1.7	Space Shuttle	181
B.1.8	SIR-C	181
B.1.9	SPOT	183
B.1.10	High Resolution Visible Sensor (HRV)	183
B.2	Airborne sensors	186

B.2.1	EMISAR	186
B.2.2	EMIRAD	187
B.2.3	ESTAR	188
B.2.4	JPL-AIRSAR	189
B.2.5	NS001	191
B.2.6	PBMR	192
C	Description of the electromagnetic field	193
C.1	Introduction	193
C.2	Theory of the electromagnetic field	193
C.2.1	The Maxwell equations	193
C.3	Wave equation	195
C.4	Polarization of electromagnetic radiation	197
D	Mathematical description and measurement of surface roughness	201
D.1	Statistical descriptions	202
D.2	Other descriptions	204
D.2.1	Fractal geometry	204
D.2.2	Discrete random process	204
D.3	Measurement of surface roughness	205
D.3.1	Contact methods	205
D.3.2	Non-contact methods	207
E	The inversion of the Fresnel equations	209
E.1	Fresnel equation for a horizontally polarized wave	209
E.2	The Fresnel equation for a vertically polarized wave	210
F	The inverse Dubois model	213
	References	215
	Curriculum Vitae	227

List of symbols and conventions

Base quantities, units and dimensions of the international system of units (SI)

<i>Base quantity</i>		<i>Base unit</i>		<i>Base dimension</i>
<i>Name</i>	<i>Symbol</i>	<i>Name</i>	<i>Symbol</i>	<i>Symbol</i>
time	t	second	s	T
length	l	meter	m	L
mass	m	kilogram	kg	M
thermodynamic temperature	T	kelvin	K	Θ
electric current	I	ampere	A	I
luminous intensity	I	candela	cd	J
amount of substance	n	mol	mol	N
plane angle	α	radian	rad	1
solid angle	Ω	steradian	sr	1

Constants

<i>Operator symbol</i>	<i>Description</i>	<i>Value</i>
c_0	speed of light in vacuum	$2.9979 \cdot 10^8 \text{ m s}^{-1}$
e	unit charge (elektron charge)	$1.6022 \cdot 10^{-19} \text{ C}$
h	Planck constant	$6.6262 \cdot 10^{-34} \text{ J s}$
k	Boltzmann constant	$1.38 \cdot 10^{-23} \text{ J K}^{-1}$
N_0	Avogadro's number	$6.02 \cdot 10^{23} \text{ mol}^{-1}$
σ	Stefan-Boltzmann constant	$5.66910 \cdot 10^{-8} \text{ W m}^{-2} \text{ K}^{-4}$
ρ_w	density of water at 3.98 °C	1000 kg m^{-3}
π	pi	3.141592654...

List of all quantities with their symbols, dimensions and units

Symbol	Name	Dimension	Unit
A	surface, area, aperture	L^2	m^2
A	amplitude	L	m
A_i	aperture where subscript i denotes target [s], receiver [r] or transmitter [t]	L^2	m^2
A_a	depolarization factor in direction of axis a	-	-
A_0	illuminated area	L^2	m^2
B	brightness or radiance	$M T^{-3}$	$W m^{-2} sr^{-1}$
$B(f)$	brightness or radiance per unit frequency	$M T^{-4}$	$W m^{-2} Hz^{-1} sr^{-1}$
B	magnetic flux density	$M T^{-2} I^{-2}$	T
C	capacitance	$L^{-2} M^{-1} T^4 I^2$	F
C	mass fraction of clay	$M M^{-1}$	-
$C^n(r)$	surface correlation function	1	-
c_0	velocity of light in free space ($= 3 \cdot 10^8 m s^{-1}$)	$L T^{-1}$	$m s^{-1}$
c	velocity of light in a medium	$L T^{-1}$	$m s^{-1}$
D	dimension	L^3	m^3
D	fractal dimension	1	-
D	electric flux density or dielectric displacement	$L^{-2} T I$	$C m^{-2}$
d	distance	L	m
E	electric field strength vector	$L M T^{-3} I$	$V m^{-1}$
E	electric field strength	$L M T^{-3} I$	$V m^{-1}$
e	emissivity	1	-
F	force	$L M T^{-2}$	N
F	Stokes vector	$M T^{-3}$	$W m^{-2} sr^{-1}$
f	fractal number	1	-
f	frequency	T^{-1}	$Hz (=s^{-1})$
f_0	relaxation frequency	T^{-1}	Hz
f_i	fraction of absorbed energy by layer i	1	-
G	soil heat flux density	$M T^{-3}$	$W m^{-2}$
G	conductance	$L^{-2} M^{-1} T^3 I^2$	s
G	gain	1	-
G_r	receiver antenna gain	1	-
G_t	transmitter antenna gain	1	-
g	empirical parameter, Eq. 3.81	1	-
H	magnetic field strength	$L^{-1} I$	$A m^{-1}$
h	height	L	m
h	empirical roughness parameter	L	m
I	electric current	I	A
I	impedance	$L^2 M T^{-3} I^{-2}$	Ω

continued on the next page

<i>Symbol</i>	<i>Name</i>	<i>Dimension</i>	<i>Unit</i>
I	radiation intensity, (cf. brightness B)	$M T^{-3}$	$W m^{-2} sr^{-1}$
i_x, i_y, i_z	cartesian unit vectors	1	-
i_r	radian unit vector	1	-
J	(convective) current density	$L^{-2}I$	$A m^{-2}$
J_0	zeroth-order Bessel function	-	-
J_a	absorption source function	$M T^{-3}$	$W m^{-2} sr^{-1}$
J_e	emission source function	$M T^{-3}$	$W m^{-2} sr^{-1}$
J_s	scattering source function	$M T^{-3}$	$W m^{-2} sr^{-1}$
K_{eff}	effective proportionality factor	-	-
k	wavenumber ($= \frac{2\pi}{\lambda}$)	L^{-1}	$rad m^{-1}$
k_0	wavenumber in free space ($= \frac{2\pi}{\lambda_0}$)	L^{-1}	$rad m^{-1}$
L	inductance	$L^2 M T^{-2} I^{-2}$	H
L	Mueller or Stokes matrix	-	-
l	length	L	m
l	autocorrelation length	L	m
$l_{exp.}$	autocorrelation length, exp. correlation	L	m
$l_{Gaussian}$	autocorrelation length, Gaussian correlation	L	m
l_f	length of facet	L	m
M	magnetization	$L^{-1}I$	Am^{-1}
M	molecular weight	MN^{-1}	$kg mol^{-1}$
M	Stokes scattering operator	-	-
m	magnetic momentum	$L^2 I$	$A m^2$
m	Root Mean Square (RMS) surface slope	1	-
N	concentration, number of entities per volume	$L^{-3}N L^{-3}$	$mol m^{-3}, m^{-3}$
N	number of entities	1	-
n	normal vector	1	-
n	index of refraction	1	-
P	electric polarization	$L^{-2}T I$	$C m^{-2}$
P	phase matrix	$L^2 M T^{-3}$	$W(=J s^{-1})$
P	power, energy current	$L^2 M T^{-3}$	$W(=J s^{-1})$
$P(\lambda)$	power fluxdensity per unit wavelength	$L^{-1}M T^{-3}$	$W m^{-3}$
$P(f)$	power fluxdensity per unit frequency	$L^2 M T^{-4}$	$W m^{-2} Hz^{-1}$
P_r	received power	$L^2 M T^{-3}$	$W(=J s^{-1})$
P_t	transmitted power	$L^2 M T^{-3}$	$W(=J s^{-1})$
p	empirical parameter, Eq. 3.77	1	-
p	electric momentum	$L T I$	$C m$
Q	(electric) charge	$T I$	$C(=A s)$
Q	empirical mixing parameter	1	-
q	empirical parameter, Eq. 3.75	1	-

continued on the next page

<i>Symbol</i>	<i>Name</i>	<i>Dimension</i>	<i>Unit</i>
$q^{(\alpha)}$	charge of particle of kind α	T I	C
R	electric resistance	$L^2 M T^{-3} I^{-2}$	Ω
R^2	linear regression coefficient	1	-
R_a	Rayleigh parameter ($k\sigma \cos \theta_{inc}$)	L	m rad
R_r	range between target and radar receiver	L	m
R_t	range between target and radar transmitter	L	m
$R_{h,v}$, or R^p	Fresnel reflection coefficient $p = h, v$ is horizontally or vertically polarized	1	-
\mathbf{r}	distance vector	L	m
r	radius, space coordinate (polar)	L	m
r_s	fraction of reradiated radiation intensity	1	-
\mathbf{S}	scattering matrix	1	-
S	mass fraction of sand	MM^{-1}	-
S_e	deviation from reference value, standard error	-	-
s	path length, distance	L	m
\mathbf{s}	scattering direction unit vector	1	-
\mathbf{s}_{inc}	incident scattering direction unit vector	1	-
T	period, oscillation time or excitation	T	s
T	(absolute) aerodynamic temperature	Θ	K
T	physical temperature	Θ	$^{\circ}C$
T	moment of force	$L^2 M T^{-2}$	N m
T_B	brightness temperature	Θ	K
T_{atm}	atmospheric brightness temperature	Θ	K
T_c	canopy temperature	Θ	K
T_s	soil temperature	Θ	K
T_{sky}	sky brightness temperature	Θ	K
t	time	T	s
\mathbf{u}	windspeed	$L T^{-1}$	$m s^{-1}$
V	electric potential or voltage	$L^2 M T^{-3} I^{-1}$	V
V	volume	L^3	m^3
$V(X)$	variance of X	-	-
\mathbf{v}	velocity	$L T^{-1}$	$m s^{-1}$
v	wave velocity or pulse speed	$L T^{-1}$	$m s^{-1}$
W	field energy	$L^2 M T^{-2}$	J
W^n	surface roughness or power spectrum	-	-

continued on the next page

Symbol	Name	Dimension	Unit
x	(horizontal) space coordinate	L	m
y	(horizontal) space coordinate	L	m
z	(vertical) space coordinate, depth	L	m
α	attenuation factor	L^{-1}	m^{-1}
α	correction or shape factor	-	-
$\alpha(f)$	absorptivity	1	-
α_s	fraction of absorbed radiation intensity	1	-
β	phase factor	L^{-1}	m^{-1}
β^1, β^2	empirical constants	-	-
$\Gamma(f)$	transmissivity	1	-
Γ_{atm}	atmospheric transmissivity	1	-
γ	propagation factor ($\gamma = \alpha - i\beta$)	L^{-1}	m^{-1}
γ	fitting parameter	-	-
γ	absorption coefficient	1	-
γ°	scattering cross section per unit area, perpendicular to beam direction ($\gamma^\circ = \frac{\sigma_0}{\cos \theta_{inc}}$)	$L^2 L^{-2}$	-
δ	phase difference ($\delta = \phi_y - \phi_x$)	1	rad or °
δ_s	skin depth	L	m
δ_p	penetration depth	L	m
$\epsilon(f)$	emissivity	1	-
ϵ_s	surface emissivity	1	-
ϵ	(complex) permittivity ($\epsilon = \epsilon' - j\epsilon''$)	$L^{-3} M^{-1} T^4 I^2$	F m^{-1}
ϵ_0	absolute permittivity	$L^{-3} M^{-1} T^4 I^2$	F m^{-1}
ϵ_a	apparent permittivity	1	-
ϵ_{eff}	effective permittivity ($\epsilon_h \leq \epsilon_{eff} \leq \epsilon_m$)	1	-
ϵ_h	permittivity of host material	1	-
ϵ_i	permittivity of inclusion	1	-
ϵ_m	apparent permittivity of mixture	1	-
ϵ_r	(complex) relative permittivity	1	-
ϵ_s	static permittivity	1	-
ϵ_w	high frequency limit permittivity for water	1	-
ϵ_∞	high frequency or optical limit permittivity	1	-
η	wave impedance	$L^2 M T^{-3} I^{-2}$	Ω
θ	volume fraction of liquid (water)	$L^3 L^{-3}$	-
θ_{LAB}	volumetric water content measured in lab.	$L^3 L^{-3}$	-
θ_t	transition volumetric water content	$L^3 L^{-3}$	-

continued on the next page

Symbol	Name	Dimension	Unit
θ_{TDR}	volumetric water content measured by TDR	L^3L^{-3}	-
θ_{veg}	volumetric vegetation water content	L^3L^{-3}	-
θ_{wp}	volumetric water content at wilting point	L^3L^{-3}	-
θ_{inc}	angle of incidence	1	rad or °
θ_n	angle between normal and directional vector	1	rad or °
θ_0	angle between the surface normal and radar beam	1	rad or °
κ_a	volume absorption coefficient	L^{-1}	$Np\ m^{-1}$
κ_{ag}	power absorption coefficient of background material	L^{-1}	$Np\ m^{-1}$
κ_e	volume extinction coefficient (homogeneous medium)	L^{-1}	$Np\ m^{-1}$
κ'_e	volume extinction coefficient (inhomogeneous medium)	L^{-1}	$Np\ m^{-1}$
κ_s	volume scattering coefficient	L^{-1}	$Np\ m^{-1}$
κ	extinction coefficient matrix	L^{-1}	$Np\ m^{-1}$
Λ	period of periodic surface	L	m
λ	wavelength	L	m
λ_0	wavelength in free space	L	m
μ	(complex) permeability ($\mu = \mu' - j\mu''$)	$L\ M\ T^{-2}I^{-2}$	$H\ m^{-1}$
μ_r	(complex) relative permeability	1	-
μ_0	permeability of vacuum ($4\pi \cdot 10^{-7}\ H\ m^{-1}$)	$L\ M\ T^{-2}I^{-2}$	$H\ m^{-1}$
μ_i	mean of distribution	-	-
Π	polarisability per mole substance	L^{-3}	m^{-3}
ρ	electric charge density	$T\ L^{-3}I$	$C\ m^{-3}$
ρ	amount of substance density		$mol\ m^{-3}$
ρ_α	density of phase α	$L^{-3}M$	$kg\ m^{-3}$
ρ_b	dry bulk density	$L^{-3}M$	$kg\ m^{-3}$
ρ_s	specific density of soil solid particles	$L^{-3}M$	$kg\ m^{-3}$
ρ_p	reflectivity, with p horizontal (h) or vertical (v) polarization	1	-
ρ_0	Fresnel surface reflectivity at nadir	1	-
ρ_{eff}^p	effective reflectivity	1	-
σ	complex electrical conductivity ($\sigma = \sigma' - j\sigma''$)	$L^{-3}M^{-1}T^3I^2$	$s\ m^{-1}$
σ	Root Mean Square (RMS) of the height differences	L	m
σ_{uncor}	RMS of the height differences	L	m

continued on the next page

Symbol	Name	Dimension	Unit
σ_{cor}	uncorrected for slope RMS of the height differences corrected for slope	L	m
σ_c	radar scattering cross-section	L^{-2}	m^{-2}
σ_a	absorption cross section	L^{-2}	m^{-2}
σ_s	scattering cross section	L^{-2}	m^{-2}
σ^0	scattering coefficient or differential scattering cross-section (per unit area)	$L^2 L^{-2}$	-
σ^c	complementary scattering coefficient	$L^2 L^{-2}$	-
σ^k	Kirchhoff scattering coefficient	$L^2 L^{-2}$	-
σ^{kc}	cross term scattering coefficient	$L^2 L^{-2}$	-
σ^m	multiple-scatter coefficient	$L^2 L^{-2}$	-
σ^s	single-scatter coefficient	$L^2 L^{-2}$	-
σ_c	dielectric conductivity ($\sigma_c = \sigma'_c - j\sigma''_c$)	$L^{-3} M^{-1} T^3 I^2$	$s m^{-1}$
σ_{eff}	effective conductivity	$L^{-3} M^{-1} T^3 I^2$	$s m^{-1}$
σ^2	variance of distribution (= V)		
τ	tangent vector	1	-
τ	relaxation time	T	s
τ	optical thickness or depth	1	-
ν	fractal exponent	1	-
ϕ	phase angle, azimuth angle	1	rad or °
ϕ	porosity	1	-
ϕ_α	volume fraction of phase α	1	-
φ	angle	1	rad or °
χ	ellipticity (angle)	1	rad or °
χ	grazing angle	1	rad or °
χ_e	electric susceptibility	1	-
χ_m	magnetic susceptibility	1	-
ψ	potential	$L^2 T^{-2}$	$J kg^{-1}$
ψ	orientation, rotation angle	1	rad or °
Ω	solid angle	1	sr
Ω_{inc}	incident solid angle	1	sr
ω	angular frequency	1	$rad s^{-1}$
ω	single-scattering albedo	1	-
ω_p	single-scattering albedo for polariza- tion p	1	-

Mathematical operators, symbols, sub- and superscripts

<i>Operator symbol</i>	<i>Description</i>
∇	gradient
∂, f_x	partial differential
\sum	summation
\int	integral, antiderivative
\oint	closed (line) integral
Δ	difference, change or increment
d, f'	derivative
\ln	natural logarithm
\log_a	logarithm with base a
$\langle A \rangle, E(A), \bar{A}$	average or expectation of A
j	$\sqrt{-1}$
$ A $	modulus of A
A^{-1}	inverse of A
A^*	conjugate of A
$\det A$	determinant of A
A^T	transpose of A
\cdot	scalar or dot product
\times	vector or cross product
∞	infinity
$\neq, <, >, \leq, \geq$	inequality
\sim	is proportional to
\approx	is approximately equal to
$\equiv, \stackrel{def}{=}$	is defined as
$\sqrt{}$	square root
$\operatorname{Re} z, z'$	real part of z
$\operatorname{Im} z, z''$	imaginary part of z
$V(X), \sigma^2(X)$	variance of X
$\operatorname{cov}(X, Y)$	covariance of X

Vector analysis

Definitions of vector operations in three dimensions

Definition of a vector:	$\mathbf{A} = (A_x, A_y, A_z)$	
Scalar or dot product	$\mathbf{A} \cdot \mathbf{B}$	
Cross or vector product	$\mathbf{A} \times \mathbf{B}$	
Divergence	$\nabla \cdot \mathbf{A}$	Flux of \mathbf{A} through a closed surface
Laplacian	$\nabla \cdot \nabla = \nabla^2$	
Rotation or curl	$\nabla \times \mathbf{A}$	(line)integral of \mathbf{A} around a loop

Complex numbers

Complex numbers are often used in the analysis of physical phenomena specially when they have a periodic character such as electromagnetic waves. This way of representing functions has numerous mathematical advantages since it is easier to work with an exponential function than with a cosine or sine. In this thesis oscillatory functions are represented by real parts of complex functions. Suppose we have a force:

$$\mathbf{F} = F_0 \cos \omega t \quad (0.1)$$

this can be written as a real part of a complex number:

$$\mathbf{F} = F_0 e^{j\omega t} \quad (0.2)$$

since

$$e^{j\omega t} = \cos \omega t + j \sin \omega t \quad (0.3)$$

From Eqs. 0.1 until 0.3 it can be seen that in the complex quantity \mathbf{F} only the real part of this number represents the actual (real!) force.

Tensors

Tensors can be ranked as follows:

zero rank tensor	the partial derivative is zero	→	scalar
first rank tensor	the partial derivative is one	→	vector
second rank tensor	the partial derivative is two	→	tensor
third and higher rank tensor	the partial derivative is three and higher	→	tensor

An example of the use of a tensor The relationship between the dielectric displacement and an electric field in an *isotropic* medium can be described as a scalar relationship i.e. the displacement \mathbf{D} is everywhere in the field equal proportional to the applied field \mathbf{E} :

$$\mathbf{D} = \epsilon \mathbf{E} \quad (0.4)$$

in which the permittivity ϵ is of type scalar.

In an *anisotropic* medium the dielectric displacement at a certain point in the respectively x , y and z direction depends on the x , y and z components of the electric field at that point the relationship between the two quantities then becomes a tensor relationship in which ϵ is of type tensor:

In the x - direction \mathbf{D} depends on \mathbf{E} :

$$D_x = \epsilon_{11}E_x + \epsilon_{12}E_y + \epsilon_{13}E_z \quad (0.5)$$

In the y - direction \mathbf{D} depends on \mathbf{E} :

$$D_y = \epsilon_{21}E_x + \epsilon_{22}E_y + \epsilon_{23}E_z \quad (0.6)$$

In the z - direction \mathbf{D} depends on \mathbf{E} :

$$D_z = \epsilon_{31}E_x + \epsilon_{32}E_y + \epsilon_{33}E_z \quad (0.7)$$

the tensor ϵ can thus be written as:

$$\epsilon_{ik} \rightarrow \begin{pmatrix} \epsilon_{11} & \epsilon_{12} & \epsilon_{13} \\ \epsilon_{21} & \epsilon_{22} & \epsilon_{23} \\ \epsilon_{31} & \epsilon_{32} & \epsilon_{33} \end{pmatrix} \quad (0.8)$$

in which the number of indices is equal to the order of the tensor. In general a tensor relationship between two quantities can be described by:

$$D_i = \sum_k \epsilon_{ik} E_k \quad (0.9)$$

Chapter 1

Introduction

In earth sciences there is a great need for data that are available globally or that at least cover larger areas than can be monitored using in situ techniques. The tool to achieve this is called remote sensing. The use of spatial data has in the last 30 years increased tremendously. With the availability of more and more types of the data that can be gathered from airborne and spaceborne platforms, the application of these data seem endless and the possible achievements limitless. Indeed remotely sensed data is a powerful tool but it has its limits.

In this thesis a framework is presented to estimate soil moisture using microwave remote sensing techniques.

1.1 Remote sensing as a measurement tool

Remote sensing can be defined as the acquisition of information without direct contact with objects that are at a certain distance. Other definitions are available but this one is general and includes e.g. medical imaging, extra terrestrial exploration, the use of acoustic waves and electromagnetic radiation. The term earth observation is reserved for remote sensing of the earth (including atmosphere, surface and subsurface and the processes that take place) using electromagnetic radiation. The electromagnetic (EM) spectrum covers all the types of radiation from X-rays to visible light to microwaves. All this radiation is energy that is transported in accordance with the wave theory.

The term microwave remote sensing is usually reserved for data that have been collected by instruments that operate in the frequency range of 0.3 to 300 GHz, i.e. wavelength λ between 1 mm and 1 m, although sometimes the submillimeter range is included too. Most of the microwave sensing of the earth's surface is done using frequencies below 40 GHz. Microwave radiometry of the atmosphere is done predominantly in the mm and sub-mm range.

Passive microwave remote sensing or microwave radiometry detects the earth's emission in the microwave region (0.3 to 300 GHz). The amount of radiation that is

emitted is relatively small so it is difficult to obtain a high spatial resolution and it is necessary to have sensitive instruments. The amount of radiation received is usually expressed as brightness temperatures, T_B which is the temperature of a blackbody that would emit the same amount of radiation. The ratio of T_B with the objects physical temperature, T gives the emissivity, ϵ .

Active microwave remote sensing uses instruments (radars, scatterometers) that both emit and detect microwave radiation (in the region of 0.3 to 300 GHz although for earth observation mostly the lower region < 20 GHz is used). Because the instrument sends out its own radiation (in the form of a pulse) it is easier to obtain higher spatial resolution (e.g. by increasing power). The disadvantage is that the technology of the instrument is more complex. With SAR (Synthetic Aperture Radar) the processing of the data becomes also complex. For SAR the movement of the instrument is used to artificially lengthen the antenna (making shorter antennas possible at low frequencies) thus the correlation of the signals that have been transmitted and received needs to be correctly correlated which can be a tedious task. The radiation that is scattered back to the sensor is expressed as a (back)scattering coefficient, σ^0 and is usually expressed in dB.

An important term in both active and passive microwave remote sensing is *sensing depth* or *sampling depth* (see also section 4.5). Because of the longer wavelength microwave radiation is capable of penetrating objects, such as clouds but also to a certain extent vegetation and soils. This unique capability enables to look into an object but how far is not always clear. The *sensing depth* is defined as *the depth over which the sensor has retrieved a return signal yielding information*. It can also be defined as *the thickness of the soil layer which gives the most significant contribution to the scattering or emission* (Raju et al., 1995). Various studies have investigated the magnitude of this sampling depth either through pure physically based models (Njoku & Kong, 1977; Wilheit, 1978) or combinations of physically based models with empirical methods (Wang, 1987).

With remote sensing measurements a set of parameters related to the radiation received is measured. We are however not interested in purely the radiation amount but more in parameters that influences this radiation amount. In general *the process of extraction of a parameter or a set of parameters from another set of (measured) parameters is called inversion*.

1.2 Problem definition

1.2.1 Temporal and spatial variability of soil moisture

The spatial variability of soil moisture is naturally time variant. The spatial correlation is highest for wet soils but it decorrelates when the soil becomes drier. Most likely the rate of spatial decorrelation of the soil moisture covariance is spatially correlated to the soil hydraulic properties such as (un)saturated hydraulic conductivity. These properties are not only dependent upon soil characteristics such as soil texture and chemical composition, but also upon meteorological conditions such as precipitation,

evapotranspiration as well as geomorphological factors such as pedology, topography, surface slope, orientation and shading. Another important factor is the type of vegetation cover along with its root distribution. All these factors (and the list is definitely not complete) have a direct impact on the soil moisture distribution and its change. In this respect it often does not make a difference to distinguish between vertical and horizontal variability since both are strongly dependent on each other.

The use of statistical methods to describe the soil moisture variability, such as semi-variograms, Fourier analysis and kriging, are useful but since there are so many factors influencing that variability they are limited. The description of the time and space dependent processes involved through e.g. hydrological/meteorological modelling would be a sound way to describe and predict the soil moisture distribution given that the most important factors are well described and that the input is spatially consistent. For example a wrong input of the spatial distribution of precipitation would inherently mean a wrong output. Fortunately for many applications such detailed information is not necessary and simplifications and assumptions can be made. One of the simplifications could be the use of characteristics scales, i.e. simply defined as the scale at which the variability -spatial covariance- becomes a constant, when present.

To measure the spatial variability is a tedious and difficult undertaking. Field measurements are often point measurements and can only be representative for a small area. The amount of labour and other expenses involved to use these methods are enormous and as such it is not possible to use these approaches at the meso- or global scales. Measurement techniques that are non-point measurements but *true spatial measurements such as remote sensing cannot be properly validated using the conventional methods.*

This is the crux, since these methods are considered to be ground truth which are used to calibrate, validate or verify other true spatial measurement approaches. This problem is nowadays referred to as *upscaling* or *downscaling*. A satisfying solution has still to be found.

1.3 A theoretical framework

The estimation of areal soil water content by means of microwave remote sensing can be set in *theoretical framework* that describes the necessary steps. This framework is with minor changes applicable for both passive and active microwave remote sensing. The framework for the active case has been published by Van Oevelen and Hoekman (1999). Each of the steps in the framework determines how accurate the inversion results will be. Although the instrument's sensitivity and accuracy in determining the measured variable can have a large influence on the inversion results, these results are independent of the methodology followed.

- The first step is to establish the relationship between the soil surface parameters, such as surface roughness and dielectric properties, and the observed radar backscatter σ^0 or brightness temperature T_B ;
- The second step is to describe the influence of vegetation on the relationship between σ^0 or T_B and the surface parameters;

- The third step is to find a relationship between the dielectric properties, ϵ and soil parameters to retrieve the soil water content, θ ;
- The fourth step is the relationship between soil moisture profile, soil heterogeneity and the sensing depth.
- The fifth and last step is the assimilation of the estimated soil water content into hydrological and meteorological models.

In this thesis the first four steps will be discussed thoroughly using both results from literature and analysis and verification from experimental data. The last two steps will only be discussed based upon literature.

1.3.1 Surface parameters, observed backscatter and microwave emission

The relationship between the observed backscatter coefficient σ^0 or microwave emission ϵ and surface parameters is the basic relationship. The σ^0 and ϵ are a function of wave parameters such as frequency f , polarization and incidence angle θ_{inc} . The surface parameters are characterised by the dielectric properties ϵ and surface roughness parameters kl and $k\sigma$. The dielectric properties determine the response (molecules with their electrons and atoms) of a material under the influence of an electromagnetic field (see Chapter 2).

In case of microwave emission the effects of surface roughness has been studied extensively but to date no real satisfying model has been developed. The model of Choudhury *et al.*, 1979 has been used extensively and seems to perform well in most cases. However, this model is empirical of nature and cannot explain all the phenomena related to surface roughness and care has to be taken when this model is used. The surface physical temperature T is important in the estimation of ϵ from measured T_B . A rough estimate of the surface temperature from thermal infrared measurements, or estimates through Soil-Vegetation-Atmosphere Transfer (SVAT) models will usually suffice. These SVAT models can be used to model the water and energy balance above, at and/or below a vegetated surface.

For the active case, an accurate description of the relationship between σ^0 and surface characteristics, ϵ , kl and $k\sigma$ is cumbersome and computationally intensive (Tsang *et al.*, 1985; Ogilvy, 1990). This can be circumvented by choosing (semi-)empirical approaches, (Dobson & Ulaby, 1986; Oh *et al.*, 1992; Dubois *et al.*, 1995), or simplified theoretical models (Chen *et al.*, 1995; Huang & Jin, 1995; Fung *et al.*, 1992; Ulaby *et al.*, 1982). The empirical approaches have the disadvantage that their validity is restricted by the conditions under which the calibration or fitting is performed. The validity of the theoretical models is usually limited by the severe assumptions adopted regarding the surface characteristics.

1.3.2 Effects of vegetation

For the passive case the effect of vegetation on the microwave emission is twofold: vegetation contributes to total surface emission and vegetation attenuates and rescatters emission from the bare soil surface. The most important object parameters influencing

this relationship are plant biomass (through the dielectric properties ϵ of vegetation) and temperature, T ; the most important sensor parameter is the frequency, f . Various simple but adequate models have been developed to correct for the effects of vegetation on microwave emission (Jackson & Schmugge, 1991; Mo et al., 1982; Schmugge & Jackson, 1992).

The effect of vegetation on microwave backscattering is complex since the structure of the vegetation and the roughness of the surface dominate. Three components contribute to the total backscatter:

- Vegetation;
- Soil surface attenuated by the vegetation;
- Interaction between vegetation and soil attenuated by the vegetation.

The latter component makes the inversion more complicated because more surface parameters are involved. However, this contribution can be significant enough to enable estimation of soil surface parameters under vegetated surfaces such as forests.

For the active case a simple model to calculate the effect of vegetation is the "CLOUD-model" which models the vegetation as a low density cloud of small identical particles on top of a dielectric surface (Attema & Ulaby, 1978). This model only assumes single scattering and for most vegetated surfaces has to be adapted to include multiple scattering, e.g. Hoekman, (1990). The Cloud model is easy to invert but has a limited validity. The models with larger validity ranges are unfortunately also more complex. Consequently, inversion of these models is either impossible or at least very tedious. However, these more complex models can yield insight into the dominating factors that determine the vegetation effects. For certain cases simplification, using dominating factors only, may yield satisfactory results (Rijckenberg, 1997; Dobson & Ulaby, 1998). Currently, such models are in general not capable of correcting for the effect of vegetation in a satisfactory manner. Until appropriate models become available it is necessary to *at least establish the pixels for which the effect of vegetation is minimal and hence, the inversion can yield reliable soil moisture estimates*. More models that describe backscattering from vegetated surfaces are described in Chapter 3.

1.3.3 Effective soil water content

In the microwave region liquid water has relatively high dielectric properties compared to that of dry soil. Thus adding water to a soil increases its dielectric constant. It is this property that enables sensing of soil moisture by microwaves. Various models have been developed to describe the relationship between the dielectric properties and the soil properties such as texture, water content, salinity and soil temperature (Dobson et al., 1985; de Loor, 1983; Hallikainen et al., 1985; Wang & Schmugge, 1980) (see Chapter 2). Although these models seem to suffice, especially for soils in the agricultural regions of the world, care has to be taken when dealing with soils from other regions, such as ferrasols with a high iron content (Nitzsche, 1994).

A microwave sensor will not observe an actual soil moisture profile but, depending upon the frequency, a *weighted average over the sensing depth*, which we call the *effective soil water content*. The weighing function depends strongly upon the dielectric properties distribution. Using multiple frequencies qualitative information can

be gathered over the average soil moisture distribution over depth. However, certain features, such as infiltration fronts, cannot be observed. Thus, from the relationship between the dielectric properties and soil parameters it is possible to retrieve an effective soil water content.

1.3.4 Soil moisture profile and sensing depth

Due to the processes in which soils are formed, natural soils usually exhibit a variation of properties both over the surface and in depth. The vertical cross-section of a soil is called a soil profile and is seldomly uniform in depth but consists of a succession of more-or-less distinct layers (Hillel, 1980). Even within a relatively uniform soil layer the variation of the soil properties, such as texture, organic matter content and bulk density can be large. The soil moisture profile can exhibit strong variation due to the soil heterogeneity and the forces acting upon the water in the soil. The soil profile, soil moisture profile and temperature profile have a strong influence on the dielectric properties of the soil column and thus on the emission or backscatter from the soil surface.

Raju et al., 1995 (Raju et al., 1995) examined the effect of soil moisture and physical temperature profiles on the microwave emission ($f > 1$ GHz) and showed that there is a considerable influence of these profiles on the emission. They noted that there is general agreement on the order of magnitude of the microwave sampling depth, in the range of $0.2\lambda_0 - 0.25\lambda_0$ where λ_0 is the wavelength in free space. These values however, are often determined empirically.

With increasing wavelength (decreasing frequency) and depending upon the dielectric properties (profile) of the soil, the type of scattering will change from pure surface scattering to volume scattering (Fung et al., 1996). At a certain point this volume scattering term cannot be ignored and needs to be accounted for. This may be true for P-band ($f \approx 0.5$ GHz) but even for higher frequencies. Surface scattering models such as the IEM model (Fung et al., 1992; Fung & Chen, 1995) are in the case of volume scattering not longer sufficient and have to be modified.

1.3.5 The role of soil moisture in hydrological models

Soil moisture represents the coupling between the energy balance and water balance at the earth's surface. However, this is not only surface soil moisture over bare soil fields but in vegetated areas more importantly the water in the root zone. Remote sensing will be capable of determining an effective water content of approximately the top 10 cm of the soil. There is still much debate as to whether the soil moisture in this top layer (< 10 cm) is of significant importance in hydrological modelling (Choudhury et al., 1995; Feddes & Koopmans, 1995). There are various ways to incorporate remotely sensed soil moisture in hydrological models. But given the constraints of hydrological models (e.g. soil water content definition, number of soil layers) this is a difficult task (see Chapter 7). Assimilation of T_B or σ^0 might be a better alternative to incorporate remotely sensed data.

To capture the heterogeneity of soil water content over large areas remote sensing is currently the only technique available that seems promising (Engman & Chauhan, 1995; Jackson *et al.*, 1995; van Oevelen & Hoekman, 1999). Thus, for mesoscale hydrological models and climate models such as General Circulation Models (GCMs) and Numerical Weather Prediction models (NWP), remotely sensed data in the form of effective soil water content or radiance will be valuable (Kalma *et al.*, 1999).

1.4 Thesis objective and outline

1.4.1 Thesis objective

The objective of this thesis is to provide, describe and illustrate a general applicable framework to estimate areal soil water content by means of microwave remote sensing. The framework should be general in the sense that it is independent of the models used and is applicable for use in hydrological and meteorological models at various scales.

1.4.2 Thesis outline

The thesis organisation follows the steps of the logical framework for remotely sensed soil moisture estimation and application as described in section 1.3, although in a different order.

The general scope of the thesis has been given in Chapter 1, where the background and rationale for this study were outlined.

In Chapter 2 the background on the dielectric properties of soils and the so-called soil mixing models are given, along with the most frequently used models for soil moisture estimation. The dielectric properties are an important link between the interaction of electromagnetic radiation and the amount of moisture present in the soil.

In Chapter 3 various types of scattering and emission models are discussed. These models give the relationship between the measured radiation for an object and its physical properties. Chapters 2 and 3 therefore give relationships between surface parameters and observed backscatter or emission.

In Chapter 4 the estimation of soil moisture using microwave data is outlined. The inversion of some of the available scattering and emission models as well as soil mixing models are illustrated.

In Chapter 5 a summary of the available data used in this study is given. Despite the large amount of remote sensing and ground truth data available it has proven tedious to find one single (field) experiment where all criteria could be met to illustrate the complete framework.

In Chapter 6 the approaches used to estimate areal soil water content are discussed and validated using the experimental data described in Chapter 5.

In Chapter 7 a discussion of different approaches towards soil moisture estimation and its application in hydrological and meteorological models is given along with an outlook on the future use of microwave data in hydrology and meteorology.

Chapter 2

Dielectric properties of soils

2.1 Introduction

The electrical properties of materials are of interest in many areas of science and engineering, because they determine the coupling and distribution of (electromagnetic) energy. The *dielectric constant*, ϵ (or *electric permittivity*) and the *magnetic permeability*, μ are the dielectric properties which describe the interaction of a dielectric with electric, magnetic and electromagnetic fields (Hippel, 1958; Mudgett, 1986). In microwave remote sensing research in general one of the basic properties is the permittivity ϵ . *In this thesis the terms permittivity and dielectric constant are considered the same and preference to the use of the term permittivity is given.* However, it should be noted that some authors use the term permittivity only for the real part of the dielectric constant and others use it exclusively for the term relative dielectric constant! To fully understand the principles of dielectric properties and to be able to describe them properly it is necessary to understand the theory of electromagnetic fields. A brief description of the fundamentals of this theory is given in section C.2. For a more thorough treatment on the theory of electromagnetics the reader is referred to the references given in this Chapter.

2.2 Theory of dielectrics

2.2.1 Description of the dielectric properties

The interaction such as reflection, refraction, attenuation and change in direction of propagation, between non-conducting matter or insulators and time varying electric fields is generally described by a complex permittivity:

$$\epsilon = \epsilon' - j\epsilon'' \quad (2.1)$$

The interaction between objects and magnetic fields by a complex permeability is described as:

$$\mu = \mu' - j\mu'' \quad (2.2)$$

Usually the dielectric properties of materials are expressed relative to the dielectric permittivity of vacuum, ϵ_0 and permeability of vacuum μ_0 . In case of electric fields by the relative complex permittivity:

$$\epsilon_r = \epsilon'_r - j\epsilon''_r \quad (2.3)$$

and in the case of magnetic fields by the relative complex permeability:

$$\mu_r = \mu'_r - j\mu''_r \quad (2.4)$$

To make the description of electrical properties complete the complex electrical conductivity is given as:

$$\sigma = \sigma' - j\sigma'' \quad (2.5)$$

which is a measure of the magnitude of the migration of charges in conducting materials.

2.2.2 Polarization and magnetization

Under influence of an external electric field small dipoles are induced in a dielectric material. Dipoles are pairs of opposite charges and can be approximated by two charges separated by a small distance. A lot of substances may be approximated by a dipole, since at large distances relative to the spaces between charges the electric field is not sensitive to the finer details.

An important example of dipoles are atomic dipoles in which electrons or rather an electron cloud, surround a positive nucleus. These electrons are subject to opposite forces due to an electric field and are as a result displaced relative to each other. This is called *electronic polarization*. Molecules often consist of different kinds of atoms each with their own electron clouds. These electron clouds are not shared symmetrically but are displaced excentric towards the stronger binding atoms (Hippel, 1958). Such molecules are called non polar molecules when they have a symmetric arrangement of atoms and thus the centres of gravity of the positive and negative charges are the same (Feynman et al., 1979). The electron clouds, which cannot move or deform very much due to the attraction of the nucleus, will in reaction to an applied field shift or deform in such a way that the charges are aligned with the applied field. This displacement of charged atoms or a group of atoms with respect to each other, is called *atomic polarization*. On the other hand in some molecules the charges are separated even without an external field, because of the asymmetric arrangement of atoms in the molecule. These molecules have a permanent dipole moment and are called polar molecules. A good example of a polar molecule is a water molecule which has a negative oxygen atom with two positive hydrogen atoms. The net charge in such a molecule as a whole and in a group of such molecules is still zero! Polar and induced polar molecules experience a torque when an electric field is applied, and they will tend to orient themselves in the direction of the applied field. This is called *orientation* or *dipole polarization*. Besides this polarization mechanism due to locally bound charges in atoms, molecules and structures of solids and liquids

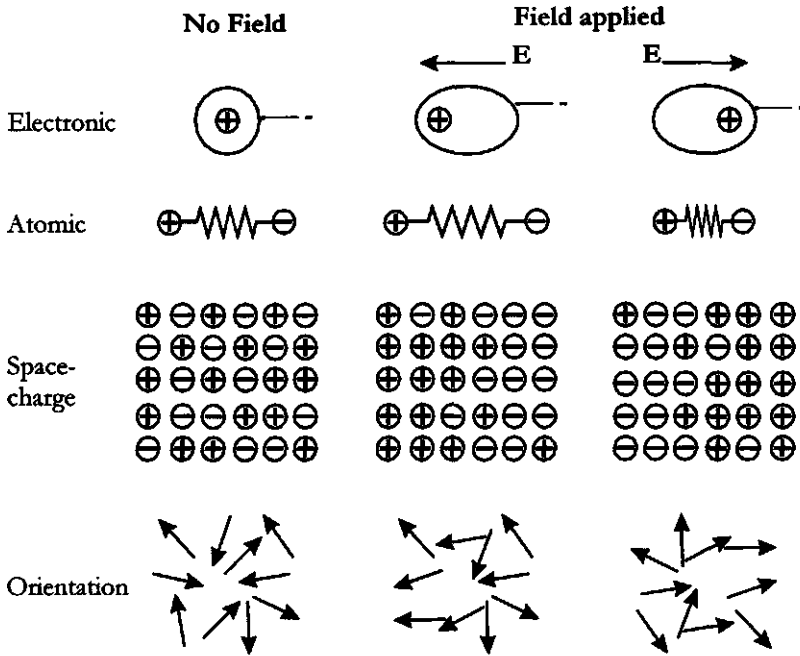


Figure 2.1: The four polarisation mechanisms: electronic, atomic, space charge (or interfacial) and orientation.

there is a mechanism which is due to migrating charge carriers. When such carriers are obstructed in their motion, either because they become trapped in the material (or on interfaces) or because they cannot be freely discharged or replaced at the electrodes, space charges and macroscopic field distortion result. This is called *space-charge* or *interfacial polarization* and is also referred to as *Maxwell-Wagner effects* or polarization (Hippel, 1958).

The total electric polarization consists of contributions caused by the four polarization mechanisms described above (see Fig.2.1). The first three mechanisms have their own characteristic times, i.e. the time needed to reach an equilibrium with respect to the applied field (Böttcher & Borderwijk, 1978a; Böttcher & Borderwijk, 1978b):

- orientational polarization, with a characteristic time greater than 10^{-12} s;
- atomic polarization, with a characteristic time of order 10^{-14} s;
- electronic polarization, with a characteristic times of the order of 10^{-17} s.

The orientation polarization is due to relaxation phenomena, i.e. molecules and ions need a certain amount of time to align themselves to an applied field and when such a field is removed they need time to reorientate. Atomic and electronic polarization are due to resonance phenomena. The intramolecular vibrations or the motions of the electrons with respect to the nuclei due to an applied electrical field have discrete energy levels. This means that only at certain field strengths the atoms or electrons will move "permanently" to another position, in any other case they will fall back immediately. Although the above is a rather crude simplification of what really happens

in dielectric materials it can serve very well in the further exploration of the subject.

The explanation of the different phenomena on a microscopic level gives a better understanding of individual particles of certain materials under the influence of an electrical field. To explain the electrodynamic processes when a large group of such particles is involved, this theory has to be extended. H.A. Lorentz (1909) has developed his nowadays classic electron theory to be able to describe certain phenomena on this macroscopic scale. The fundamentals of this theory state:

- atoms and molecules consist of charged particles;
- by mutual electromagnetic influences these particles have a position or describe a trajectory relative to each other;
- the total of charged particles are positioned in vacuum (de Hoop, 1975).

Each one of these particles has a electric momentum \mathbf{p}_k defined as:

$$\mathbf{p}_k = q_k \mathbf{r}_k \quad (k = 1, \dots, K) \quad (2.6)$$

where q_k is the charge of the particle and the distance to a origin is represented by a vector \mathbf{r}_k , with k as the rank number of the particle ($k = 1, \dots, K$): The total moment \mathbf{p} of all K particles with respect to the origin is:

$$\mathbf{p} = \sum_{k=1}^K \mathbf{p}_k = \sum_{k=1}^K q_k \mathbf{r}_k \quad (2.7)$$

In general the value of \mathbf{p} of a group of charged particles depends on the choice of the origin. The value of \mathbf{p} becomes independent of the choice of origin when the total net charge of the group of particles equals zero ($\sum_{k=1}^K q_k = 0$) (de Hoop, 1975). In the case of dipoles this is always the case, because of the definition of a dipole as a pair of positive and negative charges. For a group consisting of ΔN charged particles with concentration $N = N(\mathbf{r}, t)$ in a volume V , the vector quantity \mathbf{P} can be defined as the electric moment per unit volume which is also called electric polarization:

$$\mathbf{P} = V^{-1} \sum_{k=1}^K \mathbf{p}_k \quad (2.8)$$

Since the electric field \mathbf{E} is proportional to and depends only on \mathbf{P} (see Appendix C), Eq. C.11 can be rewritten as:

$$\mathbf{P} = \mathbf{D} - \epsilon_0 \mathbf{E} = (\epsilon - \epsilon_0) \mathbf{E} = \chi_e \epsilon_0 \mathbf{E} \quad (2.9)$$

where \mathbf{D} is the electric flux density or dielectric displacement (see Appendix C). The factor χ_e is called the electric susceptibility of a dielectric material and can be written as:

$$\chi_e = \frac{\mathbf{P}}{\epsilon_0 \mathbf{E}} \quad (2.10)$$

Another quantity of a group of charged particles is the magnetic moment \mathbf{m} which is related to their orbit, this in contrast with the electric moment which is related to

the position of the particles. In analogy with the electric moment of a particle, the magnetic moment \mathbf{m}_k can be defined as (de Hoop, 1975):

$$\mathbf{m}_k = \frac{1}{2} \mathbf{r}_k \times q_k \mathbf{v}_k \quad (k = 1, \dots, K) \quad (2.11)$$

where \mathbf{v}_k is the velocity of particle k . The total moment \mathbf{m} of all K particles with respect to the origin is:

$$\mathbf{m} = \sum_{k=1}^K \mathbf{m}_k = \sum_{k=1}^K \left(\frac{1}{2} \mathbf{r}_k \times q_k \mathbf{v}_k \right) \quad (2.12)$$

The factor $\frac{1}{2}$ which appears in Eqs. 2.11 and 2.12 is only a matter of convention and has no specific physical reason. Although a distinction can be made between the magnetic moment induced by the particles orbit and the moment induced by the particles spin movement around its own axis (de Hoop, 1975), only the total magnetic moment is considered. The total magnetic moment per unit volume V and with concentration N of ΔN charged particles can be written as:

$$\mathbf{M} = V^{-1} \sum_{k=1}^{\Delta N} \mathbf{m}_k \quad (2.13)$$

The quantity \mathbf{M} is usually referred to as the magnetization (see section C.2.1, Eq. C.12) and depends only on the magnetic field strength: in which χ_m is the magnetic susceptibility.

With the theory described thus far the reaction of a material to an applied electromagnetic field can be analysed. The following equations summarise the relationship between the different fields and a material:

$$\mathbf{J} = \sigma_c \mathbf{E} \quad (2.14)$$

$$\mathbf{D} = \varepsilon \mathbf{E} = \varepsilon_0 \varepsilon_r \mathbf{E} \quad \text{with} \quad \varepsilon = \varepsilon_0(1 + \chi_e), \quad \text{or} \quad \varepsilon_r = 1 + \chi_e \quad (2.15)$$

$$\mathbf{B} = \mu \mathbf{H} = \mu_0 \mu_r \mathbf{H} \quad \text{with} \quad \mu = \mu_0(1 + \chi_m), \quad \text{or} \quad \mu_r = 1 + \chi_m \quad (2.16)$$

where \mathbf{J} is the electric current density, \mathbf{D} is the electric flux density or dielectric displacement and \mathbf{B} is the magnetic flux density (see Appendix C). In Eq. 2.14, which is also known as Ohm's law for a conducting material, σ_c represents the dielectric conductivity which may be an actual conductivity caused by migrating charges but may also represent some other source of friction like the orientation of dipoles (Hippel, 1958). The relationships given by Eqs. 2.14, 2.15 and 2.16 become more complex with increasing complexity of the properties of the materials e.g. when materials with various properties are combined or influence each other chemical properties.

The dependence of $\mathbf{P} = \mathbf{P}(\mathbf{r})$ on $\mathbf{E} = \mathbf{E}(\mathbf{r})$ is given as a simple scalar proportionality (cf. with Eq. 2.10 which is relative to ε_0):

$$\mathbf{P} = \chi_e \mathbf{E} \quad (2.17)$$

which is in many cases a good approximation such that Eq. 2.15 can be applied. However, this proportionality is only valid for moderate field strengths and for isotropic materials and is dependent on density, temperature and chemical composition of the medium (Böttcher & Borderwijk, 1978a). In the case of non-isotropic materials the scalar electric susceptibility has to be replaced by a tensor with dimension N :

$$\mathbf{P}_k = \sum_{l=1}^N (\chi_e)_{kl} \cdot \mathbf{E}_l \quad (2.18)$$

and thus in Eq. 2.15 the permittivity becomes a tensor. At very high field intensities \mathbf{P} is no longer proportional to \mathbf{E} , which is called electric saturation, and a correction term should be added (Böttcher & Borderwijk, 1978a). The last exception mentioned here on the relationship as given by Eq. 2.15 is that $\mathbf{P} = \mathbf{P}(\mathbf{r}, t)$ and $\mathbf{E} = \mathbf{E}(\mathbf{r}, t)$ are dependent on time. If the applied electrical field changes its strength in the same order of magnitude as the characteristic time of the microscopic particles, the particles will not be able to adjust to the field and will not reach the equilibrium polarization. The actual polarization reached will lag behind the changing electrical field. The polarization is in this case no longer proportional to electric field strength, but depends on the values of \mathbf{E} at all moments before the time t at which \mathbf{P} is considered:

$$\mathbf{P}(\mathbf{r}, t) = \int_{-\infty}^t f(\mathbf{r}, t - t') \cdot \mathbf{E}(\mathbf{r}, t') dt' \quad (2.19)$$

Relaxation and resonance phenomena are covered by this equation. For electric fields which time dependence can be described by a harmonic function, the permittivity in Eq. 2.15 can be described by a complex permittivity. In the quasi static case, i.e. when time period of the electric field changes is much larger than the characteristic time of the particles, Eq. 2.15 can still be applied.

2.3 Dielectric behaviour of various materials

2.3.1 Homogenous materials

The easiest material to describe is a mono-atomic gas at low pressure. In this case the interaction between the electromagnetic field and the gas molecules, and the change of the electric field due to the presence of these molecules can be neglected. One of the first equations which describes the polarizability per mole, Π , is the Clausius-Mosotti equation (Hippel, 1958):

$$\Pi = \frac{N_0 \alpha}{3\epsilon_0} = \frac{\epsilon'_r - 1}{\epsilon'_r + 2} \frac{M}{\rho} \quad (2.20)$$

where N_0 is Avogadro's number, α is the total polarizability of the material accounting for the electric charge carriers and their polarizing action for non-alternating fields, M is the molecular weight and ρ is the particle density. To generalise the equations

for alternating electromagnetic fields, α and the permittivity ϵ become complex, consequently the so-called Clausius-Mosotti-Lorentz-Lorenz equation can be obtained:

$$\Pi = \frac{N_0 \alpha}{3\epsilon_0} = \frac{\epsilon - 1}{\epsilon + 2} \frac{M}{\rho} = \frac{n^2 - 1}{n^2 + 2} \frac{M}{\rho} \quad (2.21)$$

A disadvantage of this equation is that the effect of neighbouring molecules is not accounted for and thus neglects the distortion of the "near field". At higher densities this can give rise to erroneous results.

To describe the dielectric behaviour of pure liquid water is much more difficult, not only because the density is much higher than for a gas but also because water molecules are dipoles. In dense materials, as opposed to gasses, molecules or molecular groups need space to rotate which causes friction. Especially, in the case of dipole molecules since they are essential construction elements of a material due to their specific charge distribution. For polar molecules Debye derived his well-known formula (Debye, 1929):

$$\epsilon = \epsilon_\infty + \frac{\epsilon_s - \epsilon_\infty}{1 + j\omega\tau} \quad (2.22)$$

with,

$$\omega = 2\pi f \quad (2.23)$$

where f is the frequency and ω is the angular frequency, ϵ_∞ is the high frequency (or optical) limit of ϵ representing electronic and atomic resonance polarization of the dielectric, ϵ_s is the static permittivity representing the polarization due to the contribution of the orientation of the permanent moments and τ is the relaxation time of the material, in this case pure liquid water. Writing Eq. 2.22 separately for ϵ' and ϵ'' ,

$$\epsilon' = \epsilon_\infty + \frac{\epsilon_s - \epsilon_\infty}{1 + (\omega\tau)^2} \quad (2.24)$$

$$\epsilon'' = \frac{\omega\tau(\epsilon_s - \epsilon_\infty)}{1 + (\omega\tau)^2} \quad (2.25)$$

in which the variables ϵ_∞ , ϵ_s and τ are a function of temperature and the latter two also of frequency (Ulaby *et al.*, 1986; Tinga & Nelson, 1973). The relaxation time τ is the time required to reduce the polarisation to $1/e$ of its original value, after the applied electromagnetic field is removed. Instead of using the relaxation time often the term relaxation frequency f_0 is used:

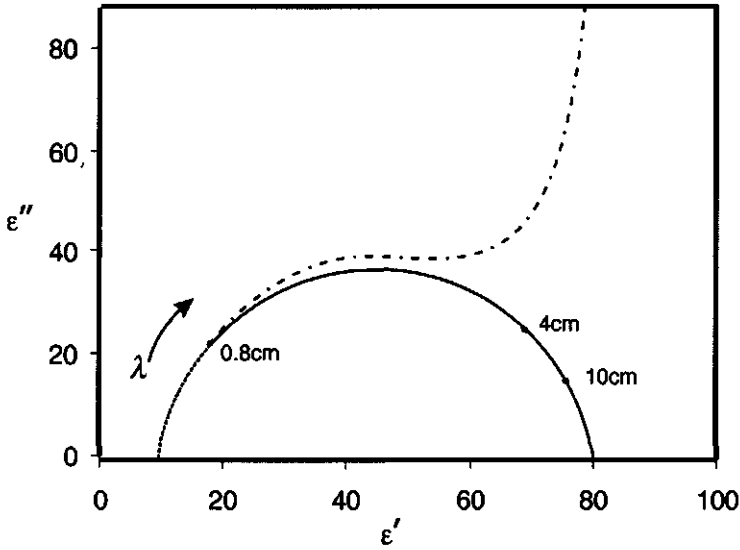


Figure 2.2: The Cole-Cole diagram for pure water (solid line) and sea water (dashed line)

$$f_0 = (2\pi\tau)^{-1} \quad (2.26)$$

The relaxation frequency of pure water lies in the microwave region, at a temperature of 0 °C around 9 GHz and at a temperature of 20 °C at 17 GHz (Ulaby *et al.*, 1986). A useful way to analyse the Debye equation is to plot the real ϵ' and the imaginary part ϵ'' of the permittivity in the complex plane with the frequency as the changing variable. Data points obeying the Debye equation will fall onto a semicircle. This plot is the so called the Cole-Cole diagram (see Fig. 2.2). Although the Debye equation is derived originally for dipolar relaxation phenomena and thus for polar materials it is often applicable in other cases.

This treatment could be somewhat more extended for materials and combination of materials e.g. like solutions of water and dissolved salts with small to moderate concentrations (Ulaby *et al.*, 1986; Lane & Saxton, 1952). The presence of salts in a solution increases the ionic conductivity. Therefore Eq. 2.22 is modified to account for the losses caused by this conductivity (Lane & Saxton, 1952):

$$\epsilon'' = \frac{\omega\tau(\epsilon_s - \epsilon_\infty)}{1 + (\omega\tau)^2} + \frac{\sigma_c}{\omega\epsilon_0} \quad (2.27)$$

with σ_c as the ionic conductivity.

In general the Debye-type of equations satisfy the simple relaxation spectra of solutions of polar materials in non polar solvents (Hippel, 1958), in other cases one has to use different approaches.

2.3.2 Soil and other heterogeneous materials

A heterogeneous material or mixture consists of two or more constituents each having its own specific dielectric behaviour. The permittivity of the mixture is determined by its constituents and has a magnitude which is between the maximum and minimum value of the permittivity of the constituents, unless they are altered when combined in the mixture. The average permittivity of the material is thus a function of:

- the individual substances;
- their relative volume fractions;
- their spatial distributions;
- their shapes;
- their orientations relative to the direction of the applied or present electromagnetic field;
- physical temperature;
- and the electromagnetic frequency.

The latter two are often interchangeable when the distribution of the relaxation times is temperature independent (Tinga & Nelson, 1973). This condition is no longer satisfied when e.g. a temperature rise causes the physical state or chemical composition to change (Engelder & Buffler, 1991). The constituent with the highest volume fraction is usually taken as the host material or continuous medium and the other constituents are then considered as inclusions (Ulaby *et al.*, 1986). To be able to relate the factors determining the average permittivity to this average permittivity it is necessary to relate the average electromagnetic field of the mixture as a whole to the electromagnetic fields within the inclusions (Ulaby *et al.*, 1986; Hasted, 1973; de Loor, 1956). According to De Loor (de Loor, 1956; de Loor, 1983) it is in fact *impossible to give one single relationship which describes the permittivity of a heterogeneous mixture*. He stated that *at best boundaries can be given between which the average value must lie*, and which come closer together the more is known about the mixture.

The difficulty in finding a solution for the magnitude of the fields is that when the position and shape of the inclusions is unknown or too complicated, an exact solution cannot be found. Different kinds of approximations have been used, with varying approaches such as ignoring the short-range or even all interactions between inclusions, assigning an effective permittivity to the immediate surroundings of an inclusion (de Loor, 1956) to accounting for first order inclusion interactions by solving Maxwell's equations with appropriate boundary conditions (Tinga & Nelson, 1973). All of these models are based upon certain specific assumptions regarding shape, size, geometry, volume fractions, the distribution of inclusions, frequency range etc. and are therefore limited to specific conditions or mixtures. In all cases the wavelength λ of the radiation propagating in the mixture medium is considered to be much larger than the size of the inclusions in the mixtures (*Rayleigh criterion* for particles with radius a : $2\pi a \ll \lambda$). The magnetic permeability of most mixtures is considered to be near that of free space. Hence, the permittivity thus characterizes fully the electromagnetic response of these mixtures. In the further text the magnetic permeability will only be mentioned where appropriate.

The mechanisms responsible for polarization in media discussed so far only took into account the displacement or orientation of bound-charge carriers (electronic, atomic

and orientation polarization). A characteristic of heterogeneous mixtures is that there are boundaries between the components. Under an applied electromagnetic field these boundaries can become a barrier for travelling charges and distortion of the electric field can result (Maxwell-Wagner effects and interfacial polarization). An additional effect of a combination of several components in a mixture is that the single relaxation times for each of the constituents broaden into relaxation spectra for the combination of the constituents. In the next sections a few of the approaches to determine the permittivity of heterogeneous mixtures will be discussed. Although soils are used most of the time as an example for an heterogeneous mixture the theory also applies to other mixtures like wood, vegetation, textiles, brick and foods. The latter have become very important since the introduction of microwave heating. In the next sections the most common mixture formulas will be given. For a thorough overview of different mixing models the reader is referred to De Loor (1956), Van Beek (1967), Tinga & Nelson (1973) and Ulaby *et al.*, (1986).

2.3.3 Semi-empirical approaches

The empirical approaches use simple, easy retrievable parameters to link the permittivities of the constituents to the permittivity of the mixture. Often polynomial expressions are derived with regression analysis to link one or more factors to the permittivity. Topp *et al.* (1980) fitted such an expression linking ϵ_r to θ for a three phase mixture of air, water and soil:

$$\epsilon_r = 3.03 + 9.3\theta + 146.0\theta^2 - 76.7\theta^3 \quad (2.28)$$

rewritten in its most used but not exactly equivalent form,

$$\theta = -5.3 \cdot 10^{-2} + 2.92 \cdot 10^{-2} \epsilon_r - 5.5 \cdot 10^{-4} \epsilon_r^2 + 4.3 \cdot 10^{-6} \epsilon_r^3 \quad (2.29)$$

with θ as the volume fraction of water.

The semi-empirical approaches relate the effective or average relative permittivity ϵ_r of a multiphase mixture to the permittivities and volume fractions of the components using a parameter or correction factor which accounts for the deviations. Often the correction factor is considered to be a shape factor which accounts for the geometry of the particles, however this factor is in these models not physically based but empirically determined. An advantage of these models is that factors that influence the permittivity like frequency can be better accounted for.

An often encountered example of such an empirical formula is that of Birchak, (1974) which is based upon volumetric mixing (Dobson *et al.*, 1985; Ulaby *et al.*, 1986):

$$\epsilon_r^\alpha = \sum_{i=1}^n \phi_i \epsilon_{ri}^\alpha \quad (2.30)$$

where n is the number of phases present and the subscript i denotes the phase, α is the correction or shape factor and ϕ the volume fraction of the constituent. Birchak *et al.* (1974) found $\alpha = 0.5$ for an isotropic two phase medium and Ansoult *et al.* (1984) used a discretized statistical model for a wet soil and found that $\alpha = -1$ and $\alpha = 1$ are the lower and upper boundaries.

Dobson *et al.* (1985) rewrote the mixing model of Birchak for a four phase mixture (where the notation ϵ instead of ϵ_r is used for clarity):

$$\epsilon^\alpha = \phi_s \epsilon_s^\alpha + \phi_a \epsilon_a^\alpha + \phi_{fw} \epsilon_{fw}^\alpha + \phi_{bw} \epsilon_{bw}^\alpha \quad (2.31)$$

where subscripts s , a , fw and bw denote solid phase, air, free water and bound water respectively. Dobson *et al.* (1985) used $\alpha = 0.65$ as average for all their soils and frequencies (1.4-18 GHz) and made the following approximation:

$$\epsilon^\alpha = 1 + \frac{\rho_b}{\rho_s} (\epsilon_s^\alpha - 1) + \theta^\beta \epsilon_{fw}^\alpha - \theta \quad (2.32)$$

Thus

$$\epsilon' = \left[1 + \frac{\rho_b}{\rho_s} (\epsilon_s^\alpha - 1) + \theta^{\beta_1} \epsilon_{fw}^\alpha - \theta \right]^{\frac{1}{\alpha}} \quad (2.33)$$

$$\epsilon'' = \left[\theta^{\beta_2} \epsilon_{fw}^\alpha \right]^{\frac{1}{\alpha}} \quad (2.34)$$

with

$$\epsilon_s = (1.01 + 0.44\rho_s)^2 - 0.062 \quad (2.35)$$

where ρ_b is the dry bulk density and ρ_s the specific density of soil solid particles (here 2.66 g cm^{-3}). The empirical constants β_1 and β_2 are soil dependent and are given by:

$$\beta_1 = 1.2748 - 0.519S - 0.152C \quad (2.36)$$

$$\beta_2 = 1.33797 - 0.603S - 0.166C \quad (2.37)$$

where S and C are the mass fractions of sand and clay respectively (Peplinski *et al.*, 1995). The relative dielectric constant of free water is given by a modified Debye dispersion equation (see Eqs. 2.22-2.27) with a term added to correct for the effective (ionic) conductivity of the soil mixture:

$$\epsilon_{fw} = \epsilon_\infty + \frac{\epsilon_s - \epsilon_\infty}{1 + j2\pi f\tau} - j \frac{\sigma_{eff}}{2\pi f\epsilon_0} \frac{\rho_s - \rho_b}{\rho_s \theta} \quad (2.38)$$

Written for ϵ'_{fw} and ϵ''_{fw} explicitly:

$$\epsilon'_{fw} = \epsilon_{\infty} + \frac{\epsilon_s - \epsilon_{\infty}}{1 + (2\pi f\tau)^2} \quad (2.39)$$

$$\epsilon''_{fw} = \epsilon_{\infty} + \frac{2\pi f\tau (\epsilon_s - \epsilon_{\infty})}{1 + (2\pi f\tau)^2} + \frac{\sigma_{eff} \rho_s - \rho_b}{2\pi f\epsilon_0 \rho_s \theta} \quad (2.40)$$

where ϵ_s is the static permittivity for water ($= 80.1$ at $T = 20^\circ\text{C}$), ϵ_{∞} is the high frequency limit for water (≈ 4.9 (Lane & Saxton, 1952)). Above 4 GHz the contribution of the conductivity to ϵ''_{fw} becomes negligible due to the inverse proportionality with f . For frequencies between 1.4 and 4 GHz the effective conductivity σ_{eff} , can be expressed as function of the soil textural properties (Dobson *et al.*, 1985):

$$\sigma_{eff} = -1.645 + 1.939\rho_b - 2.25622S + 1.594C \quad (2.41)$$

For frequencies between 0.3-1.3 GHz the following equation gave a better fit between modeled and measured ϵ'' , especially at the lower frequencies (Peplinski *et al.*, 1995):

$$\sigma_{eff} = 0.0467 + 0.2204\rho_b - 0.4111S + 0.6614C \quad (2.42)$$

At these same low frequencies (Peplinski *et al.*, 1995) found that for the real part of the permittivity only a slight correction was needed to adjust modeled ϵ' (with Eq. 2.33) to measured $\epsilon'_{meas.}$:

$$\epsilon'_{meas.} = 1.15\epsilon' - 0.68 \quad (2.43)$$

Wang and Schmugge (1980) developed a somewhat more elaborate semi-empirical model to describe the dielectric behaviour of a wet soil with volumetric soil water content ranging from 0 to $0.5 \text{ cm}^3\text{cm}^{-3}$ and for frequencies between 1 and 5 GHz. These authors employ the permittivity of ice to describe the dielectric behaviour of the bound water in the soil water mixture. They also make a distinction between cases where the volumetric soil water content θ is smaller than or equal to the transition soil moisture content ($\theta \leq \theta_t$) and cases where it is larger ($\theta > \theta_t$). The transition moisture content θ_t is the maximum bound water content, where the value of the dielectric constant of initially absorbed water approaches that of liquid water. This transition water content θ_t is found through a linear regression equation:

$$\theta_t = 0.49\theta_{wp} + 0.165 \quad (2.44)$$

in which, θ_{wp} is the amount of moisture present in the soil at a soil water pressure head $h = -16000 \text{ cm}$ (wilting point) and is calculated as a function of soil texture expressed in terms of volume fractions sand ϕ_{sand} and clay ϕ_{clay} :

$$\theta_{wp} = 0.06774 - 0.064 \times \phi_{sand} + 0.478 \times \phi_{clay} \quad (2.45)$$

If the porosity of the dry soil ϕ is known then the permittivity can be calculated for the two situations. Thus, if we express the porosity as:

$$\phi = 1 - \frac{\rho_s}{\rho_r} \quad (2.46)$$

with ρ_s density of dry soil and ρ_r as the density of associated solid rock. Then the expressions for the complex dielectric constants of a soil-water mixture for $\theta \leq \theta_t$:

$$\varepsilon = \theta \varepsilon_x + (\phi - \theta) \varepsilon_a + (1 - \phi) \varepsilon_r, \quad \theta \leq \theta_t \quad (2.47)$$

with the dielectric constant of initially absorbed water, ε_x :

$$\varepsilon_x = \varepsilon_i + (\varepsilon_w - \varepsilon_i) \frac{\theta}{\theta_t} \gamma \quad (2.48)$$

where γ is a fitting parameter which is equal to (Wang & Schmugge, 1980):

$$\gamma = -0.57\theta_{wp} + 0.481 \quad (2.49)$$

For $\theta > \theta_t$:

$$\varepsilon = \theta_t \varepsilon_x + (\theta - \theta_t) \varepsilon_w + (\phi - \theta) \varepsilon_a + (1 - \phi) \varepsilon_r, \quad \theta > \theta_t \quad (2.50)$$

with

$$\varepsilon_x = \varepsilon_i + (\varepsilon_w - \varepsilon_i) \gamma \quad (2.51)$$

In the Eqs 2.47 - 2.51, ε_a , ε_w , ε_r , and ε_i are the dielectric constants of air, water, rock and ice respectively. The dielectric constant for ice can be set at:

$$\varepsilon_i = 3.2 + j0.1 \quad (2.52)$$

To calculate the dielectric loss or the imaginary part of the permittivity at low frequencies ($f \leq 5$ GHz) a conductivity loss can be added using the following equation:

$$\varepsilon_t'' = \varepsilon'' + 60\lambda\sigma_c \Rightarrow \varepsilon'' + \alpha\theta^2$$

in which λ is the wavelength [cm] and σ_c is the ionic conductivity [mho cm⁻¹]. Wang and Schmugge assumed the total dielectric loss, ε_t'' to be proportional to θ^2 with α as a fitting parameter. In this model the permittivities of the different phases have to be known or derived and then fitted to the data using γ and θ_t as parameters.

Numerous other empirical and semi-empirical models have been developed (e.g. (Wang, 1980; Wobschall, 1977)), too many to treat them all in this Chapter. In general, the

use of semi-empirical models has the disadvantage that they are sensitive to the fitting parameter(s), that a fitting parameter is not known a priori and that apparent 'anomalous' dielectric behaviour is not accommodated for (Dirksen & Dasberg, 1993).

For most purposes within remote sensing the use of the simple empirical mixing models of Wang and Schmugge (1980) and Dobson et al. (1985) to describe the dielectric properties seems to be sufficient. In these empirical models the errors involved for most areas and types of soils are small compared to other error sources involved in remotely sensed estimation of soil moisture. These mixing models are therefore used in the rest of this thesis.

2.3.4 De Loor-Polder and Van Santen based formula

In this section the derivation of this mixture formula is given following the work of De Vries (1952) and De Loor (1956). Given is a mixture of a continuous, isotropic host medium with a permittivity ϵ_h and with, randomly ordered, N different kinds of inclusions of type i , with a permittivity ϵ_i . The total volume fraction of the mixture is thus:

$$\sum_{i=0}^N \phi_i = 1 \quad (2.53)$$

If this mixture with volume V is placed in a capacitor and side-effects can be neglected then the average electrical field $\bar{\mathbf{E}}$ strength equals:

$$\bar{\mathbf{E}} = \frac{1}{V} \int \mathbf{E} dV = \frac{1}{V} \int \sum_{i=0}^N \mathbf{E}_i dV = \sum_{i=0}^N \phi_i \bar{\mathbf{E}}_i \quad (2.54)$$

with

$$\bar{\mathbf{E}}_i = \frac{1}{V} \int \mathbf{E}_i dV_i \quad (2.55)$$

The average dielectric displacement $\bar{\mathbf{D}}$ in this situation is:

$$\begin{aligned} \bar{\mathbf{D}} &= \frac{1}{V} \int \mathbf{D} dV = \sum_{i=0}^N \phi_i \bar{\mathbf{D}}_i = \sum_{i=0}^N \phi_i \epsilon_i \bar{\mathbf{E}}_i \\ &= \epsilon_h \bar{\mathbf{E}} + \sum_{i=0}^N \phi_i (\epsilon_i - \epsilon_h) \bar{\mathbf{E}}_i \end{aligned} \quad (2.56)$$

The average or apparent permittivity ϵ_m of the material:

$$\epsilon_m = \frac{\overline{D}}{\overline{E}} = \frac{\sum_{i=0}^N \epsilon_i \phi_i \overline{E}_i}{\sum_{i=0}^N \phi_i \overline{E}_i} \quad (2.57)$$

From Eq. 2.57 it can be seen that to solve the problem it is necessary to calculate the electric field \mathbf{E}_i for every constituent. Since this gives rise to some mathematical difficulties, preliminary assumptions to simplify the problem have to be made. Suppose that an inclusion i with a permittivity ϵ_i is surrounded by a homogeneous, isotropic medium with a permittivity ϵ_{eff} (effective permittivity) and an average electric field strength \mathbf{E}_{eff} at great distance of the considered inclusion. With these assumptions the relationship between the electric field strength \mathbf{E}_i and \mathbf{E}_{eff} can be described by a tensor relationship:

$$(\mathbf{E}_i)_k = \sum_{l=1}^3 \mathbf{T}_{kl} (\mathbf{E}_{eff})_l \quad (2.58)$$

in which the tensor \mathbf{T}_{kl} depends on ϵ_{eff} , ϵ_i and the shape of the inclusions. If the average over all inclusions of type i is taken under the supposition that their arrangement is random then (Polder & van Santen, 1946):

$$\overline{\mathbf{E}}_i = \frac{1}{3} (T_{11} + T_{22} + T_{33}) \mathbf{E}_{eff} = (K_{eff})_i \mathbf{E}_{eff} \quad (2.59)$$

A closed form relationship for the diagonal elements of the tensor \mathbf{T}_{kl} can only be found in case of Rayleigh scattering for ellipsoidal shaped inclusions or particles:

$$T_{11} = T_a = \frac{1}{1 + \left(\frac{\epsilon_i}{\epsilon_{eff}} - 1 \right) A_a}, \quad (2.60)$$

in which A_a is the depolarization factor of the ellipsoidal inclusions in the direction of the a -axis. The depolarization factors A_a can be determined by (Burger, 1915; Stratton, 1941):

$$A_a = \frac{1}{2} abc \int_0^\infty \frac{ds}{(a^2 + s)^{\frac{3}{2}} (b^2 + s)^{\frac{1}{2}} (c^2 + s)^{\frac{1}{2}}} \quad (2.61)$$

with s as distance, for ellipsoidal particles or inclusions with semi-axes a , b , c . Furthermore:

$$A_a + A_b + A_c = 1. \quad (2.62)$$

Thus for spherical inclusions $a = b = c$:

$$A_a = A_b = A_c = \frac{1}{3} \quad (2.63)$$

Another example are disc-shaped granules with $a = b = 0$ and $c = 1$. For more examples of other ellipsoidal shapes the reader is referred to De Vries (1952).

The tensor T_{kl} in Eq. 2.58 can be rewritten as:

$$T_j = \sum_{j=a,b,c} \frac{1}{1 + \left(\frac{\epsilon_i}{\epsilon_{eff}} - 1 \right) A_j} \quad (2.64)$$

with j representing the directions of the three axes of the ellipsoid. Using Eqs. 2.58 and 2.64 with $E_{eff} = \bar{E}$ the relationship known as the De Loor and Polder-Van Santen equation can be obtained:

$$\epsilon_m = \epsilon_h + \sum_{i=1}^N \frac{\phi_i}{3} (\epsilon_i - \epsilon_h) \sum_{j=a_i,b_i,c_i} \frac{1}{1 + \left(\frac{\epsilon_i}{\epsilon_{eff}} - 1 \right) A_{ji}} \quad (2.65)$$

in which a_i, b_i , and c_i are the semi-axes of the ellipsoidal inclusions of material i .

Another way to derive Eq. 2.65 has been described by De Loor (1956) and Van Beek (1969). De Loor (1956) modified the mixture formula of Polder and Van Santen by assigning an effective permittivity, ϵ_{eff} . In Eq.2.65 this effective permittivity accounts for all the interactions and spatial irregularities of the other inclusions (de Loor, 1990). Since in general no information is available on ϵ_{eff} this equation can only be solved for certain assumptions concerning ϵ_{eff} . If the shape factor is known for a mixture which can be regarded as a lossless dielectric (e.g. no losses due to conduction), then the permittivity of this mixture must lie between the boundaries given by $\epsilon_{eff} = \epsilon_h$ and $\epsilon_{eff} = \epsilon_m$. With the shape factor not known then the boundaries become $\epsilon_{eff} = \epsilon_h$ with $A_j = \left\{ \frac{1}{3}, \frac{1}{3}, \frac{1}{3} \right\}$ and $\epsilon_{eff} = \epsilon_m$ with $A_j = \{ 0, 0, 1 \}$ (de Loor, 1990). According to De Loor (1990) a mixture composed of substances A and B can be distinguished in three different regions: (1) best described by a host medium A with inclusions B ($\phi_A > \phi_B$), (2) with host medium B with inclusions A ($\phi_B > \phi_A$) and one region between the two mentioned ones where it is difficult to distinguish between situation (1) or (2) ($\phi_A \approx \phi_B$). Usually the transition point between the different regions lies somewhere between a volume fraction ϕ_i of 0.2 and 0.3.

With microwave remote sensing of soils most of the phenomena responsible for dielectric losses, that make Eq. 2.65 less applicable, are absent. Only the relaxation of

water plays a role and thus the amount of free water present in the mixture is of importance. Just below the microwave frequencies ($100 \text{ MHz} < f < 1 \text{ GHz}$) effects due to conductivity, relaxation and the form of water, i.e. the transition from bound water to free water, cause the dielectric losses which are not accounted for by the model. At lower frequencies the situation gets more complicated, making it impossible to distinguish the different phenomena responsible for the losses that occur. However, all these losses cause the conductivity to be nearly constant over a fairly large frequency range (de Loor, 1990).

Dobson *et al.* (1985) modified the model of De Loor and developed a theoretical soil model which describes the presence of a hydration layer of bound water adjacent to hydrophilic soil particle surfaces. With this soil model they separated the total soil water content solution in a bound and free (bulk) water part and determined the effective conductive loss of the bulk water using the Stern-Gouy double-layer theory (van Olphen, 1963; Mitchell, 1976). The model of De Loor was modified into a four component mixing model with the following components; dry soil solids, bound water in the Stern-layer, bulk water in the Gouy layer and air. Dobson *et al.* (1985) assumed that $\epsilon_{eff} = \epsilon_m$ and that, on the basis of their soil model that the plate-like clay mineral fraction dominates both the distribution and nature of the soil water, the inclusions are disc-shaped with $A_j = \{ 0, 0, 1 \}$. Eq. 2.65 with the soil solids as host medium can then be rewritten as:

$$\epsilon_m = \frac{3\epsilon_s + 2\phi_{fw}(\epsilon_{fw} - \epsilon_s) + 2\phi_{bw}(\epsilon_{bw} - \epsilon_s) + 2\phi_a(\epsilon_a - \epsilon_s)}{3 + \phi_{fw}\left(\frac{\epsilon_s}{\epsilon_{fw}} - 1\right) + \phi_{bw}\left(\frac{\epsilon_s}{\epsilon_{bw}} - 1\right) + \phi_a\left(\frac{\epsilon_s}{\epsilon_a} - 1\right)} \quad (2.66)$$

where subscripts *bw*, *fw*, *a*, and *s* refer to bound water, free water, air and soil, respectively.

The volume fractions are calculated using a soil physical model based upon knowledge of soil texture, soil specific surface and bulk and specific density (Dobson *et al.*, 1985). The permittivity for air is: $\epsilon_a = 1.0$. They found the permittivity for the soil particles with specific density ρ_s by fitting experimental data of soils with very low moisture content: $\epsilon_s = (1.01 + 0.44\rho_s)^2 - 0.062$. And for the permittivity of bulk water they used Debye type of relations as discussed in section 2.3.1 (Eqs. 2.22 until 2.27), and the ionic conductivity calculated with their soil model. For the permittivity of bound water they tested two assumptions

1. $\epsilon_{bw} = \epsilon_{ice} = 3.15 - j0$
2. $\epsilon_{bw} = \epsilon_{saline} = 35 - j15$ of saline water with salinity $S = 5^0/_{00}$ at $T = 22^\circ\text{C}$.

Dobson *et al.* (1985) concluded that adding the component of bound water is necessary to account for the frequency and soil dependence of the permittivity and that the De Loor model is an adequate description of the permittivity of the soil with soil texture, bulk density and a frequency range from 1.4 to 18 GHz. They found that the permittivity of bound water did not match either that of ice or saline water and that comparing model predictions with the measured data the real part should be of order 20 to 40 and bound water is lossy.

The empirical model of Dobson et al. (1985) performs almost as good as their theoretical model and therefore the simpler empirical model is used in this thesis. However, in case of anomalous dielectric behaviour the empirical model will not be adequate.

The approach of De Loor was to assign an effective permittivity to account for the interaction effects, without quantifying these effects explicitly. The work of Tinga et al. (1973) gives a quantitative method for calculating the interaction effects and the correct limits for both low- and high-volume filling factors. They derived a closed form solution for the complex permittivity of a multiphase mixture with ordered confocal ellipsoidal shell inclusions. Although this approach is theoretically interesting, it is too complex to be used for practical purposes with remote sensing.

2.4 Effects of salinity and soil texture on soil dielectric properties

The various soil mixture models that have been treated in this thesis have each their specific validity range and applicability. *The dielectric properties are a function of frequency and it is noticeable that the mixture models for heterogeneous materials do not have the frequency as a parameter but instead have a frequency range of validity, assuming the frequency dependence to be constant within that region.* For soils with a low soil moisture content and/or with low salinity this assumption is applicable (Figure 2.3). However for certain type of soils with high salinity, such as bentonite or clays with a saline solution (Figure 2.3), this is not true. Especially at the lower frequencies (below 1 GHz) the imaginary part of the permittivity increases rapidly with decreasing frequency even at low θ (Figure 2.3). Most natural soils do not have such a high salinity and therefore for most practical purposes soil mixing models within the 1 to 10 GHz range do not have to be corrected for salinity effects. These findings are in agreement with the experimental data from Jackson and O'Neill, 1987.

The effect of soil texture is twofold:

- soil texture is strongly related to the specific surface area of a soil which determines along with the type of mineral the amount of bound water that can be adsorbed and the total water that can be held;
- it is an important parameter in the formation of soil aggregates and stability.

The first effect has its direct influence on the dielectric properties of a soil (Dobson et al., 1985). The effect of soil texture on the dielectric properties can be assessed through the various mixture models (Ulaby et al., 1986). The effect is most significant for clay soils especially those which have a high adsorption capacity where for the same θ the real part of the dielectric properties is lower and often the imaginary part is higher compared to soils with a coarser texture.

The second effect has its influence on the surface roughness. The effect on the surface roughness is difficult to determine and would need an extensive experimental set-up which is outside of the scope of this study.

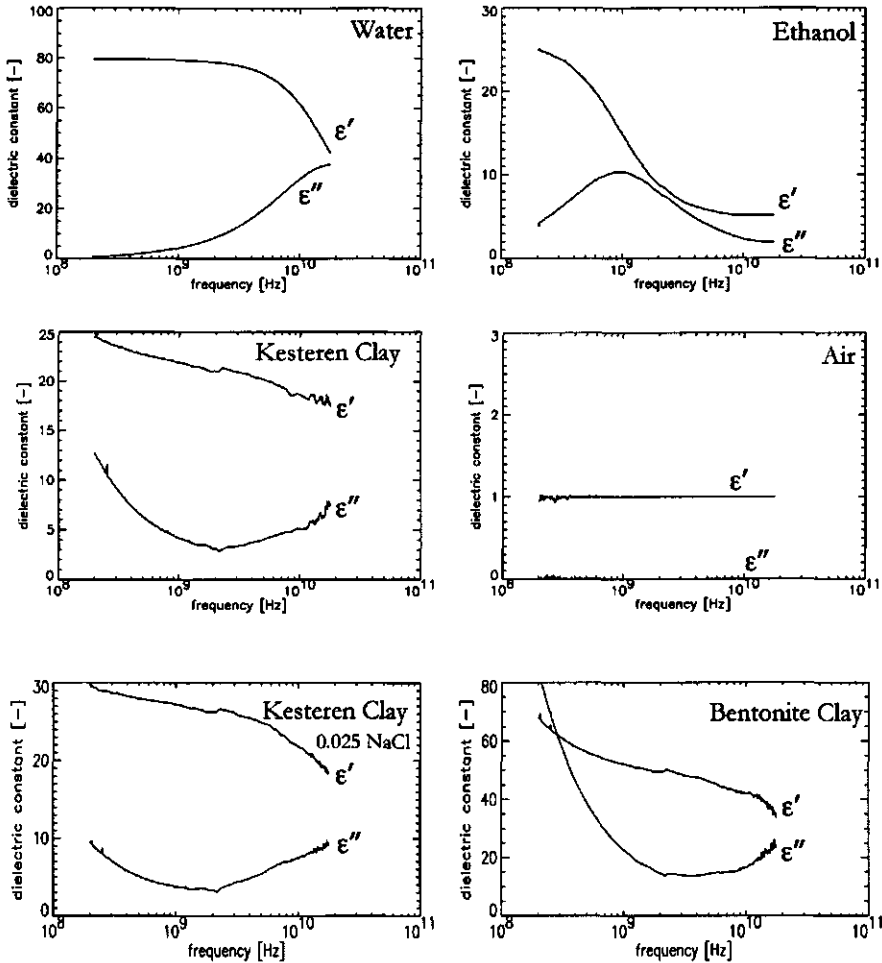


Figure 2.3: The real part (top line) and imaginary part (bottom line) of the permittivity of pure water, ethanol, Kesteren clay, air, Kesteren clay with a 0.025 NaCl solution and Bentonite clay as measured by the author. The water content θ for the soils is 0.25.

2.5 Conclusions

In this Chapter the basic theory of dielectric properties has been given. The effects of an electro-magnetic field upon various materials was explained starting from a mono-atomic gas to multi-phase heterogeneous materials such as soils.

Many models exist to describe the dielectric properties at microwave frequencies based upon soil composition and properties. The more complex models are better able to explain specific phenomena but require much more detailed information or have unrealistic assumptions (e.g. particle shape) to be of any practical use.

The semi-empirical models such as that of Wang and Schmugge (1980) relate the effective or average permittivity of a multiphase mixture to the permittivities and volume fractions of the components using a correction factor which accounts for the deviations. The use of these type of models has the disadvantage that they are sensitive to the fitting parameter(s), that the fitting parameter is not known a-priori and that apparent "anomalous" behaviour is not accommodated for.

The theoretical models such as De Loor's model (de Loor, 1956; de Loor, 1990) relate the average electromagnetic field of the mixture as a whole to the electromagnetic fields within the inclusions and calculate in this way the permittivity. The constituent with the highest volume fraction is usually taken as the host material or continuous medium and the other constituents are then considered as inclusions (Ulaby *et al.*, 1986). According to De Loor (de Loor, 1956; de Loor, 1983) it is in fact impossible to give one single relationship which describes the permittivity of a heterogeneous mixture. He stated that at best boundaries can be given between which the average value must lie, and the range by these boundaries can become smaller when more is known about the mixture. Dobson *et al.* (1985) modified the model of De Loor and concluded that *adding the component of bound water was necessary to account for the frequency and soil dependence of the permittivity and that the De Loor model was an adequate description of the permittivity of the soil with soil texture, bulk density and a frequency range from 1.4 to 18 GHz.*

The dielectric properties are a function of frequency and it is noticeable that most mixture models for heterogeneous materials do not have the frequency as a parameter but instead have a frequency range of validity, assuming the frequency dependence to be constant within that region.

The effect of soil texture on the dielectric properties is most significant for clay soils especially those which have a high adsorption capacity where for the same θ the real part of the dielectric properties is lower and often the imaginary part is higher as compared to soils with a coarser texture. The soil texture has also its influence on the surface roughness however this effect is not treated in this study.

The theory of dielectric properties of soils still requires attention in specific areas especially for soils with a distinct chemical composition such as high iron content, high salinity soils and gypsum soils. For some of these types of soils the dielectric behavior is very different but cannot be explained sufficiently.

For most purposes within remote sensing the use of empirical mixing models to describe the dielectric properties such as those of Wang and Schmugge (1980) and Dob-

son et al. (1985) seems to be sufficient. In these empirical models the errors involved for most areas and types of soils are small compared to other error sources involved in remotely sensed estimation of soil moisture. These mixing models are therefore used in the rest of this thesis.

Chapter 3

Microwave emission and scattering of bare soil and vegetated surfaces

3.1 Introduction

The behaviour of electromagnetic radiation in the microwave region, in particular at the lower frequencies ($f < 20$ GHz) is significantly different from higher frequency or optical remote sensing. In this Chapter a description of the relevant quantities and theories is given.

The earth's surface, in particular a bare soil surface can be considered as a rough surface in terms of microwave emission and scattering. Often this surface is covered by vegetation or other objects which obscure the surface underneath and can be considered perturbing factors when dealing with the estimation of soil moisture content through microwave remote sensing. As such these factors, and in particular vegetation, will be included in this Chapter.

It should be noted that most of the semi-empirical models described in the sections below are still physically based. Their simplicity and the straightforward use is usually due to a simplified description of the scattering mechanisms involved and the presence of empirically determined parameters.

Two types of scattering are present when considering scattering in natural terrain, namely *surface scattering* and *volume scattering*. When scattering takes place at the boundary of one medium to another, such as an air - soil surface interface (dielectric half-space), and no contributions from penetrated radiation at subsurface layers are present, it is called surface scattering. Volume scattering is due to inhomogeneities in the medium itself, e.g. within the soil or within vegetation. The surface scattering models will be treated in more detail in section 3.5. The volume scattering models can be separated into two main classes: the *coherent models*, where phase and amplitude

(or intensity) of the electromagnetic field are computed and the *non- or incoherent models*, where only the amplitude is taken into consideration (Kerr & Wigneron, 1995). The non-coherent models are mathematically and computationally simpler but at the cost of a lower accuracy. The difference between the coherent and incoherent models is that *in the coherent models the interference between the phases of the EM waves are accounted for*.

3.2 Coherent modelling approach

The coherent modelling approach is also referred to as the *-analytic- wave approach*, since the solutions are based upon solving the wave equations propagating through matter. This approach, which starts with the Maxwell equations (through the solution of the dyadic Green's function of the vector wave equation) tries to find the brightness temperature T_B or backscattering cross-sections σ° of the object of interest by giving the scattering and absorption characteristics of the medium. This method allows for a very rigorous formulation but to obtain useful, practical results, some approximations must be made (Ulaby *et al.*, 1986). Some examples are the Born approximation (Ishimaru, 1978; Fung, 1982), Rytov method (Ishimaru, 1978), the renormalization method (Ishimaru, 1978; Fung, 1982) and the diagram method (Frisch, 1968). Most of these approximations assume *weak scattering, where multiple incoherent scattering is ignored. This disadvantage is less present in the radiative transfer approach*, which will be discussed in section 3.3. For more detailed descriptions of the various approaches in the coherent modelling approach see Tsang *et al.* (1985), Ulaby *et al.* (1986).

3.3 Radiative transfer approach

Another often used approach to find the brightness temperature T_B or backscattering cross-sections σ° of the object of interest is the *radiative transfer theory*. This theory does not start with the Maxwell equations but *describes the traversing of electromagnetic waves through a medium or several media*. The interaction between radiation and the media is described by the *transmission, absorption, emission and scattering of the radiation* (Tsang *et al.*, 1985; Rijckenberg, 1997). Strong dielectric fluctuations and certain types of multiple scattering are included. However, diffraction effects are ignored (Ulaby *et al.*, 1986). The radiative transfer models *belong to the group of the incoherent models*. These type of models treat the surface as layered media consisting of independent particles that can scatter, absorb and emit radiation. The basic scalar transfer equation for radiation of the amount of power at a single frequency can be written as (Chandrasekhar, 1960; Tsang *et al.*, 1985; Ulaby *et al.*, 1986):

$$dP = I(\mathbf{s}) \cos \theta_n dA d\Omega \quad (3.1)$$

where P is the power [W], I intensity of unpolarized radiation [$\text{W m}^{-2}\text{sr}^{-1}$] that propagates along the direction of \mathbf{s} within a solid angle $d\Omega$ through an elementary

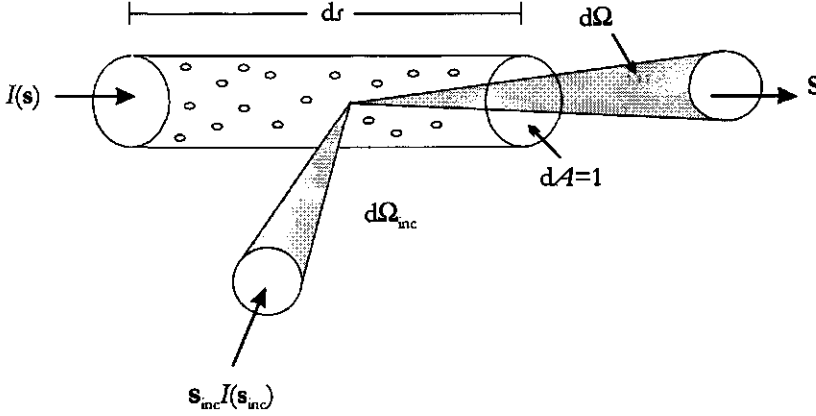


Figure 3.1: Radiative energy transfer for specific intensity $I(\mathbf{s})$ incident upon a cylindrical volume of particles.

area dA [m^{-2}]. The angle between the outward normal to dA and the unit vector \mathbf{s} is θ_n .

Consider a low density medium with N randomly distributed particles/spheres, each with a absorption cross section σ_a , and a scattering cross section σ_s . The extinction coefficient κ_e can be written as:

$$\kappa_e = N(\sigma_a + \sigma_s) = \kappa_a + \kappa_s \quad (3.2)$$

where κ_a and κ_s are the (volume) absorption and scattering coefficients respectively. The single-scattering albedo ω can now be introduced as:

$$\omega = \frac{\kappa_s}{\kappa_e} \quad (3.3)$$

or

$$1 - \omega = \frac{\kappa_a}{\kappa_e} \quad (3.4)$$

For an inhomogeneous medium, i.e. medium with a background material that is not air or a pure dielectric, the total extinction coefficient κ'_e becomes (Ulaby & Elachi, 1990):

$$\kappa'_e = \kappa_e + \kappa_{ag} \quad (3.5)$$

where

$$\kappa_{ag} = 2k_0 |\text{Im} \sqrt{\epsilon_r}| \quad (3.6)$$

is the power absorption coefficient of the background material, k_0 is the wave number in free space and ϵ_r is the relative complex permittivity of the material.

Consider a number of particles within a cylindrical volume with length ds . The change of intensity dI over the distance ds is a result of absorption loss, scattering

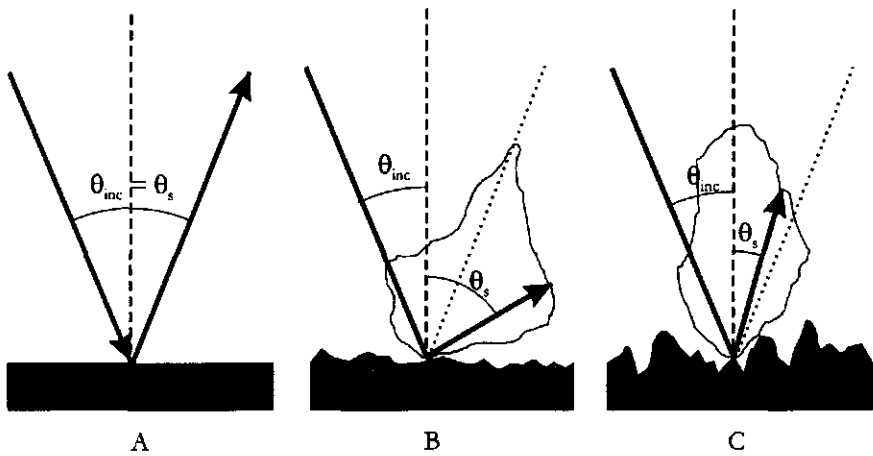


Figure 3.3: Specular and diffuse components of radiation scatter at A) perfect plane, B) slightly rough, C) very rough surface (Schanda, 1986).

angles and non-coherent term σ_{ppn}^0 , which is important at all angles (Ulaby *et al.*, 1986)

$$\sigma_{pp}^0(\theta_{inc}) = \sigma_{ppc}^0(\theta_{inc}) + \sigma_{ppn}^0(\theta_{inc}), \quad p = v \text{ or } h \quad (3.53)$$

The two limiting surface roughness cases, the plane surface and the ideal rough (Lambertian) surface, yield two distinct angular patterns of scattered radiation. The plane surface yields a delta function, meaning only that radiation striking the surface at normal incidence will be radiated back in the same direction it came from, centered at the specular direction. The rough (Lambertian) surface yields a diffuse scattering uniformly distributed in the upper half space (Schanda, 1986). Scattering of a plane surface can be described by the already mentioned Fresnel equations (Eq. 3.23 in section 3.4.1).

In microwave remote sensing the earth's surface is usually described in terms of a random rough surface. Where the roughness is described as the deviation of a reference plane and can be characterised statistically by measures such as root mean square of the height differences, surface correlation length or height probability density function. A more detailed description of the characterization of surface roughness can be found in Appendix D.

Scattering from a soil surface is a complex process because of the complex surface geometry that varies randomly in space. Because of this the *only practical way to solve the problem of surface scattering is by using simple approximate models that are valid for a certain range of roughness parameters*. Exact solutions for surface scattering problems can be obtained numerically by the method of moments, but this is computationally very demanding and only worthwhile to evaluate the validity of more simpler models. *In the microwave region the most used approximate models are the Kirchhoff approach and the small perturbation method (SPM).*

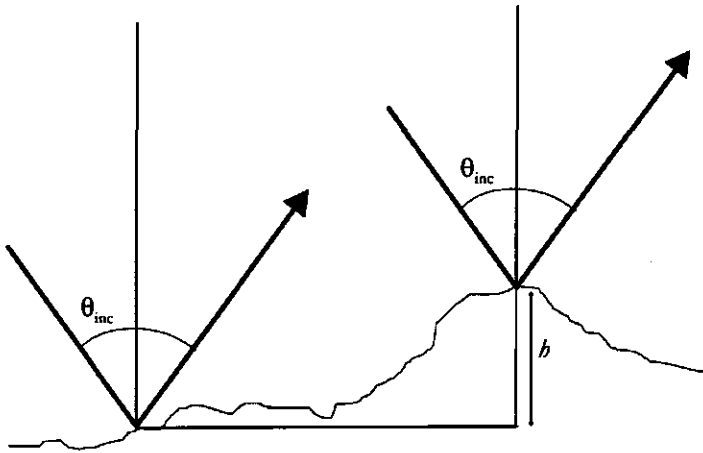


Figure 3.4: Geometry for the definition of surface roughness criteria.

Before discussing models for rough surface scattering the criterion for smooth versus rough surface has to be discussed. The most often used criterion is the *Rayleigh criterion* which states that for a surface to be smooth:

$$h < \frac{\lambda}{8 \cos \theta_{inc}} \quad (3.54)$$

where h is the height difference, λ the wavelength and θ_{inc} the angle of incidence (Fig. 3.4). For the average difference in height, h may be replaced by the root mean square of the height differences σ . The criterion becomes then

$$R_a < \frac{\pi}{4} \quad (3.55)$$

with

$$R_a = k\sigma \cos \theta_{inc} \quad (3.56)$$

where R_a is known as the Rayleigh parameter and k is the wave number (Schanda, 1986; Ogilvy, 1990). The Rayleigh criterion is useful as a first-order classifier of surface roughness but for natural surfaces where the wavelength is often in the order of h a more stringent criterion is used. Ulaby *et al.* (1982) propose the *Fraunhofer criterion* which states that for a surface to be smooth:

$$h < \frac{\lambda}{32 \cos \theta_{inc}} \quad (3.57)$$

According to Ulaby *et al.* (1982) this Fraunhofer criterion appears to be more consistent with experimental observations than the Rayleigh criterion.

Kirchhoff approach: Geometrical Optics and Physical Optics models The Kirchhoff approach is also called the *facet model* or *tangent-plane model* because the surface

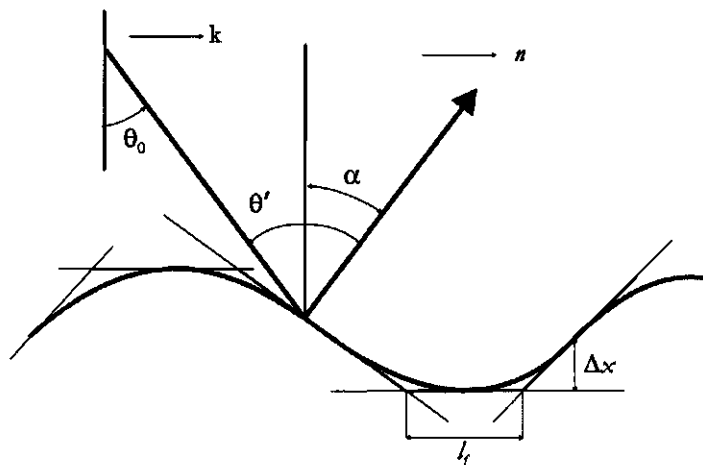


Figure 3.5: Geometry of the facet model of a rough surface.

geometry is modelled as a series of plane facets which are all tangential to the actual surface. The criteria to be met are that the length of the facet l_f is much larger than the wavelength and that the deviations Δx of the facets from the real surface are much smaller than the wavelength (Fig. 3.5). Scattering from an infinite plane facet is given by the delta function. In other words the infinite plane facet is a specular reflector and the Fresnel equations may be applied. The smaller the plane-facet becomes the wider the reradiation pattern becomes (Fig. 3.6). This re-radiation pattern resembles the pattern of the antenna but now with the same dimensions as the facet (Elachi, 1987). Another restriction of the facet model is that the angle of incidence or scattering should not be that large that one part of the surface obscures (shadows) another. If this is the case the model has to be adjusted by using for example shadowing functions, see Appendix 12K in (Ulaby *et al.*, 1982). The facet model is strictly speaking more a specular reflection model than a scattering model (Schanda, 1986; Ulaby *et al.*, 1982).

The Kirchhoff Geometrical Optics model Even with the tangent plane assumption, the mathematical formulation of the scattered field becomes a complex integral over the surface and no analytical solution is present. Hence, additional assumptions have to be made to obtain analytical solutions. In the high frequency limit the *stationary phase approximation* (Ulaby *et al.*, 1982) can be used to obtain the *geometrical optics* model for the backscattering coefficient:

$$\begin{aligned}
 \sigma_{pp}^o(\theta_{\text{inc}}) &= \frac{\rho_p(0) e^{\left(\frac{-\tan^2 \theta_{\text{inc}}}{2m^2}\right)}}{2m^2 \cos^4 \theta_{\text{inc}}} \\
 \sigma_{vh}^o &= \sigma_{hv}^o = 0 \\
 m &= \sigma |c''(0)|^{\frac{1}{2}}
 \end{aligned}
 \tag{3.58}$$

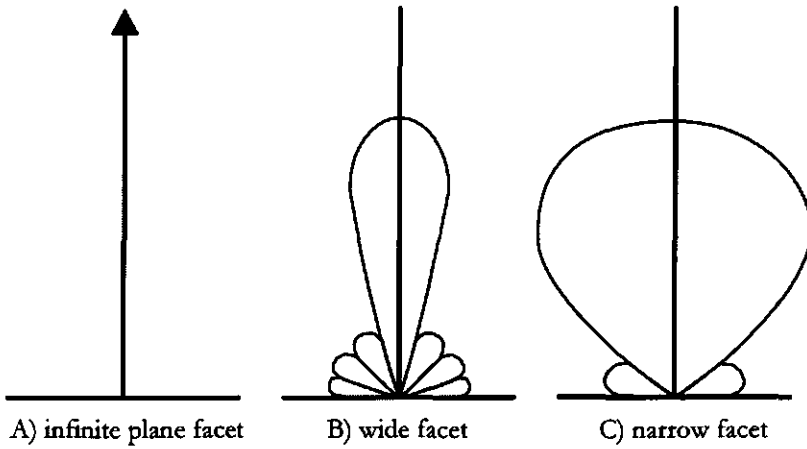


Figure 3.6: Normal-incidence reradiation patterns of facets, A) on a infinite plane facet, B) a wide facet compared to the wavelength and C) a narrow facet compared to the wavelength (Ulaby *et al.*, 1982).

Table 3.1: Validity conditions for the classical surface-scattering models. For the small perturbation model approximate values are given, no exact validity conditions have been determined.

Model	Validity conditions		
Physical Optics	$m < 0.25$	$kl > 6$	$l^2 > 2.76\sigma\lambda$
Geometric Optics	$(2k\sigma \cos \theta_{inc})^2 > 10$	$kl > 6$	$l^2 > 2.76\sigma\lambda$
Small Perturbation Model	$k\sigma < 3, m < 0.3$		

where $\rho_p(0)$ is the Fresnel reflectivity at normal incidence, m is the RMS surface slope, $c''(0)$ is the second derivative at the origin of the correlation function (see Appendix D). The model is valid when the variance of the surface height is large compared to the incident wavelength (Kuga *et al.*, 1990). Since, the Fresnel reflectivity $\rho_p(\theta_{inc})$ is evaluated at an angle of incidence $\theta_{inc} = 0$ the backscattering coefficients σ_{hh}^o and σ_{vv}^o are identical. Furthermore, the depolarized scattering coefficient σ_{ij}^o is zero because multiple scattering is neglected (Fung & Eom, 1981; Ulaby *et al.*, 1982). In general the model performs well for relatively rough surfaces whose backscattering coefficient shows a slowly varying angular dependence near nadir (Ulaby *et al.*, 1986). For large $(2k\sigma \cos \theta_{inc})^2$, where σ is the standard deviation of the surface height, thus when the model is valid, the surface generates purely incoherent radiation. For smaller $(2k\sigma \cos \theta_{inc})^2$, typically smaller than 4, the surface generates both coherent and incoherent radiation and a different approximation, discussed in the next section, is needed. The range of validity of this model along with a few others is given in Table 3.1 (page 45).

The Kirchhoff Physical Optics model For relatively smooth surfaces whose backscattering coefficient shows an exponentially decaying angular dependence the physical

optics model is valid. Basically, this is the Kirchhoff model under the *scalar approximation*, i.e. the reformulation of the vector Kirchhoff approach to a scalar approach while retaining the most important scattering terms. The general form of the physical optics model for the backscattering case is (Ulaby et al., 1986):

$$\sigma_{ppn}^o(\theta_{inc}) = 2k^2 \cos^2 \theta_{inc} \rho_p(\theta_{inc}) e^{-(2k\sigma \cos \theta_{inc})^2} \sum_{n=1}^{\infty} \left[\frac{(4k^2 \sigma^2 \cos^2 \theta_{inc})^n}{n!} \right] \int_0^{\infty} C^n(r) J_0(2kr \sin \theta_{inc}) r dr \quad (3.59)$$

where J_0 is the zeroth-order Bessel function of the first kind, $C^n(r)$ is the surface correlation function (see Appendix D). The integral term:

$$\int_0^{\infty} C^n(r) J_0(2kr \sin \theta_{inc}) r dr = W^n(2k \sin \theta_{inc}) = \left(\frac{\pi}{n}\right)^{\frac{1}{2}} l \cdot e^{\frac{-(kl \sin \theta_{inc})^2}{n}} \quad (3.60)$$

in Eq. 3.59 is the Fourier transform of the n -th power of the surface correlation function and for $n = 1$ is called the normalised surface roughness spectrum. The physical optics model has been found to agree well with experimental observations for like polarizations, but is inadequate for cross-polarization. The error by truncating the summation series at $n = 10$ is less than 0.1 dB (Ulaby et al., 1986). The range of validity of the model is given in Table 3.1 (page 45).

Small perturbation method For slightly rough surfaces with the normalised surface correlation length $kl < 6$ the Kirchhoff approach is no longer valid (Table 3.1). When both the surface standard deviation and the correlation length are smaller than the wavelength the *small perturbation model* can be used. The first order perturbation theory gives the like-polarized backscatter coefficients as:

$$\sigma_{ppn}^o(\theta_{inc}) = 8k^4 \sigma^2 \cos^4 \theta_{inc} |\alpha_{pp}(\theta_{inc})|^2(\theta_{inc}) W(2k \sin \theta_{inc}) \quad (3.61)$$

where

$$|\alpha_{hh}(\theta_{inc})|^2 = \rho_h(\theta_{inc}) \quad (3.62)$$

$$\alpha_{vv}(\theta_{inc}) = (\epsilon - 1) \frac{\sin^2 \theta_{inc} - \epsilon(1 + \sin^2 \theta_{inc})}{\left[\epsilon \cos^2 \theta_{inc} + (\epsilon - \sin^2 \theta_{inc})^{\frac{1}{2}} \right]^2} \quad (3.63)$$

and $W(2k \sin \theta_{inc})$ is the normalised roughness spectrum. The cross-polarized backscatter coefficient can be found by using the second order perturbation method

$$\sigma_{vh}^o(\theta_{inc}) = \sigma_{hv}^o(\theta_{inc}) = \pi k^4 \sigma^4 \cos^2 \theta_{inc} \frac{|(\epsilon - 1)(R_{hh} - R_{vv})|^2}{2} f(W) \quad (3.64)$$

with $f(W)$ a function of the roughness spectrum (see Eq. 12.113 (Ulaby et al., 1982)).

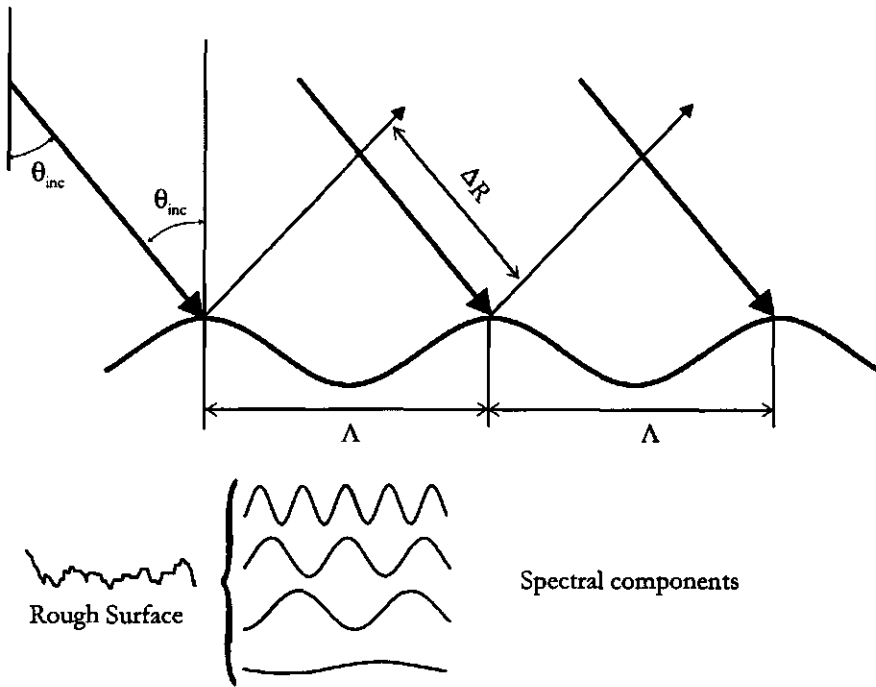


Figure 3.7: Bragg resonance scattering from the spectral components of the rough surface that correspond to the condition $\Lambda = \frac{n\lambda}{2 \sin \theta_{inc}}$.

Conceptually, the small perturbation model is a Bragg model. The concept of Bragg resonance is often used for surfaces with vertical and horizontal roughness parameters in the order of the wavelength. Such a rough random surface can be subdivided into its Fourier spectral components (see Fig. 3.7). Then the total backscatter of the surface is a summation of its spectral components, mainly the component that corresponds to the Bragg resonance condition:

$$\Lambda = \frac{n\lambda}{2 \sin \theta_{inc}} \quad n = 1, 2, 3 \dots$$

The first term ($n = 1$) leads to the strongest scattering.

Validity conditions for physical optics, geometrical optics approach and small perturbation method In Table 3.1 the validity ranges of the classical surface scattering models have been given. These models represent scattering from surfaces that can be described by a single set of roughness parameters. Oh *et al.* (1992) conclude from comparison with measured data that the predictions of the geometrical optics, physical optics and small perturbation method that:

- Some natural surface conditions fall outside the regions of validity of all three models;
- None of the models provides consistently good agreement with the measured data, in particular at incidence angles large than 40° ;

- The physical optics model predicts that $\sigma_{vv}^o < \sigma_{hh}^o$ contrary to all their observations
- Both the physical optics and geometrical optics model are first order solutions and cannot be used for cross polarization

Because of the limited validity of each of these models, alternative approaches have been developed which will be discussed in the next sections.

Two-scale model Most natural surfaces can be mathematically approximated by large facets on which the small scale roughness is superimposed. Thus, scattering from such surface will consist of contributions from both small and large scale geometry. Such models are called *composite* or *two-scale* models. The most simple approach is that the total backscatter coefficient, σ^T is a summation of the Kirchhoff approaches, σ^K with the small perturbation model, σ^S :

$$\sigma^T = \sigma^K + \sigma^S$$

However, assumptions have to be made regarding the form of each of the models and the way they are averaged. The predicted scattering coefficient for such a two-scale approach is shown in Fig. 3.8 (Ogilvy, 1990).

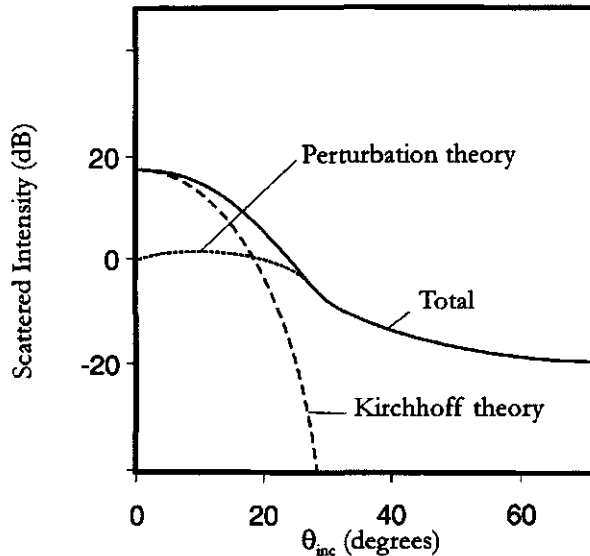


Figure 3.8: Scattering coefficient σ^o as a function of incident angle θ_{inc} for a composite rough surface. The total scattering consists of a contribution of large scale roughness (Kirchhoff theory) and small scale roughness (perturbation theory).

The validity of the two-scale models is restricted to the validity range of either of the approaches (Kirchhoff and small perturbation method) used, outside their range the performance becomes less (Fung & Chen, 1985; Ogilvy, 1990). According to McDaniel

and Gorman (1983) inclusion of higher order perturbation terms, or curvature corrections for the Kirchhoff approach does not lead to significant improvement of the performance.

3.5.3 A more general model: Integral Equation Method (IEM)

The *Integral Equation Method* (IEM) model is a theoretical model that attempts to give a more general solution than the Kirchhoff and small perturbation methods. In its complete version the model can be applied with no limitations regarding roughness scales or frequencies (Fung, 1994; Altese et al., 1996). Since, the model is too complex to be used for practical purposes, simplifications have to be made. The IEM model can be summarized as (Fung, 1994):

$$\sigma_{pq}^o = \sigma_{pq}^k + \sigma_{pq}^{kc} + \sigma_{pq}^c \quad (3.65)$$

where σ_{pq}^o is the total (bistatic) scattering coefficient, σ_{pq}^k is the Kirchhoff term, σ_{pq}^{kc} is the cross term and σ_{pq}^c is the complementary term. The complete description of each of these terms can be found in (Fung, 1994, Chapters 4 and 5).

To obtain more simple models which can be interpreted more easily, the backscatter coefficient σ_{pq}^o of the IEM model can be shown to have two types of terms: a *single-scatter term*, σ_{pq}^s and a *multiple-scatter term*, σ_{pq}^m :

$$\sigma_{pq}^o = \sigma_{pq}^s + \sigma_{pq}^m \quad (3.66)$$

For like polarized ($p = q$) backscatter coefficients multiple scattering is negligible, in particular for small RMS slopes (m) which is common for most natural terrain. Thus, the single scattering formulation (Fung et al., 1992; Fung, 1994; Dawson et al., 1995) will be more often used. The single scattering coefficient for the backscatter case is given by :

$$\sigma_{pq}^s = \frac{k^2}{2} e^{(-2\sigma^2 k_z^2)} \sum_{n=1}^{\infty} \sigma^{2n} |I_{pq}^n|^2 \frac{W^n(-2k_x, 0)}{n!} \quad (3.67)$$

where $k_z = k \cos \theta_{inc}$ and $k_x = k \sin \theta_{inc}$ and

$$I_{pq}^n = (2k_z)^n f_{pq} e^{(-\sigma^2 k_z^2)} + \frac{k_x [F_{pq}(-k_x, 0) + F_{pq}(k_x, 0)]}{2} \quad (3.68)$$

with $W^n(-2k_x, 0)$ the Fourier transform of the n^{th} power of the surface correlation function normalised to the surface variance. For a specific polarization f_{pq} and $F_{pq}(-k_x, 0)$ and $F_{pq}(k_x, 0)$ can be given as:

$$f_{vv} = \frac{2R_v}{\cos \theta_{inc}} \quad (3.69)$$

$$f_{hh} = \frac{-2R_h}{\cos \theta_{inc}} \quad (3.70)$$

$$F_{vv}(-k_x, 0) + F_{vv}(k_x, 0) = \frac{2 \sin^2 \theta_{\text{inc}} (1 + R_v)^2}{\cos \theta_{\text{inc}}} \left[\frac{\left(1 - \frac{1}{\epsilon_r}\right) + \frac{\mu_r \epsilon_r - \sin^2 \theta_{\text{inc}} - \epsilon_r \cos^2 \theta_{\text{inc}}}{\epsilon_r^2 \cos^2 \theta_{\text{inc}}}}{\cos \theta_{\text{inc}}} \right] \quad (3.71)$$

$$F_{hh}(-k_x, 0) + F_{hh}(k_x, 0) = \frac{2 \sin^2 \theta_{\text{inc}} (1 + R_h)^2}{\cos \theta_{\text{inc}}} \left[\frac{\left(1 - \frac{1}{\mu_r}\right) + \frac{\mu_r \epsilon_r - \sin^2 \theta_{\text{inc}} - \mu_r \cos^2 \theta_{\text{inc}}}{\mu_r^2 \cos^2 \theta_{\text{inc}}}}{\cos \theta_{\text{inc}}} \right] \quad (3.72)$$

In Eq. 3.67 it is assumed that the local incidence angle in the Fresnel coefficients can be approximated by the incidence angle. Hence, the application of Eq. 3.67 is restricted depending upon the surface roughness parameters, surface correlation function and the relative permittivity of the surface (Fung, 1994, Chapters 4 and 5). For the range of validity for surfaces with a Gaussian correlation function, Fung (1994) gives as restriction

$$(k\sigma)(kl) < 1.2\sqrt{\epsilon_r} \quad (3.73)$$

with the note that in the case of an exponential correlation function the restriction is less severe. For a non-Gaussian correlated surface Fung (1994) gives as rule of thumb for the IEM to be valid:

$$(k\sigma)(kl) < 1.6\sqrt{\epsilon_r} \quad (3.74)$$

In Fung et al., (1992) the above model is called the *small to moderate $k\sigma$ approximation* and is employed by Altese et al., (1996) for soil moisture estimation with ERS-1. The validity criterium is given as $k\sigma < 3$. Fung and Chen (1995) did a validation of the model for a frequency range from 5 to 10 GHz, a root mean square height range of 0.85 mm to 8.4 cm, a correlation length range of 6.2 mm to 8.4 cm and for various types of surfaces. They concluded that the model is applicable to surface scattering of these surfaces but that for natural surfaces that are inhomogeneous volume scattering may be present and for those surfaces the model underpredicts the backscatter coefficient.

The first order solution of the IEM model reduces to the small perturbation model for slightly rough surfaces. The model approaches the physical optics model for surfaces with surface slopes that are small compared to the surface roughness. For large surface slopes the model reduces to the geometrical optics model (high frequency limit). Hence, it is expected that the *IEM model has a larger validity range than the Kirchhoff approaches and small perturbation method combined*. For surfaces which are skewed an additional term has to be added which can be found in (Fung, 1994, Chapter 7).

For surfaces which have a dielectric gradient, such as a drying soil, the IEM model has been extended by including a transitional dielectric layer (Fung et al., 1996). This transition layer has a permittivity ϵ_r that varies with depth z . To date no results regarding the validity have been published and this model has not been used in the work presented in this thesis.

3.5.4 (Semi-)empirical approaches: The OSU model

Many empirical models have been developed over the years, mostly to overcome the difficulties when dealing with purely theoretical models that require extensive knowledge about the surface characteristics and often have a limited validity. One of the more recent empirical models will be discussed in more detail, namely the model by Oh *et al.*, (1992). Since the model of Dubois *et al.*, (1995) has been widely used also it will be briefly described.

The empirical model of Oh, Sarabandi and Ulaby (1992), is hereafter referred to as OSU. This model is based upon field measurements over bare soils using a L-, C-, and X-band radar. The model consists of a set of empirical relations as a function of normalised surface roughness $k\sigma$, the permittivity ϵ_r through the Fresnel reflectivity ρ_0 :

$$q \stackrel{\text{def}}{=} \frac{\sigma_{hv}^o}{\sigma_{vv}^o} = 0.23\sqrt{\rho_0} [1 - e^{-k\sigma}] \quad (3.75)$$

where ρ_0 is the Fresnel reflectivity of the surface at nadir

$$\rho_0 = \left| \frac{1 - \sqrt{\epsilon_r}}{1 + \sqrt{\epsilon_r}} \right|^2 \quad (3.76)$$

and

$$\sqrt{p} \stackrel{\text{def}}{=} \sqrt{\frac{\sigma_{hh}^o}{\sigma_{vv}^o}} = 1 - \left(\frac{2\theta_{\text{inc}}}{\pi} \right)^{\frac{1}{3\rho_0}} e^{-k\sigma} \quad (3.77)$$

From these equations the authors derived empirical expressions for σ_{vv}^o , σ_{hh}^o and σ_{hv}^o with p and q being given explicitly in terms of $k\sigma$ and ϵ_r , the function g being governed by only $k\sigma$:

$$\sigma_{vv}^o(\theta_{\text{inc}}, \epsilon_r, k\sigma) = \frac{g \cos^3 \theta_{\text{inc}}}{\sqrt{p}} \cdot [\rho_v(\theta_{\text{inc}}) + \rho_h(\theta_{\text{inc}})] \quad (3.78)$$

$$\sigma_{hh}^o(\theta_{\text{inc}}, \epsilon_r, k\sigma) = g\sqrt{p} \cos^3 \theta_{\text{inc}} \cdot [\rho_v(\theta_{\text{inc}}) + \rho_h(\theta_{\text{inc}})] \quad (3.79)$$

$$\sigma_{hv}^o(\theta_{\text{inc}}, \epsilon_r, k\sigma) = q\sigma_{vv}^o(\theta_{\text{inc}}, \epsilon_r, k\sigma) \quad (3.80)$$

with

$$g = 0.7 \left[1 - e^{-0.65(k\sigma)^{1.8}} \right] \quad (3.81)$$

The model was tested over a large range of soil moisture and surface roughness conditions: $0.09 < \theta_{\text{inc}} < 0.31$, $2.6 < kl < 19.7$ and $0.1 < k\sigma < 6.0$ and showed good agreement with the data. The model also performed well when tested against data measured for surfaces with parameters outside the above mentioned ranges (Oh *et al.*, 1992). However, at steep incidence angles, $\theta_{\text{inc}} < 20^\circ$ and for smooth surfaces there is a strong contribution from the coherent backscattering term that is not included in the model and the model therefore underpredicts the total backscattering. The rougher the surface the more negligible the coherent term becomes.

Model of Dubois et al. (1995) The model by Dubois *et al.*, (1995) was developed to retrieve soil moisture and surface roughness estimates from SAR data with three main goals in mind. The algorithm should:

- Be applicable to radar data measured over as wide a range of surfaces as possible;
- Require data calibration that is achievable in practice;
- Provide accurate results even for surfaces with a moderate vegetation cover.

Using truck mounted radar data sets they derived the following two empirical equations for the backscattering coefficients σ_{hh}^o and σ_{vv}^o :

$$\sigma_{hh}^o = 10^{-2.75 \frac{\cos^{1.5}(\theta_{inc})}{\sin^5(\theta_{inc})}} 10^{0.028\epsilon_r' \tan \theta_{inc}} (k\sigma \sin \theta_{inc})^{1.4} \lambda^{0.7} \quad (3.82)$$

$$\sigma_{vv}^o = 10^{-2.35 \frac{\cos^3(\theta_{inc})}{\sin^3(\theta_{inc})}} 10^{0.046\epsilon_r' \tan \theta_{inc}} (k\sigma \sin \theta_{inc})^{1.1} \lambda^{0.7} \quad (3.83)$$

which are valid for a frequency range of 1.5 - 11 GHz. The various validity conditions regarding surface roughness are summarised in Table 3.2.

To exclude areas for which the influence of vegetation on the backscatter coefficient is too high Dubois *et al.*, (1995) employed a mask based upon the $\frac{\sigma_{hv}^o}{\sigma_{vv}^o}$ ratio. They stated that for

$$\frac{\sigma_{hv}^o}{\sigma_{vv}^o} > -11\text{dB} \quad (3.84)$$

the surface was too heavily vegetated and corresponds to NDVI values greater than 0.4. Furthermore, this classifier would also exclude surfaces for which the surface roughness conditions exceeds the models validity range. As with most models the effects of periodicity of the surface is not included, thus care has to be taken when, for example dealing with furrowed agricultural fields.

The model of Dubois *et al.*, 1995 has a slightly different range of validity than the OSU model. It is difficult to say which model performs better since both models are empirical and similar of nature and depending upon the data set used will produce different results.

Table 3.2: Validity conditions for the semi-empirical surface-scattering models

Model	Validity conditions		
	Surface roughness		Incidence angles
Oh, Sarabandi & Ulaby, (1992)	$k\sigma > 0.1$	$kl > 2.6$	$\theta_{inc} > 30^\circ$
	$k\sigma < 6.0$	$kl < 19.7$	$\theta_{inc} < 50^\circ$
Dubois <i>et al.</i> , (1995)		$kl > 2.5$	$\theta_{inc} \geq 30^\circ$
	$k\sigma \leq 2.5$	$kl < 20$	$\theta_{inc} < 65^\circ$

3.6 Scattering from vegetated surfaces

The models for bare soil surface, such as OSU and IEM perform well enough and are general enough to be used to estimate surface parameters. For vegetated surfaces many models are available but are either too complicated and require too much *a priori* knowledge to be used in inversion schemes, or when they are simpler have a too small range of validity.

Objects that are on top of the rough surface, e.g. vegetation, are usually modelled as statistical ensembles of simple shapes like ellipses and cylinders. In case of vegetation this requires extensive knowledge about the dielectric properties and the density, shape, size and orientation angle distributions of leaves and branches. Based upon this information the contribution of each of these objects to the total scattering can be calculated.

Many different models are available varying from very simple empirical approaches, simple radiative transfer models - Cloud model, (Attema & Ulaby, 1978) - to complex multilayer radiative transfer approaches - UTA model (Karam *et al.*, 1992a; Karam *et al.*, 1992b; Karam *et al.*, 1995) and MIMICS (Ulaby *et al.*, 1990)-, which have been discussed in section 3.3. In general the radiative transfer approach for backscattering from vegetated surface can be written as:

$$\sigma_{total}^o = \sigma_v^o + \Gamma^2 \sigma_s^o + \sigma_{sv}^o \quad (3.85)$$

where subscripts *v*, *s*, *sv* denote volume, surface and surface-volume contributions, respectively. The two-way transmissivity Γ^2 of the vegetation layer is (see also Eq. 3.39):

$$\Gamma^2 = e^{(-2\tau \sec \theta_{inc})} \quad (3.86)$$

where τ is the optical thickness. The soil surface contribution σ_s^o may be calculated using a surface backscattering model. The volume contribution term σ_v^o is much more complex, especially because the single scattering assumption (first order approximation) does not hold for many vegetated surfaces and thus the cross-polarized backscatter coefficient cannot be assumed negligible.

In this thesis only the bare soil surface scattering models, IEM and OSU, have been used. When vegetation is present it has been filtered out using a vegetation mask before applying the surface scattering models.

3.7 Conclusions

Two types of scattering are present when considering scattering in natural terrain, namely *surface scattering* and *volume scattering*. When scattering takes place at the boundary of one medium to another, such as an air - soil surface interface (dielectric half-space), and no contributions from penetrated radiation at subsurface layers are present, it is called surface scattering. Volume scattering is due to inhomogeneities in the medium itself, e.g. within the soil or within vegetation.

The volume scattering models can be separated into two main classes: the *coherent models*, where phase and amplitude (or intensity) of the electromagnetic field are computed; *non- or incoherent models*, where only the amplitude is taken into consideration (Kerr & Wigneron, 1995). The non-coherent models are mathematically and computationally simpler but at the cost of a lower accuracy. The difference between the coherent and incoherent models is that *in the coherent models the interference between the phases of the EM waves are accounted for*.

The *radiative transfer theory* belongs to the group of incoherent models and *describes the traversing of electromagnetic waves through a medium or several media*. The interaction between radiation and the media is described by the *transmission, absorption, emission and scattering of the radiation*.

Passive case For the passive case, thus dealing with microwave emission the radiative transfer approach yields good results. *The parametric model of Mo et al., 1982 will be used in this thesis to estimate soil moisture*. This model and its modified versions have proven to be simple radiative transfer models that can effectively estimate the radiation emitted by the soil surface even under vegetation. Scattering is assumed negligible and only three components, soil emission attenuated by the vegetation, emission by the vegetation itself and the downward emitted radiation from the vegetation that is reflected upwards by the soil surface, are used. Two parameters in the model have to be estimated through empirical models namely the roughness parameter h and the optical depth τ .

For soil water content estimation purposes an emission model is needed that is simple enough to invert but has a large range of validity. For the passive case the *simplified theoretical radiative transfer approaches perform well*, even when some of the parameters need to be estimated using semi-empirical approaches.

Active case For the active case, thus dealing with microwave scattering, the volume scattering components and radiative transfer approaches are still too complex i.e. require too much a priori information, to be used in practice for the description of radiation from natural surfaces. The validity of the surface scattering models such as the small perturbation method (SPM) or the Kirchhoff approaches namely, geometrical optics (GO) and physical optics (PO) models, is usually limited by the severe assumptions regarding the surface characteristics.

The *integral equation method (IEM)* model is a theoretical surface scattering model that attempts to give a more general solution than the Kirchhoff and small perturbation methods. *In its complete version the model can be applied with no limitations regarding roughness scales or frequencies*. The model is applicable to natural surfaces but for surfaces that are inhomogeneous volume scattering may be present and for those surfaces the model underpredicts the backscatter coefficient. For surfaces which are skewed or have periodic roughness an additional term has to be added which can be found in (Fung, 1994, Chapter 7).

The semi-empirical OSU model is a surface scattering model that was tested over a large range of soil moisture and surface roughness conditions: $0.09 < \theta_{\text{inc}} < 0.31$,

$2.6 < kl < 19.7$ and $0.1 < k\sigma < 6.0$ and showed good agreement with the data. The model also performed well when tested against data measured for surfaces with parameters outside the above mentioned ranges (Oh *et al.*, 1992). However, at steep incidence angles, $\theta_{inc} < 20^\circ$ and for smooth surfaces there is a strong contribution from the coherent backscattering term that is not included in the model and the model therefore underpredicts the total backscattering. The rougher the surface the more negligible the coherent term becomes.

The scattering of bare soil surfaces can be described by the theoretical IEM model (Fung, 1994; Altesse *et al.*, 1996) which has a large range of validity but is in its most general form too complex to invert. Semi-empirical models such as Oh *et al.*, (1992) are simpler but have limited range of validity.

For vegetated surfaces, no satisfying simple model exists yet. Complex radiative transfer models are available and show acceptable results but require too much information beforehand. The more simple models are shown to have a too small range of validity. The latter applies also to the empirical and semi-empirical approaches which range of validity is limited by the calibration set.

In this thesis therefore the scattering from bare soil surfaces is considered and where vegetation is present these data are eliminated and kept out of the analysis. Both the IEM model and OSU model are used.

Chapter 4

Soil moisture estimation by inversion techniques

4.1 Introduction

The estimation of soil moisture from microwave measurements requires that either the forward formulation be inverted or that through an iterative procedure the parameters -including soil moisture- in the forward formulation are adapted to bring the model output in agreement with the measurements. *The latter approach is applied in most data assimilation techniques* for example in numerical weather prediction and climate models where soil moisture is considered as a quantity to partition the available energy for evaporation over latent heat and sensible heat. This quantity is difficult to compare with the actual soil moisture as it is measured in the field. Hence, different or additional information, such as brightness temperature T_B , can be used to increase the model performance, constrain the solution space and prevent or limit e.g. model drift (van Oevelen *et al.*, 1998).

In this Chapter the *emphasis will be on the inversion of the various steps to retrieve soil moisture from either microwave backscatter coefficients σ° or microwave brightness temperatures T_B* . Basically, the distinction will be made between inversion of the scattering/emission models and the inversion of soil dielectric mixing models. The latter step is the same for both active and passive microwave remote sensing of soil moisture.

Regression analysis approaches, including the more complex non-linear neural network approaches linking soil moisture measurements directly to backscatter or emission measurements are not discussed here. Although these approaches have their usefulness their validity is by definition limited to the conditions imposed by the calibration data set. Furthermore they do not consider the physics and therefore do not provide much insight into the problems encountered. However, these approaches can fit in the general framework to estimate and implement soil moisture from remote sensing measurements.

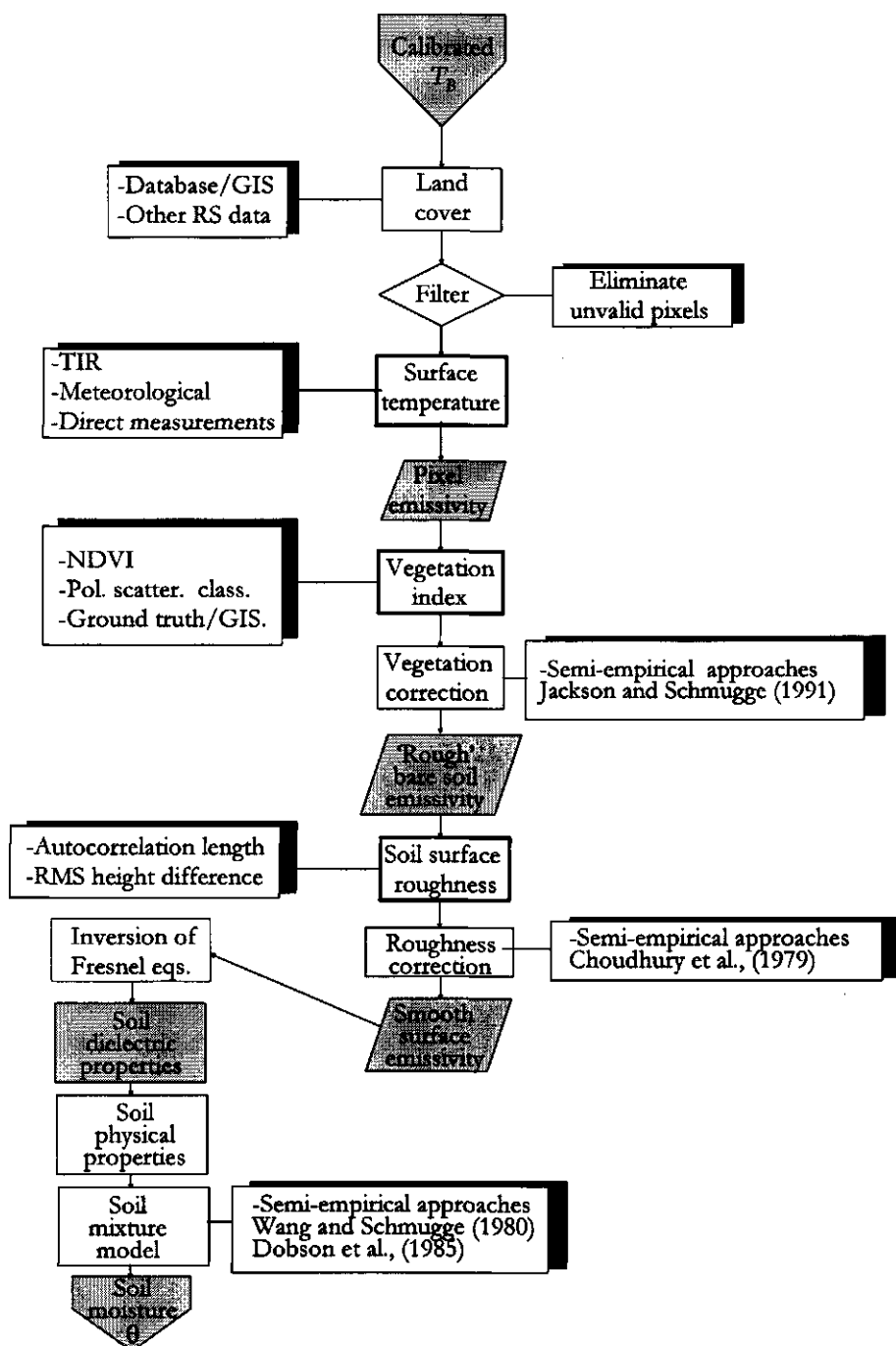


Figure 4.1: The various steps in the inversion of soil moisture θ from microwave brightness temperature T_B .

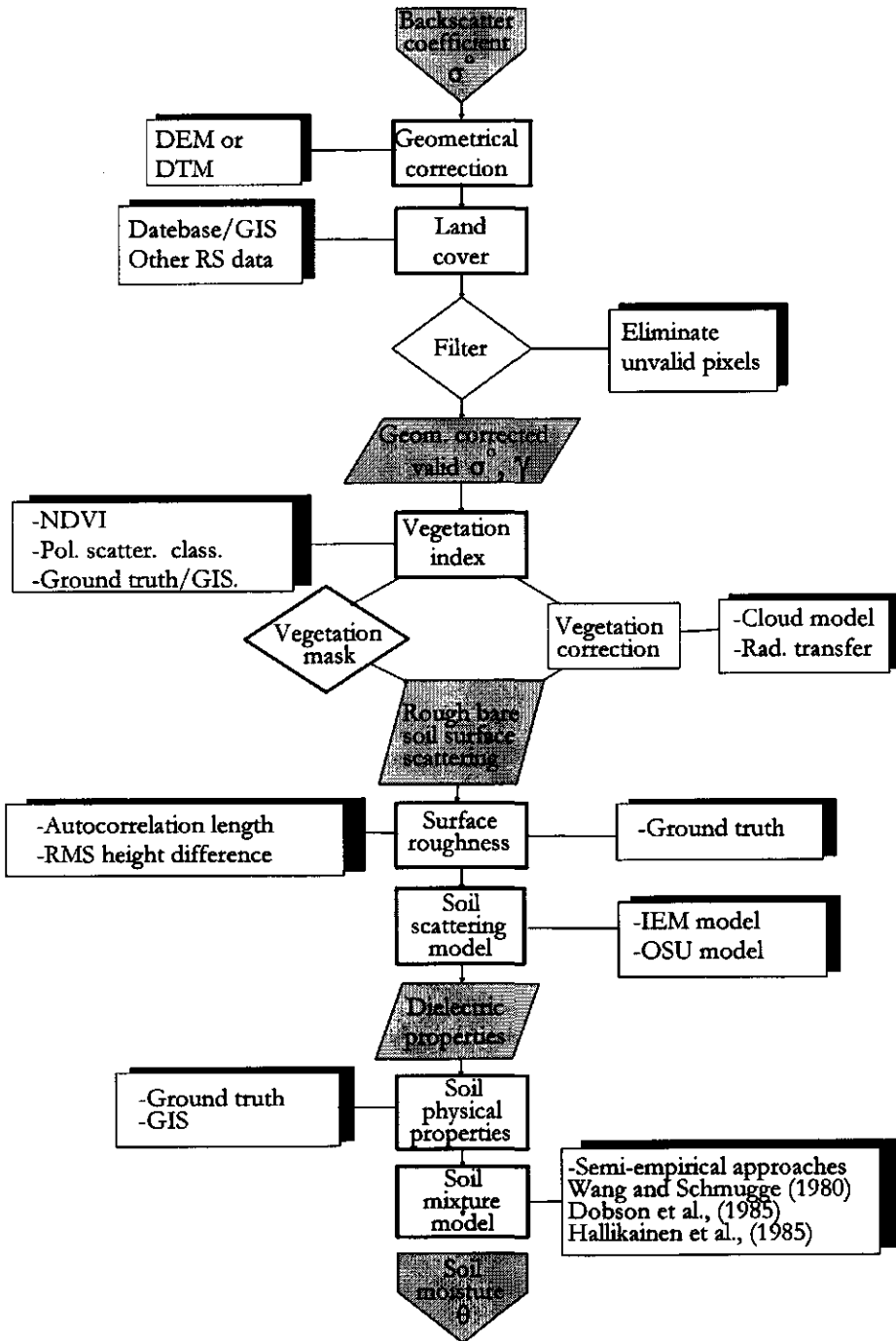


Figure 4.2: The various steps in the inversion of soil moisture from microwave backscatter measurements.

Passive microwave soil moisture retrieval The process of retrieving soil moisture content from microwave brightness temperature T_B can be followed in Figure 4.1. Certain surfaces or pixels containing certain surface types and/or objects that are of no interest can be eliminated from the inversion such as urban areas, roads or large water bodies. From the measurement of emitted microwave radiation expressed as T_B the surface emissivity ϵ can be calculated if the surface physical temperature T is known ($T_B = \epsilon T$, see Eq. 3.19). Effects of background and cosmic radiation can be simply added in the scheme and used to retrieve the correct surface emissivity. Using a vegetation index such as the Normalized Difference Vegetation Index (NDVI), or ground truth the type and/or amount of vegetation can be estimated and used to correct for the influence of this vegetation on the microwave emission of the soil. The emission of the soil is further depending upon the roughness which can be corrected using a simple empirical model such that the emissivity ϵ_0 of a smooth surface is retrieved. Using the Fresnel equations the soil dielectric properties can be estimated. Soil water content θ is retrieved from these soil dielectric properties ϵ by inversion of a soil dielectric mixing model (Wang and Schmugge (1980) or Dobson *et al.*, (1985)) assuming *a priori* knowledge of the soil textural properties (see section 4.2). The scheme presented is very general and assumes physical relationships which can be represented by different models. The inversion of a radiative transfer model will be more thoroughly discussed in Section 4.3.

Active microwave soil moisture retrieval The inversion steps for active microwave measurements are illustrated in Figure 4.2. Although the inversion could be followed exactly as represented in the chart, the method followed in this thesis is for practical reasons slightly different. The calibrated backscatter coefficient σ^0 needs to be corrected for surface geometry in most (non-flat) terrains. Using a Digital Elevation Model (DEM) or Digital Terrain Model (DTM) correction for this geometry can be made. However, this correction can be limited. For example a surface slope facing towards the sensor is different from the same type of surface slope facing away. The surface sloping away may give a σ^0 that is so small that other (instrument) errors may become large. Using a geographical information system (GIS) or other remote sensing data the surface cover can be related to the backscatter. Unwanted pixels or pixels for which the inversion is invalid (such as open water, urban areas) can be eliminated. The next step would be to correct σ^0 for the influence of vegetation. Current models, such as the CLOUD model (Attema & Ulaby, 1978), are not well developed enough yet to do this correction in a satisfying and general applicable manner. Therefore, the approach in this thesis is to mask out the pixels which suffer from the influence of vegetation. This can be done using remotely sensed information or information from land surveys e.g. GIS. To retrieve the surface dielectric properties ϵ from the rough bare soil surface scattering a surface scattering model can be applied (e.g. OSU or IEM model). Soil water content θ is retrieved from these soil dielectric properties ϵ by inversion of a soil dielectric mixing model from Wang and Schmugge (1980), Dobson *et al.*, 1985 and Hallikainen *et al.*, (1985) assuming *a priori* knowledge of the soil textural properties.

In this thesis the OSU model and IEM model are inverted. The IEM model is inverted

using a Look Up Table (LUT) (see section 4.4.2). This approach avoids the inversion of the IEM model which is in its most general form too complex to invert.

4.2 Inversion of soil dielectric mixing model of Wang and Schmugge

Most of the dielectric mixing models cannot be written explicitly for soil moisture content θ , and can therefore only be solved numerically. An exception however is the model of Wang and Schmugge (1980) and this inversion will therefore be shown as an example.

The dielectric mixing model of Wang and Schmugge (1980) (see section 2.3.3 and Figure 4.1) can only be inverted by an iterative procedure. First the transition moisture content θ_t has to be determined by inserting equation 2.45 in equation 2.44. :

$$\theta_t = 0.49(0.06774 - 0.00064\phi_{\text{sand}} + 0.00478\phi_{\text{clay}}) + 0.165 \quad (4.1)$$

where ϕ_{sand} and ϕ_{clay} are the volume fractions of sand and clay respectively. The next step is to determine the fitting parameter γ by inserting equation 2.45 into 2.49:

$$\gamma = -0.57(0.06774 - 0.00064\phi_{\text{sand}} + 0.00478\phi_{\text{clay}}) + 0.481 \quad (4.2)$$

Equation 2.47 can be rewritten as:

$$\theta = \frac{(1 - \phi)\epsilon_r + \phi\epsilon_a - \epsilon}{(\epsilon_a - \epsilon_x)} \quad (4.3)$$

with

$$\epsilon_x = \epsilon_i + (\epsilon_w - \epsilon_i) \frac{\theta}{\theta_t} \quad (4.4)$$

Since equation 4.3 is not explicit for θ , it has to be solved by writing it as an quadratic equation:

$$\theta(\epsilon_w - \epsilon_i) \frac{\gamma}{\theta_t} + \theta(\epsilon_i - \epsilon_a) + (1 - \phi)\epsilon_r + \phi\epsilon_a - \epsilon = 0 \quad (4.5)$$

with the following two solutions of which only one is physically possible:

$$\theta = \frac{-(\varepsilon_i - \varepsilon_a) \pm \sqrt{(\varepsilon_i - \varepsilon_a) - 4 \left[(\varepsilon_w - \varepsilon_i) \frac{\gamma}{\theta_t} \right] [(1 - \phi)\varepsilon_r + \phi\varepsilon_a - \varepsilon]}}{2(\varepsilon_w - \varepsilon_i) \frac{\gamma}{\theta_t}} \quad (4.6)$$

Equation 2.50 written explicitly for θ , reads as:

$$\theta = \frac{\theta_t(\varepsilon_x - \varepsilon_w) + (1 - \phi)\varepsilon_r + \phi\varepsilon_a - \varepsilon}{(\varepsilon_a - \varepsilon_w)} \quad (4.7)$$

with

$$\varepsilon_x = \varepsilon_i + (\varepsilon_w - \varepsilon_i)\gamma \quad (4.8)$$

The iterative procedure is as follows; a known dielectric constant ε is inserted in equation (4.7). The resulting θ is compared with the transition moisture θ_t . If the resulting θ is smaller or equal to θ_t then equation (4.6) should be used. The resulting θ should be smaller or equal to θ_t .

4.3 Inversion of microwave emission models using a simple radiative transfer approach

The basic quantity to start with is the microwave brightness temperature T_B obtained through a microwave radiometer. This quantity represents the temperature that a black body would have if it emitted the same amount of radiation at these frequencies. In the following section all the properties mentioned are to be considered 'effective' or 'representative' of the area under consideration, i.e. of the resolution cell. Spatial variability is therefore ignored as are also instrument imperfections. The radiative transfer microwave emission model of Mo *et al.*, (1982) can in fact be regarded as the basis of the inversion approach used in this thesis and is illustrated in Figure 4.1.

The brightness temperature of a vegetation covered soil surface as measured by a microwave radiometer can be described by a simple model (Ulaby *et al.*, 1986; Schmugge & Jackson, 1991; Schmugge *et al.*, 1992):

$$T_B = \tau_{atm}(\rho T_{sky} + (1 + \rho\gamma)(1 - \gamma)(1 - \omega)T_v + (1 - \rho)\gamma T_s) + T_{atm} \quad (4.9)$$

where, T_B is the brightness temperature of the vegetation and soil observed, T_s is the physical temperature of the soil, T_v is the physical temperature of the vegetation, T_{sky} is the sky temperature and T_{atm} atmospheric temperature (all temperatures in K). τ_{atm} is the atmospheric transmissivity, ω is the single scattering albedo, γ is the transmissivity of the vegetation layer and ρ is the surface reflectivity (all dimensionless).

In this model the vegetation is considered to absorb the emission of the soil and add its own emission to the total emission. This assumes that scattering can be neglected, which is true for the longer wavelengths ($f < 5$ GHz). The reflected sky brightness, which depends on atmospheric conditions and frequency, and the atmospheric brightness are small for frequencies below 5 GHz (less than 10 K). Both quantities can generally be neglected. The major contribution to T_{sky} at 21 cm is the cosmic background radiation at 2.7 K. The atmosphere is close to transparency for microwaves and has an atmospheric transmission which is about 0.99.

When these considerations are taken into account Eq. 4.9 can be simplified to:

$$T_B = (1 + \rho\gamma)(1 - \gamma)(1 - \omega)T_v + (1 - \rho)\gamma T_s \quad (4.10)$$

The single scattering albedo ω has a small dynamic range for the longer wavelengths varying between 0.05 and 0.10 (Jackson & Schmugge, 1991; van de Griend *et al.*, 1991). Very little data are available to estimate this parameter and it is usually neglected (Jackson & O'Neill, 1990). If the temperature of the soil is assumed to be equal to that of the vegetation, which for healthy vegetation under natural conditions is a reasonable approximation (Jackson *et al.*, 1982b) Eq. 4.10 reduces to:

$$T_B = (1 - \rho\gamma^2)T_s \quad (4.11)$$

The transmissivity γ is the attenuation of radiation by the absorbing vegetation layer and can be described by:

$$\gamma = \exp\left(\frac{-\tau}{\cos\theta_{inc}}\right) \quad (4.12)$$

where τ is the optical depth which is a function of vegetation dielectric properties, plant shape, density and structure, wavelength, polarization and look angle. For incidence angles close to nadir Eq. 4.11 becomes:

$$T_B = [1 - \rho \exp(-2\tau)] T_s \quad (4.13)$$

Following the work by Shutko (1986) and Jackson and O'Neill (1990), Jackson and Schmugge (1991) found that the optical depth could easily be described as a linear function of the vegetation water content θ_{veg} (which is the main contribution to the change in plant dielectric properties) and a plant dependent factor b to account for other parameters such as vegetation shape/structure, polarization and wavelength:

$$\tau = b \theta_{veg} \quad (4.14)$$

where b is a plant dependent constant [kg^{-1}m^2] and θ_{veg} is the vegetation water content [$\text{kg m}^{-1}\text{m}^{-1}$].

The constant b is almost proportional to the frequency and ranges for the 21 cm wavelength for short grasses and grains to broad leafed vegetation from 0.1 to 0.03. Jackson and Schmugge (1991) have summarized in their Table 1. the values of τ , θ_{veg} and b from various studies. For completeness that data have been included here in Table 4.1.

Table 4.1: Vegetation parameters, (after Jackson and Schmugge, 1991). Data are for H-polarization, corrected look angle of 0°.

Source	Cover type	λ [cm]	τ [-]	θ_{veg} [kg m ⁻²]	b [kg ⁻¹ m ²]
Shutko (1986)	Broad leaf	3	0.950	2.0	0.475
		20	0.150	2.0	0.075
Jackson & O'Neill (1990)	Corn	6			0.150
		21			0.115
	Soybeans	6			0.288
		21			0.086
Kirdiashev et al., (1979)	Winter rye	2.25	0.310	0.7	0.442
		10	0.160	0.7	0.229
		20	0.080	0.7	0.114
		30	0.030	0.7	0.043
Ulaby & Wilson (1985)	Wheat	2.8	1.980	5.2	0.380
		6.5	0.780	5.2	0.150
		18.2	0.270	5.2	0.050
	Soybeans	2.8	2.410	1.8	1.340
		6.5	0.800	1.8	0.440
		18.2	0.180	1.8	0.100
Pampaloni & Paloscia (1986)	Alfalfa	0.8			1.850
		3.1			0.930
	Corn	0.8			0.600
		3.1			0.340
Ulaby et al., (1983)	Corn	6	0.744	4.0	0.186
		21	0.452	4.0	0.113
Brunfeldt & Ulaby (1984,1986)	Soybeans	5.9	1.025	2.8	0.366
		11.1	0.749	2.8	0.264
Chukhlantsev & Shutko (1988)	Cereals	18	0.284	2.0	0.142
	Alfalfa	18	0.364	2.0	0.182
Jackson et al., (1982)	Corn	6	0.199	1.2	0.162
		21	0.163	1.2	0.133
	Soybeans	6	0.240	1.0	0.240
		21	0.087	1.0	0.087
O'Neill et al., (1983)	Corn	6	0.785	6.0	0.131
		21	0.611	6.0	0.102
	Sweet sorghum	6	0.750	5.4	0.138
		21	0.613	5.4	0.105
Wang et al, (1980, 1982)	Short grass	6	0.550	0.3	1.770
		21	0.093	0.3	0.300
	Tall grass	6	0.797	0.4	1.990
		21	0.288	0.4	0.720
Wang et al., (1990)	Tall grass	21		0.5	0.150

continued on the next page

Source	Cover type	λ [cm]	τ [-]	θ_{veg} [kg m ⁻²]	b [kg ⁻¹ m ²]
Mätzler (1990)	Oats	1.4			0.010
		2.9			0.621
		6.1			0.120
Vyas (1990)	Broad leaf	19.3			0.092

For a bare soil the vegetation dependent parameters can be eliminated and Eq. 4.13 can be further simplified to:

$$T_B = (1 - \rho)T_s = \epsilon T_s \quad (4.15)$$

The roughness of the surface h has a significant effect on the emissivity ϵ . Choudhury *et al.*, (1979) accounted for this roughness by an empirical model (Schmugge, 1983; van de Griend *et al.*, 1991):

$$\rho = \rho_0 \exp(-h \cos^2 \theta_{inc}) \quad (4.16)$$

where ρ_0 is the smooth surface reflectivity [-] and h is a empirical roughness parameter [-].

The empirical roughness parameter h , which is a measure for the surface height variance and the horizontal correlation length, varies from 0 for a smooth surface to 0.5 for a very rough surface (Choudhury *et al.*, 1979; Schmugge *et al.*, 1992). In practice h varies usually between 0.1 and 0.3. According to Wang (1983) the correlation of the incidence angle θ_{inc} with h is small and therefore $\cos^2 \theta_{inc}$ can be neglected.

The effects of vegetation and surface roughness described above can be combined in a simple emission model for nadir incidence angles:

$$\epsilon_0 = 1 + (\epsilon - 1) \exp(h + 2\tau) \quad (4.17)$$

where, ϵ_0 is the smooth surface emissivity (-) with $\rho_0 = 1 - \epsilon_0$. In case the dielectric properties are uniform with depth the squared Fresnel equations can be used. Through inversion of these equations the dielectric properties can be obtained from ρ_0 (see Appendix E).

For nadir incidence angles and for horizontal and vertical polarization the Fresnel equation reads as:

$$\rho_h(\epsilon_r) = \rho_v(\epsilon_r) = \left| \frac{1 - \sqrt{\epsilon_r}}{1 + \sqrt{\epsilon_r}} \right|^2 \quad (4.18)$$

where ϵ_r is the relative permittivity. To convert the dielectric properties to soil moisture, a soil mixture model can be employed such as those from Wang and Schmugge (1980) or Dobson *et al.*, (1985).

Van de Griend and Owe (1991) used basically the approach described above with a few adaptations for their data. Since they used SMMR 6.6 GHz and 37 GHz dual

polarization data, they could use both horizontal and vertical brightness temperatures to derive the single scattering albedo and optical depth under the assumption that these temperatures are the same for both polarizations.

The inversion of the microwave emission model by Mo *et al.*, (1982) as is developed by and extended by various authors (Schmugge, 1983; van de Griend *et al.*, 1991; Jackson & Schmugge, 1991; Jackson *et al.*, 1995) is a straightforward and simple approach that combines physical understanding of microwave emission with a few empirical but general applicable parametrisations for roughness parameter h and vegetation parameters, b and θ_{veg} . In combination with the inversion of the dielectric model of Wang and Schmugge it is an effective inversion approach to retrieve soil moisture content θ from microwave brightness temperatures T_B . This approach is therefore used in this thesis.

4.4 Inversion of microwave scattering models

Various (semi-)empirical models have been developed with the specific task to estimate soil moisture. Two of them that are used in this thesis, IEM and OSU model will be shown here. However, most emphasis will be on the inversion of the IEM model (Fung *et al.*, 1992) as has been developed by Van Oevelen and Hoekman (1998). Although the inversion of this model is a relatively simple "Look Up Table" approach, it does give good insight in the physics and complexity of the inversion. The inversion of the Dubois *et al.*, (1995) model is given for reference in Appendix F but will not be discussed here since it has not been used in the analysis for this thesis.

4.4.1 The INVOSU model

The inverted semi-empirical OSU model developed by Oh, Sarabandi and Ulaby (1992), hereafter referred to as INVOSU model is an empirical model based upon the knowledge of scattering behavior in the limiting cases (e.g. large $k\sigma$) using measured backscatter and ground truth data. The range of validity for this model is large: values for the scaled roughness parameter $k\sigma$ should be in the range of 0.1 to 6 and for the kL in the range of 2.6 to 19.7. Here k is the wave number ($k = \frac{2\pi}{\lambda}$), σ is the root mean square of the height variation and L is the autocorrelation length of the surface height. The inverse model yields estimates of the surface roughness ($k\sigma$) and the real part of the soil dielectric constant (ϵ'). This model is a semi-empirical model. Actually, the OSU model consists of two models: one using HH and HV polarization and one using VV and HV polarization. Each model can be independently used and it is up to the user to decide which one to employ. Thus the model needs always the cross polarized radar data along with either HH or VV and incidence angle θ_{inc} as input.

The mathematical formulation of the OSU model is the non-linear function (see section 3.5.4):

$$\left(\frac{2\theta_{inc}}{p}\right)^{1/3p} \left[1 - \frac{q}{0.23\sqrt{p}}\right] + \sqrt{p} - 1 = 0 \quad (4.19)$$

with

$$p = \sigma_{hh}^0 / \sigma_{vv}^0 \quad (4.20)$$

$$q = \sigma_{hv}^0 / \sigma_{vv}^0 \quad (4.21)$$

and

$$\rho = \left| \frac{1 - \sqrt{\epsilon_r}}{1 + \sqrt{\epsilon_r}} \right|^2 \quad (4.22)$$

where σ_{ij}^0 is the backscatter coefficient with subscripts i and j denoting receiving and sending polarization respectively [- or dB], ρ is the squared Fresnel reflection coefficient of the surface at nadir [-], ϵ_r is the relative dielectric constant [-] and θ_{inc} is the incidence angle [rad].

Solving Eq. 4.19 iteratively for ρ , the dielectric constant ϵ_r can be found through Eq. 4.22. Using a soil mixing model of Wang and Schmugge (1980) or Dobson *et al.*, (1985) ϵ_r can be converted to a volumetric soil moisture content θ . The soil surface roughness $k\sigma$ can be found through:

$$\sqrt{\rho} = 1 - \left(\frac{2\theta_{inc}}{p} \right)^{\frac{1}{3p}} \exp(-k\sigma) \quad (4.23)$$

4.4.2 The INVIEM model

The IEM model (Fung *et al.*, 1992; Fung, 1994) in its full form is too complex to invert to retrieve soil moisture content θ . The model can be simplified so that it can be inverted but that compromises the range of validity. To keep this range another yet simple approach, called INVIEM has been applied in thesis. The INVIEM model (van Oevelen & Hoekman, 1999; van Oevelen, 1998) uses a Look Up Table with the Integral Equation Method (IEM) (Fung *et al.*, 1992; Fung, 1994) simulation results. This comprises a range of θ -values, with e.g. $0 < \theta < 0.45$ and a step size of 0.05, and a range of incidence angles (θ_{inc}), covering the variation in the image. For the simulations a number of surface roughness conditions covering the extremes of $k\sigma$ and kl in for example a reference field data set can be used. For the various frequencies and the different types of soil, several soil mixing models have been applied to relate the complex soil dielectric constant ϵ to the soil moisture content θ . For P-band data Hallikainen *et al.*, (1985), for L-band data Wang and Schmugge (1980) and for C-band data Dobson *et al.*, (1985) have been used. For each frequency band and polarization combination used (for example *HH* and *VV* polarization), the soil moisture extremes, related to the different roughness conditions, are determined by linear interpolation for the appropriate incidence angle and measured backscatter value. Since this interpolation can be done for *HH* and *VV* the range of possible solutions is limited to the overlap of the soil moisture ranges resulting from the backscatter of both polarizations (Figure 4.3). The whole procedure can be done for one band but also for multiple bands.

Thus, the INVIEM model estimates a range of soil moisture values for an assumed range of roughness conditions using one single backscatter value. The *HH* and *VV*

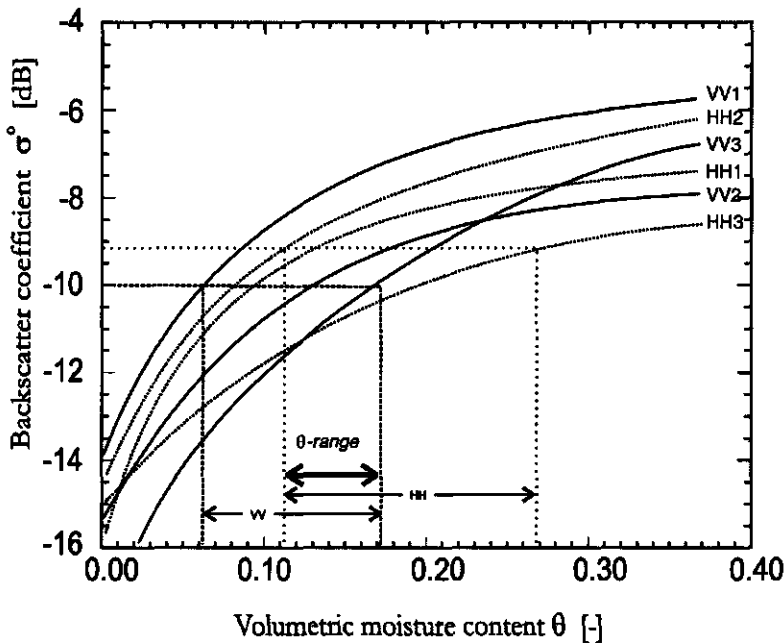


Figure 4.3: A graphical representation of the INVIEM model using a Look Up Table of the IEM simulation results for C-band with three different roughness cases. The backscatter behaviour as function of soil moisture content is given for HH and VV polarizations and for each roughness case indicated by $HH1, HH2, HH3$ and solid lines, $VV1, VV2, VV3$ and dashed lines. For each polarization the minimum and maximum soil moisture estimate is determined. Both polarizations are combined to limit the soil moisture range (θ -range). Thus each low and high estimate of soil moisture content θ corresponds to one of the three roughness cases for every backscatter σ° .

inversions are combined to narrow this range (Figure 4.3). The low and upper boundary of the estimated soil moisture range can be averaged to give a “medium” estimate. Depending upon the roughness classes, the sensitivity of the backscatter σ° on soil moisture content θ as predicted by the IEM model decreases with increasing soil moisture content (Figure 4.3) which can result in large ranges of soil moisture content estimates when the INVIEM model is applied. The effect of the correlation length is more difficult to describe. As can be seen in Figure 4.4 the backscatter can both increase and decrease with increasing correlation length. Furthermore this figure shows that it is possible to find different combinations of input parameters in the IEM model that will result in the same backscatter coefficient. The inversion of the IEM model will therefore not yield a unique solution.

4.5 Sensing-, skin- and penetration depth

In the previous sections the depth over which the soil moisture content θ is estimated is not mentioned. This sensing depth is difficult to determine because it is dependent

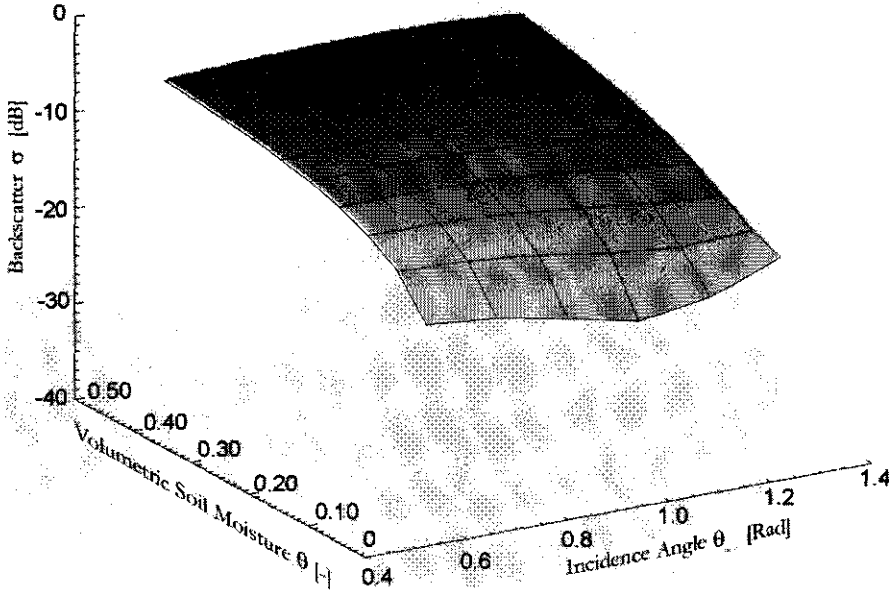


Figure 4.4: The effect of the surface roughness parameters $k\sigma$ and kl on the backscatter coefficient σ^0 at $\theta = 0.15$ and $\theta_{inc} = 23^\circ$. Increase or decrease of θ would result mainly in an increase or decrease resp. and not in a change of the shape of the plane.

upon various factors. Some confusion exists about the terms *sensing depth*, *penetration depth* and *skin depth*. For an air-soil surface interface the following definitions are used:

- The *skin depth* which is the depth over which the wave amplitude has attenuated by a factor $1/e$, is defined as (Schanda, 1986; Ulaby et al., 1982):

$$\delta_s \equiv \frac{1}{\alpha} = \frac{1}{\frac{2\pi}{\lambda_0} |\text{Im} \sqrt{\epsilon}|}, \quad (4.24)$$

where, α is the field attenuation coefficient and λ_0 is the wavelength in free space;

- Another term frequently encountered is the *penetration depth*, δ_p which for a natural uniform object (except those with a high permittivity such as water), and where scattering within the object is ignored, can be defined approximately as (Schanda, 1986; Ulaby et al., 1982; Ulaby et al., 1986):

$$\delta_p \equiv \frac{1}{2\alpha} \cong \frac{\lambda_0 \sqrt{\epsilon'}}{2\pi \epsilon''} \quad (4.25)$$

The penetration depth can be regarded as the depth over which the power or intensity is attenuated by a factor $1/e$. From the equations above it becomes clear that the *skin depth* is half of the *penetration depth*. Both the skin-

depth and penetration depth assume a homogeneous soil, thus non-varying ϵ .

- The *sensing depth* or *sampling depth* is the depth over which the sensor has retrieved a signal yielding information. It is this depth which is important, since it is the depth over which the parameter of interest can be directly estimated. The sensing depth is difficult to estimate because it depends on many factors such as temperature and water profiles, texture variations, surface roughness, angle of incidence etc.

In most inversion schemes the soil is assumed to be homogeneous for ϵ . This is seldomly true and is an additional source of error in the determination of soil moisture.

Raju et al., 1995 (Raju et al., 1995) examined the effect of soil moisture and physical temperature profiles on the microwave emission ($f > 1$ GHz) and showed that there is a considerable influence of these profiles on the emission. They noted that there is general agreement on the order of magnitude of the microwave sampling depth, in the range of $0.2\lambda_0 - 0.25\lambda_0$ where λ_0 is the wavelength in free space. Several other studies have investigated the magnitude of this sampling depth either through pure physically based models (Njoku & Kong, 1977; Wilheit, 1978) or combinations of physically based models with empirical methods (Wang, 1987).

4.6 Conclusions

The estimation of soil moisture from both passive as well as microwave measurements requires several steps. The most important steps are the *inversion of the emission or scattering model* resulting in the surface *dielectric properties* and *roughness* and the *inversion of the soil dielectric mixture model* which inversion leads to a *soil water content*. No matter which model is taken *additional information is always needed*, of which the vegetation amount, vegetation type and soil textural composition are the most important.

In this thesis the inversion of the microwave emission model by Mo et al., (1982) is applied. The inversion of this simplified radiative transfer model is a straightforward and simple approach that combines physical understanding of microwave emission with a few empirical but general applicable parametrisations for roughness parameter h and vegetation parameters, b and θ_{veg} . In combination with the inversion of the dielectric model of Wang and Schmugge (1980) it is an effective inversion approach to retrieve soil moisture content θ from microwave brightness temperatures T_B .

For the active microwave case the results are less straightforward because of the higher sensitivity of the backscatter coefficient σ^0 to vegetation (structure) and surface roughness. Two models have been used in this Thesis the INVOSU model and the INVIEM model. The INVOSU model (Oh et al., 1992) is an empirical model based upon the knowledge of scattering behavior in the limiting cases (e.g. large $k\sigma$) using measured backscatter and ground truth data. The range of validity for this model is large: values for the scaled roughness parameter $k\sigma$ should be in the range of 0.1 to 6 and for the kL in the range of 2.6 to 19.7. The model needs either HH and

HV or VV and VH polarization. The inversion of the IEM model, INVIEM (van Oevelen & Hoekman, 1999; van Oevelen, 1998), is a simple Look Up Table approach, applicable over a large range of surface roughness but does not take vegetation into account. The INVIEM model estimates a range of soil moisture values for an assumed range of roughness conditions using one single backscatter value. The HH and VV inversions are combined to narrow this range. Depending upon the roughness classes, the sensitivity of the backscatter σ^0 on soil moisture content θ as predicted by the IEM model decreases with increasing soil moisture content, which can result in large ranges of soil moisture content estimates. Other inversions of the IEM model usually limit the roughness range for which the model can be used. The more empirical models such as Dubois et al., (1985) can take into account some vegetation influence but are limited in their applicability over different surfaces and surface roughness types.

The *sensing depth* or *sampling depth* is the depth over which the sensor has retrieved a signal yielding information. It is this depth which is important, since it is the depth over which the soil water content θ can be directly estimated. The sensing depth is difficult to estimate because it depends on many factors such as soil temperature and soil water content profiles, texture variations, surface roughness, angle of incidence etc.. Currently no satisfying model is available that gives reliable estimates of the sensing depth.

Chapter 5

Description of data sets

5.1 Introduction

To test the various methods to estimate soil moisture through remote sensing it is necessary to have first of all the required remote sensing measurements preferably combined with the appropriate ground truth such that verification of the models is possible. Since, both passive and active microwave remote sensing of soil moisture content at various spatial resolutions is being the central issue in this study it was requisitory to use data of various field experiments to be able to meet the objectives. These field experiments are usually set-up in the framework of international climatological/hydrological research programmes.

The following sections provide a description of the remote sensing and ground truth data that have been used and where necessary additional information has been added.

5.2 EFEDA-Spain

The European Field Experiment in Desertification threatened Areas (EFEDA) was a large scale experiment within the framework of HAPEX (Hydrologic Atmospheric Pilot EXperiment) with an Intensive Observation Period (IOP) being held during June of 1991 (Bolle *et al.*, 1993).

5.2.1 Site Description

Location

The EFEDA experimental area is located between $38^{\circ} 55' - 40^{\circ} 05' \text{ N}$ and $2^{\circ} 11' - 3^{\circ} 11' \text{ W}$ and is situated on the central plateau of Spain with typical altitudes of 700 to 800 m. Within this area three sub-sites were chosen for intensive field studies: Barrax, Tomelloso and Radar de Haro (Belmonte). The main site for ground truth data collection is the Barrax area in the Castilla-La Mancha region in Spain. More specifically

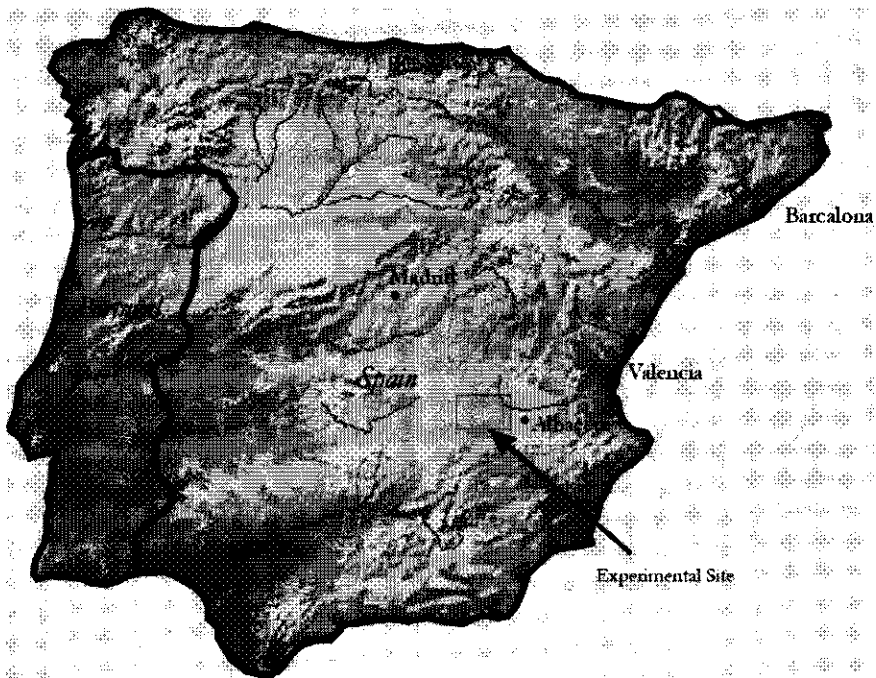


Figure 5.1: Location of the EFEDA-Spain experimental area.

this site is situated in the western part of the province of Albacete, 28 km from the capital town with the same name (Figure 5.1). The approximate centre coordinates are $39^{\circ}2'N$ and $2^{\circ}10'W$. This area was selected for its flatness and the presence of large uniform land-use units, thus minimizing the complications introduced by topographic structure and highly variably roughness. The elevation differences that can be found in this area are not more than 2 m.

Climate

The climate is of the Mediterranean type, with the heaviest rainfall in spring and autumn and lowest in summer. It exhibits a high grade of continentality, with quite sudden changes from cold months to warm months and high thermic oscillations between the maximum and minimum daily temperatures in all seasons. The average annual temperature is $14.1^{\circ}C$. The hottest month is July with an average temperature of $24.6^{\circ}C$ and the coldest January with an average temperature of $3.9^{\circ}C$. The yearly average maximum temperature is $21.1^{\circ}C$, the minimum $7.1^{\circ}C$ with the absolute extremes being $42.8^{\circ}C$ and $-18.0^{\circ}C$. The average period of frost goes from the middle of November to the middle of April. The first date frost has ever been recorded is 27th of October, the last date 2nd of May. The average rainfall is 474 mm with 72 rainy days. The evapotranspiration according to the method by Thornthwaite is 775 mm yr^{-1} , being higher than the precipitation from April to October.

Soils

The soils of the area are poorly developed and present a profile type, that belongs to the order of *Inceptisols* of the Soil Taxonomy (Soil Survey Staff, 1975). Taking into account the humidity regime *xerico* of the soils, the subgroups present are the "*Xerochrepts Calcixerollics*" or "*Xerochrepts*" "*Calcixerollix-Petrocalcics*", with a superficial horizon "*ochric*" and as subsuperficial horizons of diagnostic, the horizons "*calcic*" and/or "*petrocalcic*"

The main limitation by the soils imposed upon crop productivity capacity is the actual soil profile depth which is small in the area, due to the presence of the petrocalcic horizon with large amounts of total and/or active limestone. The stoniness is in many cases excessive due to the presence on the surface of remains of the petrocalcic horizon. The textures are generally quite balanced, with the open-clay predominating, whereas there aren't usually structural problems due to the stabilizing effect of the ion calcium on the structure.

The chemical properties are not too unfavourable for vegetation growth, although the lack of organic matter and the prolonged cultivation, have contributed to decreasing content of nutritious elements for the plants. The pH oscillates between 7.5 and 8.2 and the contents of limestone are between 30% and 60%. The soils are poor in phosphorus and relatively rich in potassium.

5.2.2 Remote sensing data collection

Various instruments have been flown during the Intensive Observation Period (IOP), with here only the NASA Thematic Mapper Simulator (TMS-NS001) and the JPL-AIRSAR being discussed.

The JPL -AIRSAR (see Appendix B) was flown on two days namely, June 19, 1991 and July 14, 1991. Data were acquired over the three main EFEDA sites covering the area using a triangular flight pattern. The flight lines were chosen such that over each test site almost a 40° radar look direction was achieved (Saatchi *et al.*, 1993).

The SAR data were calibrated using two procedures:

1. *Internal calibration*: using information from system tests to ensure that for each frequency all four channels (four polarizations) were calibrated relative to each other;
2. *External calibration*: to achieve an absolute value for the measured radar cross sections and to remove the cross talk and the channel imbalance. For this purpose trihedral corner reflectors and scene information have been used.

More information on the calibration can be found in Van Zyl *et al.*, 1992 and Saatchi *et al.*, 1993.

The TMS-NS001 has flown various lines over the Castilla La Mancha area on June 29. The instrument has 8 bands in the range of 0.458 to 12.3 μm .

5.2.3 In situ data collection

The intensive field campaign took place during the month of June. During the SAR flights time ground truth data were collected over a limited number of fields and plots in the Barrax and Tomelloso sites. The fields of Barrax are described in Table 5.1.

Table 5.1: Description of 9 fields in the Barrax area in Spain where soil moisture and surface roughness ground data are available.

No.	Field #	Description
1	Barrax #1	Irrigated maize
2	Barrax #2	Bare soil
3	Barrax #3	Non-irrigated barley (stubble field)
4	Barrax #4	Irrigated alfalfa
5	Barrax #5	Irrigated maize
6	Barrax #6	Non-irrigated barley
7	Barrax #7	Irrigated barley
8	Barrax #8	Irrigated maize
9	Barrax #9	Bare soil

Soil moisture

Soil moisture measurements were performed using various methods, mostly gravimetric core sampling and neutron probe measurements. During the first SAR flight on June 19, the volumetric soil water content θ was measured of the surface layers of 0-5 cm and 5-10 cm. At a few other sites the time evolution of θ at various depths was measured. An extensive description of the measurements and results are given by Visser and Hoekman (1992). The soil moisture measurements are summarized in Table 5.2.

Table 5.2: Volumetric soil moisture values θ ($\text{cm}^3\text{cm}^{-3}$) and roughness parameters σ and l for the four fields in the Barrax area in Spain measured on June 19, 1991.

Field	No.	Depth [m]						Roughness [cm]	
		0.02	0.05	0.10	0.20	0.25	0.30	σ	l
Bare	2	-	0.034	0.071	-	-	0.16	1.4	37
Alfalfa	4	0.231	0.306	0.322	-	-	-	0.5	104
Maize	5	0.130	0.186	0.261	-	-	-	1.8	91
Barley	7	-	0.054	0.097	0.122	0.140	-	1.0	140

Surface Roughness

The soil surface roughness, an important quantity in microwave remote sensing modelling, was determined using a needle board (see Figure D.2 in Appendix D). The needle board consists of two aligned areas with different density of needles by which the measurements can be made. Macro roughness can be measured with low density

sampling (1 needle per cm) and micro roughness with high density sampling (3 needles per cm). Each measurement yielded 151 samples in both high and low density: the high density was measured over 50 cm and the low density over 150 cm (Vissers and Hoekman, 1992). The needle board has to be level placed over the surface, the needles can then be lowered such that the top of the needles just hit the surface and altogether give a profile of the soil surface. Of the whole board a photograph was taken and the profile can then be digitised. In this way two sets of x, y co-ordinates are given for each pair of needles, where 'x' stands for the distance between the needles and 'y' is the height of the needles. The measurements are summarized in Table 5.3.

Table 5.3: Surface roughness parameters $k\sigma$ and kl normalised to wavelength for C-, L- and P-band for the 9 fields in Barrax, the units are both cm.

Field No.	C		L		P	
	$k\sigma$	kl	$k\sigma$	kl	$k\sigma$	kl
1	1.4	9.1	0.33	2.1	0.12	0.75
2	1.6	4.4	0.37	1.0	0.13	0.37
3	1.7	9.2	0.40	2.2	0.14	0.76
4	0.6	12.5	0.15	3.0	0.05	1.04
5	2.0	11.0	0.47	2.6	0.16	0.91
6	1.0	5.3	0.23	1.3	0.08	0.44
7	1.1	16.9	0.26	4.0	0.09	1.40
8	1.9	11.7	0.45	2.7	0.16	0.96
9	1.7	16.1	0.40	3.7	0.14	1.33

5.3 HAPEX-Sahel

The Hydrologic Atmospheric Pilot EXperiment in the Sahel (HAPEX-Sahel) was an international, multi disciplinary measurement and modelling campaign executed under the auspices of the World Climate Research Programme (WCRP), the International Geosphere-Biosphere Programme (IGBP) and the Government of Niger. The aim of the experiment was to increase our understanding of the energy, water and carbon cycles at different scales in the Sahel to improve the Global and Regional Circulation Models (P. Kabat & (Eds.), 1997). Most studies took place during the Special Observation Period (SOP) from August to October 1992. Some measurements however were taken during the whole experimental period which lasted from 1991 until 1993. The scientific effort was concentrated in three so-called Supersites (West Central, East Central and Southern Supersite) located within a $1^\circ \times 1^\circ$ area (Figure 5.2). More detailed information on the experimental set-up, framework and research activities can be found in Kabat *et al.*, (1997) and Goutourbe *et al.*, (1994).

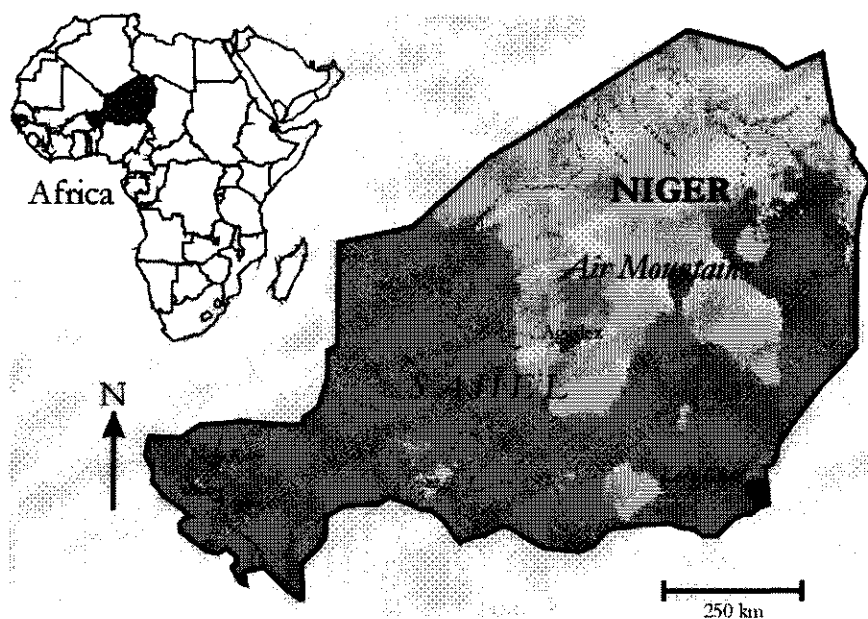


Figure 5.2: Map of the location of the experimental areas, S, W and E near Niamey during HAPEX-Sahel in Niger.

5.3.1 Site description

Location

The West Central Supersite (WCSS) of the Hydrologic Atmospheric Pilot Experiment in the Sahel was a 15 km² area approximately 50 km to the east of Niamey the capital of Niger, centred around the village of Fandou Beri (approx. 13° 32' N, 2° 30' E). Within this supersite four sub-sites are located, each on a typical land cover class (van Oevelen *et al.*, 1993; van Oevelen & Schmugge, 1997):

- Fallow bush/grassland on a sandy skirt with a slope of 0.5-2.0 %, for a number of years uncultivated agricultural land to recuperate;
- Millet on a sandy skirt with a slope of 0.5-2.0 %, an annually grown traditional crop;
- Tiger bush on the laterite plateau, a flat crusted bare surface interspersed by series of bushes of varying sizes, mainly used for fire and construction wood and grazing;
- Degraded fallow bush land on shallow sandy soil over shallow laterite.

Climate

In Niger the rainfall decreases sharply from south to north. The Sudan-Guinee region in the south has a yearly rainfall of more than 600 mm, going to the north this sharply decreases and in the arid Sahara region the rainfall drops below 200 mm a⁻¹. The Sahelian region has a continental climate with a dry season that lasts from October

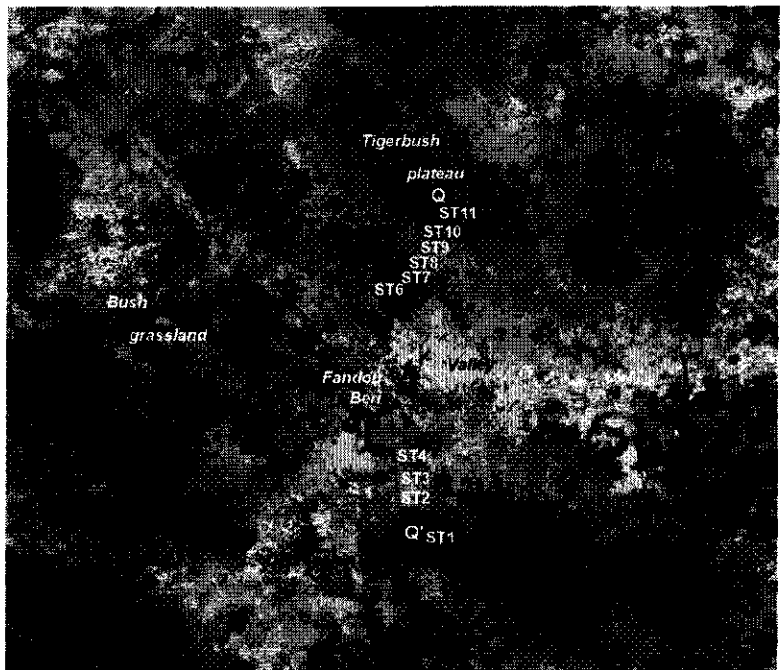


Figure 5.3: SPOT image with the location of Fandou Beri, the transect and subtransects within the West Central Supersite. SPOT data by courtesy of Dr. G.F. Epema, Department of Soil Science and Geology, Wageningen Agricultural University.

till May. In June the rainy season begins with the Southwest monsoon, which can last until October. The Capital of Niamey receives during this period about 590 mm of rainfall. The rainfall events are of a convective nature with irregular intervals and highly varying amounts of precipitation (up to 100 mm per event).

The temperatures vary between 14 and 46 °C with an yearly average of 28 °C. The highest temperatures occur between March and May and in October (monthly average 32 °C). The lowest temperatures are in August (monthly average 27 °C) during the rainy season and in December and January (monthly average 23 °C).

Geomorphology, Soils and Vegetation

The area is characterised by a typical valley-plateau morphology which consists of laterite-capped plateaus that are separated by sandy valley floors. The average topographic height difference between the plateaus and the valley bottom is less than 25 m. The edges of the plateaus have steep rocky escarpments of varying height but usually not much more than 3-5 m. The soils on the flat plateaus are classified as red-brown sand (clay) loams (*Leptosols*) some times covered by aeolian sand or sand dunes (*Arenosols*, *Leptosols* and *Cambisols*). Towards the valley the soils get more sandier and brighter of colour, in some places almost white. In some places underlying terraces of plinthite surface and red sandy and clay loams are found. In the valley bottom aeolian sand can be found (*Podzols* and *Arenosols*) as well as parts with heavy clays, sometimes covered by sand depositions (*Regosols* and *Gleysols*) (Figure 5.4) (Legger & van der Aa, 1994).

The vegetation in this area is typical and strongly location dependent. On the plinthite plateaus with their shallow soils a 'tiger bush' pattern of vegetation can be found consisting of *Guiera Senegalensis* and *Combretum Micranthum* bushes. In the valleys and on the slopes the Sahelian savannah vegetation is present. Also in the valleys and on the gentle undulating slopes agricultural crops (like pearl millet, cow peas and peanuts) can be found. Shifting cultivation is common practice and on the fallow sites various types of grasses and bushes can be found. Due to the increasing population along with increasing livestock the pressure on the land is increasing, notable by shorter rotation cycles in the shifting cultivation practice and the decreasing number of trees.

Wind and water erosion are important land degrading processes. Water erosion has locally a very strong impact, but wind erosion is considered much more severe because it removes or diminishes the (already thin) A-horizon over large areas. The villages in this area are mostly located in the valley bottoms and have in contrast with their surroundings quite some trees around them. The villages are usually connected by unconsolidated roads or tracks. The road from Niamey to the Supersite is a tarmac road and the road towards Fandou Beri and Dantiandou a laterite road.

5.3.2 Ground truth data collection

Numerous types of measurements are available for this site and we limit our selves here to the description of surface soil moisture and surface roughness measurements.

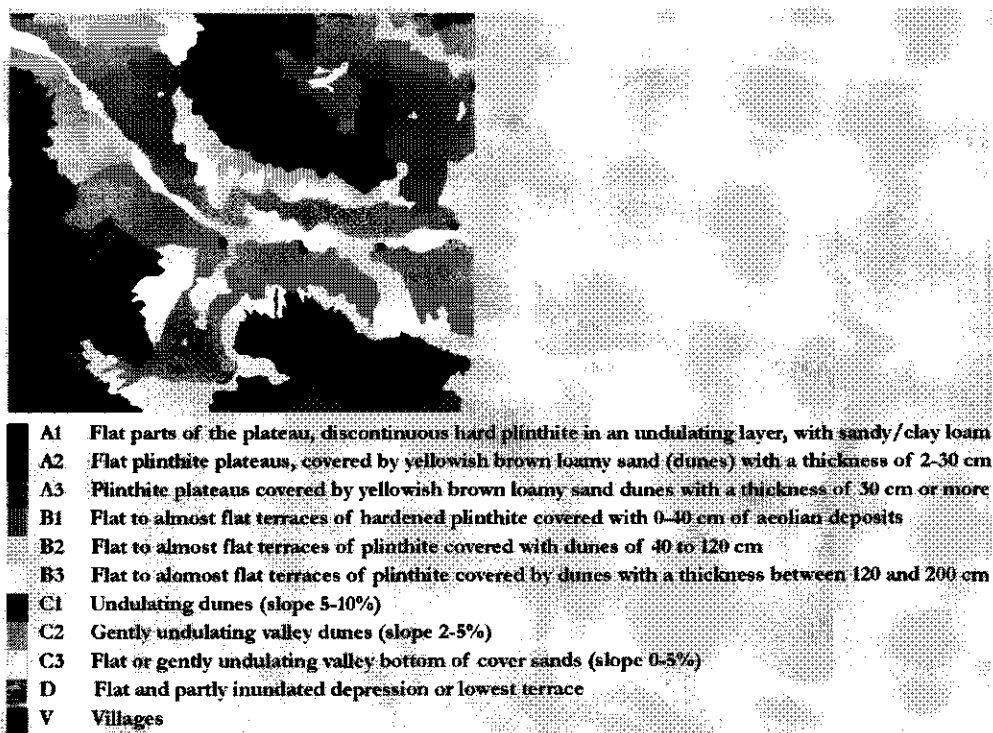


Figure 5.4: The soil map of the West Central Supersite in Niger (Legger & Van der Aa, 1994).

Soil moisture measurements

Most of the soil moisture measurements were performed along a North-South transect chosen for its diversity and easy access. The transect is about 5 km long and is divided into 11 different measurement areas or subtransects (ST) (see also Figure 5.5 and Figure 5.3). A description of the subtransects with their total length and number of measurement locations (locs.) per TDR is given below (van Oevelen *et al.*, 1993; Legger & van der Aa, 1994):

- ST1 (length \pm 100 m; 6 locs.). The southern laterite plateau on which also the sub site 'c' is located with the flux station (mast) of the Winand Staring Centre. The tiger bush is the dominant vegetation type on the plateau. Under the heating of the sun the bare laterite (brownish red coloured) soil mixed with laterite nodules ("gravel") becomes very hard, like brick. Only under the bush the soil is softer and stays much longer wet. The soil contains a lot of clay compared to the most other soils found in this area and is mixed with gravel. The plateau is nearly level with a slope of 0-1%.
- ST2 (length \pm 125 m; 6 locs.). Piedmont and escarpment of the southern laterite plateau is characterised by a very hard and rocky soil with scattered shrubs upon it. The surface under influence of intense showers becomes

easily eroded resulting in more (laterite or Continental Terminal) rocks than on the plateau. Water erosion produces also the gullies. The escarpment is very steep and sometimes almost vertical. The piedmont is less steep with a slope of 5-8%.

- ST3 (length \pm 250 m; 11 locs.). A millet field just below the piedmont of the southern plateau on glaciis. The soil is fine textured, light brownish red to yellow sand. The condition of the crop on this field is very poor, partly due to overland flow that forms gullies in this field during heavy showers. The field has a 2-5% slope.
- ST4 (length \pm 100 m; 5 locs.). Fallow land on a yellow sandy soil and covered with a fast growing herbaceous vegetation. Hardly any bushes are present and only some scattered trees are found. This subtransect is probably left fallow for the first year. The site is almost level with a 0-2% slope.
- ST5 (length \pm 200 m; 9 locs.). A millet field near the village of Fandou Beri in an alluvial valley bottom with white fine textured sands. The soil is almost purely quartz and due to the manure coming from the village the millet is growing fairly well. (0-2% slope)
- ST6 (length \pm 250 m; 11 locs.). The degraded bush land located near sub-site 'd' with a mast of the German group of the Free University of Berlin. The soil is yellow and fine textured. The vegetation is nearly exclusively dominated by *Guiera Senegalensis*. Normally under *Guiera Senegalensis* there is also a herbaceous layer present but at this site hardly any can be found. Only in the rain season a fast growing very thin layer of one type of herb (not known to the authors) is present. This site is located on partly lower lying glaciis and partly on the lower lying plateau (subplateau) with a 0-2% slope. Heavy showers have produced numerous gullies that are not very deep.
- ST7 (length \pm 100 m; 5 locs.). Sub plateau with laterite (gravel) surfacing and a 0-2% slope. This lower lying plateau separates the higher laying aeolian sand covered slopes from the lower laying sand covered slopes and is at this point very small but at other locations can be much larger.
- ST8 (length \pm 250 m; 11 locs.). Degraded bush land is found on the higher lying plateau with a 0-2% slope. This site is comparable with ST6.
- ST9 (length \pm 250 m; 11 locs.). Millet on the higher lying glaciis with a 2-5% slope. The soil is yellow fine textured sand. The millet is doing poorly on this site, although there are spots in the field where it grows very well. In general such spots can often be found around trees where cattle, like goats, cows etc., is tied down regularly and thus a higher deposition of manure takes place.
- ST10 (length \pm 75 m; 4 locs.). Piedmont of the northern laterite plateau with a 5-8% slope. This site is comparable to the ST2
- ST11 (length \pm 75 m; 6 locs.). Northern laterite plateau looks much like the southern plateau (ST1) is covered with tiger bush and is nearly level with a 0-1% slope.

The number of (sub)plateaus indicated in Figure 5.5 are those observed in the field. After a more thorough geomorphological study of the area it may be possible that

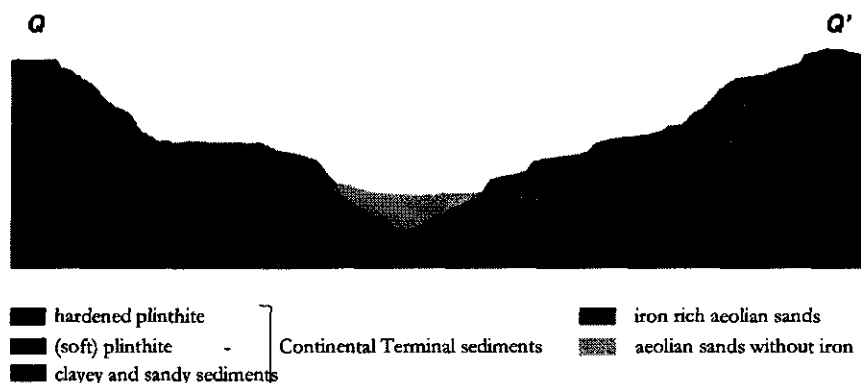


Figure 5.5: Schematic drawing of a cross-section of the area along the transect.

more plateaus exist. These plateaus are probably remnants of old river terraces covered with aeolic deposits. This deposition layer is at some places very thin or absent, e.g. subtransect ST7, and thus the laterite surfaces. In the valley bottom a very thick layer of white sands with a high permeability is present, which acts as a drainage canal for the valley.

The soil moisture data were collected over a depth of 5 cm using a Time Domain Reflectometry (TDR) system. The system used was the TRIME P2¹ system consisting of a probe with two parallel rods of 10 cm length connected with a coax cable to the main module which had a digital display giving the volumetric soil moisture content. The rods of the probe were fully inserted into the ground under an angle of 45° with the ground surface resulting in a measurement of the average volumetric soil moisture content over a depth of 5 cm. For a detailed discussion about TDR the reader is referred to Heimovaara and Bouten (1990) and Dasberg and Dalton (1985).

The soil moisture data were collected along the transect for 9 of the 11 subtransects during the 6 flights of the Push Broom Microwave Radiometer (PBMR). Two TDR's, referred to their serial numbers 1812 and 1696, were used to perform simultaneously the measurements with about 25 m distance between them. The shortest subtransect was about 50 m long and the longest was about 250 m long. With each TDR every 25 m a series of measurements were taken within a square meter (called a measurement location) until the readings of the TDR gave two values that were less than 1.5% different from each other (see Figure 5.6). This was done to avoid outsprings due to the large variability of soil moisture; thus using both TDR's an averaged volumetric soil moisture content value could be obtained.

The measurements indicated that there were sometimes substantial differences between the given soil moisture values of the two TDR readings. For the drier periods it was more than 5% on average. Therefore both TDR's were tested and compared to another calibrated cable tester (Tektronix 1502) as well as volumetric soil moisture measurements in the soil physics laboratory. From information from the supplier and

1. The name of the manufacturer is given for the benefit of the reader and does not imply any endorsement by the Wageningen University.

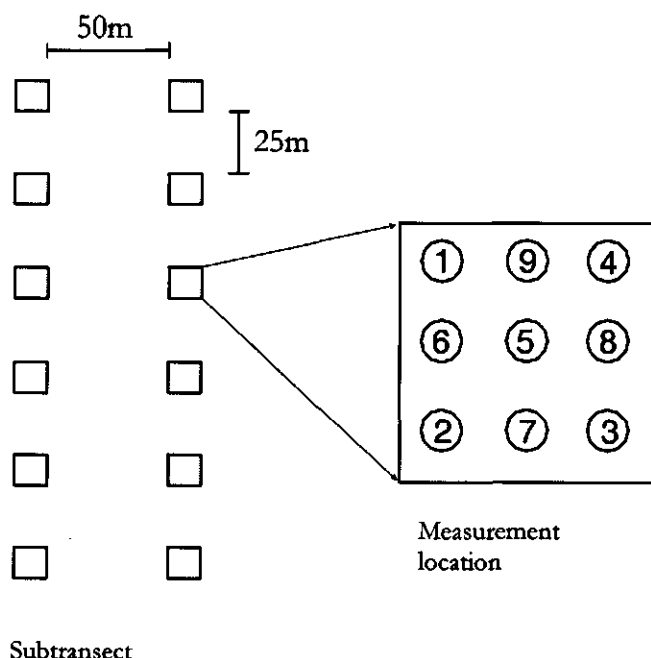


Figure 5.6: A schematic representation of the measurement set-up.

from the tests performed two major conclusions can be drawn. Firstly, one of the TDR's was insensitive for low volumetric soil moisture values ($< 3\%$). Secondly the way the probes were inserted into the ground was of major influence on the readings. One or both of these influences would explain the large differences observed in the measurements.

Because the PBMR did not cover the whole area no data were collected for subtransects ST1 and ST2. The other data that are missing is because of the impossibility to insert the probes of the TDR's into the soil at that time. The subtransects where laterite soil surfaced, especially ST7 and ST11 bare, which became under the heating of the sun hard as rock and could not be penetrated without the danger of breaking or damaging the rods.

Surface roughness measurements

Since it became clear that the surface was everywhere rather smooth and alike, the number of measurements made was therefore limited to those surfaces that were distinct and representative for the area. For each site two pairs of measurements using a needle-board were taken, resulting in two measurements directed towards the magnetic north pole (0° , the 'y' direction) and two perpendicular to it (90° , the 'x' direction). Since we assumed that the physical processes that cause surface roughness were uncorrelated for both directions, measurements restricted to these two directions are sufficient.

There are several ways to express the surface roughness. Here the root mean square (RMS) (mm) of the height differences of the needles, σ (Table 5.4) and the autocorrelation length (cm), l , was taken as a measure of surface roughness. With these values the power density spectrum using the fast Fourier Transform (FFT), and the Autocorrelation function using an inverse FFT were calculated using the algorithms from Numerical Recipes (1990) (Press *et al.*, 1992).

Table 5.4: Averaged surface roughness parameters $\overline{k\sigma}$ and \overline{kl} for the measured subtransects in the West Central Supersite, with $k=0.1785 \text{ cm}^{-1}$ (ERS C-band).

Measurement site	$\overline{k\sigma}$	\overline{kl}
ST3	5.22	16.10
ST4	7.42	8.73
ST5	11.02	11.31
ST7	3.20	3.93
ST8	4.61	10.39
ST10	9.30	12.79
ST11	5.60	4.21

5.3.3 Remote sensing data collection

The PORTOS radiometer operates at frequencies of 5.05, 10.65, 23.8, 36.5 and 90.0 GHz. Only the 5.05 GHz channel is of relevance for soil moisture studies and this band was available on August 23, 24, 25, September 1, 2 and 12. The first three days in both H - and V -polarization and for the remainder only in H -polarization. Most of the measurements were taken at a 45° angle of incidence. The calibration of the PORTOS instrument has been described in (Chanzy *et al.*, 1996).

The Push Broom Microwave Radiometer (PBMR) is a passive microwave instrument operating at a frequency of 1.42 GHz ($\lambda=21 \text{ cm}$) with four horizontally polarized beams centered at 8° and 24° which cover a swath of 1.2 times the aircraft altitude. The instrument has been in use for over 10 years and has been employed in numerous field experiments such as FIFE (Wang *et al.*, 1990) and Monsoon'90 (Schmugge *et al.*, 1994). Measurements of T_B at the wavelength of 21 cm gives estimates of soil moisture content θ for approximately the top 5-cm layer of the soil. The instrument was flown nine times during the Intensive Observation Period (IOP) with two type of flight patterns, one north-south at a altitude of 1500m and one east-west at altitudes between 250 and 600 m (~ 80 to 200 m spatial resolution), which covered the supersites (Schmugge *et al.*, 1994). Data flights used in this study were performed on August 25, 26, September, 2, 4 and 12. Along with the PBMR flights infrared surface brightness temperatures were measured using the PRT5 radiometer (Chanzy *et al.*, 1996). Detailed information about the PBMR calibration and geolocation can be found in Chanzy *et al.* (1996).

The ERS-1 SAR data are available for four dates, namely July 4, August 8, September 12 and October 14, 1992. Only the September 12, 1992 image coincided with a PBMR image over the West Central Supersite.

5.4 Little Washita River Watershed

5.4.1 Site description

Location

The Little Washita River Watershed covers about 605 km² and is a tributary of the Washita River in southwest Oklahoma. The watershed is situated in the southern part of the Great Plains of the United States (Figure 5.7).

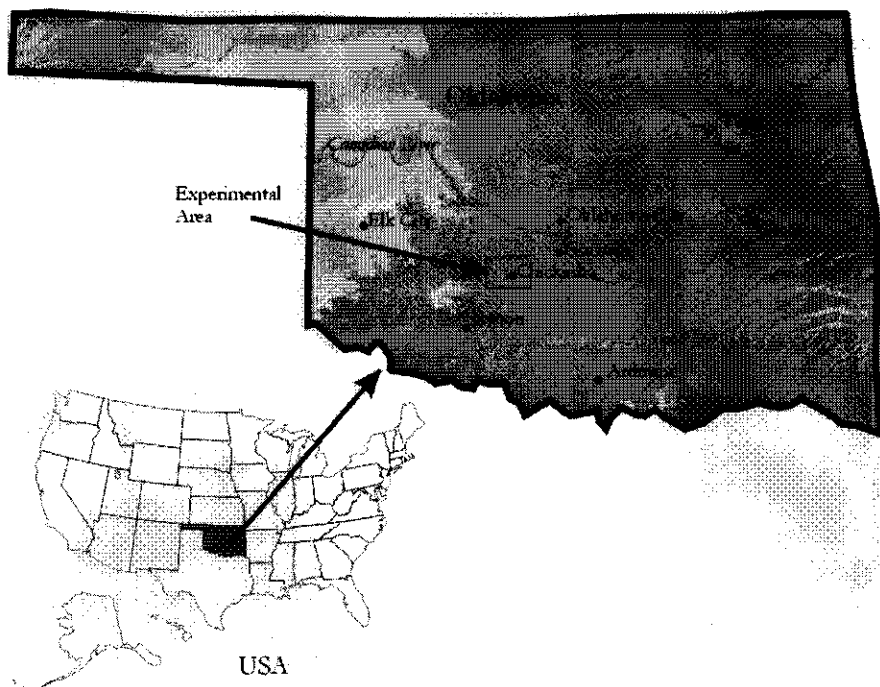


Figure 5.7: Location of the Washita'92 and '94 Little Washita river experimental site.

Climate

The region has a continental climate and is classified as moist and subhumid. The average rainfall is about 747 mm. The winters are short, temperate and dry but usually a few very cold weeks occur. The summers are typically long, hot and relatively dry. Much of the annual precipitation and most of the large floods occur in the spring and fall. The average high temperature for July is 34 °C and the average daily low temperature for January is -4 °C.

Geomorphology, soils and vegetation

The topography in the area is gently to moderately rolling except for a few rocky, steep hills near Cement, Oklahoma. The maximum relief is about 200 m. The bedrock

exposed in the watershed consists of Permian age sedimentary rocks. The formations dip gently to the southwest but the surface drainage is generally to the east. The Chickasha formation is the oldest and outcrops can be found in the eastern (outlet) side of the watershed. This formation comprises about 4.6 % of the total area and consists of brick-red sandy shale that is gypsiferous. The largest formation is the Rush Springs formation which outcrops in a central portion of the watershed covering 45.6 % of the area. This formation consists of fine-grained sand stone and silt stone strata. The soils in the area vary mostly from fine sandy loam to silty clay loam.

The land use in the region can be grouped in eight categories: range, pasture, forest, cropland, oil waste land, quarries, urban/highways, and water. Crops such as wheat and corn are dominant in the area.

5.4.2 Washita'92

Washita'92 was a co-operative experiment between NASA, USDA and several other government agencies and universities. The objective of the experiment was to collect a time series of spatially distributed hydrologic data, focusing on soil moisture and evaporative fluxes, using both conventional and remotely sensed methods. Most of the experiment focussed on the Little Washita River Watershed and a few surrounding areas in the general vicinity of Chickasha, OK.

The data are described below and ancillary information is given by Jackson *et al.*, (1993).

5.4.3 Ground truth data collection

The Little Washita Watershed was selected for this effort because of the extensive hydrological research that has been conducted there in the past, its ongoing data collection, extensive meteorological network and other facilities and their staff. Data collection was conducted from June through June 18, 1992. The experiment took place just after a period of extensive rainfall which had lasted several weeks. The soils over the entire watershed were therefore at field capacity and standing water was quite commonly encountered. No rainfall occurred during the experimental period thus allowing for observation of dry down conditions.

Soil moisture measurements

The sampling scheme was set up with the intention that the average of all surface soil moisture samples of each site represented the mean surface soil moisture value for that site. Measurements were taken over 35 sites distributed over the whole watershed and representing the various soil texture and land cover class types. Two major types of sites can be distinguished: small sites which are more uniform and where 9 samples were collected, large sites (at least 0.8 km \times 0.8 km) where at least 16 samples were taken. The sampling procedure consisted of making 5 cm deep gravimetric soil samples using a scoop, placing the soil in cans, seal them and weigh and dry them to calculate the gravimetric soil moisture content. Using bulk density measurements which

were performed for most of the sites, these gravimetric values were then converted to volumetric moisture contents.

Profile soil moisture measurements were taken with a resonant frequency capacitance probe at 14 rain gauge locations and 4 meteorological observation sites. These measurements give an indication of the changes in the soil moisture profile but due to difficulties in the calibration large uncertainty exists in the absolute values that were obtained.

In support of the determination of the surface emissivity ϵ from brightness temperatures T_B soil temperatures were collected at depths of 5 cm and 15 cm using metal dial type thermometers as well as digital probes.

Surface roughness measurements

The surface roughness measurements were done for 7 sites using a laser profiler and "paint and paper" profiler (Jackson & Schiebe, 1993) (see Appendix D). The latter was especially necessary to determine the correlation length of sites where this length was too large to be measured by the laser profiler (max. linear dimension is 95 cm).

Table 5.5: Average surface roughness parameters, $\bar{\sigma}$ and \bar{l} for the measured sites in the Little Washita watershed.

Measurement site	Type	$\bar{\sigma}$ [cm]	\bar{l} [cm]
PR001	Bare	2.29	8.75
AG005	Bare	1.29	16.25
AG002	Bare	1.82	17.75
AG001	Corn	1.23	11.25
AG006	Wheat	0.68	17.25
AG007	Alfalfa	0.50	13.25
MS001	Rangeland	1.23	7.75

5.4.4 Remote sensing data collection

Various instruments were flown during the campaign in Washita. An experimental passive microwave instrument, the electronically steered thinned array radiometer (ESTAR) was flown on the C-130n along with the NS001, an optical instrument. The ESTAR instrument was operated daily from June 10 until June 18, 1992 and covered for each of the eight days the whole watershed producing brightness temperature maps covering about 704 km². The NS001 instrument was operated on the same days but unfortunately due to the weather condition most of the time the area was partly clouded. Only on June 18 good clear sky conditions were present and cloud free images could be obtained.

The JPL-AIRSAR was flown on a DC-8 and was operated from June 10 until June 18, with a crew rest day on June 15. The strategy for coverage was twofold:

- To provide complete coverage of the whole watershed at lower spatial resolution (synoptic data 120 m);

- To cover specific agricultural areas where ground data have been obtained at the spatial higher resolution of approx. 10 m.

A cloud free SPOT scene was acquired on July 3, 1992. Since this was after the experiment the data could primarily be used for mapping and land-use classification.

5.4.5 Washita'94/SIR-C

The Washita'94 experiment was a large scale hydrologic field experiment conducted over the Little Washita watershed. The primary objective of this experiment was to provide combined ground and remotely sensed data sets for modelling and analysis of hydrologic state and flux variables. The third Space shuttle Imaging Radar (SIR-C) mission was planned for April and August of 1994 (later the august mission was postponed until October) and was one of the determining factors in the set-up of the Washita'94 experiment. The SIR-C mission was to consist of one week of daily observations for the Watershed site, with as principle variable of interest surface soil moisture.

The measurements presented here were taken in "Area 1" one of the key areas selected during the experiment for detailed field measurements. More detailed information can be found in Starks and Humes, 1996

5.4.6 Ground truth data collection

Surface soil moisture measurements

Two types of surface soil moisture field measurements were available, gravimetric soil moisture sampling and volumetric soil moisture sampling using TDR's.

All the volumetric measurements were performed using two portable TDR's in "Area 1", on of the measurement sites. Within this site 5 agricultural fields with different crops were sampled. The crops were: Alfalfa/winterwheat (11); Corn field (almost bare)(12); Winter wheat (13); Rangeland (14); Oat (early growing stage) (15.) The purpose of these detailed soil moisture measurements was to provide insight in the spatial variability of soil moisture en to enable a better comparison between SAR retrieved soil moisture and the soil moisture measured in the field. In Figure 5.8 a schematic representation of the site is given.

In Figure 5.8, the transects along which the measurements were performed are indicated. There were two long transects AT1 and AT2 and 5 cross transects (CT1..CT5). Only along the two long transects measurements were performed daily. On the cross transects only the first two days (April 6, 7). In general the measurements were taken walking the long transects from North to South. The second week (April 12-16) also measurements were performed on the oat field (15).

During the first two days one of the probes of each instrument broke off and had to be shortened. Most of the data that were measured was done with these shorter probes. The calibration curve for the 'short' probes was determined using soil from the

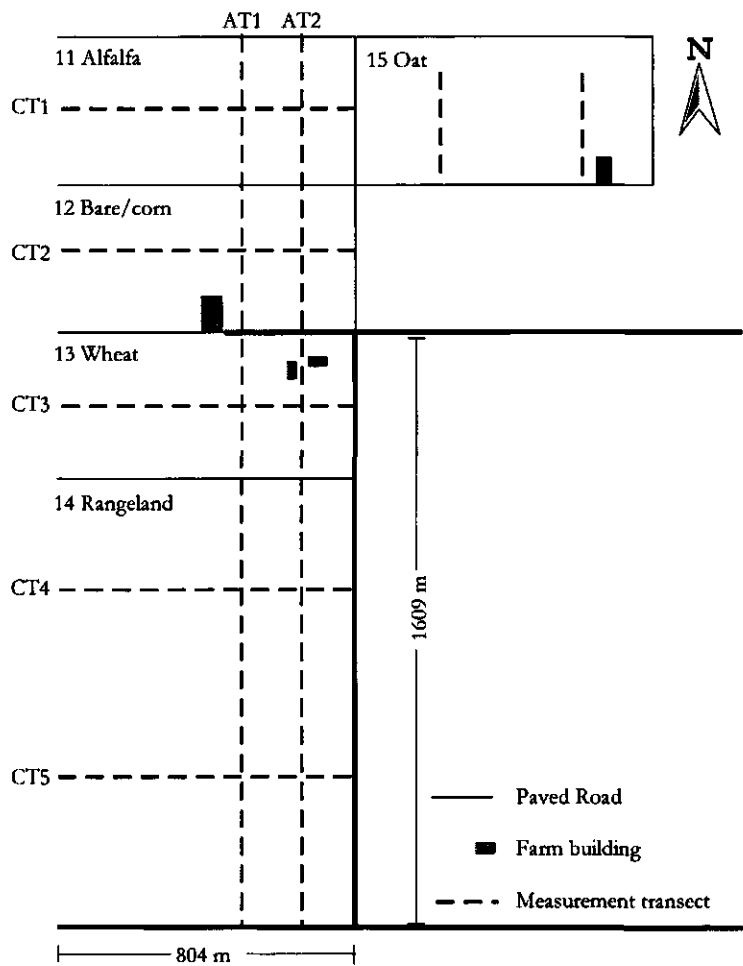


Figure 5.8: Schematic representation of area 1 on which the measurement transects are indicated.

Table 5.6: Volumetric soil moisture measurements θ on fields 11-14 along transects AT1 and AT2

Distance	25m	25m	25m	25m	25m	25m	25m
Date	6 April	6 April	7 April	7 April	9 April	9 April	11 April
Transect	AT1	AT2	AT1	AT2	AT1	AT2	AT1
TDR nr.→	1502	1437	1437	1502	1437	1502	1502
Field 11							
Mean	24.52	13.74	16.91	8.73	15.77	11.82	27.65
St. Dev.	6.46	4.14	4.90	2.26	5.06	4.15	3.05
Field 12							
Mean	32.54	26.06	21.35	20.58	24.39	26.73	28.88
St. Dev.	4.33	9.19	9.25	7.91	4.77	6.27	2.46
Field 13							
Mean	15.59	11.51	10.97	8.51	11.38	7.77	23.57
St. Dev.	6.45	3.61	6.15	5.96	5.71	2.95	6.27
Field 14							
Average	28.53	27.19	25.66	25.92	22.79	23.31	NA
Std. Dev.	4.34	5.63	3.75	4.66	4.96	3.91	NA

bare corn field. The volumetric soil moisture content using TDR θ_{TDR} vs. laboratory measured volumetric soil moisture content θ_{LAB} yielded a regression curve:

$$\theta_{TDR} = 1.12\theta_{LAB} - 1.44 \quad (5.1)$$

with st. dev. = 2.78 with a linear regression coefficient $R^2 = 0.94$. The other data should be calibrated using the longer probes.

In Tables 5.6 and 5.7 the soil moisture measurement using two TDR's are summarized for 4 fields in "Area 1".

The gravimetric soil moisture sampling was performed to enable calibration and verification of the data produced using the ESTAR microwave radiometer. Sites were selected to include a representative sampling of the various soil textures and land cover conditions. The primary goal was to average all samples from all sites to compare with the average of the microwave data. Comparison on point by point basis is not possible due to the low accuracy in geographical position of the point measurements. These data were collected over an grid with 100 m spacing, where possible and resulted on average in 14 samples per site. The sampling procedure and conversion to volumetric values based on dry bulk density measurements is the same as explained in the section 5.4.3. The data of four fields in "Area 1" are summarized in Table 5.8.

Surface roughness measurements

On selected fields in the watershed surface roughness measurements were performed using the "paper-spray" method (Appendix D). The results for the sites measured in "Area 1" are given in Table 5.10.

Table 5.7: Volumetric soil moisture measurements θ on fields 11-14 along transects AT1 and AT2

Distance	50m	50m	50m	50m	50m	50m
Date	12 April	12 April	13 april	14 April	15 April	16 April
Transect	AT1	AT1	AT1	AT1	AT1	AT1
TDR nr.	1502	1502	1502	1502	1502	1502
Field 11						
Mean	28.11	27.06	25.87	24.72	21.24	20.44
St. Dev.	2.04	2.46	2.60	2.78	5.39	6.14
Field 12						
Mean	27.63	25.78	25.05	25.06	21.05	23.29
St. Dev.	3.66	5.56	2.04	2.98	8.31	9.55
Field 13						
Mean	23.30	20.11	20.07	14.90	16.23	12.77
St. Dev.	2.48	2.28	2.09	1.91	2.96	2.83
Field 14						
Average	28.43	NA	26.81	26.15	26.89	26.07
Std. Dev.	1.36	NA	2.51	2.32	2.51	2.60

Table 5.8: Gravimetric soil moisture measurements θ on fields 11-14 using a grid with 100 m spacing for April 6 -12.

Date	6 April	7 April		9 April	10 April	11 April	12 April	
Time	11.00h	10.00h	15.00h	16.00h	12.00h	13.00h	10.00h	15.00h
Field 11								
Mean	0.073	0.083	0.076	0.084	0.095	0.246	0.242	0.202
St. Dev.	0.032	0.033	0.029	0.030	0.015	0.082	0.063	0.058
Field 12								
Mean	0.115	0.12	0.111	0.125	0.109	0.251	0.184	0.159
St. Dev.	0.064	0.048	0.046	0.060	0.035	0.048	0.060	0.045
Field 13								
Mean	0.084	0.087	0.078	0.092		0.268	0.247	0.247
St. Dev.	0.044	0.062	0.056	0.066		0.029	0.023	0.032
Field 14								
Mean	0.169	0.193	0.175	0.182	0.171	0.253	0.232	0.239
Std. Dev.	0.051	0.062	0.056	0.054	0.050	0.033	0.026	0.048

Table 5.9: Gravimetric soil moisture measurements θ on fields 11-14 using a grid with 100 m spacing for April 13 -16.

Date	13 april		14 April		15 April	16 April
Time	10.00h	15.00h	10.00h	15.00h	11.00h	14.00h
Field 11						
Mean	0.193	0.201	0.164	0.134	0.132	0.109
St. Dev.	0.057	0.069	0.046	0.054	0.053	0.058
Field 12						
Mean	0.145	0.122	0.126	0.1	0.099	0.101
St. Dev.	0.051	0.045	0.054	0.044	0.046	0.049
Field 13						
Mean	0.22	0.185	0.177	0.155	0.143	0.114
St. Dev.	0.031	0.072	0.032	0.041	0.036	0.048
Field 14						
Mean	0.241		0.24		0.21	0.193
Std. Dev.	0.047		0.057		0.061	0.046

Table 5.10: Average surface roughness parameters, $\bar{\sigma}$ and \bar{l} for the measured sites in Area 1 in the Little Washita watershed.

Measurement site	Type	$\bar{\sigma}$ [cm]	\bar{l} [cm]
11-1	Alfalfa/winterwheat	0.70	3.98
11-2	Alfalfa/winterwheat	0.91	18.53
12-1	Corn field	3.85	12.92
12-2	Corn field	4.11	14.20
12-3	Corn field	4.93	13.47
12-4	Corn field	3.40	13.12
12-5	Corn field	0.86	11.42
13-2	Winterwheat	0.52	5.45
13-3	Winterwheat	1.09	6.64
14-1	Rangeland	0.73	8.77

5.4.7 Remote sensing data collection

As stated in the introduction the SIR-C mission was one of the drivers of the experiment and various types of data became available. Unfortunately over the main site of interest the data of the Space Shuttle radar became corrupted due to interference with a transponder in a nearby field. These data have therefore not been used.

On the C-130 were, the same as in 1992, the ESTAR and NS001 instruments operated. These data were recorded in principle every day of the experiment.

The objectives of the JPL-AIRSAR which was mounted on the NASA DC-8 were to extend the data collection window of the Shuttle mission and to provide at least one data collection flight concurrent with the Shuttle overpass. The AIRSAR flight dates were on April 10 and 12, 1992.

5.5 NOPEX/Forest-Dynamo

5.5.1 Site description general NOPEX area

The NOPEX study site lies north west of Uppsala, Sweden, in an area that is dominated by forests of predominantly pine and spruce (approx. 15% are deciduous trees). The site was chosen mainly for its flatness (about 30-70 m above sea level -asl-, with extremes at 1 and 131m asl) and the presence of large patches of mixed boreal-forest and agricultural areas. Furthermore, the distance to the sea is approximately 50 km, avoiding complications of land-sea circulation. The site is on the southern limit of the boreal forest zone with a climate that is more maritime than is usual for boreal forest. The geology of the region is characteristically Northern European: granite, sedimentary gneiss and leptite. The main measurement sites for this study are located in the forest at Siggefora, Östfora, about 30 km Northwest of Uppsala, and the agricultural area around Tisby near Fjärdhundra, about 35 km West of Uppsala (Fig. 5.9).

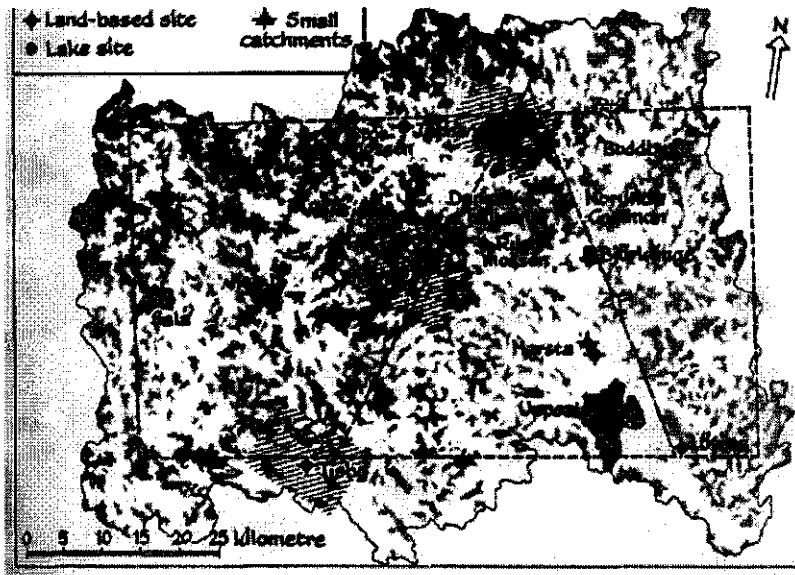


Figure 5.9: Map of the NOPEX region in Sweden. Dotted lines are flight "legs" which are over the measurement sites located in forest and bogs (grey), agricultural land (white) and lakes (black). The three dashed areas are EMISAR targets. Notice the location of the test sites near Siggefora(Östfora) and Fjärdhundra. Drawing by Hans Nilsson (Halldin *et al.*, 1995).

Site description Siggefora

The Siggefora site is located near a little lake called Siggeforsjön about 25 km from Uppsala. The site is dominated by Norwegian Spruce (*Picea abies*) and Scots Pine (*Pinus sylvestris*). Height differences throughout the forest are small with a total change of elevation of less than 15 m over the 4 km² area of the Siggefora test site.

Individual stands were chosen for ground truth measurements on the basis of species homogeneity and spatial uniformity (van Oevelen & Woodhouse, 1996).

Site description Fjärdhundra

The agricultural area around Tisby near Fjärdhundra is characterised by gentle slopes. The soil types are predominantly clay and clay-loams. The dominant crops are wheat and barley, other crops like peas and rape seed can also be found. In Figure 5.10 a detailed map is given showing the location and measurement transects.

5.5.2 Ground truth data collection

Soil moisture content

The soil moisture data were collected over a depth of about 6 cm using a Time Domain Reflectometry (TDR) system (Topp *et al.*, 1980). The system used was the TRIME P2 system consisting of a probe with two parallel rods of 12 cm length connected with a coax cable to the main module which has a digital display yielding the volumetric soil moisture content. The rods of the probe were fully inserted into the ground under an angle of about 30° with the surface resulting in a measurement of the average volumetric soil moisture content over a depth of approximately 6 cm. During the 1995 campaigns the rods were also inserted at an even larger angle to obtain measurements over an depth of approximately 3 cm.

Soil moisture measurements are available for 1 day (June 23) in 1994 during the first Concentrated Field Effort (CFE1), and 3 days (May 3 and July 5, 6) in 1995 during the CFE2. Snow cover prevented soil moisture measurements on May 1, 1995. Soil moisture measurements are available for 6 transects covering various fields. The original data can be found in Van Oevelen and Woodhouse (1996).

Surface roughness

During the 1994 campaign (CFE1) only qualitative soil roughness data are available in the form of photographs showing a transparent pane with 1 cm grid (see Figure D.3 in Appendix D). These data are difficult to interpret and therefore not used in the quantitative analysis (c.f. needleboard in Figure 5.11). These data indicate that the surface roughness appears to be comparable to the situation in the summer of 1995. However, the pictures of the transparent gridded pane could be very well used for interpretation of vegetation height characteristics.

For 1995 two sets of roughness measurements are available. The first set was measured in April of 1995 over bare soils under saturated conditions (Table 5.11). The second set was measured during July of 1995 when the crops were present (Table 5.12). Both data sets were collected using the same type of needleboard.

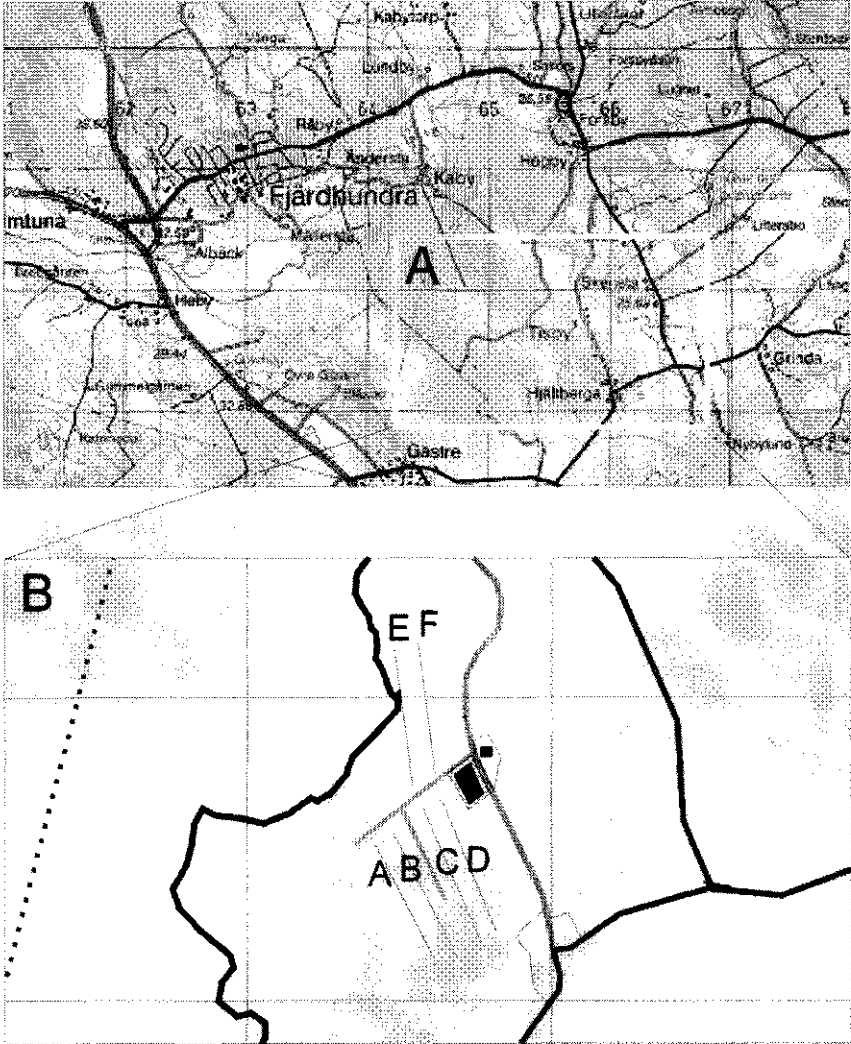


Figure 5.10: More detailed map of the Fjärdhundra site. A through F indicate the transects of soil moisture measurements.

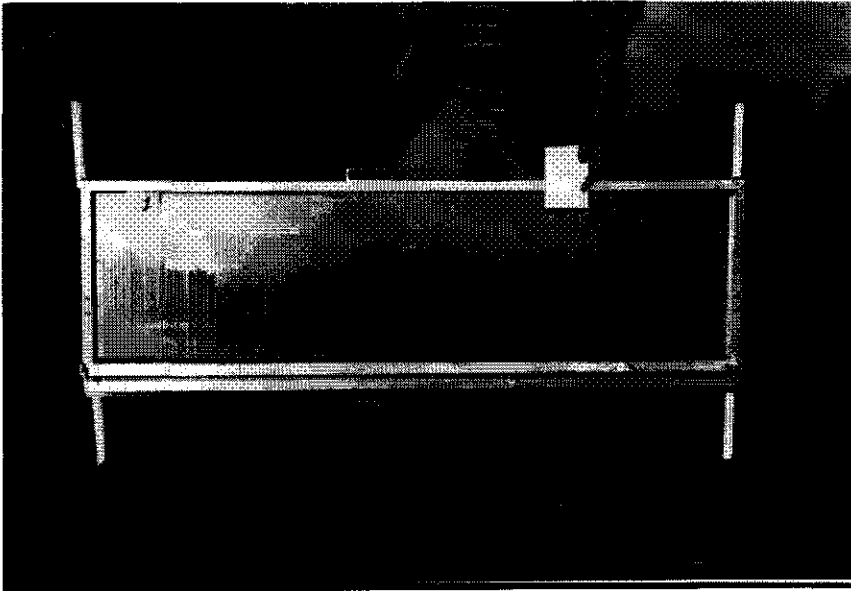


Figure 5.11: Photograph demonstrating the use of a needleboard to obtain a surface roughness profile.

5.5.3 Remote sensing data collection

Airborne SAR data, EMISAR

Multipolarization, C-band (5.3 GHz) SAR data of the Siggefora region were acquired on 23 June 1994 with the airborne SAR system of the Danish Center for Remote Sensing (EMISAR) flown on a Gulfstream G-3 aircraft of the Royal Danish Air Force. The flight of the EMISAR instrument covered a triangular flight line with an image centre incidence angle of 50° and a single look ground resolution of 2.0 m in both range and azimuth. An additional L-band option with full polarimetric capability has been implemented during the 1995 NOPEX field campaign (van Oevelen & Woodhouse, 1996).

The EMISAR instrument was flown in 1994 on June 23 (C-band, 3 scenes) and in 1995 employed on May 1 (L-band, 4 scenes), May 3 (C-band, 2 scenes), July 5 (L-band, 2 scenes) and July 6 (C-band, 2 scenes). The scenes always included the Fjärdhundra and Siggefora sites.

In 1994 only one dataset became available, namely a C-band ($f = 5.3$ GHz) full polarimetric data set acquired on June 23. The original single look complex data with a spatial resolution of 1.5×1.5 m have been ground range projected to 1.5×1.5 m resolution in ground grid, amplitude detected and lowpass filtered and spatially resampled and averaged to 4.5×4.5 m. The cross-polarization dataset is the sum of the HV and VH dataset. The look angle range was from 35.9° near range, 52.0° mid range to 60.2° far range. The data give the backscatter parameter γ (linear). For the ground range projection an altitude of 12391 m above a flat earth was assumed.

Table 5.11: Surface roughness data σ and l for the April, 1995 measurements. The numbers refer to the location and are described in detail in Van Oevelen and Woodhouse (1996). σ_{uncor} refers to data that is uncorrected for surface slope. σ_{cor} refers to data that is corrected for surface slope. The correlation length is given for both exponential $l_{exp.}$ and Gaussian $l_{Gaussian}$ correlation functions.

Nr	Slope [-]	σ_{uncor} [mm]	σ_{cor} [mm]	$l_{exp.}$ [cm]	$l_{Gaussian}$ [cm]
1	-0.0402014	15.8764	15.5949	14.4931	16.8811
2	0.0261485	26.3429	26.2716	13.9301	16.0743
3	0.0377664	26.7692	26.6227	14.9282	16.8595
4	0.0882091	17.3780	16.1039	17.2897	20.8329
5	-0.0852646	27.1016	26.3560	11.3076	12.9208
6	-0.1704777	21.5509	17.4672	9.24651	-
7	-0.0509065	11.1582	10.5023	6.57298	7.53122
8	-0.0043845	6.49966	6.49154	5.43765	-
9	0.0700566	11.2073	9.93415	4.36390	5.41132
10	-0.0648753	8.94319	7.54356	2.31321	1.71303
11	-0.0237138	31.3960	31.3468	13.3034	16.1142
12	-0.0817147	17.3832	16.2962	14.8373	17.8325
13	-0.0773413	21.6041	20.8313	16.8266	19.4734
14	-0.0716952	14.9215	13.9453	12.3246	15.2340

In 1995 two datasets became available, namely a C-band full polarimetric data set acquired on July 6 and a L-band ($f = 1.25$ GHz) full polarimetric data set acquired on July 5. The original complex scattering matrix data with a spatial resolution of 1.499×1.500 m have been converted to covariance matrix data in ground range lowpass filtered and spatial resampled to 5×5 m. The cross-polarization dataset is the sum of the HV and VH dataset divided by 2. The look angle range is from 33.9° near range, 51.0° mid range to 59.6° far range. The data give the backscatter parameter σ° (linear). For the ground range projection an altitude of 12387m above a flat earth was assumed. In Table 5.13 the most important characteristics of the data are summarised.

Table 5.12: Surface roughness data σ and l for the June 1995 measurements. The numbers refer to the location and are described in detail in Van Oevelen and Woodhouse (1996)

Nr	Slope [-]	σ_{uncor} [mm]	σ_{cor} [mm]	$l_{exp.}$ [cm]	$l_{Gaussian}$ [cm]
1	0.0456530	35.3098	35.1476	-45.7385	-
2	-0.0285678	16.0481	15.9081	1.35443	-
3	-0.0536696	29.0454	28.7722	1.68244	2.01082
4	0.0641569	23.1963	22.7046	6.32779	-
5	-0.181366	18.0265	12.0254	5.40011	5.93728
6	0.0276190	11.2222	11.0343	1.28038	-

Table 5.13: Some of the more important characteristics of the EMISAR data available

Date	Frequency [GHz]	Resolution [m]	Polarizations [-]	Look angle range
23-06-1994	5.3	4.5	all	35.9° - 60.2°
05-07-1995	1.25	5.0	all	33.9° - 59.6°
06-07-1995	5.3	5.0	all	33.9° - 59.6°

Table 5.14: Dates of ERS-1 images that are available

1994		14-05	24-06	07-07	10-07
1995	02-04	07-05	11-06	11-07	16-07

Spaceborne SAR data: ERS-1 SAR

The ERS-1 SAR is a single frequency and polarization radar operating at C-band (5 GHz) and VV-polarization. The spatial resolution of the instrument is approximately 25 m and data are delivered with a pixel size of 12.5 m. The look angle of the instrument at the center of the swath is 23°.

The dates of the available ERS-1 instrument data are summarised in Table 5.14.

The ERS-1 SAR data were only preprocessed by the Department of Water Resources, WAU, i.e. calibrated and converted to sigma nought σ^0 , and subdivided into smaller scenes. Most of the analysis of the data has been performed by the Institute of Earth Sciences, Free University of Amsterdam.

Chapter 6

Application of remote sensing soil moisture estimation techniques

6.1 Introduction

The inverted models described in Chapter 4 have been used with the data from the various experiments described in Chapter 5. Several experiments were needed because none of the experiments contained all the necessary data to validate the models with ground truth. In the next sections the application and validation of the passive microwave methods will be described followed by the active microwave methods.

The validation of the soil moisture techniques using microwave remote sensing is tedious. The remote sensing measurement is a true spatial average, although the weighing functions of that spatial average may be unknown. Ground truth measurements are either point measurements or spatial averages derived from point measurements which depending upon the variability of the soil moisture can be very dependent upon the location and the number of measurements. Unknown sensing depth, location uncertainty of ground truth with respect to remote sensing measurement and errors in a priori information are a few of the factors that can make validation cumbersome.

6.2 Passive microwave remote sensing techniques

6.2.1 Push Broom Microwave Radiometer (PBMR) measurements during HAPEX-Sahel

The PBMR microwave observations were compared with the soil moisture observations in Figure 6.1 (van Oevelen & Hoekman, 1994; van Oevelen & Schmugge, 1997).

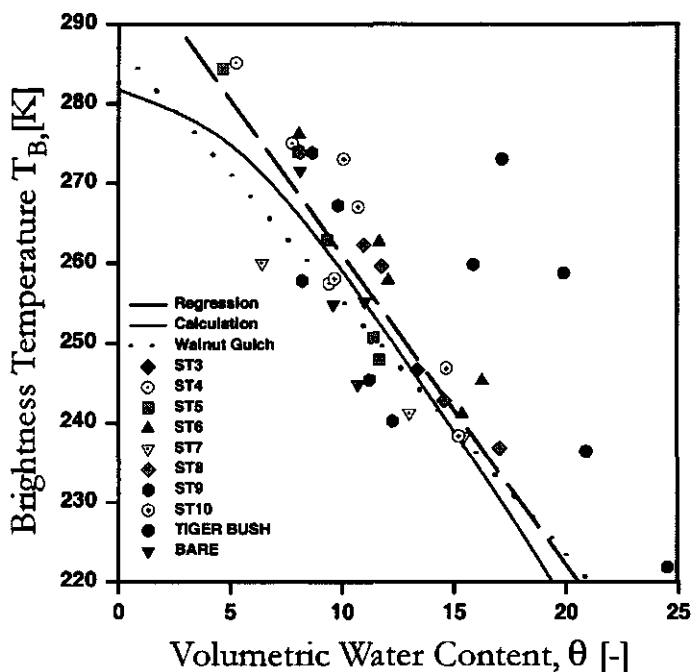


Figure 6.1: Soil moisture measurements θ (42 points) versus the PBMR Brightness temperatures T_B from the HAPEX-Sahel experiment (Van Oevelen and Hoekman, 1994, Van Oevelen and Schmugge, 1997).

The pixels corresponding to the ground measurement site were extracted using polygons that approximately delineate the sampling area. An exact match is impossible due to the low resolution and the accuracy of the georeferenced data . Figure 6.1 shows that an approximately linear relationship exists between the brightness temperatures, T_B and soil moisture content, θ of the top 6 cm, which is regarded to be an appropriate depth for comparisons with L-band emission (Wang, 1987), although measurements with depths ranging between 2 to 5 cm are preferable (Raju *et al.*, 1995; Chanzy *et al.*, 1996). The exception is the site -ST11- in the tiger bush area (Figure 5.3). The deviation from the other sites can be attributed to the ground sampling difficulties. The soils in the tiger bush area are covered by plinthite which is hard to penetrate when dry. Consequently only in the wetter parts measurements could be performed resulting in an overestimation of the actual regional soil moisture content. When these points are excluded from the analysis a linear regression coefficient between PBMR brightness temperatures T_B and measured volumetric soil moisture content θ of R^2 of 0.72 with a standard deviation of less than 2% is obtained (van Oevelen & Schmugge, 1997). Similar results were obtained over the East-Central supersite using a different sampling strategy (Chanzy *et al.*, 1996). Using the thermal infrared measurements from the PRT5 instrument as soil surface temperature estimates to convert the brightness temperature T_B to emissivities ϵ did not improve the correlation much ($R^2 = 0.74$). Furthermore, anomalous behavior in the PRT5 estimates was observed for which at present we cannot give a satisfactory explanation.

Hence, further analysis will be performed using the T_B data only.

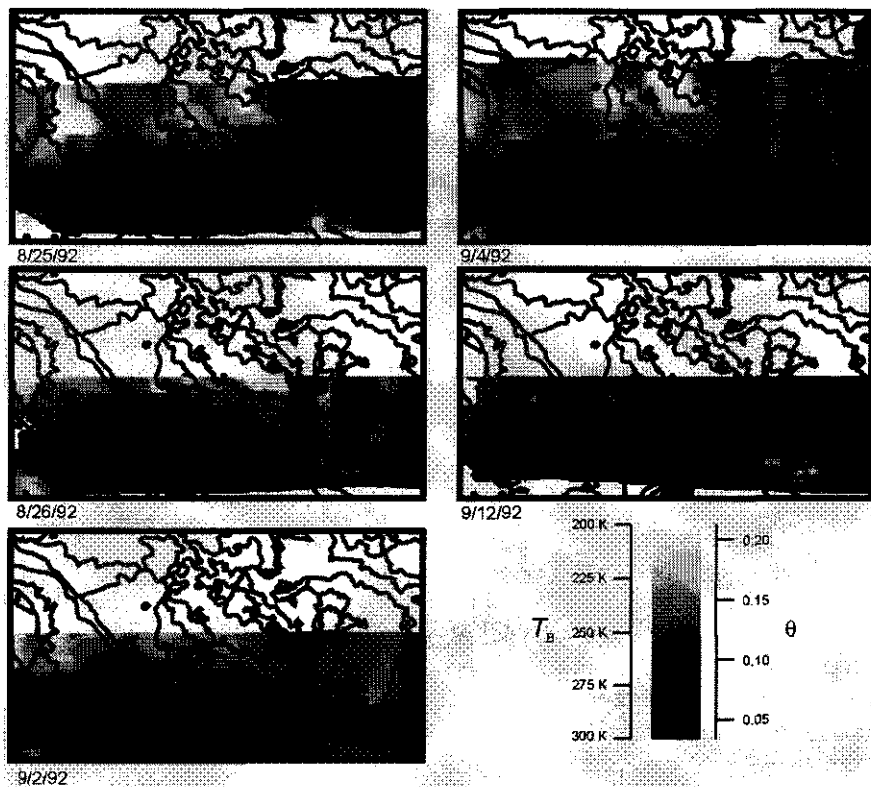


Figure 6.2: PBMR brightness temperature (T_B) images of the HAPEX-Sahel experiment with the boundaries of soil units of Figure 5.4. In the legend the corresponding volumetric soil moisture content, θ is given using the regression curve: $\theta = 0.18T_b + 57.2$ ($R^2 = 0.72$).

The effects of vegetation on the emission were studied by employing a Normalized Difference Vegetation Index (NDVI) calculated from two SPOT images acquired on August 20 and September 24, 1991. However, this procedure did not improve the soil moisture estimates significantly. This confirms the *small influence of the vegetation at 1.42 GHz on land microwave emission in the studied Sahelian region*.

From Figure 6.2 the spatial and temporal distribution of T_B or θ can be seen. There is a large contrast between the driest day (August 25, 5 days after rain) and the wettest day (September 4, less than 12 hours after a rainfall event) as well as within one map of one day. *These spatial patterns can be explained by either the heterogeneity in precipitation amounts or a difference in soil hydraulic properties*. With the available ground data validation of spatial variability of rainfall is difficult. Although there is a strong variation of rainfall over short distances it is difficult to link this directly and

solely to the spatial patterns observed in the brightness temperatures. Comparison with the soil map (Legger & van der Aa, 1994) contours reveals that it is feasible to link T_B and θ to soil type patterns. This has been confirmed by Hollenbeck *et al.*, (1996) who demonstrated that the soil hydraulic heterogeneity can be identified through the relative change in T_B observations.

6.2.2 ESTAR

The soil moisture data presented in Figure 6.3 are from Jackson *et al.*, 1995 and follows mostly the soil moisture retrieval presented in Figure 4.1 on page 58. The data show a clear dry down over nine days starting from near saturated to saturated conditions in the whole watershed area at the beginning of the period. Jackson *et al.*, 1995 give a standard error of estimates for the bare fields of 3.5% and 5.7% for the vegetated fields. The spatial patterns observed in the Figure 6.3 are due to differences in soil texture, precipitation, hydraulic properties, topography and vegetation influences.

6.2.3 Conclusions of passive microwave results

The strong relationship between the dielectric properties and microwave emission along with the relatively small influence of surface roughness makes the application of passive microwave data to estimate soil moisture very straightforward and has especially at the lower frequencies such as at L-band great potential for hydrological applications. *Between the brightness temperatures, T_B and soil moisture content, θ of the top 6 cm an approximately linear relationship is present. A problem exists with high vegetation cover and this is the area where considerable improvement can be made: better modelling of the vegetation influence, or a combination of more frequencies.* The errors involved in the estimation of soil moisture using passive microwave remote sensing are small, i.e. usually less than 5% even for areas with moderate vegetation cover and is often lower than that of the ground truth measurements.

The effects of surface roughness are small for the emission case, especially the influence of the surface correlation length is almost negligible (Borgeaud *et al.*, 1995; Davidson *et al.*, 2000). With respect to soil moisture estimation the effect can for most circumstances easily be accounted for by a simplified model like that of Choudhury *et al.*, 1979.

Although the L-band penetration of vegetation forms a physical limitation, the sensitivity to the soil moisture content as a function of vegetation water content is for L-band still present at a vegetation water content of 4 kg m^{-2} . For C-band this amount of vegetation content would already obscure the signal from the soil (Jackson & Schmugge, 1991).

Extrapolation of the results to measurements from space would mean that the influence of mixed pixels due to the low resolution of approx. 30 km for L-band would increase. Also the effect of macroscale roughness would need more attention at that scale. The AMSR and AMSR-E will, with C-band, be the first radiometers that can provide more insight into the estimation of soil moisture from space with a spatial

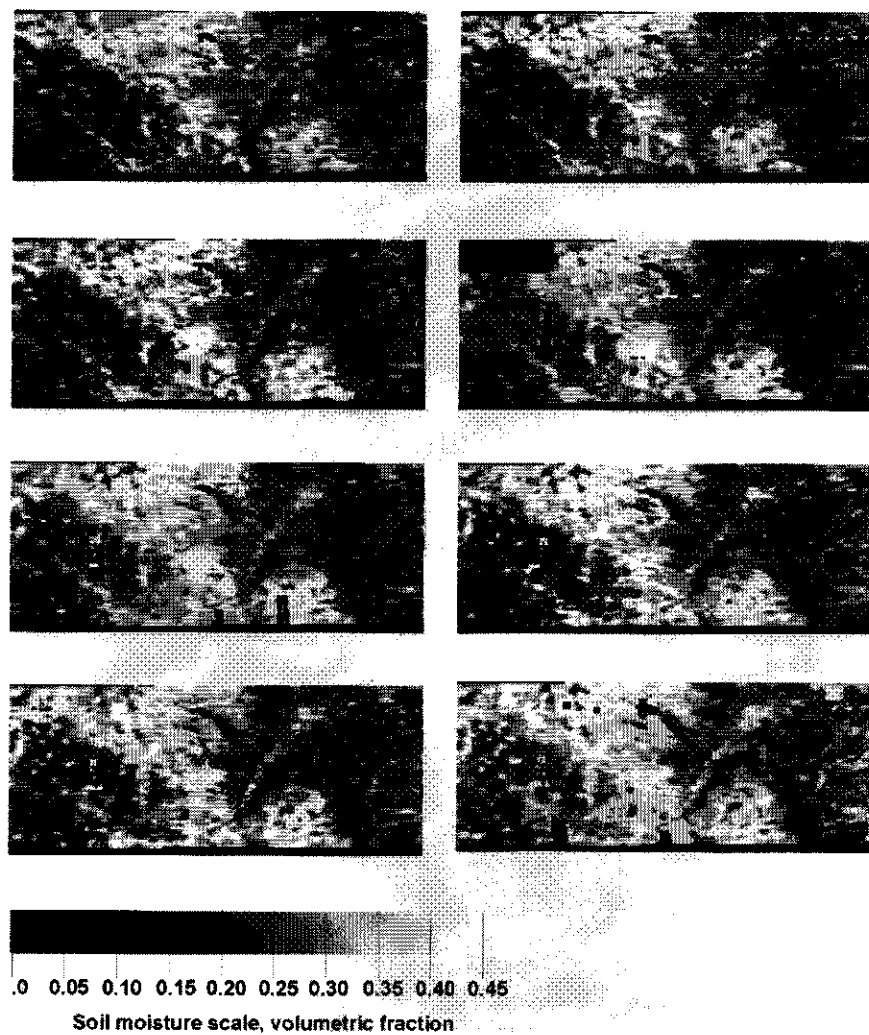


Figure 6.3: Soil moisture estimates using ESTAR data for the Washita'92 experiment (Jackson *et al.*, 1995).

resolution of approximately 50 km although the vegetation would still be a significant problem. The planned L-band space-borne radiometer, SMOS (Soil Moisture and Ocean Salinity mission) will be a significant step towards operational use of microwave soil moisture estimates at the global scale (Kerr, 1998; Wigneron *et al.*, 2000).

6.3 Active microwave remote sensing techniques

6.3.1 ERS-1

The IEM model (section 3.5.3) was applied to ERS-1 SAR data of Niger. Soil moisture content, θ was measured in situ over a depth of 6 cm and in some areas at 2 and 5 cm depth. For comparison with the C-band soil moisture estimates of ERS-1 *the in situ measurement depth of 6 cm is probably larger than the associated sensing depth of the ERS-1 SAR*. The results in Table 6.1 show that the θ -value used in the forward simulation has to be smaller than the measured soil moisture content for most of the fields to yield a match between measured and modelled backscatter. The application of INVIEM (see section 4.4.2) using ERS-1 data in Niger shows that the estimates are within the expected θ -range and that the in situ measured θ -values are consistently higher (Fig. 6.4).

Table 6.1: C-band backscatter values (σ° in dB) measured (VV_m) and modelled by IEM model (VV_{iem}) for a number of subtransects in Niger. θ_{iem} is the soil moisture input in the IEM model. θ_m is the averaged in situ measured θ using the TDR's. Subtransects 6 and 9 are not represented here because surface roughness measurements were not available for these sites. (* θ estimated because TDR measurements were impossible due to dry crust . ** range of θ since measurements varied strongly over short distances).

Subtransect	VV_m	VV_{iem}	θ_m	θ_{iem}
3	-11.36	-11.94	0.13	0.10
		-10.71		0.15
4	-11.21	-12.68	0.09	0.00
		-9.04		0.05
5	-10.31	-11.81	0.09	0.00
		-8.16		0.05
7	-14.52	-16.23	0-0.05*	0.00
		-12.62		0.05
8	-14.12	-16.50	0.11	0.00
		-12.88		0.05
10	-10.38	-12.80	0.11	0.00
		-9.15		0.05
11	-14.03	-12.63	0.06-0.29**	0.00
		-9.01		0.05

The climate in Niger is characterised by a short monsoon period in which short intensive rainfall events are followed by warm and sunny periods. Under these circumstances and given the fine sandy texture of most of the soils the soil moisture profile

dries out very quickly towards the surface. The C-band θ estimates are therefore expected to be lower than the in situ measured θ , as already could be seen from the forward simulation. The measured values would also deviate stronger from the estimated values because the difference in θ between the surface layer and the layer beneath is less for drier profiles than for wetter profiles. The results in Table 6.2 confirm this for all the plots and for the whole range of soil moisture estimates. Only a few soil moisture measurements were taken at a depth of 2 and 5 cm (thus not from 0 to 2 cm and 0 to 5 cm). Following the explanation given above, the 2 cm measurements should be lower than the 5 cm measurements and these measurements should compare better to the ERS-1 estimates. Although there are only four points available, this reasoning is confirmed in Figure 6.4. However, the 2 cm measurements are still higher than the corresponding estimates indicating that the sensing depth of ERS-1 is either less than 2 cm or presents a kind of average over the top few centimetres, both of which would result in lower data values.

For the Niger experiment the range of roughness classes did not include the edges of the plinthite plateaux, which were definitely much rougher than the rest of the area. None of the measurement sites were situated on these edges and therefore such areas were not included in the comparison with in situ measured data. However, the INVIEM model is expected to overpredict the soil moisture content θ at these locations because of its higher roughness and given its higher backscatter (i.e. it is outside the roughness range assumed for the inversion procedure and it is most likely even outside the validity range of the IEM model).

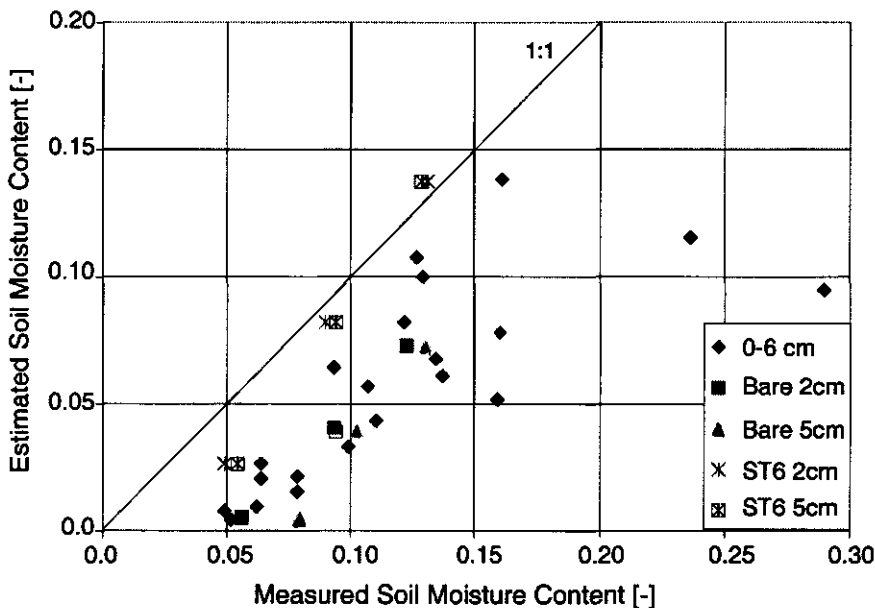


Figure 6.4: ERS-1 θ estimates using the INVIEM model (see section 4.4.2) versus TDR measured θ at 5 cm and 2 cm depth during the HAPEX-Sahel experiment.

The ERS-1 soil moisture estimates for the four dates, July 4, August 8, September 12

Table 6.2: INVIEM θ estimates (est.) using C-band VV polarization of ERS-1 (September, 12, 1992) for the a number of subtransects in Niger compared with averaged TDR measurements over 6 cm depth (meas.). Given are the lowest, mean and highest values of both measurements and estimates. For subtransect 7 no measurements were available because the soil surface was too hard to be penetrated by the TDR rods. For subtransect 4 no estimates are available because of too much vegetation.

Subtransect		θ_{low}	θ_{med}	θ_{high}
3	est.	0.021	0.068	0.115
	meas.	0.078	0.134	0.236
4	est.	-	-	-
	meas.	0.056	0.094	0.134
5	est.	0.020	0.064	0.100
	meas.	0.064	0.093	0.126
6	est.	0.026	0.082	0.130
	meas.	0.064	0.121	0.161
7	est.	0.051	0.100	0.160
	meas.	-	-	-
8	est.	0.008	0.043	0.078
	meas.	0.049	0.110	0.160
9	est.	0.004	0.033	0.061
	meas.	0.052	0.099	0.137
10	est.	0.015	0.057	0.100
	meas.	0.078	0.107	0.129
11	est.	0.009	0.052	0.095
	meas.	0.062	0.159	0.290

and October 15, 1992 are shown in Figure 6.5. The estimates show clearly the effect of the monsoon which started in August and ended before October.

The influence of soil texture on the ERS-1 retrieval results has been studied and is small compared to other effects such as speckle or vegetation. In Figure 6.6 the variation caused by speckle clearly overrides the variation caused by different soil types.

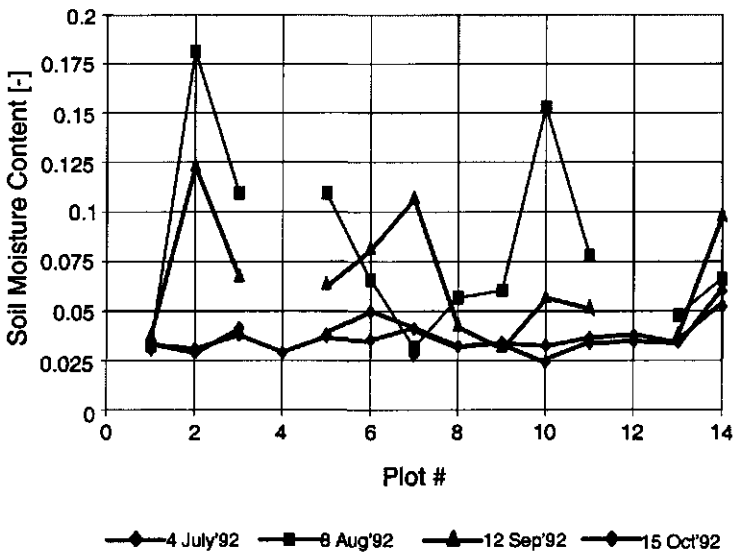


Figure 6.5: ERS-1 θ -estimates using the INVIEM model (see section 4.4.2) in HAPEX-Sahel experiment for 14 different plots.

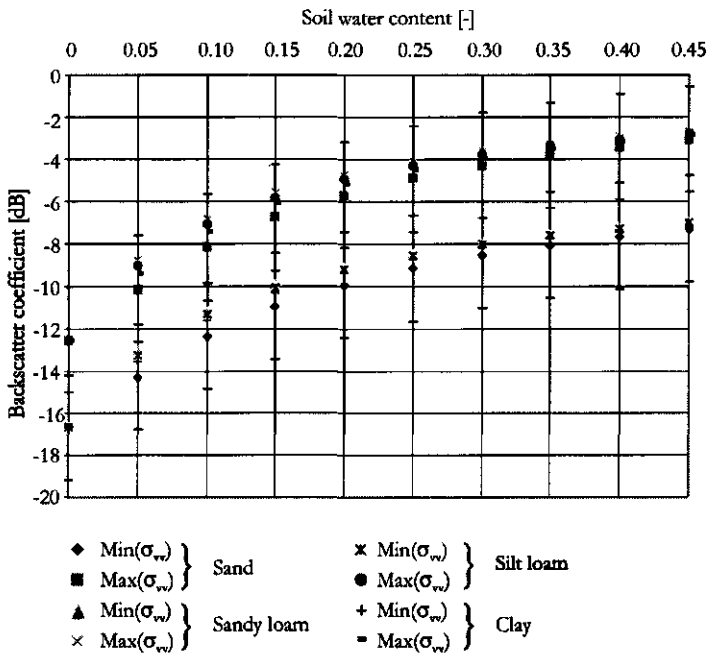


Figure 6.6: Simulation of the effect of soil texture on ERS-1 backscatter as a function of soil water content using the IEM model and the Dobson soil mixture model (Dobson *et al.*, 1985) with an incidence angle of 23° . The error bars indicate a speckle level of about 2.5 dB for ERS-1 (speckle has uniform distribution).

6.3.2 AIRSAR

INVIEM model results of HAPEX-EFEDA'91

The IEM (section 3.5.3) and INVIEM (section 4.4.2) models have been applied to the AIRSAR data taken in Spain. Table 6.3 shows the comparison between the AIRSAR backscatter σ^0 computed by the IEM model using field data as input and the averaged measured backscatter values per field. Clearly the vegetated alfalfa field shows the bad performance of the model in case of non-bare surface conditions by underestimating the backscatter due to neglect of the vegetation scattering contribution. However, when the vegetation is very dry, such as the barley field which is in the senescent stage, or when the vegetation cover is very low like the maize field, the influence clearly diminishes. *Using a vegetation mask to remove the pixels (e.g. Eq. 3.84) influenced by vegetation assures that fields like the alfalfa field will not be included in the inverse approach.*

Table 6.3: Backscatter values of C-, L- and P-band (σ^0 in dB) JPL-AIRSAR measured data and modeled using the IEM model for four fields in Spain during HAPEX-EFEDA'91 experiment.

C				
Field	HH_m	HH_{iem}	VV_m	VV_{iem}
Bare (2)	-13.0	-10.7	-13.7	-12.9
Alfalfa (4)	-7.2	-16.5	-9.5	-13.2
Maize (5)	-8.6	-7.4	-9.3	-10.0
Barley (7)	-13.0	-18.4	-15.4	-19.4
L				
Field	HH_m	HH_{iem}	VV_m	VV_{iem}
Bare (2)	-21.5	-20.7	-19.6	-16.5
Alfalfa (4)	-16.2	-23.9	-14.6	-19.0
Maize (5)	-17.1	-15.4	-15.5	-11.9
Barley (7)	-22.9	-29.6	-22.9	-24.3
P				
Field	HH_m	HH_{iem}	VV_m	VV_{iem}
Bare (2)	-25.5	-32.2	-22.4	-28.1
Alfalfa (4)	-26.7	-31.4	-20.6	-26.4
Maize (5)	-23.5	-23.3	-21.5	-19.3
Barley (7)	-28.4	-35.8	-24.3	-29.9

Table 6.4 shows that the INVIEM model gives a possible range of θ values, which can become very large. For C-band this range varies for example for the bare soil field (no. 2) from approximately $\theta = 0.024$ to 0.121 between the low and high estimates. Compared to the in situ measured soil moisture data given in Table 6.5, the results appear to be within the given range.

Table 6.4: INVIEM low, medium and high soil moisture estimates for AIRSAR C-, L-, and P-band for 10 fields in Barrax Spain during HAPEX-EFEDA'91. Fields 2, 4, and 5 correspond to the bare, alfalfa and maize field of Table 7.3. The extension "ci" indicates that these fields are segments of an irrigation circle. The alfalfa field is left out using the vegetation mask. For L- and P-band no inversion was possible for two out of the three roughness cases.

Field	No. of pixels	C			L			P		
		low	med.	high	low	med.	high	low	med.	high
1	250	0.096	0.208	0.332	0.303	0.319	0.417	-	-	-
Bare	122	0.024	0.072	0.121	0.013	0.055	0.111	0.117	0.151	0.215
2										
Alfalfa		-	-	-	-	-	-	-	-	-
4										
Maize	76	0.074	0.134	0.196	0.076	0.120	0.197	0.165	0.192	0.263
5										
8	18	0.150	0.231	0.314	0.241	0.278	0.328	0.209	0.271	0.376
9	91	0.083	0.142	0.212	0.091	0.134	0.210	0.254	0.282	0.357
10ci	699	0.103	0.194	0.293	0.311	-	-	0.352	-	-
11ci	377	0.200	0.289	0.399	0.337	-	-	0.371	-	-
12ci	374	0.180	0.253	0.368	0.271	-	-	0.326	-	-
13ci	522	0.195	0.270	0.391	0.297	-	-	0.366	-	-

Table 6.5: Ground measurements of volumetric θ values ($\text{cm}^3\text{cm}^{-3}$) and roughness parameters σ and l for the four fields in the Barrax area in Spain, during HAPEX-EFEDA'91, June 19.

Depth [m]	0.02	0.05	0.10	0.20	0.25	0.30	σ	l
Field (No.)							[cm]	[cm]
Bare (2)	-	0.034	0.071	-	-	0.16	1.4	37
Alfalfa (4)	0.231	0.306	0.322	-	-	-	0.5	104
Maize (5)	0.130	0.186	0.261	-	-	-	1.8	91
Barley (7)	-	0.054	0.097	0.122	0.140	-	1.0	140

INVOSU model results

The INVOSU model (section 4.4.1) is only applied to the JPL-AIRSAR data from Spain, since it needs multi-polarized data. In Table 6.6 the results are shown using inversion of the Wang and Schmugge model (section 4.2) (Wang & Schmugge, 1980) to retrieve the θ -values from the dielectric constant, ϵ' . Comparison with the ground measurements presented in Table 6.5 shows that estimates from C-band are in general too high and that there is little variation in the estimates. Apparently the conditions for which the INVOSU model is valid are different from the conditions related to these data. Since there are only a few measurements at larger depths, comparison with L- and P-band estimates is difficult. However, the L-band estimates seem to be close to the C-band estimates and also show little variation over the various fields. P-band estimates clearly show more variation and higher (or wetter) estimates.

Table 6.6: The AIRSAR C-, L- and P-band INVOSU results for 10 fields in Barrax Spain during HAPEX-EFEDA'91. Fields 2, 4, and 5 correspond to the bare, alfalfa and maize fields of Table 7.3. The inverse model of Wang and Schmugge (1980) is used to retrieve θ from ϵ' .

	No. of pixels	C		L		P	
		ϵ'	θ	ϵ'	θ	ϵ'	θ
1	250	4.67	0.160	4.28	0.156	4.58	0.159
Bare 2	122	4.36	0.157	4.52	0.159	17.99	0.318
Alfalfa 4	-	-	-	-	-	-	-
Maize 5	76	4.63	0.160	4.11	0.154	15.90	0.296
8	18	4.96	0.163	8.09	0.199	34.37	0.453
9	91	4.47	0.158	4.00	0.153	5.41	0.169
10ci	699	4.74	0.161	4.00	0.153	4.07	0.153
11ci	377	4.88	0.162	5.39	0.168	5.91	0.174
12ci	374	4.86	0.162	5.14	0.165	5.09	0.165
13ci	522	4.90	0.163	4.35	0.157	4.21	0.155

Comparison between INVOSU and INVIEM soil moisture estimates

Only a few measurements are available for comparison but there is a considerable difference between the results from INVOSU (section 4.4.1) and INVIEM (section 4.4.2). Although both model results are within the range of measured soil moisture, the INVIEM data appear to capture the variance in the field better. If the soil moisture estimates are visualized, as in Figure 6.7 and Figure 6.8 the difference becomes even more apparent. The INVIEM estimates in Figure 6.7 show a clear spatial variation in soil moisture content due to the irrigation practices. The same irrigation circles can be observed in Figure 6.8 but the soil moisture variation within these circles is not as apparent. Overall, *INVIEM as compared to INVOSU yields more reasonable estimates of soil moisture content as far as can be deduced from the limited ground truth data and visual inspection.*

The advantage of using INVIEM over INVOSU is that it can be applied to both single polarization and polarimetric data. However, for both algorithms the use of polarimetric data is preferable because it simplifies the masking of the vegetation influence and enhances the estimation of soil moisture since more than one polarization can be used. The INVOSU model requires no a priori knowledge about the surface characteristics except for information on the type of soil. INVIEM does require in its present form the input of surface roughness characteristics. *At present, the applicability of both models is restricted to bare soils only and therefore is of limited practical use.*

Active microwave remote sensing observations from the Washita'94 experiment

On April 12, 1994 the JPL-AIRSAR, was deployed in the Little Washita River watershed. The INVIEM model (section 4.4.2) was applied to these data using both *HH*- and *VV*-polarization for all three bands. Although the calibration of the P-band is less reliable than that of the C-, and L-band, it still can be used in a qualitative manner.

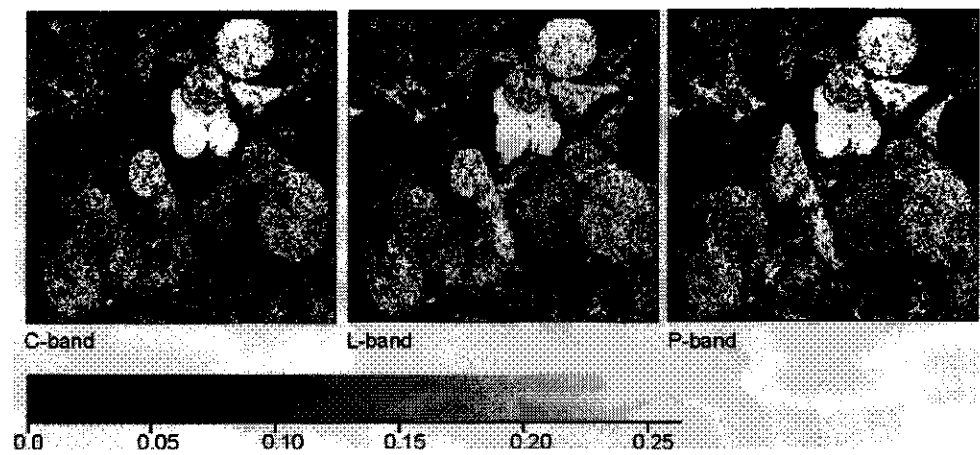


Figure 6.7: Multiband (AIRSAR C-, L- and P-band) volumetric soil moisture estimates using the medium (=average of the high and low estimates) INVIEM estimates in Barrax, HAPEX-EFEDA '91 experiment.

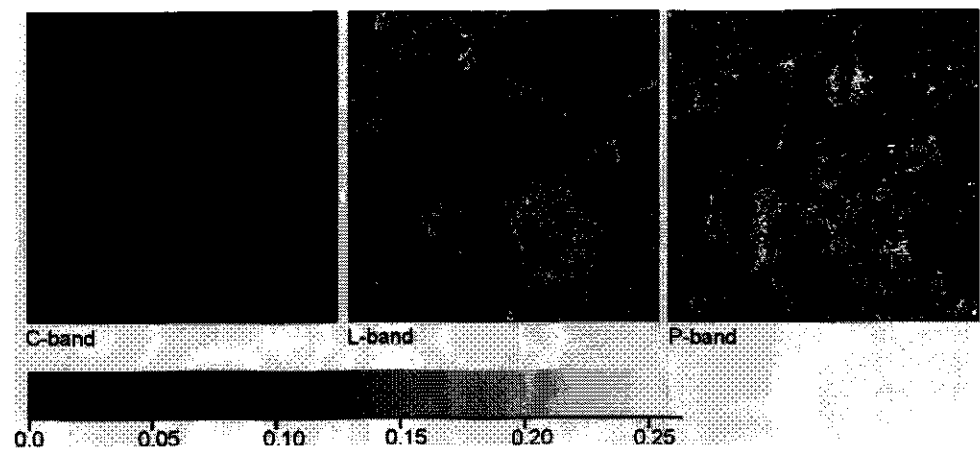


Figure 6.8: Multiband (AIRSAR C-, L- and P-band) volumetric soil moisture estimates using the INVOSU model in Barrax, HAPEX-EFEDA '91 experiment.

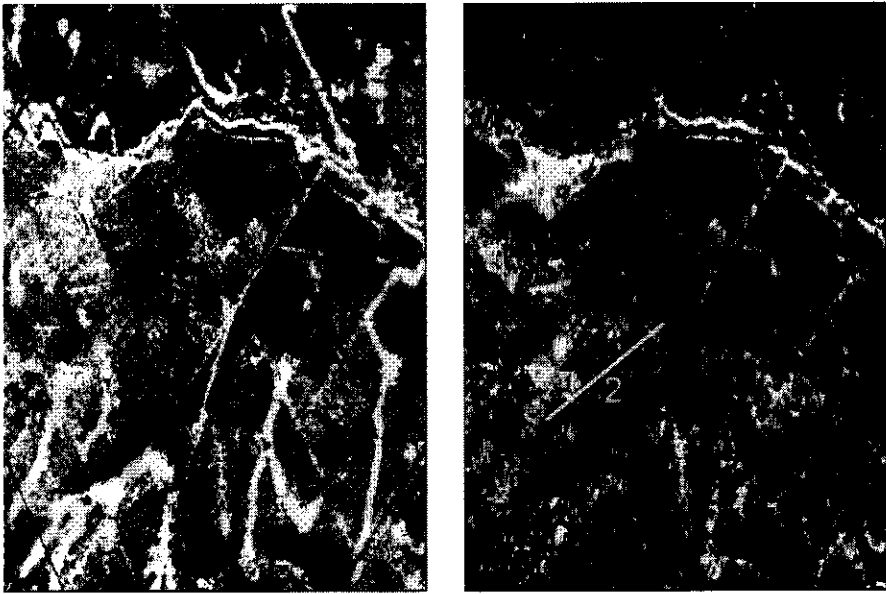


Figure 6.9: Image of JPL-AIRSAR L-band *HH* soil moisture estimates on April 12, 1994 in "Area 1" of the Little Washita River Watershed. On the left image the data are unfiltered and vegetation not masked, right image the data are filtered with a 3 by 3 averaging filter and the vegetation is masked out (black). The measurement transect is indicated by the white line.

In Figure 6.9 the soil moisture estimation applying INVIEM on L-band *HH*-polarization is shown. On Figure 6.9A the vegetation is not masked out and clearly the run-off gullies (with trees growing along/in them) come out bright resulting in over-estimation of soil moisture due to presence of vegetation. On Figure 6.9B the vegetation is masked out using a filter based upon scattering mechanisms which can be deduced from polarimetric radar data (van Zyl *et al.*, 1987). Most of the gullies are masked out, only the riverbank is still showing. The bare corn field gives soil moisture overestimates due to the roughness effects caused by the tilling rows. Transect 2 indicates the line used for comparison with TDR soil moisture measurements in the rangeland.

A comparison between the TDR soil moisture measurements in the rangeland plot over a depth of 6 cm with the C-, L- and P-band INVIEM estimates along transect 2 shows good agreement for both C- and L-band (Figure 6.10). Since the use of L-band gives estimates over a larger depth than C-band the soil moisture profile must be fairly uniform in the top layer (C- and L-band estimates are of the same order). The root mean square error (RMSE) for C-, and L-band estimates is 3%. Since the in situ measured soil moisture content is within a small range (mostly between 0.25 - 0.30) the correlation coefficient is very low ($R^2 = 0.01$). The fluctuations or variations of the TDR measurements are hardly reflected in the estimates. This is partly due to the discrepancy between point measurements and the remotely sensed areal averaged estimates. However, when trends are present in the measurements

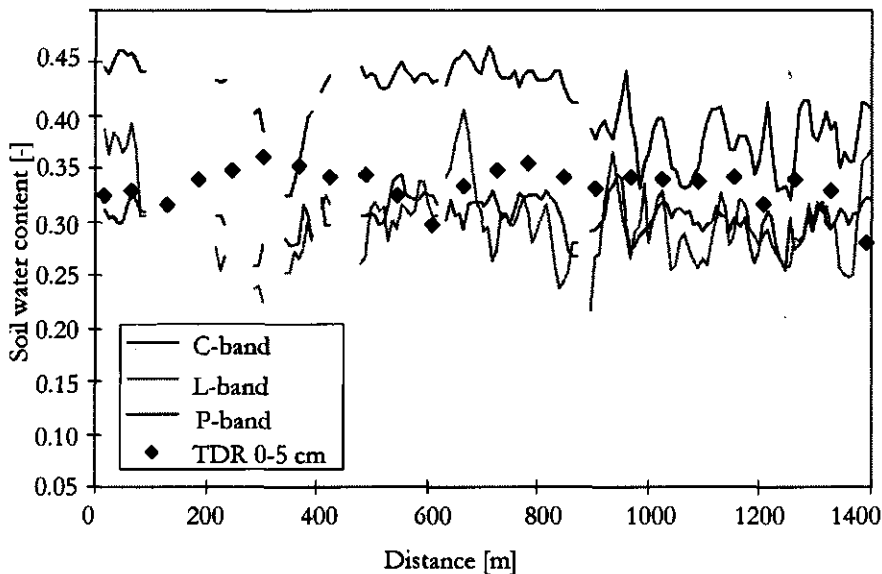


Figure 6.10: Soil moisture estimates from the JPL-AIRSAR compared with TDR measurements over 6 cm taken during the Washita 1994 SIR-C campaign on April 12.

these should be captured by the remotely sensed estimates. As can be seen in Figure 6.10 there is no clear trend (for all bands). Furthermore, the semi-variogram of the TDR measurements showed that no spatial correlation could be found, which is in agreement with Schmugge & Jackson (1996).

The P-band soil moisture estimates are consistently higher which is to be expected since these estimates represent an effective average soil moisture content over a larger depth than C-, and L-band. From routinely taken profile TDR measurements this could be verified (Heathman, 1995).

The rangeland plot is characterized by contours which are remnants from erosion prevention measures (Figure 6.11). These contours have a height of less than one meter and are fairly regularly spaced. Detailed soil moisture measurements taken every 3 m show that the top of the contours are consistently drier than their surroundings (Figure 6.12). Comparison of these TDR soil moisture measurements with C-, L- and P-band estimates show that the effects of the contours cannot be seen in the AIRSAR estimates (Figure 6.12). The AIRSAR spatial resolution of approximately 10 m is apparently too coarse to capture this variability of θ .

This type of variability has however to be considered carefully when developing a spatial measurement scheme or grid and when averaging point measurements. Otherwise, systematic measurement errors can be introduced. Note that the variability of the SAR data is larger or of the same order of the ground measurements. This variability is caused by the viewing geometry, vegetation, surface roughness etc. and not only by the spatial variation of soil moisture!



Figure 6.11: Detailed imaged (NS001) of the rangeland area during Washita'94 experiment, where the erosion contours can be seen. Indicated is the measurement transect (T3) used in Figure 6.12.

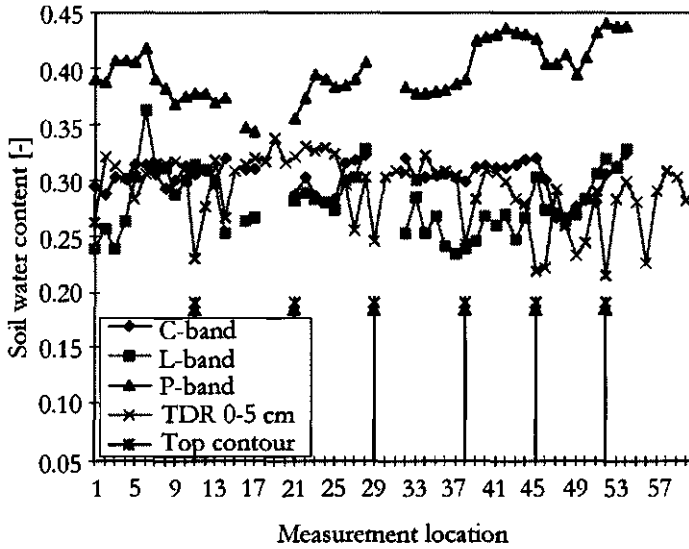


Figure 6.12: Soil water content θ estimates from the JPL-AIRSAR compared with TDR measurements over 6 cm during the Wasita'94 experiment. Detailed measurements reveal the effect of local topography, top of soil erosion contours have systematic lower soil moisture values than the rest of the measurements. The location of the top of the contours is indicated by the upright arrows.

6.3.3 EMISAR

The INVIEM model (section 4.4.2) has been applied on an object as well as on a pixel basis on EMISAR data from the FOREST/DYNAMO experiment.

Table 6.7: Surface roughness parameters $k\sigma$ and kl for the three selected cases used in the INVIEM model for the FOREST-DYNAMO experiment, 1995.

Roughness case	C		L	
	$k\sigma$	kl	$k\sigma$	kl
1	2.4	18.92	0.56	4.41
2	1.18	8.45	0.27	1.97
3	0.85	1.92	0.19	0.45

Simulations with the IEM model (section 4.4.2) were made for a number of surface roughness conditions covering the extremes of $k\sigma$ and kl in the reference field data set. The values of the surface roughness cases used for the INVIEM model are given in Table 6.7. For the various frequencies and the different types of soil several soil mixing models have been applied to relate the complex soil dielectric constant to the soil moisture content (Dobson *et al.*, 1985; Hallikainen *et al.*, 1985; Wang *et al.*, 1980). For the data from this experiment all the estimates were used and averaged to give a "medium" or "average" estimate.

Table 6.8: TDR volumetric soil moisture content θ compared with L-band EMISAR estimates using the INVIEM model during FOREST-Dynamo'95, for June 5, 1995.

Track	A		B		C		D		E		F	
Depth [cm]	0-3	0-6	0-3	6	0-3	0-6	0-3	0-6	0-3	0-6	0-3	0-6
TDR												
avg	20.07	19.19	24.66	27.63	18.49	24.54	22.89	26.64	16.15	23.53	22.83	27.94
st.dev	4.68	6.53	3.35	4.07	6.42	6.44	3.29	4.54	5.88	5.08	4.44	4.85
L-band												
avg	14.19		14.36		17.45		18.22		14.59		15.35	
st.dev	2.72		2.14		2.84		3.28		2.29		1.99	

Table 6.9: TDR volumetric soil moisture content θ compared with C-band EMISAR estimates during FOREST-Dynamo'95, for June 6, 1995.

Track	A		B		C		D		E		F	
Depth [cm]	0-3	0-6	0-3	0-6	0-3	0-6	0-3	0-6	0-3	0-6	0-3	0-6
TDR												
avg	15.78	19.93	15.67	22.28	16.23	23.25	14.36	22.95	16.42	23.87	17.79	25.66
st.dev	3.58	6.04	4.16	4.42	3.49	5.53	3.99	3.27	3.97	4.62	4.08	3.63
C-band												
avg	11.49		11.27		14.44		15.38		12.28		12.74	
st.dev	3.76		3.91		4.33		4.49		4.07		4.32	

Results

The soil moisture content θ has been estimated for the days that the available EMISAR data coincided with the ground truth measurements, i.e. June 5 and 6, 1995. The results of the comparison of estimated soil moisture with the in situ measured soil moisture content along the transects, indicated as track A to F, are summarised in Tables 6.8 and 6.9.

An example of the same transects are also represented in graphical form in Figure 6.13. The overall comparison shows that the *EMISAR soil moisture estimates in general are lower than the measured soil moisture content*. This can be contributed to the fact that the *IEM model does not account for periodicity or anisotropy in the surface roughness characteristics* and therefore in those case gives a lower backscatter coefficient than actually measured. Furthermore, there might be an *inconsistency between measured surface roughness and the way it is represented in the model*. The in situ measured RMS height and correlation length does not necessary resemble the surface roughness relevant for the radar backscattering. The backscattering is likely to be caused by a smoother subsurface. However, this could not be verified and inconsistent calibration of the EMISAR data might also be a reason for the deviating results of the INVIEM model. Especially since C- and L-band tracks were not flown simultaneously but after each other.

Both the C- and L-band estimates seem to agree better with the soil moisture measurements taken with the TDR rod at a shallower angle with respect to the surface,

resulting in a measurement depth of about 2-3 cm. Most estimates are within 5% of the measurements. Since the standard deviation of the measurements lies mostly between 4 and 6% these results are acceptable. Only the comparison with L-band on June 5 for track A, B and F are outside the 5% range. No particular reason could be found for these exceptions and again calibration issues might be one of the causes.

6.3.4 Effect of surface roughness on soil moisture estimation

The surface roughness is in most cases described by a single scale roughness (see Appendix D). However, natural surfaces exhibit roughness at many different scales. A way to describe these type of rough surfaces is that they consist of a *periodic* as well as a *random* component. Up to this point we have assumed that the roughness of the surfaces was at a single scale and was not periodic of nature. For most natural soils this is an acceptable assumption, clear exceptions are e.g. the sand dunes and ripples in desert areas and non-natural rough surfaces such as row-tilled or ploughed agricultural fields. A more detailed theoretical description on the effects of multi-scale (such as periodic roughness) surface roughness can be found in Ulaby *et al.*, 1986 and Ogilvy 1991.

The effects of surface roughness are in general stronger for the scattering case than for the emission case, especially the influence of the surface correlation length is almost negligible for the latter (Borgeaud *et al.*, 1995; Davidson *et al.*, 2000). For the scattering case the surface roughness is as important as the dielectric properties of the surface and therefore greatly limit the possibilities for soil moisture retrieval. Using the INVIEM model (section 4.4.2) the effect of the surface roughness can be seen on the width of the soil moisture range that is estimated which can become extremely large.

Another question that arises is if the parameters used to describe surface roughness are adequate. The surface correlation length for example is generally not an indicator of the type of surface and exhibits large variability independent of the type of surface roughness (Borgeaud *et al.*, 1995). Although different descriptions of surface geometry are present (see Appendix D), currently most models that describe surface scattering use the root mean square of the height differences along with the surface correlation length. Replacement of the latter with a more adequately responding parameter could yield improvement in the behaviour and application of surface scattering models.

6.3.5 Conclusions of active microwave results

The INVIEM model was applied to ERS-1 SAR data of Niger (HAPEX-Sahel) and the results compared with soil moisture content, θ measured over a depth of 6 cm. Although this depth is probably larger than the associated sensing depth of the instrument (about 2 cm) it is shown that the estimates are within the expected θ -range and that the in situ measured θ -values are consistently higher. The latter is expected because the surface layer of 0-2 cm is drier than the measured layer of 0-6cm.

The influence of soil texture on the ERS-1 retrieval results has been studied and is small compared to other effects such as speckle or vegetation.

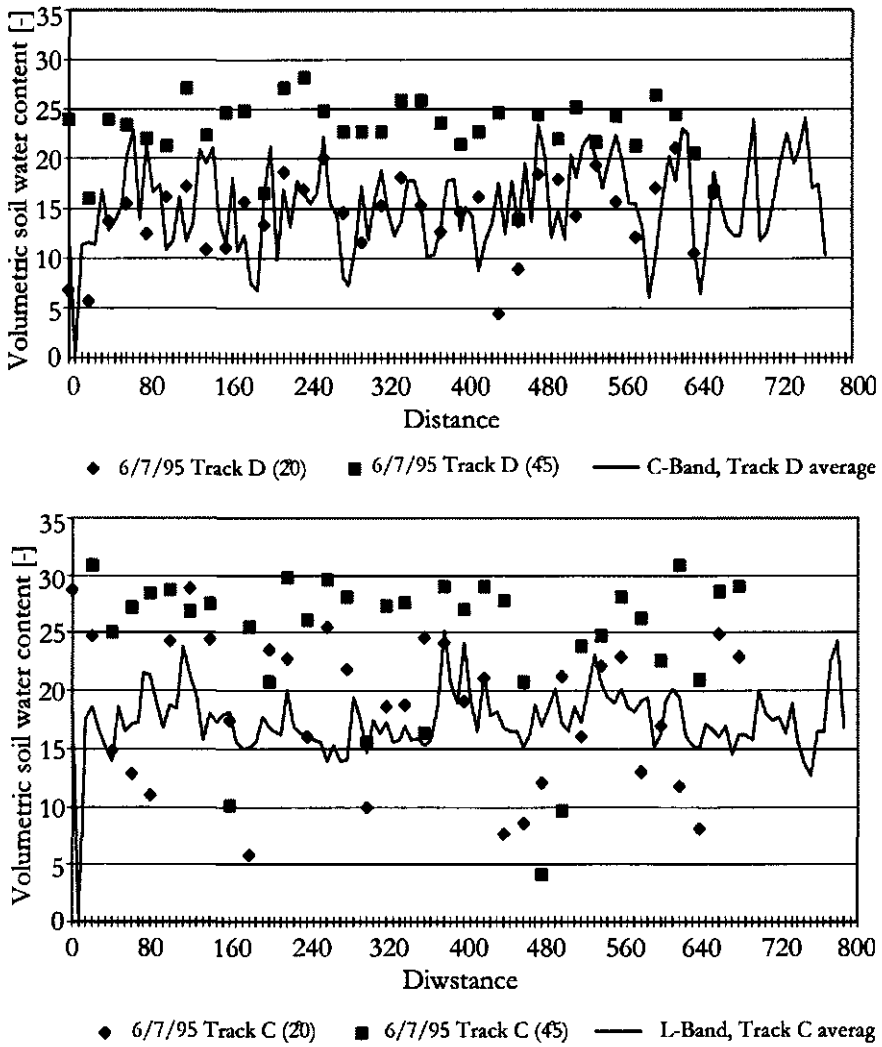


Figure 6.13: An example of EMISAR C- and L-band soil moisture estimates using the IN-VIEM model compared with TDR measurements for tracks A and B during FOREST-Dynamo'95.

JPL-AIRSAR data have been applied using data from Spain (EFEDA-Spain). Both the INVIEM model and INVOSU model could be applied because AIRSAR provides multi-polarized data. Overall, *INVIEM* as compared to *INVOSU* yields more reasonable estimates of soil moisture content as far as can be deduced from the limited ground truth data and visual inspection.

The advantage of using *INVIEM* over *INVOSU* is that it can be applied to both single polarization and polarimetric data. The *INVOSU* model requires no a priori knowledge about the surface characteristics except for information on the type of soil. *INVIEM* does require in its present form the input of surface roughness characteristics. At present, the applicability of both models is restricted to bare soils only and therefore is of limited practical use.

JPL-AIRSAR data have also been used in the Washita'94 experiment. A comparison along transect 2 between the TDR soil moisture measurements in the rangeland plot over a depth of 6 cm with the C-, L- and P-band *INVIEM* estimates shows good agreement for both C- and L-band. The root mean square error (RMSE) for C-, and L-band estimates is 3%. The P-band soil moisture estimates are consistently higher which is to be expected since these estimates represent an effective average soil moisture content over a larger depth than C-, and L-band.

The effects of the erosion contours on the in-situ soil moisture measurements cannot be seen in the AIRSAR soil moisture estimates. The AIRSAR spatial resolution of approximately 10 m is apparently too coarse to capture this variability of θ .

In Sweden the EMISAR data was used during the FOREST-Dynamo experiments. *EMISAR* soil moisture estimates in general underestimate the measured soil moisture content. This can be contributed to the fact that the *IEM* model doesn't account for periodicity or anisotropy in the surface roughness characteristics and therefore in these case gives a lower backscatter coefficient than actually measured. Furthermore, there might be an inconsistency between measured surface roughness and how it is represented in the model. The in situ measured RMS height and correlation length does not necessary resembles the radar backscattering relevant surface roughness. The backscattering is likely to be caused by a smoother subsurface.

Both the C- and L-band estimates seem to agree better with the soil moisture measurements taken with the TDR rod at a shallower angle with respect to the surface, resulting in a measurement depth of about 2-3 cm. Most estimates are within 5% of the measurements.

For all experiments the standard error in the active microwave soil moisture estimates in absence of vegetation is often lower (<5%) than that of the ground truth measurements.

The effects of surface roughness are in general stronger for the scattering case than for the emission case, especially the influence of the surface correlation length is almost negligible for the latter (Borgeaud et al., 1995; Davidson et al., 2000). For the scattering case the surface roughness is as important as the dielectric properties of the surface and therefore greatly limit the possibilities for soil moisture retrieval.

Most models that describe surface scattering use the root mean square of the height

differences along with the surface correlation length. Replacement of the latter with a more adequately responding parameter could yield improvement in the behaviour and application of surface scattering models

The use of active microwave measurements to estimate soil moisture is not as straight forward as in the passive case. The models perform well as long as they are within their range of validity (regarding e.g. surface roughness and vegetation cover). Of the three bands used in the models the preferable wavelength is L-band because :

- it has a larger sensing depth and is less hampered by vegetation cover than C-band;
- is already available from space borne sensors (JERS-1, SIR-C) and;
- is within a protected frequency allocation which is not the case for P-band.

P-band provides estimates over larger depths which is more favorable for hydrological purposes. However for P-band the pure surface scattering approach is not valid and in a lot of cases volume scattering will be present. To account for this effect different models need to be developed which combine the surface scattering and volume scattering effects. Furthermore, the calibration of the airborne data is difficult and the data sometimes prove to be inconsistent due to human errors (e.g. software errors), which makes validation difficult. The lack of availability of P-band data (esp. the absence of space-borne P-band data) and the difficulty in validation of the results (conventional methods are unsuitable due to P-bands large sensing depth) make P-band currently less favourite over L-band. More research and data is needed to show the possibilities of P-band microwave remote sensing because it is the only band that has a sensing depth that comes near the root zone depth.

In general two problem areas need to be addressed if active microwave remote sensing can be used operationally to estimate surface soil water content.

- The effects of surface roughness at various scales needs to be better accounted for.
- The effect of vegetation (cover) needs to be accounted for. Vegetation, when using active microwaves, can seldomly be modelled as an attenuation layer as in the passive case. Current radiative transfer models are too complicated to be inverted, plus the amount of input parameters needed to describe the vegetation is too large, even for a uniform vegetation cover within one resolution cell. Mixed pixels would make the problem even more complex.

A multi temporal change detection approach in which the surface roughness and in specific cases also the vegetation can be regarded as a constant might provide a solution. Practically, this implies either lower resolutions from space borne sensors, or less spatial coverage. Simplified radiative transfer models that handle the vegetation in structure classes for instance might provide a solution to tackle the problem of vegetation influence.

In summary the high attainable resolution along with a good temporal resolution would make the active microwave remote sensing instruments a good addition to the passive sensors (naturally under the condition that useful frequencies such as C-, and L-band are used). This situation would be ideal, which currently is seldomly the case.

6.4 Assessment of soil moisture estimation performance

6.4.1 Introduction

The assessment of the performance of soil moisture estimation using microwave remote sensing will be done in statistical terms. To determine the reliability of the estimation i.e. what is the error of the estimation is not a simple task because of the many error sources involved. The Central Limit Theorem (CLT) states that the sum X of N independent variables x_i , where $i = 1, 2, 3, \dots, N$, each taken from a distribution of mean μ_i and variance V_i or σ_i^2 , the distribution for X has:

an expectation value

$$\langle X \rangle = \sum \mu_i \quad (6.1)$$

a variance

$$V(X) = \sum V_i = \sum \sigma_i^2 \quad (6.2)$$

and becomes Gaussian as $N \rightarrow \infty$, (in practice $N \geq 10$).

Unfortunately it is not known if all the errors involved are independent and if a certain type of error is dominating.

The error sources involved in the *radiation measurements* are depicted in Figure 6.14. These measurement errors can be taken into account by a calibration procedure. For SAR data this procedure can be divided into an internal and external calibration. The internal calibration accounts for errors in the electronics and signal processing. The external calibration accounts for errors due to atmospheric influence, antenna and platform orbit instability (esp. for airborne systems). The internal calibration is performed transmitting known signals through system using built-in devices. External calibration is done using targets/objects with a known radar cross-section. A more extensive treatment on SAR calibration can be found in Ulaby *et al.*, 1992 and Curlander and McDonough (1991). For passive sensors similar procedures exist where for example for microwave radiometers the external calibration is performed using targets/objects with known emissivity. A relatively calibrated system can contain data with a bias, but the measurements are repeatable and consistent since the bias is time constant. A good absolute calibration will result in data which is both repeatable and has a accurate (absolute) value.

In the *inversion process* however we not only deal with the remotely sensed measured data but also with models that describe the interaction between radiation and object as well as the path it follows. The errors in the quantitative description of parameters and/or the incomplete description of the physical processes involved introduce additional errors which only can be revealed through intensive comparison with measured data (from other sources) and/or sensitivity analysis. The latter reveals how sensitive the model is in change of certain parameters and thus also where the largest errors can be expected.

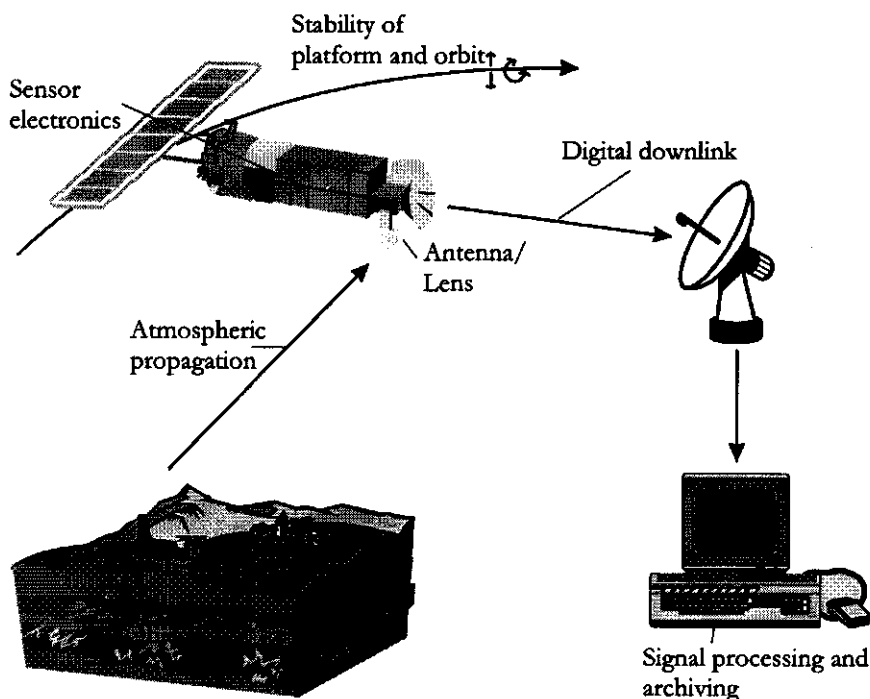


Figure 6.14: The error sources that need to be taken into account when dealing with a complete space-borne "end-to-end" system (adapted from Van der Sanden (1997) and Curlander and McDonough (1991)). For an airborne system the downlink can be omitted.

Another problem related to the model errors are errors due to the so-called *mixed pixels* (i.e. pixels which represent radiation from different kinds of objects with different -spectral, scattering- signatures). These pixels are outside the validity of most inversion procedures since they do not meet the boundary conditions. However, do not confuse the mixed pixels with speckle, because this is an instrument related error caused by interference due to the changing summation of the contributions of a group scatterers within a resolution cell in continuously changing combinations. The problem associated with these types of errors are generally referred to as the up- (or -down) scaling problem and are directly related to the instruments spatial, temporal and radiometric resolution.

6.4.2 Sensitivity analysis of soil moisture estimation of bare soil fields through Monte Carlo simulations

Description of methods

Estimation of systematic and random errors Consider a bare soil field with a field averaged soil moisture content and field averaged roughness parameters $\langle k\sigma \rangle$ and $\langle kl \rangle$. The field consists of n -pixels, each with a soil moisture content θ_i ($i = 1, \dots, n$) and roughness parameters, $k\sigma_i$ and kl_i that deviate from the field average values. The

distribution of the variables is considered to have a Gaussian distribution with the mean equal to the field averages and a standard deviation determined from field observations. Furthermore each pixel has an incidence angle (θ_{inc})_i which is not exactly known. The above mentioned variation in surface parameters can be considered as random errors.

Another source of errors in radar observations is speckle which statistics are well known (Hoekman, 1991). For logarithmically scaled data, i.e. σ^0 in dB, the standard deviation is a constant depending only on the number of looks and the distribution can be approximated by a Gaussian distribution for a large number of looks. To simulate as a first attempt the influence of errors and error propagation on the model performance the following method is employed (Bastiaanssen *et al.*, 1994; van Oevelen *et al.*, 1996).

Given a random variable X , e.g. the radar backscatter, which is a function of the input parameters x_i , e.g., $k\sigma$ etc., with $i = 1, 2, \dots, n$:

$$X = f(x_1, \dots, x_i, \dots, x_n) \quad (6.3)$$

and a set of reference input parameters of x_i , called r_i , e.g. field averages of $k\sigma$ etc., determined from field observations which give as a result the reference value of X hereafter called R :

$$R = f(r_1, \dots, r_i, \dots, r_n) \quad (6.4)$$

Thus R is the backscatter coefficient of the field using the field averaged values of $k\sigma$, $k\sigma$ etc.. The input parameters are assumed to have a random error that is normally distributed with the reference value as a mean and the standard deviation set at a percentage of the mean. Using sets of the randomly distributed input parameters to simulate errors in model input parameters, model output X can be generated from which the probability density function or distribution of X can be generated. A large number of realizations of X is necessary to retrieve meaningful statistics. One of the important conditions is that the number of realizations must be large enough that the statistics become constant. The above described simulation method is generally known as the Monte-Carlo method.

However, one is usually not interested in the distribution of X but in the distribution of the deviation S_e from the reference value. The error S_e is defined as:

$$S_e = |X - R| \quad (6.5)$$

The cumulative probability density function or distribution of S_e can thus be calculated.

In this thesis it is assumed that the reference value is the true value for X . However, the reference value for the backscattering coefficient σ^0 is determined using the reference input parameters, which were considered to be the true values. For the soil

Table 6.10: Parameters for bare soil fields from EFEDA-Spain and HAPEX-Sahel Niger. The parameters are considered to have a random error with the standard deviation of the mean used in the simulation.

Parameter	Standard Deviation (as % of mean)	
	Spain JPL-AIRSAR	Niger, ERS-1
Autocorrelation length kl	32	70
RMS of height differences $k\sigma$	39	60
Volumetric moisture content θ		
(converted to a complex ϵ)	20	20
Incidence angle θ_{inc}	1	1

moisture retrieval algorithm the areal or field averaged value used to generate the backscattering coefficients is taken as the reference value. This implies that only the true value of X is retrieved when a perfect model is used.

Two basic different situations are now discussed. The first situation is the estimation of the soil moisture on a pixel by pixel basis for both pixels with or without speckle (referred to as pixel-based). The second situation is the estimation of soil moisture on a field or object basis using field averaged backscatter values also for fields (number of pixels per field is varied to a maximum of 10^4) with or without speckle (referred to as field-based).

Results and discussion

Error analysis As was done in a previous study by Bastiaanssen *et al.* (1994) the statistics needed to perform the simulation were estimated from field data from the EFEDA-Spain (sections 5.2 and 6.3.2) and HAPEX-Sahel (sections 5.3 and 6.3.1) experiments (Bastiaanssen *et al.*, 1993; van Oevelen *et al.*, 1993). The standard deviations of the parameters that are considered as sources of random errors in this simulation are listed in Table 6.10, the field average or mean values of these parameters can be found in Table 6.11. For both ERS-1 and AIRSAR three bare soil fields with different roughness cases have been chosen, each field can thus be considered to be representative for a certain roughness case. The simulation for 10.000 pixels for these fields or roughness cases will give a distribution of the backscatter coefficient σ^0 for each field or roughness case. INVIEM was applied on these backscatter coefficients to yield a distribution of soil moisture estimates. The speckle is determined from 6 bare soil fields both in Spain for AIRSAR data and in Niger for ERS-1 data and compared with theoretical values from Hoekman (1991). For ERS-1 the standard deviation is about 2.5 dB (3 looks) and for the AIRSAR about 1.33 dB (16 looks). Hoekman (1991) gives for 3- and 16-look data, a standard deviation of 2.73 dB and 1.10 dB respectively. Thus the experimental data are in good agreement with the theoretical values.

Two examples of the probability density function (pdf) of error of estimates for VV-polarized C-band for two surface roughness cases are shown in Figure 6.15. In Table 6.12 the results are listed for three different roughness cases, from which it becomes apparent that the error in backscatter coefficient σ^0 for an individual pixel can become

Table 6.11: The mean parameter values of three bare soil fields from Spain and Niger used in the simulation of the backscatter coefficient σ^0

Case	Spain				Niger			
	$k\sigma$	kl	θ	θ_{inc}	$k\sigma$	kl	θ	θ_{inc}
	[-]	[-]	[-]	[Rad]	[-]	[-]	[-]	[Rad]
1	1.6	4.4	0.10	0.780	0.34	4.49	0.10	0.401
2	1.6	11.0	0.10	0.780	0.79	11.22	0.10	0.401
3	1.1	16.9	0.10	0.780	1.24	17.95	0.10	0.401

Table 6.12: The standard deviation (St.Dev), the mean standard error (S_e) and mean of the backscatter coefficient σ^0 simulation ($n=10^4$) for C-band and three different roughness cases with and without speckle (see Table 6.11). For the JPL-AIRSAR (Spain) both results for both HH and VV polarization are given, for ERS-1 (Niger) only for VV-polarization.

Roughness Case	Spain						Niger		
	VV pol.			HH pol.			VV pol.		
	Mean	St.Dev	S_e	Mean	St. Dev.	S_e	Mean	St. Dev	S_e
1	-7.67	2.26	0.82	-10.77	2.43	1.28	-10.42	2.48	3.37
speckle	-7.69	2.36	1.25	-10.77	2.53	1.46	-10.34	2.86	3.61
2	-8.74	1.22	0.36	-11.49	1.75	1.22	-7.95	2.62	1.92
speckle	-8.78	1.27	0.89	-11.54	1.48	1.40	-8.05	2.68	2.36
3	-12.27	1.70	0.52	-17.00	2.12	1.03	-7.26	3.04	1.91
speckle	-12.29	1.75	0.91	-17.04	1.90	1.21	-7.34	2.99	2.44

very large. On average ERS-1 has a standard error S_e varying from 1.91 dB to 2.94 dB. For the AIRSAR it is considerably less, namely from 0.82 dB to 1.56 dB for VV-polarization and from 1.03 dB to 1.72 dB for HH-polarization. The contribution of speckle to the standard error varies from approximately 0.4 dB to 0.9 dB.

Soil moisture content θ estimates are listed in Table 6.13 and two examples of the pdf are given in Figure 6.16. Clearly, the average standard errors are in most cases much larger for the individual pixel soil moisture estimates from Niger compared to those of Spain. However, if looked at the field estimates the error decreases significantly, i.e. even lower than those of the field estimates of Spain. The most likely explanation are the higher standard deviations for the surface parameters for Niger, which give large deviations from the true mean backscatter coefficient σ^0 for a low number of pixels and thus introduce an error when inverted. Because of the strong non linearity in the relationship between σ^0 and surface parameters such as θ the results of the inversion can even become better when noise (such as speckle) is added (see case 2 Niger in Table 6.13). The standard error in estimating the soil moisture content for an individual pixel ranged for the Niger data set from 10% to 15% for pixel-based estimates and from 1% to 3% for field-based estimates (Table 6.13). For Spain the errors ranged from 5% to 10% for pixel-based estimates and from 3 to 8% for field-based estimates.

Currently the INVIEM model uses, when available, both VV- and HH-polarizations

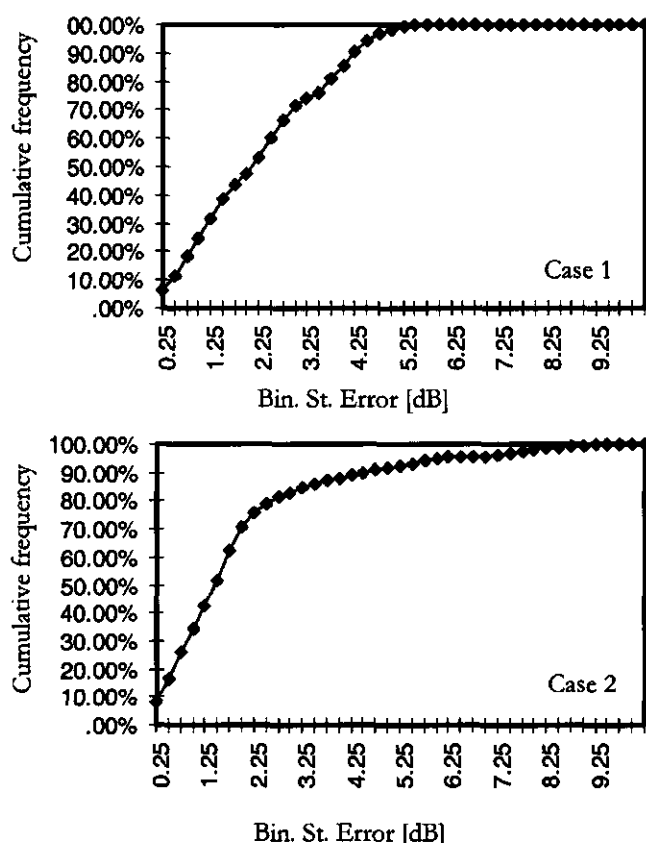


Figure 6.15: Probability density functions for C-band VV polarization for two surface roughness cases 1 and 2 for Niger (reference values are given in Table 6.11)

to obtain soil moisture estimates. Usually, the ranges of soil moisture estimates from VV and HH have overlap. In that case the minimum and maximum of the overlap are taken as the boundaries of the soil moisture estimate range. The problem arises when there is no overlap, in that case the inversion is not possible. This has been the case for field 3 for which for a large number of pixels no inversion was possible.

For each case the soil moisture estimate results are plotted for each pixel and cumulatively averaged as shown in Figure 6.17. After averaging over a certain number of pixels the average soil moisture estimate becomes almost constant. Each individual estimate can however deviate strongly from the reference or true value. When for all separate surface roughness cases or fields the estimates are averaged the result generally becomes closer to the reference value (Figure 6.17, Tables 6.14 and 6.15). In the case where all values are averaged over a number of pixels larger than 25 there is only a slight deviation of the soil moisture estimates from the reference values (Tables 6.14 and 6.15). For the field-based estimates there is almost no difference between the cases with speckle and without. For the pixel-based estimates even after averaging over a large number of pixels there is a constant difference of θ between the cases

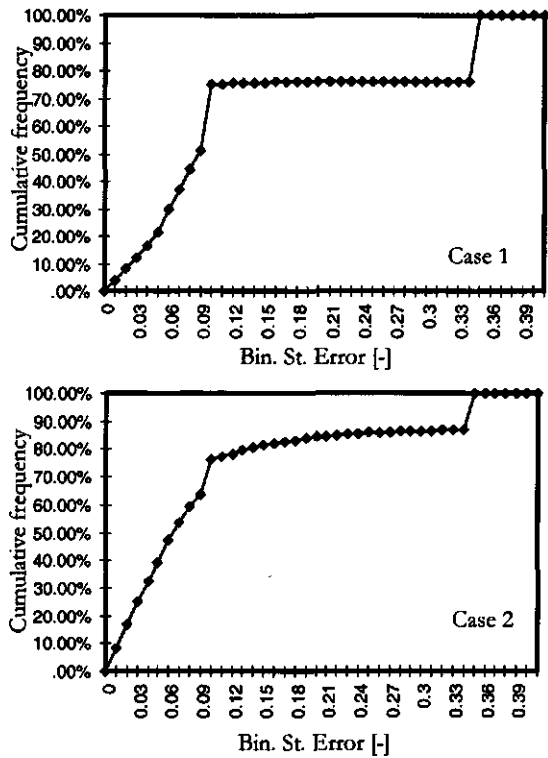


Figure 6.16: Probability density functions for C-band soil moisture estimates for the surface roughness cases of Figure 6.15. The discontinuous look of the high estimates is a result of the cut-off values in the soil moisture algorithm used ($\theta = 0.0$ and 0.45 which give a S_e of 0.1 and 0.35 respectively).

Table 6.13: The standard error S_e for the results of the soil moisture content estimation using C-band and three different roughness cases in Spain and Niger (see Table 6.11). Given is a comparison between pixel based estimates and field based estimates, i.e. using the average backscatter over all the pixels ($n=10^4$). For case 3 in Spain, the field average backscatter coefficients did not give a solution. For this case the pixel based estimation yielded only a result in 60% of the pixels. In all the other inversions the outfall was less then 15%.

Roughness Case	Spain		Niger	
	pixel	field	pixel	field
1 no speckle	0.09	0.08	0.13	0.03
speckle	0.10	0.08	0.13	0.03
2 no speckle	0.04	0.03	0.15	0.01
speckle	0.05	0.03	0.10	0.01
3 no speckle	0.05	-	0.10	0.03
speckle	0.05	-	0.12	0.03

Table 6.14: The standard error of the soil moisture estimates as function of the number of pixels for a single realisation over which the ERS-1 backscatter coefficients for Niger are averaged.

Number of pixels	Niger			
	Case 1		Case 2	
	No Speckle	Speckle	No Speckle	Speckle
2	0.05	0.09	0.03	0.07
10	0.05	0.02	0.01	0.02
25	0.03	0.01	0.02	0.01
50	0.03	0.01	0.01	0.01
100	0.03	0.02	0.02	0.00
250	0.03	0.03	0.01	0.00
500	0.03	0.03	0.00	0.00
1000	0.04	0.03	0.00	0.01

Table 6.15: The standard error of the soil moisture estimates as function of the number of pixels for a single realisation over which the JPL-AIRSAR backscatter coefficients for Spain are averaged.

Number of pixels	Spain			
	Case 1		Case2	
	No Speckle	Speckle	No Speckle	Speckle
2	0.11	0.00	0.01	0.00
10	0.10	0.04	0.03	0.05
25	0.07	0.06	0.03	0.03
50	0.08	0.07	0.03	0.03
100	0.08	0.06	0.03	0.03
250	0.08	0.07	0.03	0.04
500	0.08	0.08	0.03	0.04
1000	0.08	0.07	0.03	0.03

with and without speckle. *Speckle introduces thus an off-set or additional constant error in pixel-based soil moisture estimation (Figure 6.17).*

The results of the error analysis provide a basis to assess the quantitative value of the spatial information provided by detailed remote sensing data. *The advantage of remote sensing data, especially at high resolution is that a number of samples (i.e. pixels) can be used to obtain estimates with smaller random errors. This can be done by averaging over a limited number of pixels, at the price of degrading the spatial resolution. However, to avoid mixing measurements relating to different physical objects, this averaging can be performed over stationary heterogeneous targets only.*

6.4.3 Consistency between passive and active microwave soil moisture estimates

In this Chapter both passive and active microwave remote sensing approaches have been analysed to estimate soil moisture content θ . Naturally, there is a difference in sensitivity between both passive and active methods to various factors such as surface roughness and vegetation even when the instrument characteristics are comparable. However, for areas that have a low amount of vegetation and a relatively constant surface roughness these factors should be of limited influence. Hence, if the methods presented are sound than the application of the passive and active methods over the same area should give comparable and consistent results.

In the next section L-band radiometer data will be compared with C-band SAR data to show the consistency between the two types of data and their retrieval methods.

Comparison between passive and active microwave remote sensing observations from HAPEX-Sahel'92

The soil moisture estimates of two microwave instruments are observed and compared: PBMR, the low resolution passive sensor and ERS-1, the high resolution active sensor.

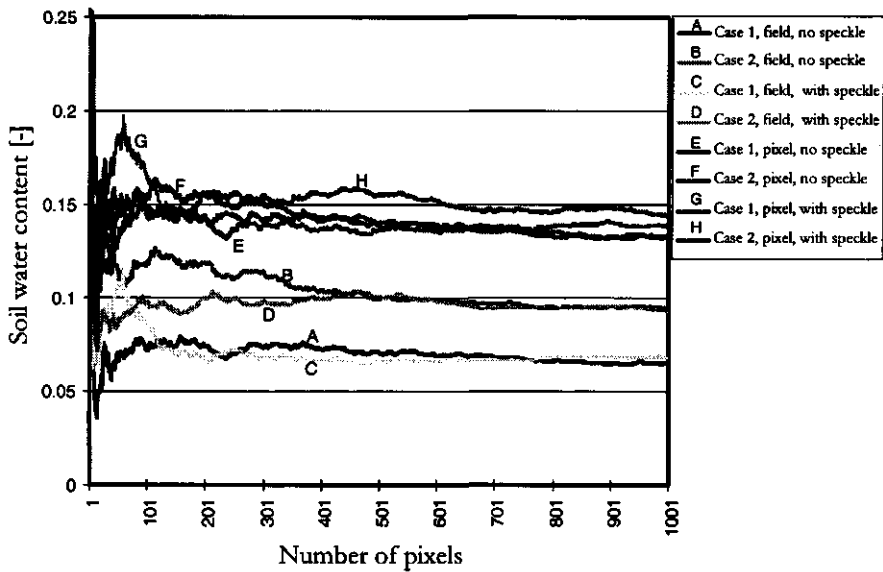


Figure 6.17: The soil water content θ estimates of the cumulatively averaged backscatter coefficient σ^0 . Lines A through D are for Niger, using ERS-1 simulated data. Lines E through H are for Spain, using AIRSAR simulated data. Roughness cases 1 and 2 refer to the roughness cases from fields 1 and 2 in Table 6.11. In Table 6.14 some of the numerical results are listed.

The data of the PBMR and ERS-1 taken on 12 September, 1992 were co-registered and the PBMR data were resampled (nearest neighbour) to match the pixel size (not spatial resolution!) of the ERS-1 purely for data extraction purposes. Within the study area, West-Central Supersite, of the HAPEX-Sahel experiment a transect was chosen with a length of 5000 m. This transect was chosen such that areas where the INVIEM model is not valid are excluded such as certain geomorphological features, e.g. the plinthite plateaus which have strong roughness features along the edges of the plateaus.

Three different scenarios were used to compare the PBMR data with the ERS-1 data

Scenario 1: ERS-1 data have been filtered using a 3×3 moving average filter (size is 37.5 m) to reduce the speckle influence. (Figure 6.18). The PBMR data has an overall higher soil moisture value than ERS-1 which can be explained by the longer wavelength at L-band (≈ 21 cm) compared to C-band (≈ 5.6 cm). The soil moisture profile in semi-arid regions is mostly drier at the top of the profile often even shortly after rainfall events because the sandy soils quickly percolate the precipitation and the top-layer is quickly dried by the sun. Despite the filtering, the ERS-1 data show large fluctuations in soil moisture values. Either the soil moisture has such a large variance and/or the effect of speckle has not been significantly reduced by the moving average filter. **Scenario 2:** To remove the speckle or high variance in SAR data often a LEE filter is applied which filters out the high variance pixels. By applying this filter to the ERS-1 data the variance is greatly reduced (Figure 6.19). However, a LEE filter (IDL-ENVI, 1999) has no physical basis but only a statistical one. The comparison

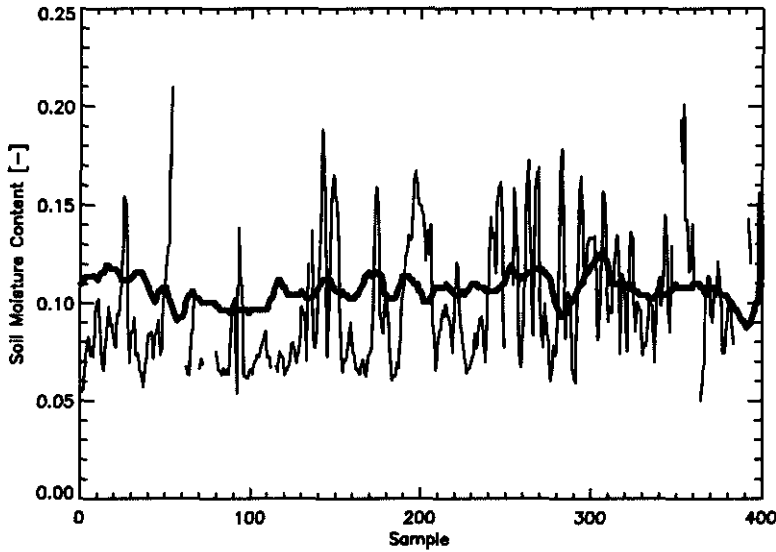


Figure 6.18: Scenario 1: Comparison of ERS-1 SAR soil moisture estimates (thin line) with PBMR soil moisture estimates (thick line). The ERS-1 data were filtered by a 3 by 3 moving average filter with a size of 37.5 m..

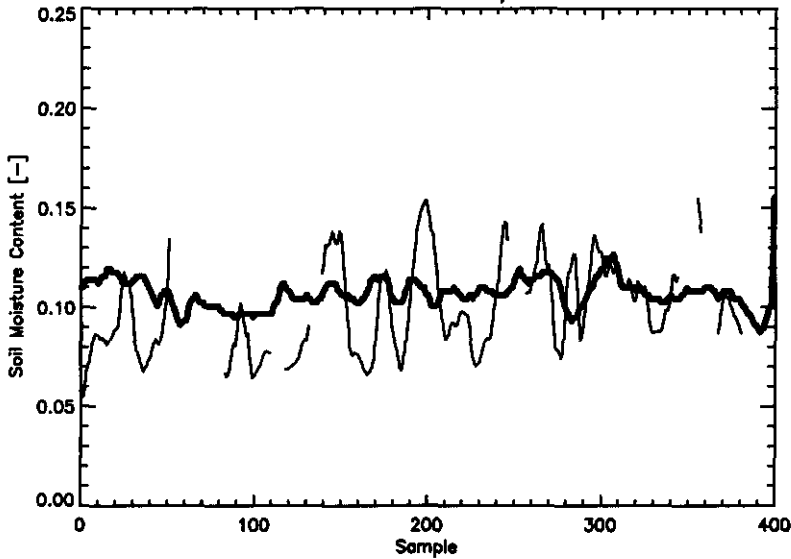


Figure 6.19: Scenario 2: Comparison of ERS-1 SAR soil moisture estimates (thin line) with PBMR soil moisture estimates (thick line). The ERS-1 data were filtered by a 3 by 3 (size is 37.5 m) Lee filter (high variance pixels are filtered out)

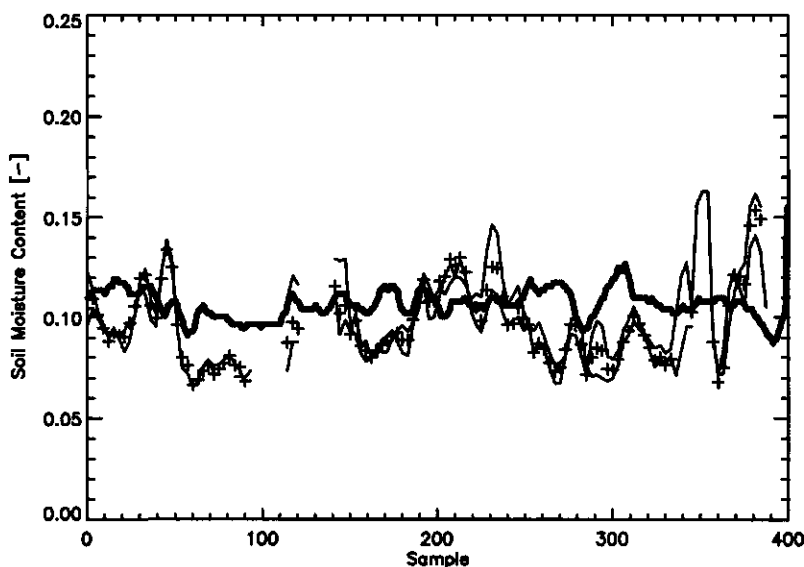


Figure 6.20: Scenario 3: Comparison of ERS-1 SAR soil moisture estimates (thin line) with PBMR soil moisture estimates (thick line). The ERS-1 data were spatially averaged (linearly) such that the size (112.5 m) is similar to that of the PBMR (100 m).

with the PBMR data is better than in the first scenario but no physical explanation can be given.

Scenario 3: the ERS-1 data has been linearly averaged over a 9×9 window resulting in a filter size of 112.5 m (Figure 6.20). Since there are geometrical differences between the two images this spatial averaging can be done over different boxes which all could be considered correct (Figure 6.21). Therefore two different averaging boxes have been applied and compared to the PBMR data. The two averaging schemes show local differences but overall are very comparable.

The comparison with the PBMR shows that the trend seems to be in agreement but that certain fluctuations in the ERS-1 data are much stronger. The latter can be explained by the greater sensitivity of SAR data to other surface characteristics (e.g. vegetation) than soil moisture and these features can override the effect of soil moisture. The results are promising in that they show that *two different types of sensors can provide consistent results albeit within the restrictions of the boundary conditions of the models used. Here, over spatially stationary homogeneous surfaces with low vegetation cover.*

6.4.4 Conclusions of soil moisture estimation performance

Sensitivity analysis of soil moisture estimation of bare soil fields through Monte Carlo simulations provides a basis to assess the quantitative value of the spatial information provided by detailed remote sensing data. The advantage of remote sensing data, especially at high resolution is that a number of samples (i.e. pixels) can be used to

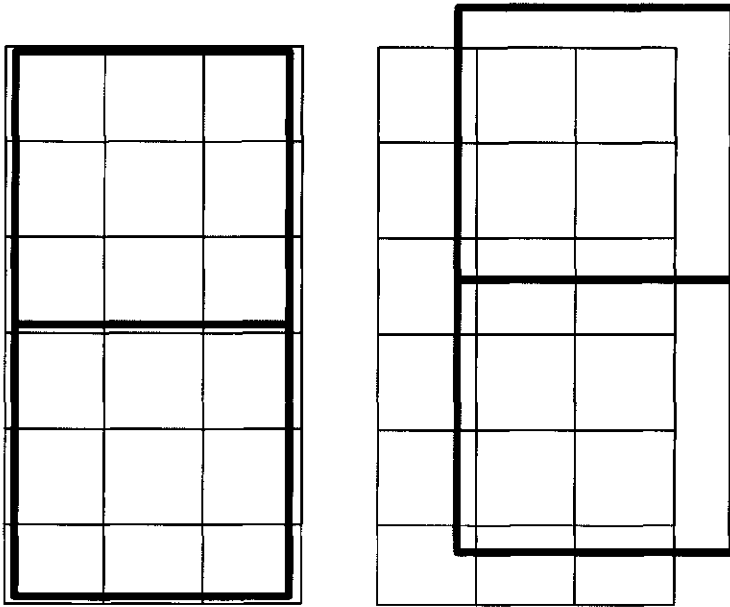


Figure 6.21: Geometrical considerations when comparing ERS-1 SAR data with PBMR data. The different resolutions give rise to various scenarios of comparison of data.

obtain estimates with smaller random errors. This can be done by averaging over a limited number of pixels, at the price of degrading the spatial resolution. However, to avoid mixing measurements relating to different physical objects, this averaging can be performed over stationary heterogeneous targets only.

In general the average standard errors are larger for the individual pixel soil moisture estimates from Niger compared to those of Spain. However, if looked at the field estimates the error decreases significantly, i.e. even lower than those of the field estimates of Spain. For the *field-based estimates* there is almost no difference between the cases *with speckle and without*. For the *pixel-based estimates* even after averaging over a large number of pixels there is a constant difference of θ between the cases *with and without speckle*. Speckle introduces thus an off-set or additional constant error in pixel-based soil moisture estimation.

The comparison of ERS-1 soil moisture estimates with the PBMR soil moisture estimates shows that the trend seems to be in agreement but that certain fluctuations in the ERS-1 data are much stronger. The latter can be explained by the greater sensitivity of SAR data to other surface characteristics (e.g. vegetation) than soil moisture and these features can override the effect of soil moisture. It is shown that two different type of sensors can provide consistent results albeit within the restrictions of the boundary conditions of the models used, i.e. over spatially stationary homogeneous surfaces with low vegetation cover.

6.5 Conclusions

Passive microwave data The strong relationship between the dielectric properties and microwave emission along with the relatively small influence of surface roughness makes the application of passive microwave data to estimate soil moisture very straight forward and has especially at the lower frequencies such as at L-band great potential for hydrological purposes. Between the brightness temperatures, T_B and soil moisture content, θ of the top 6 cm an approximately linear relationship is present. A problem exists with high vegetation cover and this is the area where considerable improvement can be made: better modelling of the vegetation influence, or a combination of more frequencies. The errors involved in the estimation of soil moisture using passive microwave remote sensing are small, i.e. usually less than 5% even for areas with moderate vegetation cover and is often less than the standard deviation of the soil moisture ground truth measurements.

The effects of surface roughness are small for the emission case, especially the influence of the surface correlation length is almost negligible. With respect to soil moisture estimation the effect can for most circumstances easily be accounted for by a simplified model like that of Choudhury et al., 1979.

Although the L-band penetration of vegetation forms a physical limitation, the sensitivity to the soil moisture content as a function of vegetation water content is for L-band still present at a vegetation water content of 4 kg m^{-2} . For C-band this amount of vegetation content would already obscure the signal from the soil.

Extrapolation of the results to measurements from space would mean that the influence of mixed pixels due to the low resolution of approx. 30 km for L-band would increase. Also the effect of macroscale roughness would need more attention at that scale. The AMSR and AMSR-E will, with C-band, be the first radiometers that can provide more insight into the estimation of soil moisture from space with a spatial resolution of approximately 50 km although the vegetation would still be a significant problem. The planned L-band space-borne radiometer, SMOS (Soil Moisture and Ocean Salinity mission) will be a significant step towards operational use of microwave soil moisture estimates at the global scale.

Active microwave data The relationship between the dielectric properties and microwave backscatter is not as strong as in the emission case because of the larger influence of surface roughness and vegetation structure.

The INVIEM model was applied to ERS-1 SAR data of Niger (HAPEX-Sahel) and the results compared with soil moisture content, θ measured over a depth of 6 cm. Although this depth is probably larger than the associated sensing depth of the instrument (about 2 cm) it is shown that the estimates are within the expected θ -range and that the in situ measured θ -values are consistently higher. The latter is expected because the surface layer of 0-2 cm is drier than the measured layer of 0-6cm. The influence of soil texture on the ERS-1 retrieval results has been studied and is small compared to other effects such as speckle or vegetation.

JPL-AIRSAR data have been applied using data from Spain (EFEDA-Spain). Both

the INVIEM model and INVOSU model could be applied because AIRSAR provides polarimetric data. Overall, *INVIEM as compared to INVOSU yields more reasonable estimates of soil moisture content as far as can be deduced from the limited ground truth data and visual inspection.*

The advantage of using INVIEM over INVOSU is that it can be applied to both single polarization and polarimetric data. The INVOSU model requires no a priori knowledge about the surface characteristics except for information on the type of soil. INVIEM does require in its present form the input of surface roughness characteristics. At present, the applicability of both models is restricted to bare soils only and therefore is of limited practical use.

JPL-AIRSAR data have also been used in the Washita'94 experiment. A comparison along transect 2 between the TDR soil moisture measurements in the rangeland plot over a depth of 6 cm with the C-, L- and P-band INVIEM estimates shows good agreement for both C- and L-band. The root mean square error (RMSE) for C-, and L-band estimates is 3%. The P-band soil moisture estimates are consistently higher which is to be expected since these estimates represent an effective average soil moisture content over a larger depth than C-, and L-band.

The effects of the erosion contours on the in-situ soil moisture measurements cannot be seen in the AIRSAR soil moisture estimates. The AIRSAR spatial resolution of approximately 10 m is apparently too coarse to capture this variability of θ .

In Sweden the EMISAR data were used during the FOREST-Dynamo experiments. EMISAR soil moisture estimates in general underestimate the measured soil moisture content. This can be contributed to the fact that the IEM model does not account for periodicity or anisotropy in the surface roughness characteristics and therefore in these case gives a lower backscatter coefficient than actually measured. Furthermore, there might be an inconsistency between measured surface roughness and how it is represented in the model. The in situ measured RMS height and correlation length does not necessarily resembles the radar backscattering relevant surface roughness. The backscattering is likely to be caused by a smoother subsurface. The sometimes poor agreement between estimated and measured soil water content might also be due to callibration errors in the EMISAR data. Especially since the L- and C-band flights were not simultaneously.

Both the C- and L-band estimates seem to agree better with the soil moisture measurements taken with the TDR rod at a shallower angle with respect to the surface, resulting in a measurement depth of about 2-3 cm. Most estimates are within 5% of the field measurements. *For all experiments the standard error in the active microwave soil moisture estimates in absence of vegetation is often lower (<5%) than that of the ground truth measurements.*

The effects of surface roughness are in general stronger for the scattering case than for the emission case, especially the influence of the surface correlation length is almost negligible for the latter. For the scattering case the surface roughness is as important as the dielectric properties of the surface and therefore greatly limit the possibilities for soil moisture retrieval. Most models that describe surface scattering use the root mean square of the height differences along with the surface correlation

length. Replacement of the latter with a more adequately responding parameter could yield improvement in the behaviour and application of surface scattering models

The use of active microwave measurements to estimate soil moisture is not as straightforward as in the passive case. The models perform well as long as they are within their range of validity (regarding e.g. surface roughness and vegetation cover). Of the three bands used in the models the preferable wavelength is L-band because :

- it has a larger sensing depth and is less hampered by vegetation cover than C-band;
- is already available from space borne sensors (JERS-1, SIR-C) and;
- is within a protected frequency allocation which is not the case for P-band.

P-band provides estimates over larger depths which is more favorable for hydrological applications. However for P-band the pure surface scattering approach is not valid and in a lot of cases volume scattering will be present. To account for this effect different models need to be developed which combine the surface scattering and volume scattering effects. Furthermore, the calibration of the airborne data is difficult and the data sometimes prove to be inconsistent due to human errors (e.g. switching of tape labels, software errors), which makes validation difficult. The lack of availability of P-band data (esp. the absence of space-borne P-band data) and the difficulty in validation of the results (conventional methods are unsuitable due to P-bands large sensing depth) make P-band currently less favourite over L-band. More research and data is needed to show the possibilities of P-band microwave remote sensing because it is the only band that has a sensing depth that comes near the root zone depth.

In general two problems areas need to be addressed if active microwave remote sensing can be used operationally to estimate surface soil water content.

- The effects of surface roughness at various scales needs to be better accounted for.
- The effect of vegetation (cover) needs to be accounted for. Vegetation, when using active microwaves, can seldomly be modelled as an attenuation layer as in the passive case. Current radiative transfer models are too complicated to be inverted, plus the amount of input parameters needed to describe the vegetation is too large, even for a uniform vegetation cover within one resolution cell. Mixed pixels would make the problem even more complex.

A multi temporal change detection approach in which the surface roughness and in specific cases also the vegetation can be regarded as a constant might provide a solution. Practically, this implies either lower resolutions from space borne sensors, or less spatial coverage. Simplified radiative transfer models that handle the vegetation in structure classes for instance might provide a solution to tackle the problem of vegetation influence.

In summary the high attainable resolution along with a good temporal resolution would make the active microwave remote sensing instruments a good addition to the passive sensors (naturally under the condition that useful frequencies such as C-, and L-band are used). This situation would be ideal, which currently is seldom the case. For hydrological purposes a dual frequency L- and P-band fully polarimetric system would be the most versatile, especially with a high temporal resolution.

Sensitivity analysis of soil moisture estimation of bare soil fields through Monte Carlo simulations provides a basis to assess the quantitative value of the spatial information provided by detailed remote sensing data. The advantage of remote sensing data, especially at high resolution is that a number of samples (i.e. pixels) can be used to obtain estimates with smaller random errors. This can be done by averaging over a limited number of pixels, at the price of degrading the spatial resolution. However, to avoid mixing measurements relating to different physical objects, this averaging can be performed over stationary heterogeneous targets only.

In general the average standard errors are larger for the individual pixel soil moisture estimates from Niger compared to those of Spain. However, if looked at the field estimates the error decreases significantly, i.e. even lower than those of the field estimates of Spain. For the field-based estimates there is almost no difference between the cases with speckle and without. For the pixel-based estimates even after averaging over a large number of pixels there is a constant difference of θ between the cases with and without speckle. *Speckle thus introduces an off-set or additional constant error in pixel-based soil moisture estimation.*

The comparison of ERS-1 soil moisture estimates with the PBMR soil moisture estimates shows that the trend seems to be in agreement but that certain fluctuations in the ERS-1 data are much stronger. The latter can be explained by the greater sensitivity of SAR data to other surface characteristics (e.g. vegetation) than soil moisture and these features can override the effect of soil moisture. It is shown that two different type of sensors can provide consistent results albeit within the restrictions of the boundary conditions of the models used, i.e. over spatially stationary homogeneous surfaces with low vegetation cover.

Chapter 7

Remotely sensed soil moisture in hydrological models

7.1 Introduction

The main goal of this thesis is the estimation of areal soil water content by means of microwave remote sensing. The estimation of such a parameter is only useful when it can be used in hydrological and meteorological modelling. The argument to estimate areal soil water content is that it is a direct link between the soil water balance and the surface energy balance. The amount of water in the soil and especially the root zone determines how much can be evapotranspired by the soil and vegetation.

Remotely sensed soil water content represents an weighted average over depth (see Section 1.3.3). This effective water content is often difficult to compare with the water content used in most models. In numerical multi-layer models and SVAT models based upon Richards' equation the soil moisture state and flow are modelled on a physical basis (Kim, 1995). Comparison with remotely sensed or measured soil moisture data is theoretically possible with these types of models. However, since the sensing depth and weighting functions are unknown in practice comparison proves to be difficult. Another problem is that most of the current SVAT models are still based on the 1 dimensional Richard's equation and do not take horizontal spatial variability into account.

In parametric bucket type models (Deardorff, 1977; Warrilow, 1986) the soil is regarded as a reservoir and the soil moisture state greatly depends on the soil reservoir depth. The comparison of these models with multi-layer models or verification with remotely sensed or measured data does not make sense (Kim, 1995) because the reservoir does not represent the actual amount of soil water present in the soil or soil surface layer. Therefore the estimation of surface soil moisture using remotely sensed data needs to be coupled to a model that can assimilate such remotely sensed data. It might then be possible to use these type of models to relate, for instance, this surface soil water content to profile or root zone soil water content (van Oevelen & Hoekman,

1999).

With the improvement of the land surface parameterisation in SVAT and climate models and their linkage to remotely sensed observables the model parameters can be better described, their errors better quantified and easier assimilated using remotely sensed information (Kalma *et al.*, 1999).

Incorporating remotely sensed data directly in hydrological models should ultimately improve the performance. Where the performance can be measured as for example improved predictions, better fit, smaller error, better spatial representation depending upon the application and objective considered.

During the research done in the framework of this thesis my ideas on the usefulness of remotely sensed estimated soil moisture changed. Although I still believe the estimation of soil moisture by means of remote sensing has its value in various applications, *I am now of the opinion that the assimilation of brightness temperatures or scattering coefficients is more effective than incorporating soil moisture from those measurements.* In the next few sections I hope to explain and exemplify this.

When dealing with the estimation of soil water content θ , there are two distinct problems connected with almost any remote sensing problem:

1. The *forward problem*: Given the values of all relevant environmental variables including soil water content θ in a scene, predict the radiances that will be observed by each channel or a particular sensor. The solution of this problem involves straightforward application of the radiative transfer equation to suitable models for absorption, emission and scattering of radiation by surface and atmospheric constituents. Thus, use θ with a soil mixing model to estimate the dielectric properties ϵ . The dielectric properties along with other surface characteristics can be used with a radiation model to calculate the radiance expressed as σ° or T_B from the surface at observation height.
2. The *inverse problem*: Given the radiances σ° or T_B observed by a satellite sensor, a useful estimate of one or more environmental parameters including θ can be obtained. By "useful", we mean an estimate whose uncertainty is significantly smaller than the *a priori* uncertainty in the value of the variable e.g. θ . For example, prior to the application of a retrieval algorithm, the *a priori* value and uncertainty of a θ might be its climatological mean and standard deviation. The optimal solution of this problem is less straightforward due to usually *strong non-linearities in the forward model resulting in non-unique solutions.*

G.W. Petty (1999) states: *The ability to solve the forward problem is neither a necessary nor sufficient condition for obtaining a satisfactorily solution of the inverse problem.* The solution of the forward problem is in general easier to handle than the inverse problem. Unfortunately our knowledge of the physical processes involved necessary to describe the forward problem is not always sufficient. Furthermore, when we are interested in a specific parameter such as soil moisture the solution of the forward problem will not always yield that parameter.

7.2 Data assimilation in mesoscale hydrological models: variational analysis

The variational approach to the assimilation of data into mesoscale hydrological models and in particular NWP modelling has been described by various authors e.g. (Rodgers, 1976; Eyre, 1997; English et al., 1999). In Figure 7.1 a schematic represen-

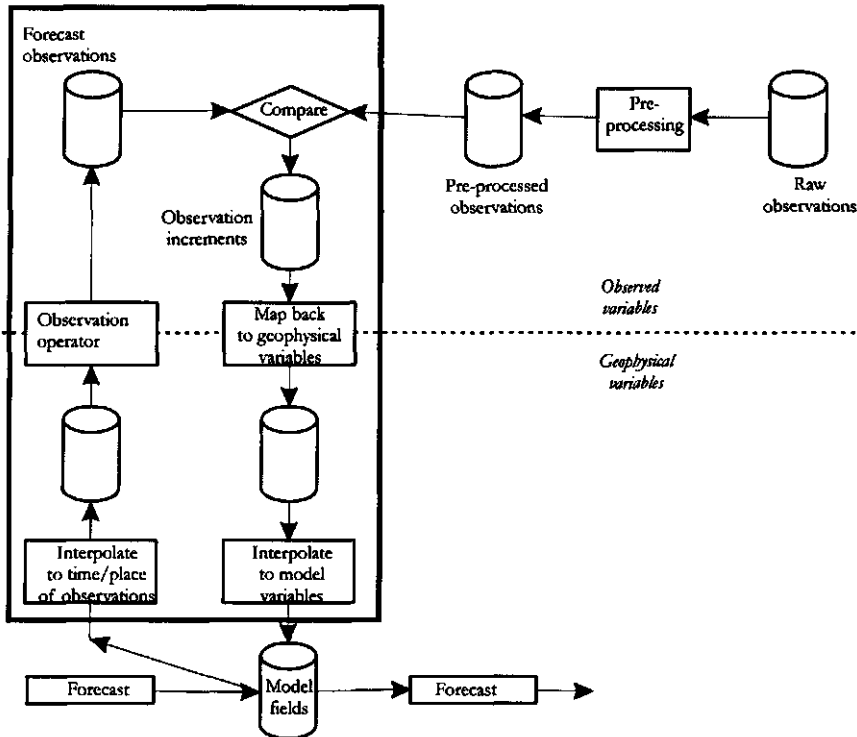


Figure 7.1: Illustration of the variational data assimilation scheme for a geophysical model using remotely sensed data (adapted from Eyre, 1997).

tation of the variational assimilation scheme is given.

The variational approach can be applied to a one-dimensional problem or "1DVAR" (cf. retrieval of vertical profile), a two-dimensional problem (e.g. a surface field) ("2DVAR"), a 3-dimensional problem (analysis of GCM or NWP model state at a single time) ("3DVAR") and the 4-dimensional problem which is similar to the 3DVAR but with observations distributed over time.

At the bottom of Figure 7.1 the continuous cycle of forecast and assimilation is shown. At the top the raw observations are given which can undergo certain preprocessing before put into the data assimilation system itself (e.g. observed microwave brightness temperatures) where they can be compared with the "forecast observations" (e.g. modelled microwave brightness temperatures). The data assimilation is nothing more than a comparison between model generated "observations" from geophysical

variables and actual observations. The difference between the two (the observation increment) can be mapped back into the modelling space as geophysical variables and the process can be iterated. The process of mapping involves both interpolation and weighting, and it is the main concern of data assimilation theory (Eyre, 1997). In the next paragraph a few different methods are illustrated. The effect of assimilation can be studied by giving a weight of zero to the observations (i.e. they do not affect the analysis) the observations increments are still stored and their spatial and statistical properties. Hence, also the error characteristics of the observation type and its operator and the error characteristics of the predicted model fields can be analysed. Thus, valuable information can be obtained on model performance, use of new observations and systematic errors.

Special attention needs to be given to assimilation of remotely sensed observations which contain non-local information (information that is usually not represented in the control variable) or is sensitive to variables that are difficult to parameterize. For example microwave brightness temperatures T_B for a land surface can be simulated in a NWP domain where the cosmic background radiation is outside of this domain and therefore needs to be accounted for separately. Another example of a difficult variable to model or which effects are difficult to incorporate in the assimilation scheme are clouds which are highly variably in time and space.

In the above we assumed that assimilation of the raw observations e.g. brightness temperatures T_B or backscattering coefficients σ^0 are optimal. In most cases this is true but there are exceptions. When the mapping of the observed variable to a geophysical variable is dependent upon a strongly non-linear transfer function the error characteristics might be difficult to represent. In that case assimilation of retrieved parameters through a separate modelling scheme may be advantageous. Also the pre-processing necessary for most remotely sensed observations may introduce errors and needs careful matching with the observation operator. An example here is the effect of sensor viewing geometry and associated problems such as beam filling (caused by a distribution of different contributing brightness temperatures within the antenna beam). In the next paragraph the use of the retrieved parameter in a data assimilation scheme will be illustrated.

In conclusion the variational approach is an elegant and consistent method to assimilated remotely sensed observations into a geophysical model. A drawback is the detailed information needed on the error covariance structure especially when dealing with complicated relationships between the observed quantities and the variables of the geophysical model.

7.3 Assimilation of remotely sensed soil moisture in hydrological modelling

Remotely sensed soil moisture estimates can be assimilated into a hydrological model to update and improve the performance of the model. Houser et al., 1998 give a good overview of the various statistical methods that can be applied in what they

refer to as four-dimensional data assimilation (4DDA). The concept is similar to the 4DVAR, which will be explained in the next paragraph, but uses the remotely sensed retrieved parameter (here soil moisture) and the comparison is done between *estimated* soil moisture fields and *modeled* soil moisture fields. The modeled fields are strongly dependent upon the meteorological forcing and a useful assimilation will be only possible if this forcing is correctly taken into account. This is of course less of a problem in NWP models where the meteorological forcing is inherent in the model. Mesoscale hydrological models and numerical weather prediction models are becoming more and more similar and thus this problem will become less important in the near future.

Houser et al., 1998 give various procedures to establish the assimilation (perform goodness of fit) based upon the work of Stauffer and Seaman (1990). These procedures are summarised below, where parameter can be replaced by e.g. θ , T_B , or σ^0 :

- *Control simulation*: the estimated/measured parameter is assimilated in the model but contains no information or is given zero weight. This approach enables to study the statistical behaviour of the assimilated parameter in comparison with an assimilation where the estimated parameter does influence the model;
- *Direct insertion*: the estimated/measured parameter is directly used in the model and the model parameter is assumed to contain no information;
- *Statistical correction assimilation method*: the modeled parameters mean and standard deviation are matched to the observed mean and standard deviation
- *Newtonian nudging assimilation method*: The model state is adjusted to the observed state by adding small forcing terms to the prognostic equation. Works for both regularly and randomly spaced observational data.
- *Nudging towards a gridded analysis*: Interpolation of observation data to the model data grid for data that is regularly spaced in time and or space.
- *Nudging to individual observation*: For observations that are randomly spaced the difference between the simulated and observed state is determined and consequently interpolated back to the model grid.
- *Statistical interpolation assimilation method*: Assimilation type which is closely related to kriging and is based on a minimum variance method.

The implementation of these assimilation methods is based upon various assumptions about the correlation between the observed parameters both spatially and temporally. Likewise, for the use of the statistical interpolation techniques assumptions are made about the correlation of the error of the observations. By using the first two methods these types of information can be obtained. Naturally under the limitation of the used data set.

Houser (1998) found that the Newtonian nudging method had the most desirable features, such as near continuous soil moisture time series and reasonable spatial patterns. The statistical methods are however extremely efficient and take less computational time. The ultimate choice depends thus more on available computational resources. However, in the near future complex data assimilation methods will become more common.

Besides 4DVAR methods other methods such as Kalman filtering, or Neural Network approaches can be used to assimilate microwave data in hydrological models. However, 4DVAR is the most flexible but also most complex method.

7.4 Outlook on applications and operationalisation of remotely sensed soil moisture

In this thesis the objective was to investigate the use of microwave remote sensing to estimate areal soil water content. This *areal soil water content* is an *effective soil water content*, where effective means a *spatially weighted average over the sensing depth*. This can be different from root zone soil moisture which is the amount of soil moisture over the rooting depth. Although limited, the estimation of surface soil water content is still of practical use. For example, in modelling the complete soil-vegetation-atmosphere (SVAT) system the surface soil moisture can be linked to deeper layers. It may however be clear that in this case also other parameters such as the meteorological forcing play an essential role. With the increasing importance of the land surface parameterization in NWP, climate and mesoscale hydrological models, a strong need for measurements of land surface variables is developing (Cox & Best, 1999). The importance of an accurate representation of land surface processes and the impact on the moisture budget has been shown by e.g. Warrilow and Buckley (1989). It is in this area where both passive and active microwave remote sensing can contribute, not only in the estimation of soil water content but also other surface characteristics as surface roughness and vegetation type and/or structure.

Real time applications of remotely sensed soil moisture on an operational basis is not being done yet. One of the main reasons is the lack of suitable data. Longer wavelengths such as L-band on a space-borne platform along with a 2-3 day overpass time are best suited for soil moisture monitoring but no microwave instrument with those characteristics is available. For many years various initiatives have tried to get a L-band radiometer in space. The latest effort with a synthetic aperture L-band radiometer called SMOS (Soil Moisture Ocean Salinity mission) has proved to be successful and has been selected by ESA to be launched somewhere around 2005. These type of developments will boost the science in the area of soil moisture estimation using microwaves. Current sensors such as the recently launched AMSR, although with C-band as the lowest frequency, have stimulated the operationalisation of microwave data. Due to the relatively low resolution of the space-borne sensors (approx. 30-50 km) the first operational applications will be at mesoscale.

The sensitivity of active microwave instruments to vegetation structure and surface roughness along with a higher achievable spatial resolution makes that these instruments are suited to be used for hydrological applications, especially for surface characterization. The sensitivity to these other factors makes active microwave remote sensing of soil moisture much more complicated compared to passive microwave techniques but still feasible. The planned launches of platforms such as PALSAR and ALOS will add new capabilities to already operational space-borne SAR instruments.

Summary and conclusions

In earth sciences there is a great need for data that are available globally or covers areas which otherwise cannot be measured. Remote sensing is the tool to achieve this goal. In this thesis the use of microwave remote sensing to estimate areal soil water content was investigated. A general framework has been developed which describes the various steps necessary to derive soil water content from remotely sensed measurements.

Soil moisture represents the coupling between the surface energy balance and soil water balance and is therefore a crucial parameter in hydrology and meteorology over land surfaces. Soil moisture exhibits large variability both in space and time and is therefore difficult to measure. Remotely sensed measurements give the opportunity to estimate soil water content over larger areas as well as an integrated effective value over these areas. The difficulty arises to validate these estimation since no direct comparable ground truth exists.

The theoretical framework to estimate soil moisture by means of passive (see Fig. 4.1) and active (see Fig. 4.2) microwave remote sensing can be separated into five distinct steps:

- The first step is to establish the relationship between the soil surface parameters and the observed brightness temperature T_B or radar backscatter coefficient σ^0 ;
- The second step is to describe the influence of vegetation on the relationship between σ^0 or T_B and the surface parameters;
- The third step is to find a relationship between the dielectric properties, i.e. permittivity ϵ and soil parameters to retrieve the soil water content θ ;
- The fourth step is the relationship between soil moisture profile, soil heterogeneity and the sensing depth.
- The fifth and last step is the assimilation of the estimated soil water content θ into hydrological and meteorological models.

In Chapter 2 the relationship between the dielectric properties and soil characteristics was explored and the basic theory of dielectric properties has been given. The effects of an electro-magnetic field upon various materials was explained starting from a mono-atomic gas to multi-phase heterogeneous materials such as soils.

Many models exist to describe the dielectric properties at microwave frequencies based upon soil composition and properties. The more complex models are better able to

explain specific phenomena but require much more detailed information or have unrealistic assumptions (e.g. particle shape) to be of any practical use.

The semi-empirical models such as that of Wang and Schmugge (1980) relate the effective or average permittivity ϵ of a multiphase mixture to the permittivities and volume fractions of the components using a correction factor which accounts for the deviations. The use of these type of models has the disadvantage that they are sensitive to the fitting parameter(s), that the fitting parameter is not known a-priori and that apparent "anomalous" behaviour is not accommodated for.

The theoretical models such as De Loor's model (de Loor, 1956) relate the average electromagnetic field of the mixture as a whole to the electromagnetic fields within the inclusions and calculate in this way the permittivity ϵ . The constituent with the highest volume fraction is usually taken as the host material or continuous medium and the other constituents are then considered as inclusions. According to De Loor (1956) it is in fact impossible to give one relation which describes the permittivity of a heterogeneous mixture. He stated that at best boundaries can be given between which the average value must lie, and which come closer together the more is known about the mixture. Dobson *et al.* (1985) modified the model of De Loor and concluded that adding the component of bound water was necessary to account for the frequency and soil dependence of the permittivity and that the *De Loor model was an adequate description of the permittivity of the soil with soil texture, bulk density and a frequency range from 1.4 to 18 GHz.*

The dielectric properties are a function of frequency and it is noticeable that most mixture models for heterogeneous materials do not have the frequency as a parameter but instead have a frequency range of validity, assuming the frequency dependence to be constant within that region.

The effect of soil texture on the dielectric properties is most significant for clay soils especially those which have a high adsorption capacity where the real part of the dielectric properties is lower and often the imaginary part is higher (for the same θ) as compared to soils with a coarser texture. The soil texture has also its influence on the surface roughness, however this effect is not treated in this thesis.

The theory of dielectric properties of soils still requires attention in specific areas especially for soils with a distinct chemical composition such as high iron content soils, high salinity soils and gypsum soils. For some of these types of soils the dielectric behavior is very different but cannot be explained sufficiently.

For most purposes within remote sensing the use of empirical mixing models to describe the dielectric properties such as those of Wang and Schmugge (1980) and Dobson et al. (1985) seems to be sufficient. In these empirical models the errors involved for most areas and types of soils are small compared to other error sources involved in remotely sensed estimation of soil moisture.

In Chapter 3 the relationship between surface characteristics and emission ϵ and microwave backscatter σ^0 were investigated. Two types of scattering are present when considering scattering in natural terrain, namely surface scattering and volume scattering. When scattering takes place at the boundary of one medium to another, such

as an air - soil surface interface (dielectric half-space), and no contributions from penetrated radiation at subsurface layers are present, it is called surface scattering. Volume scattering is due to inhomogeneities in the medium itself, e.g. within the soil or within vegetation.

The volume scattering models can be separated into two main classes: the coherent models, where phase and amplitude (or intensity) of the electromagnetic field are computed; non- or incoherent models, where only the amplitude is taken into consideration. The non-coherent models are mathematically and computationally simpler but at the cost of a lower accuracy. The difference between the coherent and incoherent models is that in the coherent models the interference between the phases of the electromagnetic waves are accounted for.

The radiative transfer theory belongs to the group of incoherent models and describes the traversing of electromagnetic waves through a medium or several media. The interaction between radiation and the media is described by the transmission, absorption, emission and scattering of the radiation.

For the passive case, thus dealing with microwave emission the radiative transfer approach yields good results. The parametric model of Mo *et al.*, (1982) and its modified versions have proven to be simple radiative transfer models that can effectively estimate the radiation emitted by the soil surface even under vegetation. Scattering is assumed negligible and only three components, soil emission attenuated by the vegetation, emission by the vegetation itself and the downward emitted radiation from the vegetation that is reflected upwards by the soil surface, are used. Two parameters in the model have to be estimated through empirical models namely the roughness parameter h and the optical depth τ .

For the active case, thus dealing with microwave scattering, the volume scattering components and radiative transfer approaches are still too complex i.e. require too much a priori information, to be used in practice for the description of radiation from natural surfaces. The validity of the surface scattering models such as the small perturbation method or the Kirchhoff approaches namely, geometrical optics and physical optics models, is usually limited by the severe assumptions regarding the surface characteristics.

The Integral Equation Method (IEM) model (Fung, 1994, Chapter 7) is a theoretical surface scattering model that attempts to give a more general solution than the just mentioned methods. In its complete version the model can be applied with no limitations regarding roughness scales or frequencies. The model is applicable to natural surfaces but for surfaces that are inhomogeneous volume scattering may be present and for those surfaces the model underpredicts the backscatter coefficient. For surfaces which are skewed or have periodic roughness an additional term has to be added which can be found in (Fung, 1994, Chapter 7).

The semi-empirical model of Oh, Sarabandi & Ulaby, (1992) (OSU) is a surface scattering model that was tested over a large range of soil moisture and surface roughness conditions: $0.09 < \theta_{\text{inc}} < 0.31$, $2.6 < kl < 19.7$ and $0.1 < k\sigma < 6.0$ and showed good agreement with the data. The model also performed well when tested against data measured for surfaces with parameters outside the above mentioned ranges. However,

at steep incidence angles, $\theta_{\text{inc}} < 20^\circ$ and for smooth surfaces there is a strong contribution from the coherent backscattering term that is not included in the model and the model therefore underpredicts the total backscattering. The rougher the surface the more negligible the coherent term becomes.

For soil water content θ estimation purposes an emission or scattering model is needed that is simple enough to invert but has a large range of validity. For the passive case the simplified theoretical radiative transfer approaches perform well, even when some of the parameters need to be estimated using semi-empirical approaches.

For the active case, the scattering of bare soil surfaces can be described by the theoretical IEM model which has a large range of validity but is in its most general form too complex to invert mathematically. Semi-empirical models such as Oh *et al.*, (1992) are simpler but have a limited range of validity. For vegetated surfaces, no satisfying simple model exist yet. Complex radiative transfer models are available and show acceptable results but require too much information beforehand. Simplified radiative transfer models that handle the vegetation in structure classes for instance might provide a solution to tackle the problem of vegetation influence. The more simple scattering models were shown to have a too small range of validity. The latter applied also to the empirical and semi-empirical approaches which range of validity was limited by the calibration set. *However, in this thesis only the scattering from bare soil surfaces was considered and where vegetation was present these data were eliminated and kept out of the analysis*

In Chapter 4 the inversion of the emission and microwave backscatter has been illustrated. The estimation of soil moisture from both active and passive microwave measurements requires several steps. The most important steps are the *inversion of the emission or scattering model* resulting in the surface dielectric properties ϵ and roughness and the *inversion of the soil dielectric mixture model* which inversion leads to a soil water content θ . No matter which model is taken *additional information is always needed*, of which the vegetation amount, vegetation type and soil textural composition are the most important.

In this thesis the inversion of the microwave emission model of Mo *et al.*, (1982) has been applied. The inversion of this simplified radiative transfer model is a straightforward and simple approach that combines physical understanding of microwave emission with a few empirical but general applicable parametrisations for roughness parameter h and vegetation parameters, b and θ_{veg} . In combination with the inversion of the dielectric model of Wang & Schmugge (1980) it is an effective inversion approach to retrieve soil moisture content θ from microwave brightness temperatures T_B .

For the active microwave case the results were less straightforward because of the higher sensitivity of the backscatter coefficient σ° to vegetation (structure) and surface roughness. Two models have been used in this study the inversion of the OSU model (INVOSU) and the inversion of the IEM model (INVIEM).

The INVOSU model (Oh *et al.*, 1992) is an empirical model based upon the knowledge of scattering behavior in the limiting cases (e.g. large $k\sigma$) using measured backscatter and ground truth data. The range of validity for this model is large: values for the

scaled roughness parameter $k\sigma$ should be in the range of 0.1 to 6 and for the kL in the range of 2.6 to 19.7. The model needs either HH and HV or VV and VH polarization.

The INVIEM model (van Oevelen & Hoekman, 1999; van Oevelen, 1998), is simple Look Up Table approach, applicable over a large range of surface roughness but does not take vegetation into account. The INVIEM model estimates a range of soil moisture values for an assumed range of roughness conditions using one single backscatter value. The HH and VV inversions are combined to narrow this range. Depending upon the roughness classes, *the sensitivity of the backscatter σ^0 on soil moisture content θ as predicted by the IEM model decreases with increasing soil moisture content*, which can result in large ranges of soil moisture content estimates.

Other inversions of the IEM model usually limit the roughness range for which the model can be used. The more empirical models such as Dubois *et al.*, (1985) can take into account some vegetation influence but are limited in their applicability over different surfaces and surface roughness types.

The *sensing depth* or *sampling depth* is the depth over which the sensor has retrieved a signal yielding information. It is this depth which is important, since it is the depth over which the soil water content θ can be directly estimated. The sensing depth is difficult to estimate because it depends on many factors such as temperature and water profiles, texture variations, surface roughness, angle of incidence etc.. Currently no satisfying model is available that gives reliable estimates of the sensing depth.

In Chapter 5 the data is summarised from the following experiments:

- HAPEX-EFEDA, Spain 1991 which provided C-, L- and P-band polarimetric data from the JPL-AIRSAR which in combination with the pivot irrigation systems enabled the detection of soil water content patterns over different depths, unfortunately the ground truth data set regarding soil water content was limited. The area consisted of irrigated and non-irrigated agricultural land in mediterranean climate.
- HAPEX-Sahel, Niger 1992 which provided both passive PBMR L-band radiometer data and active ERS-1 C-band SAR data along with extensive soil water content ground truth data. The area was sparsely vegetated and has a dry Sahelian climate.
- Little Washita River Watershed experiments in Oklahoma, USA 1992 and 1994 provided ESTAR L-band radiometer data and JPL-AIRSAR data along with extensive ground truth data. The region has large mainly non-irrigated agricultural areas in subhumid continental climate.
- NOPEX/Forest-Dynamo, Sweden 1994 and 1995 provided the C-, and L-band EMISAR data along with an extensive ground truth data set. The area is mixed forest and agricultural land in a maritime boreal climate.
The great number of experiments was needed because none of the experiments included all the necessary ground truth and remote sensing data to illustrate the objective of this thesis. Another problem existed in the availability and quality of the data which varied strongly.

In Chapter 6 the results are shown of various approaches to estimate soil water content

θ from both passive and active microwave data.

The strong relationship between the dielectric properties and microwave emission along with the relatively small influence of surface roughness makes the application of passive microwave data to estimate soil moisture very straightforward and has especially at the lower frequencies such as at L-band great potential for hydrological purposes. Between the brightness temperatures, T_B and soil moisture content, θ of the top 6 cm an approximately linear relationship is present. A problem exists with high vegetation cover and this is the area where considerable improvement can be made: better modelling of the vegetation influence, or a combination of more frequencies. The errors involved in the estimation of soil moisture using passive microwave remote sensing are small, i.e. usually less than 5% even for areas with moderate vegetation cover. *The standard error in the estimates (< 5%) is often lower than that of the ground truth measurements.*

The effects of surface roughness are small for the emission case, especially the influence of the surface correlation length is almost negligible. With respect to soil moisture estimation the effect can for most circumstances be accounted for by a simplified model like that of Choudhury *et al.*, (1979).

Although the L-band penetration of vegetation forms a physical limitation, the sensitivity to the soil moisture content as a function of vegetation water content is for L-band still present at a vegetation water content of 4 kg m⁻². For C-band this amount of vegetation content would already obscure the signal from the soil.

Extrapolation of the results to measurements from space would mean that the influence of mixed pixels due to the low resolution of approx. 30 km for L-band would increase. At that scale the effect of macroscale roughness would need more attention. The AMSR and AMSR-E, with C-band, will be the first radiometers that can provide more insight into the estimation of soil moisture from space with a spatial resolution of approximately 50 km although the vegetation would still be a significant problem. The planned L-band space-borne radiometer, SMOS (Soil Moisture and Ocean Salinity mission) will be a significant step towards operational use of microwave soil moisture estimates at the global scale.

In the active case the relationship between the dielectric properties and microwave backscatter is not as strong as in the emission case because of the larger influence of surface roughness and vegetation structure on the backscatter coefficient σ^0 .

The INVIEM model was applied to ERS-1 SAR data of Niger (HAPEX-Sahel) and the results compared with soil moisture content, θ measured over a depth of 6 cm. Although this depth is probably larger than the associated sensing depth of the instrument (about 2 cm) it is shown that the estimates are within the expected θ -range and that the in situ measured θ -values are consistently higher. The latter is expected because the surface layer of 0-2 cm is drier than the measured surface soil layer of 0-6 cm. The influence of soil texture on the ERS-1 retrieval results has been studied and is small compared to other effects such as speckle or vegetation.

JPL-AIRSAR data have been applied using data from Spain (EFEDA-Spain). Both the INVIEM model and INVOSU model could be applied because AIRSAR provides

polarimetric data. Overall, INVIEM as compared to INVOSU yields more reasonable estimates of soil moisture content as far as can be deduced from the limited ground truth data and visual inspection.

The advantage of using INVIEM over INVOSU is that it can be applied to both single polarization and polarimetric data. The INVOSU model requires no a priori knowledge about the surface characteristics except for information on the type of soil. INVIEM does require in its present form the input of surface roughness characteristics. At present, the applicability of both models is restricted to bare soils only and therefore is of limited practical use.

JPL-AIRSAR data have also been used in the Washita'94 experiment. A comparison along transect 2 between the TDR soil moisture measurements in the rangeland plot over a depth of 6 cm with the C-, L- and P-band INVIEM estimates shows good agreement for both C- and L-band. The root mean square error (RMSE) for C-, and L-band estimates is 3%. The P-band soil moisture estimates are consistently higher which is to be expected since these estimates represent an effective average soil moisture content over a larger depth than C-, and L-band.

The effects of the erosion contours on the in-situ soil moisture measurements cannot be seen in the AIRSAR soil moisture estimates. The AIRSAR spatial resolution of approximately 10 m is apparently too coarse to capture this variability of θ .

In Sweden the EMISAR data were used during the FOREST-Dynamo experiments. EMISAR soil moisture estimates generally underestimate the measured soil moisture content. This can be contributed to the fact that the IEM model doesn't account for periodicity or anisotropy in the surface roughness characteristics and therefore in these cases yields a lower backscatter coefficient σ^0 than actually measured. Furthermore, there might be an inconsistency between measured surface roughness and how it is represented in the model. The in situ measured RMS height and correlation length does not necessary resembles the radar backscattering relevant surface roughness. The backscattering is likely to be caused by a smoother subsurface. The sometimes poor agreement between estimated and measured soil water content might also be due to callibration errors in the EMISAR data. Especially since the C- and L-band flights were not simultaneously.

Both the C- and L-band estimates seem to agree better with the soil moisture measurements taken with the TDR rod at a shallower angle with respect to the surface, resulting in a measurement depth of about 2-3 cm. Most estimates are within 5% of the measurements. For all experiments *the standard error in the active microwave soil moisture estimates in absence of vegetation is often lower (<5%) than that of the ground truth measurements.*

The effects of surface roughness are in general stronger for the scattering case than for the emission case, especially the influence of the surface correlation length is almost negligible for the latter. For the scattering case the surface roughness is as important as the dielectric properties of the surface and therefore greatly limit the possibilities for soil moisture retrieval. Most models that describe surface scattering use the root mean square of the height differences along with the surface correlation length. Replacement of the latter with a more adequately responding parameter could

yield improvement in the behaviour and application of surface scattering models

The use of active microwave measurements to estimate soil moisture is not as straight forward as in the passive case. The models perform well as long as they are within their range of validity (regarding e.g. surface roughness and vegetation cover). Of the three bands used in the models the preferable wavelength is L-band because :

- it has a larger sensing depth and is less hampered by vegetation cover than C-band;
- is already available from space borne sensors like JERS-1 and SIR-C;
- is within a protected frequency allocation which is not the case for P-band.

P-band provides estimates over larger depths and is even less affected by vegetation which is more favorable for hydrological purposes. However for P-band the pure surface scattering approach is not valid because in a lot of cases soil volume scattering will be present. To account for this effect different models need to be developed which combine the surface scattering and volume scattering effects. Furthermore, the calibration of the airborne data is difficult and the data sometimes prove to be inconsistent due to human errors (e.g. software errors), which makes validation difficult. The lack of availability of P-band data (esp. the absence of space-borne P-band data) and the difficulty in validation of the results (conventional methods are unsuitable due to P-bands large sensing depth) make P-band currently less favourite over L-band. More research and data is needed to show the possibilities of P-band microwave remote sensing because it is the only band that has a sensing depth that comes near the root zone depth.

In general three problems areas need to be addressed if active microwave remote sensing can be used operationally to estimate surface soil water content.

- The effects of surface roughness at various scales needs to be better accounted for.
- The effect of vegetation (cover) needs to be accounted for. Vegetation, when using active microwaves, can seldomly be modelled as an attenuation layer as in the passive case. Current radiative transfer models are too complicated to be inverted, in addition the amount of input parameters needed to describe the vegetation is too large, even for a uniform vegetation cover within one resolution cell.
- Mixed pixels and in general the problem of 'upscaling' would make the operationalisation even more complex.

A multi temporal change detection approach in which the surface roughness and in specific cases also the vegetation can be regarded as a constant might provide a solution. Practically, this implies either lower resolutions from space borne sensors, or less spatial coverage.

In summary the high attainable resolution along with a good temporal resolution would make the active microwave remote sensing instruments a good addition to the passive sensors, under the condition that useful frequencies such as C-, L- or P-band are used. For many hydrological purposes a dual frequency L- and P-band fully polarimetric or multi-polarized system would be the most versatile, especially with a high temporal resolution.

Sensitivity analysis of soil moisture estimation of bare soil fields through Monte Carlo simulations provides a basis to assess the quantitative value of the spatial information provided by detailed remote sensing data. The advantage of remote sensing data, especially at high resolution is that a number of samples (i.e. pixels) can be used to obtain estimates with smaller random errors. This can be done by averaging over a limited number of pixels, at the price of degrading the spatial resolution. However, to avoid mixing measurements relating to different physical objects, this averaging can be performed over stationary heterogeneous targets only.

In general the average standard errors are larger for the individual pixel soil moisture estimates from Niger compared to those of Spain. However, if looked at the field estimates the error decreases significantly, i.e. even lower than those of the field estimates of Spain. For the field-based estimates there is almost no difference between the cases with speckle and without. For the pixel-based estimates even after averaging over a large number of pixels there is a constant difference of θ between the cases with and without speckle. *Speckle introduces thus an off-set or additional constant error in pixel-based soil moisture estimation.*

The comparison of ERS-1 soil moisture estimates with the PBMR soil moisture estimates shows that the trend seems to be in agreement but that certain fluctuations in the ERS-1 data are much stronger. The latter can be explained by the greater sensitivity of SAR data to other surface characteristics (e.g. vegetation) than soil moisture and these features can override the effect of soil moisture. It is shown that two different type of sensors can provide consistent results albeit within the restrictions of the boundary conditions of the models used, i.e. over spatially stationary homogeneous surfaces with low vegetation cover.

In Chapter 7 the use of the remotely sensed estimated soil water content θ with respect to the application in hydrological and meteorological models has been discussed. These applications of θ can vary from being initial or boundary conditions for the model or to calibrate and validate model performance. Data assimilation of directly measured parameters such as T_B and σ^0 instead of using the remotely sensed θ can be a more elegant and widely applicable approach of incorporating remotely sensed parameters in hydrological and meteorological models. Furthermore, an outlook is given on the use of microwave remote sensing data within hydrology and meteorology. With the launch of an L-band radiometer around 2005 it can be expected that real time applications of remotely sensed soil moisture will become operational. Other planned sensors and platforms such as PALSAR and ALOS will only strengthen this by adding new capabilities to already operational space-borne SAR instruments.

Samenvatting en conclusies

In de aardwetenschappen bestaat een grote behoefte aan globale data of in iedere geval data voor grote gebieden die op een andere wijze niet te bemeten zijn. Remote sensing is het gereedschap om dit doel te bereiken. In dit proefschrift is het gebruik van microgolf remote sensing om ruimtelijk bodemvocht te schatten onderzocht. Een algemeen raamwerk is ontwikkeld dat de verschillende stappen beschrijft die nodig zijn om bodemvocht af te leiden uit remote sensing metingen.

Bodemvocht is de schakel tussen de energiebalans aan het oppervlak en de waterbalans van de bodem en is daarom een cruciale parameter in de hydrologie en meteorologie van het landoppervlak. Het is lastig om bodemvocht te meten omdat het een grote variabiliteit in zowel ruimte als tijd heeft. Remote sensing metingen geven zowel de mogelijkheid om bodemvocht te schatten over grote oppervlakten als wel een geïntegreerde effectieve waarde over deze gebieden. De moeilijkheid bestaat in het valideren van deze schattingen omdat geen direct vergelijkbare grondmetingen beschikbaar zijn.

Het raamwerk om bodemvocht te schatten met behulp van passieve and actieve microgolf metingen bestaat uit vijf verschillende stappen:

- De eerste stap is het bepalen van de relatie tussen de bodemoppervlakte parameters en de waargenomen helderheidstemperatuur (radiantie) T_B of radar verstrooiingscoëfficiënt σ° ;
- De tweede stap is het beschrijven van de invloed van vegetatie op de relatie tussen T_B of σ° en de oppervlakte parameters;
- De derde stap is het bepalen van de relatie tussen de dielectriche eigenschappen, nl. de permittiviteit en de bodemparameters zodat het bodemvocht verkregen kan worden;
- De vierde stap is de relatie tussen het bodemvochtprofiel, heterogeniteit van de bodemeigenschappen en de bemonsteringsdiepte van de sensor;
- De vijfde en laatste stap is de assimilatie van het geschatte bodemvocht θ in hydrologische en meteorologische modellen.

In Hoofdstuk 2 wordt de relatie tussen de dielectriche eigenschappen en de bodemkarakteristieken bepaald en de basistheorie van dielectriche eigenschappen gegeven. De invloed van een electromagnetisch veld op verschillende materialen is uitgelegd, beginnende met een mono-atomisch gas en eindigend met meefase heterogene materialen zoals bodems.

Er bestaan vele modellen die de dielectriche eigenschappen bij microgolffrequenties beschrijven op basis van bodemcompositie en eigenschappen. De complexere model-

len zijn beter in staat om specifieke fenomenen te verklaren maar hiervoor is gedetailleerdere informatie nodig of zijn onrealistische aannamen (bijv. vorm van de deeltjes) nodig waardoor het gebruik in de praktijk weinig nuttig is.

De semi-empirische modellen zoals het model van Wang en Schumugge (1980) bepalen de effectieve of gemiddelde permitiviteit van een meerasemengsel aan de hand van de permitiviteit en volumefracties van de afzonderlijk componenten en een correctiefactor om de afwijkingen te corrigeren. Het gebruik van dit soort modellen heeft het nadeel dat ze gevoelig zijn voor de correctiefactor(en), dat de correctiefactor niet van tevoren bekend is en dat duidelijk afwijkend gedrag niet wordt meegenomen.

De theoretische modellen zoals het model van De Loor (1956) relateren het gemiddelde electromagnetische veld van het mengsel als geheel aan de electromagnetische velden van de inclusies en bepalen zo de gemiddelde permitiviteit ϵ van het mengsel. Het bestanddeel met de grootste volumefractie wordt als basis materiaal of continu medium genomen terwijl de andere bestanddelen dan als inclusies worden beschouwd. Volgens De Loor (1956) is het onmogelijk om een relatie te geven die de permitiviteit van een heterogeen mengsel beschrijft. Hij beweert dat in het meest gunstige geval de grenzen kunnen worden aangegeven waarbinnen de gemiddelde permitiviteit van het mengsel moet liggen. Deze grenzen kunnen dicht bij elkaar komen te liggen naarmate meer bekend is van het mengsel. Dobson *et al.*, (1985) hebben het model van De Loor aangepast en concludeerden dat het toevoegen van een gebonden watercomponent nodig was om de frequentie en bodemafhankelijkheid van de permitiviteit te verklaren. Verder verklaarden zij dat het model van De Loor een adequate beschrijving van de permitiviteit van bodems met bodemtextuur en bulkdichtheid was voor een frequentiebereik van 1.4 tot 18GHz.

De dielectrische eigenschappen zijn een functie van de frequentie en het is opvallend dat de meeste mengmodellen deze frequentie niet als parameter hebben maar in plaats daarvan geldig zijn voor een bepaald frequentiebereik waarbinnen de afhankelijkheid constant wordt beschouwd.

Het effect van bodemtextuur op de dielectrische eigenschappen is het duidelijkst voor kleibodems, met name die bodems met een hoge adsorptiecapaciteit waar het reële deel van de dielectrische eigenschappen lager is en het imaginaire deel hoger is (bij dezelfde θ) vergeleken met bodems met een grovere textuur. De bodemtextuur is ook van invloed op de bodemruwheid, echter dit effect wordt niet behandeld in dit proefschrift.

De theorie van de dielectrische eigenschappen van bodems behoeft nog steeds aandacht met name voor bodems met een afwijkende chemische compositie, zoals sterk ijzerhoudende bodems, gronden met een hoog zoutgehalte en kalkhoudende gronden. Voor een aantal van dit soort type bodems is het gedrag van de dielectrische eigenschappen sterk afwijkend en kan nog niet worden verklaard met de huidige modellen.

Voor de meeste toepassingen binnen de remote sensing is het gebruik van empirische mengmodellen, zoals het model van Wang en Schumugge (1980) en Dobson *et al.*, (1985), om de dielectrische eigenschappen te beschrijven voldoende. De fouten die gemaakt worden door het gebruik van deze empirische modellen zijn klein in verhouding tot andere foutenbronnen bij het schatten van bodemvocht met behulp van

microgolf remote sensing.

In Hoofdstuk 3 wordt de relatie tussen de oppervlaktekarakteristieken en de emissiviteit ϵ en verstrooiingscoëfficiënt σ^0 onderzocht. Twee vormen van verstrooiing zijn aanwezig wanneer men verstrooiing van natuurlijk terrein beschouwt, namelijk oppervlakteverstrooiing en volumeverstrooiing. Bij verstrooiing op de grens van een medium met een ander, zoals de grens tussen lucht en bodem, en als er geen bijdrage is van dieper doorgedrongen straling van dieperliggende lagen, spreekt men van oppervlakteverstrooiing. Volumeverstrooiing is het gevolg van inhomogeniteiten in het medium zelf, bijv. in een bodem of vegetatie.

De modellen voor volumeverstrooiing kunnen worden onderverdeeld in twee klassen: de coherente modellen, waarbij de fase en amplitude (of intensiteit) van de elektromagnetische straling wordt berekend; en de incoherente modellen waarbij alleen de amplitude wordt beschouwd. De incoherente modellen zijn wiskundig en rekentech-nisch eenvoudiger maar dit gaat ten koste van een lagere nauwkeurigheid. Het verschil tussen coherente en incoherente modellen is dat de fasen van de elektromagnetische golven in de coherente modellen worden meegenomen.

De theorie van stralingstransport behoort tot de groep van incoherente modellen en beschrijft het transport van straling door een medium of verscheidene media. De interactie tussen straling en de media wordt beschreven door transmissie, absorptie, emissie en verstrooiing van straling.

In het geval van passieve microgolf remote sensing, dus bij microgolf emissie geeft het gebruik van de theorie van stralingstransport goede resultaten. Het parametrische model van Mo *et al.*, (1982) en aangepaste versies hiervan zijn eenvoudige stralingstransportmodellen die effectief de straling van de bodem schatten zelfs bij aanwezigheid van vegetatie. Verstrooiing wordt in deze modellen als verwaarloosbaar beschouwd en alleen de volgende drie componenten worden meegenomen: bodememissie gedempt door vegetatie, emissie van de vegetatie zelf en de naar beneden gerichte emissie van vegetatie die door de bodem wordt gereflecteerd. Twee parameters in het model moeten worden geschat door middel van het gebruik van empirische modellen namelijk de bodemruwheid parameter h en de optische diepte τ .

In het geval van actieve microgolf remote sensing, dus bij microgolf verstrooiing, zijn de volume verstrooiing componenten en stralingstransport theorie te complex, dat wil zeggen dat er teveel a-priori informatie nodig is bij praktisch gebruik van de beschrijving van straling van natuurlijk terrein. De geldigheid van de oppervlakte verstrooiingsmodellen zoals "small perturbation method" of de "Kirchhoff" benaderingen, namelijk "geometrical optics and physical optics", wordt voornamelijk beperkt door de strenge randvoorwaarden ten aanzien van de eigenschappen van het oppervlak.

Het "Integral Equation Method" (IEM) model (Fung *et al.*, 1992) is een theoretisch oppervlakte verstrooiingsmodel dat poogt een meer algemeen geldende oplossing te geven dan de in de vorig alinea genoemde modellen. In de volledige vorm kan het model toegepast worden zonder beperking ten aanzien van ruwheidsschalen of frequenties. Het model is toepasbaar op natuurlijke oppervlakken maar voor inhomogene oppervlakken kan volume verstrooiing plaatsvinden en in deze gevallen voorspelt het model

een te lage verstrooiingscoëfficiënt. Een extra term dient te worden toegevoegd voor scheve oppervlakken en oppervlakken met een periodiciteit in de ruwheid, deze term is te vinden in Fung (1994).

Het semi-empirische model van Oh, Sarabandi & Ulaby (1992) (OSU) is een oppervlakte verstrooiingsmodel dat is getest voor een groot aantal bodemvocht- en oppervlakteruwheidsomstandigheden: $0.09 < \theta_{inc} < 0.31$, $2.6 < kl < 19.7$ en $0.1 < k\sigma < 6.0$ en gaf een goede vergelijking met de gemeten data. Het model gaf zelfs goede resultaten voor oppervlakken waarvan de parameters buiten het hiervoor genoemde bereik lagen. Echter bij kleine inkijkhoeken, $\theta_{inc} < 20^\circ$ en voor gladde oppervlakken is er een grote bijdrage van de coherente verstrooiingsterm die niet in het model is verwerkt en het model onderschat dan ook de total grootte van de verstrooiing. Des te ruwer het oppervlak des te kleiner en dus meer te verwaarlozen de coherente term wordt.

Voor het schatten van bodemvocht θ is een emissie- of verstrooiingsmodel nodig dat eenvoudig genoeg is om te inverteren en een groot geldigheidsgebied heeft. In het geval van passieve microgolf remote sensing voldoen vereenvoudigde stralingstransportmodellen, zelfs wanneer enkele van de parameters geschat dient te worden met behulp van semi-empirische modellen.

In het geval van actieve microgolf remote sensing kan de verstrooiing van kale bodemoppervlakken beschreven worden met behulp van het theoretische IEM model, dat een groot geldigheidsgebied heeft maar in de meest algemene vorm te complex is om te inverteren (uitgezonderd de Look Up Table benadering beschreven in dit proefschrift). Semi-empirische modellen zoals het model van Oh *et al.*, (1992) zijn eenvoudiger maar hebben een beperkt geldigheidsgebied. Voor met vegetatie bedekte oppervlakken is nog geen geschikt model aanwezig. Er zijn complexe stralingstransport modellen die redelijke resultaten boeken, maar deze vereisen te veel informatie vooraf. Om het probleem van vegetatie invloed op te lossen kunnen vereenvoudigde stralingstransportmodellen die bijvoorbeeld de vegetatie in structuur klassen behandelen een oplossing zijn. Er is aangetoond dat de meer eenvoudige verstrooiingsmodellen een te klein geldigheidsgebied hebben. Dit geldt ook voor de empirische en semi-empirische benaderingen waarbij het geldigheidsgebied is beperkt tot die van de calibratieset. *Echter, in dit proefschrift is alleen verstrooiing van kale bodemoppervlakken in beschouwing genomen en daar waar vegetatie aanwezig was in de data is deze verwijderd en buiten de analyse gehouden.*

In Hoofdstuk 4 wordt de inversie van emissie- en verstrooiingsmodellen behandeld. De schatting van bodemvocht met behulp van zowel passieve als actieve microgolf remote sensing behelst verscheidene stappen. De meest belangrijke zijn de inversie van het emissie- of verstrooiingsmodel wat leidt tot de dielectrische ϵ en ruweidseigenschappen van het bodemoppervlak en de inversie van het mengmodel leidt tot een bodemvocht θ . Welk model ook wordt gehanteerd, *additionele informatie is altijd nodig* waarvan met name de hoeveelheid vegetatie, vegetatietype en bodemtextuur de meest belangrijke zijn.

In dit proefschrift is de inversie van het microgolf emissiemodel van Mo *et al.*, (1982) toegepast. De inversie van dit vereenvoudigde stralingstransportmodel is een eenvoudige en directe benadering waarbij fysische kennis van microgolf emissie wordt

gekoppeld aan enkele empirische maar vrij algemeen geldende parametrisaties voor de ruwheidsparameter h en de vegetatie parameters, b en θ_{veg} . In combinatie met de inversie van het dielectrische mengmodel van Wang & Schmugge (1980) is het een effectieve inversie benadering om bodemvocht te schatten uit microgolf helderheids-temperaturen T_B .

In het geval van actieve microgolf remote sensing zijn de resultaten minder eenduidig vanwege de hogere gevoeligheid van de verstrooiingscoëfficiënt σ^0 voor vegetatie (structuur) en oppervlakteruwheid. Twee modellen zijn gebruikt in deze studie, de inversie van het OSU model (INVOSU) en de inversie van het IEM model (INVIEM).

Het INVOSU model is een empirisch model gebaseerd op de kennis van verstrooiingsgedrag in de limiterende gevallen (bijv. grote $k\sigma$) gebruikmakend van gemeten verstrooiings- en gronddata. het geldigheidsgebied van dit model is groot: waarden voor de geschaalde ruwheidsparameter $k\sigma$ moeten liggen tussen 0.1 en 6 en voor kL tussen 2.6 en 19.7. Het model maakt gebruik van of HH en HV of VV en VH polarizaties.

Het INVIEM model (van Oevelen & Hoekman, 1999; van Oevelen, 1998) is een eenvoudige Look Up Table benadering, toepasbaar over een groot bereik van ruwheidsparameterwaarden maar de effecten van vegetatie worden niet meegenomen. Het INVIEM model geeft voor een verstrooiingswaarde en een bepaald bereik van ruwheidswaarden een bereik van geschatte bodemvochtwaarden. De HH en VV inversie worden gecombineerd om dit bereik zo klein mogelijk te maken. Afhankelijk van de ruwheidsklassen neemt de gevoeligheid van de verstrooiingscoëfficiënt σ^0 voor bodemvocht zoals voorspeld door het IEM model af bij toenemende bodemvochtwaarden.

Andere typen inversies van het IEM model beperken in het algemeen het ruwheids geldigheidsgebied. De meer empirische modellen zoals het model van Dubois *et al.*, (1995) zijn ook nog toepasbaar bij een bepaalde hoeveelheid vegetatiebedekking, maar zijn in het algemeen beperkt in hun geldigheid voor verschillende typen oppervlakken en ruwheid.

De "sensing" diepte of bemonsteringsdiepte is de diepte waarover de sensor nog een signaal ontvangt dat bruikbare informatie bevat. Het is deze diepte die belangrijk is, omdat dit de diepte is waarover het bodemvocht direct geschat kan worden. De bemonsteringsdiepte is moeilijk te schatten omdat het van vele factoren afhankelijk is zoals temperatuur- en watergehalteprofielen, textuur variaties, oppervlakteruwheid, inkijkhoek etc.. Tot op heden is er nog geen goed bruikbaar model beschikbaar dat betrouwbare schattingen van de bemonsteringsdiepte geeft.

In Hoofdstuk 5 worden de data samengevat van de volgende experimenten:

- HAPEX-EFEDA, Spanje (1991) geeft C-, L- en P-band polarimetrische JPL-AIRSAR data die in combinatie met de aanwezigheid van roterende irrigatiesystemen het mogelijk maakt om bodemvocht patronen te schatten over verschillende diepten. Helaas is echter de hoeveelheid beschikbare en bruikbare gronddata erg beperkt. Het gebied bestaat uit geïrrigeerde en niet geïrrigeerde landbouw in een mediterrane klimaat.

- HAPEX-Sahel, Niger (1992) geeft zowel passieve PBMR L-band radiometer data en actieve ERS-1 C-band SAR data samen met een uitgebreide bodemvocht en gronddataset. Het gebied is schraal begroeid in een droog Sahel klimaat.
- Little Washita River Watershed experiment in Oklahoma, USA (1992, 1994) geeft ESTAR L-band radiometer data en JPL-AIRSAR data in combinatie met een uitgebreide gronddataset. Het gebied heeft voornamelijk niet geïrrigeerde landbouw en een subhumide landklimaat.
- NOPEX/Forest-Dynamo, Zweden (1994, 1995) geeft C- en L-band EMISAR data samen met een uitgebreide gronddataset. Het gebied bestaat uit gemengd bos en landbouw areaal in een maritiem boreaal klimaat.

Het grote aantal experimenten was nodig, omdat geen enkele van de bovengenoemde experimenten alle benodigde gronddata en remote sensing data bevatte om de doelstelling van dit proefschrift te illustreren. Een ander probleem was de beschikbaarheid en kwaliteit van de data die sterk wisselde.

In Hoofdstuk 6 worden de resultaten beschreven van de verschillende benaderingen om bodemvocht θ te schatten met behulp van zowel passieve als actieve microgolf data.

De sterke relatie tussen de dielectrische eigenschappen en microgolfemissie in combinatie met de relatief beperkte invloed van de bodemruwheid zorgt ervoor dat de toepassing van passieve microgolfddata om bodemvocht te schatten vrij recht toe recht aan is en in het bijzonder voor de lage frequenties zoals L-band grote mogelijkheden biedt voor hydrologische toepassingen. Er bestaat een vrijwel lineaire relatie tussen de helderheidstemperatuur T_B en bodemvochtgehalte θ van de bovenste 6 cm. Bij hoge vegetatiebedekking is er een probleem en het is dan ook hier waar nog vooruitgang geboekt kan worden: beter modelleren van de vegetatieïnvloed of een combinatie van meerdere frequenties. De fouten in het schatten van bodemvocht met passieve microgolfttechnieken zijn klein, d.w.z. in het algemeen minder dan 5% zelfs voor gebieden met een gematigde hoeveelheid vegetatiebedekking. De standaardfout in de schatting (<5%) is vaak lager dan die van de grondmetingen.

De gevolgen van oppervlakteruwheid zijn klein in het geval van microgolf emissie, de invloed van de oppervlakte correlatielengte is zelfs verwaarloosbaar. Voor het schatten van bodemvocht kan dit effect goed beschreven worden door een eenvoudig model zoals dat van Choudhury *et al.*, (1979).

De penetratie van L-band in vegetatie is onderhevig aan fysische grenzen, echter de gevoeligheid voor bodemvocht als een functie van het vegetatiewatergehalte is voor L-band nog steeds voldoende bij een vegetatiewatergehalte van 4 kg m^{-2} . Voor C-band zou deze hoeveelheid vegetatiewatergehalte al betekenen dat het signaal van de bodem verdwenen is.

Extrapolatie van de resultaten naar metingen vanuit de ruimte zou betekenen dat de invloed van "mixed pixels" zou toenemen als gevolg van de lage ruimtelijke resolutie van ongeveer 30 km voor L-band. Bij deze schaal wordt ook de macroruwheid van belang. De AMSR en AMSR-E, met C-band, zullen de eerste radiometers zijn met een ruimtelijke resolutie van ongeveer 50 km die inzicht kunnen verschaffen in de schatting

van bodemvocht vanuit de ruimte, ondanks de aanzienlijke invloed van vegetatie. De geplande L-band ruimteradiometer SMOS (Soil Moisture Ocean Salinity missie) zal een belangrijke stap in de richting worden van operationeel gebruik van microgolf bodemvochtschatten op globale schaal.

In het actieve geval is de relatie tussen de dielectrische eigenschappen en microgolfverstrooiing niet zo sterk als in het passieve geval, omdat de oppervlakteruwheid en vegetatiestructuur een grotere invloed hebben op de microgolfverstrooiingscoëfficiënt σ^0 .

Het INVIEM model is toegepast op ERS-1 SAR data van Niger (HAPEX-Sahel) en de resultaten zijn vergeleken met het bodemvocht gemeten over de bovenste 6 cm van de bodem. Hoewel deze diepte groter is dan de 'sensing' diepte die bij dit instrument wordt aangenomen (namelijk 2 cm) is aangetoond dat de schattingen binnen het verwachte θ -bereik liggen en dat de in-situ gemeten θ -waarden constant hoger zijn. Dit laatste is verklaarbaar omdat de bovenste laag van 0-2 cm normaal gesproken droger is dan de bemeeten laag van 0-6 cm. De invloed van bodemtextuur op de ERS-1 bodemvochtschatten is klein vergeleken bij de effecten van speckle en vegetatie.

JPL-AIRSAR data is toegepast met behulp van de gegevens van Spanje (EFEDA-Spain). Zowel het INVIEM model als het INVOSU model konden worden toegepast omdat AIRSAR beschikt over polarimetrische data. In het algemeen geeft het INVIEM model vergeleken met het INVOSU model meer aannemelijke schattingen van bodemvocht voor zover dat kan worden afgeleid uit de beperkte gronddata en visuele interpretatie.

Het voordeel van het INVIEM model over INVOSU is dat het kan worden toegepast op zowel enkelvoudig polarisatie als mede polarimetrische data. Het INVOSU model behoeft geen a-priori kennis ten aanzien van de karakteristieken van het oppervlak, behalve gegevens over het type bodem. INVIEM behoeft in de huidige vorm invoer van oppervlakteruwheden. Tot op heden is de toepassing van beide modellen beperkt tot kale bodems en ze zijn daarom beperkt in hun toepasbaarheid.

JPL-AIRSAR data zijn ook gebruikt in het Washita'94 experiment. Een vergelijking langs transect 2 in het 'rangeland' veld tussen TDR bodemvochtmetingen over een diepte van 6 cm en C-, L- en P-band INVIEM bodemvochtschatten geeft goede resultaten voor C- en L-band. De 'root mean square' (RMS) fout voor C- en L-band schatting is 3%. De P-band bodemvochtschatten zijn constant hoger, hetgeen te verwachten is omdat deze schattingen een effectief gemiddelde hoeveelheid bodemvocht voorstellen over een grotere diepte dan voor C- en L-band.

De effecten van erosiecontouren op de in-situ bodemvochtmetingen kunnen niet worden waargenomen in de AIRSAR bodemvochtschatten. De ruimtelijke resolutie van ongeveer 10 m van AIRSAR is blijkbaar niet hoog genoeg om deze variabiliteit van θ op te pakken.

In Zweden zijn de EMISAR data gebruikt tijdens de FOREST-Dynamo experimenten. EMISAR bodemvochtschattingen zijn in het algemeen te laag vergeleken bij de gemeten bodemvochtwaarden. Dit kan worden toegeschreven aan het feit dat het IEM model niet geschikt is voor periodiciteit of anisotropie in de ruwheidskarakteristieken en

daarom in deze gevallen een te lage verstrooiingscoëfficiënt σ^0 voorspelt dan werkelijk is gemeten. Daarnaast kan er ook nog een verschil zijn tussen de gemeten ruwheid en de wijze waarop deze is meegenomen in het model. De in-situ gemeten RMS hoogte en correlatielengte hoeven niet overeen te komen met de voor radarverstrooiing relevante ruwheidsmaten. De verstrooiing is waarschijnlijk veroorzaakt door een gladdere onderlaag. De soms slechte overeenkomst tussen geschat en gemeten bodemvocht kan ook nog worden veroorzaakt door callibratiefouten in de EMISAR data. Met name omdat C- en L-band niet gelijktijdig zijn gevolgen.

Zowel C- en L-band schattingen komen beter overeen met de bodemvochtmetingen genomen met de TDR probe die onder een vlakkere hoek ten opzichte van het oppervlak gestoken zijn, resulterend in een bemonsteringsdiepte van ongeveer 2-3 cm. De meeste schattingen liggen binnen 5% van de metingen. *Voor alle experimenten is de standaardfout in de actieve microgolf bodemvochtschattingen in afwezigheid van vegetatie vaak lager (<5%) dan de grondmetingen.*

De effecten van oppervlakteruwheid zijn in het algemeen groter in het geval van verstrooiing dan in het geval van emissie, met name voor de laatste is de invloed van de oppervlaktecorrelatielengte verwaarloosbaar. De mogelijkheden voor bodemvochtbepaling worden sterk beperkt in het geval van verstrooiing omdat de oppervlakteruwheid net zo belangrijk is als de dielectrische eigenschappen van het oppervlak. De meeste modellen die de verstrooiing aan het oppervlak beschrijven gebruiken de RMS van de hoogteverschillen en de oppervlaktecorrelatielengte. Vervanging van met name de laatstgenoemde parameter door een meer geschikte, meer gevoelige parameter zou het gedrag en toepassing van oppervlakteverstrooiingsmodellen kunnen verbeteren.

Het gebruik van actieve microgolfmetingen om bodemvocht te schatten is niet zo eenduidig als in het passieve geval. De modellen presteren goed binnen hun geldigheidsbereik (aangaande oppervlakteruwheid en vegetatiebedekking). Van de drie in de modellen gebruikte banden heeft L-band op dit moment de voorkeur omdat:

- het een grotere 'sensing' diepte heeft en vergeleken met C-band minder door vegetatie belemmerd wordt;
- het al beschikbaar is vanuit de ruimte met sensoren zoals: JERS-1 en SIR-C;
- het in een beschermd frequentiegebied ligt hetgeen niet geldt voor P-band.

P-band geeft schattingen over grotere diepten en wordt zelfs nog minder door vegetatie belemmerd, wat voor hydrologische toepassing de voorkeur heeft. Echter voor P-band is een pure oppervlakteverstrooiings benadering niet geldig omdat in veel gevallen volumeverstrooiing plaatsvindt. Om dit effect mee te nemen moeten andere modellen ontwikkeld worden die zowel oppervlakte als volumescattering combineren. Verder is de calibratie van vliegtuigmicrogolfddata lastig en de data blijken soms niet consistent te zijn vanwege menselijke fouten (bijv. fouten in de software), wat de validatie moeilijk maakt. Het gebrek aan P-band data (en met name het ontbreken daarvan vanuit de ruimte) en de moeilijkheid van de validatie van de resultaten (conventionele methoden zijn ongeschikt vanwege de grote 'sensing' diepte van P-band) zorgen dat P-band tot op heden minder favoriet is vergeleken met L-band. Meer onderzoek en gegevens zijn nodig om de mogelijkheden van P-band microgolf remote sensing aan te tonen, omdat het de enige band is met een 'sensing' diepte die in de buurt komt van de diepte van de wortelzone.

In het algemeen zijn er drie probleemgebieden die aangepakt moeten worden voordat actieve microgolf remote sensing operationeel gebruikt kan worden om bodemvocht aan het oppervlak te schatten.

- De effecten van oppervlakteruwheid op verschillende schalen moet beter worden beschreven en meegenomen.
- De effecten van vegetatie (-bedekking) moet meegenomen worden. Vegetatie kan, in het geval van actieve microgolven, zelden gemodelleerd worden als een dempingslaag zoals in het passieve geval gebeurt. Huidige stralingstransportmodellen zijn te complex om te inverteren. Daarnaast is de hoeveelheid invoerparameters nodig om de vegetatie te beschrijven te groot, zelfs voor uniforme vegetatiebedekking binnen een resolutiecel.
- Mixed pixels (gemengde beeldelementen) en in het algemeen het probleem van opschaling maken operationalisering nog complexer.

Een oplossing zou een benadering kunnen zijn die gebruik maakt van multitemporele veranderingsdetectie waarbij de oppervlakteruwheid en in bepaalde gevallen ook de vegetatie als constant kunnen worden beschouwd. In de praktijk betekent dit ofwel lagere ruimtelijke resolutie vanuit de ruimte of wel een lagere bedekkingsgraad.

Samenvattend kan men stellen dat de hoger haalbare ruimtelijke resolutie in combinatie met een goede temporele resolutie ervoor zorgen dat actieve microgolfinstrumenten een goede aanvulling zijn op de passieve instrumenten, onder de voorwaarde dat bruikbare frequenties zoals C-, L- en P-band gebruikt worden. Voor de meeste hydrologische toepassingen zou een combinatie van een volledig polarimetrisch of multipolarisatie L- of P-band systeem het meest geschikt zijn, met name bij een hoge temporele resolutie.

Een gevoeligheidsanalyse van bodemvochtschattingen van kale bodems door middel van Monte Carlo simulaties geeft een basis om de kwantitatieve waarde te bepalen van de ruimtelijke informatie van gedetailleerde remote sensing data. Het voordeel van remote sensing data, met name bij een hoge ruimtelijke resolutie is dat het aantal elementen (pixels) gebruikt kan worden om schattingen te verkrijgen met kleinere random fouten. Dit kan worden bewerkstelligd door het middelen over een beperkt aantal elementen ten koste van een lagere ruimtelijke resolutie. Dit middelen kan alleen worden gedaan over stationaire heterogene doelen zodat er geen menging plaatsvindt van metingen die aan verschillende fysieke objecten gerelateerd zijn.

In het algemeen zijn de gemiddelde standaardfouten groter voor de individuele pixel bodemvochtschattingen van Niger vergeleken met die van Spanje. Bij vergelijking van de schattingen op veldbasis wordt de fout beduidend lager, zelfs lager dan de schatting op veldbasis van Spanje. Voor de schatting op veldbasis is er nauwelijks verschil tussen die gevallen met of zonder speckle. Voor de individuele pixel schatting is er een constant verschil van θ tussen de gevallen met en zonder speckle. *Speckle introduceert dus een off-set of additionele constante fout in de schatting op individuele pixelbasis.*

De vergelijking van ERS-1 bodemvochtschatting met de PBMR bodemvochtschattingen laten zien dat de trend tussen beide overeenkomt maar dat de fluctuaties in ERS-1 data veel meer fluctueert. Dit laatste kan verklaard worden door de grotere

gevoeligheid van SAR data voor andere oppervlaktekarakteristieken (bijv. vegetatie) dan bodemvocht en dat deze kenmerken sterker zijn dan het effect van bodemvocht. Er is aangetoond dat twee verschillende typen sensoren consistente resultaten kunnen geven, al is het dan wel binnen de grenzen van de modellen die gebruikt zijn, d.w.z. over ruimtelijk stationaire homogene oppervlakken met lage vegetatiebedekking.

In Hoofdstuk 7 is het gebruik van remote sensing bodemvochtschattingen θ in het kader van toepassingen in hydrologische en meteorologische modellen geplaatst. Deze toepassing van θ kan variëren van gebruik als initiële of randvoorwaarde voor het model tot het calibreren en valideren van modelresultaten. Data-assimilatie van direct gemeten parameters zoals T_B en σ^0 in plaats van met behulp van remote sensing geschatte θ is een elegantere en breder toepasbare benadering van gebruik van remote sensing parameters in hydrologische en meteorologische modellen. Verder is nog een blik op de toekomst geworpen ten aanzien van het gebruik van microgolf remote sensing binnen de hydrologie en meteorologie. Met de lancering van een L-band radiometer rond 2005 mag men verwachten dat 'real time' toepassingen van met remote sensing bepaald bodemvocht operationeel gaat worden. Andere geplande sensoren en platformen zoals PALSAR en ALOS zullen alleen maar bijdragen aan deze ontwikkeling door het toevoegen van nieuwe mogelijkheden aan de al operationele SAR instrumenten in de ruimte.

Appendix A

Determination of dielectric properties of materials

A.1 Time domain reflectometry

Time domain reflectometry has become a popular way of determining indirectly soil moisture since the beginning of the 1980's. It is based on the principle that electromagnetic waves are attenuated in soils, depending on their dielectric properties. These properties are considerably influenced by the soil water content (Topp *et al.*, 1980; Heimovaara, 1988). Time domain reflectometry is a relatively fast and easy method to perform in situ soil moisture measurements. It is almost non destructible, non hazardous and accurate especially when calibrated for the soils under investigation. For an overview of other methods to determine soil moisture content the reader is referred to Schmugge *et al.*(1980) and Stafford (1987).

Time domain reflectometry uses an electromagnetic pulse which is sent through a transmission line. The propagation velocity of the electromagnetic wave or pulse is measured by detecting the reflected pulse from the end of the line and measuring the delay time between transmitted and reflected pulse. The dielectric constant can be found by applying the following equations. The speed of a pulse or the wave velocity in a transmission line or a medium of permittivity ϵ and permeability μ is: .

$$v = \frac{c_0}{\sqrt{\epsilon\mu}} \quad (\text{A.1})$$

It is usually assumed that the soil has $\mu = \mu_0 = (c_0^2\epsilon_0)^{-1}$ (c.f. Eq. C.5), i.e. the soil is non-magnetic (this may not always be the case).

If the length l of the transmission line is known then the wave velocity can be deduced from the measured time difference Δt , i.e. the time between sending the pulse and receiving the reflected pulse: .

$$v = \frac{2l}{\Delta t} \quad (\text{A.2})$$

Combining Eqs. A.1 and A.2 gives the apparent dielectric constant:

$$\epsilon_a = \left(\frac{c_0 \Delta t}{2l} \right)^2 \quad (\text{A.3})$$

The apparent dielectric constant will approach the true value of the permittivity of the mixture only if the medium is not dispersive, i.e. their dielectric behaviour varies with varying frequency. Since wet soils are generally dispersive at frequencies in the low gigahertz range (Hoekstra & Delaney, 1974) the TDR pulse should contain no such frequencies by the time it returns from the end of the transmission line (Smith & Tice, 1988). This can be achieved by using a relatively slow rise time of the pulse, e.g. 140 ps, resulting in hardly any frequencies above 800 MHz and making the length of the transmission line exceed 20 cm such that low frequencies dominate the reflection because the high frequencies are dispersed along the line (Smith & Tice, 1988). Compared to the dielectric probe discussed in the next paragraph time domain reflectometry is more accurate and sensitive, but provides results over a smaller range of frequencies.

A.2 Other methods

There are numerous methods to determine the permittivity of a material. They all have there strong and weak points depending on the type of material, frequency range, accuracy and rapidness required. In this paragraph three of the most popular methods will be briefly discussed.

The first method uses an open ended coaxial probe. This probe is an coaxial line that ends abruptly at the tip, which is in contact with the material under investigation (Gabriel & Grant, 1989; Engelder & Buffler, 1991). The signal reflected from this interface can be related to the materials dielectric properties. This method is relatively fast, easy to use and gives information over an large frequency range (e.g. 200 MHz - 20 GHz, other ranges are also possible). A disadvantage is that it has a limited accuracy especially for materials with low permittivities, but for most purposes it is more than adequate. An important restraint is that the probe surface must have full contact with the material under test. Small irregularities like air cavities, when they are not a constituent of the material, will influence the measurements greatly.

The second method is based upon resonant cavities. These cavities resonate at a known microwave frequency. When a small sample of a material is put inside this cavity it will change the amount of microwave energy that is absorbed, reflected and transmitted and thus change the resonance frequency of the cavity. Using a network analyzer one can detect these changes and calculate the dielectric properties of the material. By using resonant cavities it is possible to get very accurate information, however only at one particular frequency on the dielectric properties even for very low values of ϵ'' . Other disadvantages of the method are that resonant cavities are difficult to design and use (Engelder & Buffler, 1991).

A third method is based upon the transmission line theory like TDR, but is now capable of providing information over the whole frequency spectrum. A network analyzer generates a signal and measures the amount of energy reflected and transmitted through the material that is placed inside the transmission line. Subsequently the permittivities can be determined. This method is more accurate and sensitive than the coaxial probe method but it is less suited for lower frequencies and it has a narrower range of frequencies. The measurements are also more time consuming and more difficult.

The last method mentioned here is naturally the use of remote sensing instruments, especially microwave instruments, to determine the dielectric properties of the soil surface. In the next chapter a more thorough treatment on the use of these instruments is given. Derivations and inversion of soil dielectric mixture models

Appendix B

Platform and Sensor Description

The data give in this appendix is in part from Morain and Budge (1997) and Kramer (1994).

B.1 Space-borne platforms and sensors

B.1.1 ERS

The European Remote Sensing (ERS) satellite has been developed and operated under auspices of the European Space Agency (ESA). The satellite has various types of instruments. The ERS-SAR and the wind scatterometer (WSC) are part of the active microwave instrument (AMI) which has four antennas (three for the windscatterometer and one for the SAR). The SAR and the WSC cannot operate simultaneously since certain instruments of the AMI are shared by both sensor systems. Two ERS platforms have been launched and its successor will be ENVISAT

Mission Objectives

ERS-1 is intended for global measurements of sea wind and waves, ocean and ice monitoring, coastal studies, and limited land sensing. ERS-2 will augment the land sensing capabilities by adding three visible channels.

*System Characteristics***ERS-1**

Launch:	
Date:	1991
Vehicle:	Ariane V44
Site:	Kourou, French Guiana
Orbit:	
Altitude:	782-785km
Type:	LEO, sun-synchronous (13 orbits/day)
Inclination:	98.52
Revisit:	35 days (501 revolutions) 6 days at 60°latitude
Coverage:	Global
Equatorial crossing:	10:15
Period:	100 minutes
Stabilization:	3 axis
Dimensions:	
Mass:	2384kg MS
Size:	11.8m x 11.7m x 2.4m
	Solar paddles: 2.4m x 5.8m
Instruments:	AMI-SAR, RA, ATSR, PRARE ¹ , MS
Design lifetime:	3 years
Prime Contractors	Dornier, Deutsch Aerospace

Data Availability

There is world-wide cooperation in data reception and exchange. Data processing and archiving facilities are located in France, Italy, the UK, and Germany. In 1992 ESA authorized three data distributors: RADARSAT (Ottawa, for Canada and USA); Eurimage (Rome, Italy for Europe, North Africa and Middle East); and SPOT Image (Toulouse, France for remainder of world).

B.1.2 AMI-SAR*Sensor Description*

Active Microwave Imager-Synthetic Aperture Radar (AMI-SAR) operates as a synthetic aperture radar and as a wind/wave scatterometer

;

Data Availability

Data are down-linked to Kiruna, Sweden; Gatineau, Canada; and Maspalomas, Canary Islands (Spain). Image data are normally collected only 7.5 minutes on each 90

1. PRARE is used for accurate orbit determination in support of RA. It failed after 3 weeks in orbit.

Table B.1: ERS SAR instrument characteristics

Dates of Operation:	1991-
Primary Mission:	Measure wind speed and direction; monitor ocean waves, land resources, and sea ice
Owner/ Operator/ Platform:	European Space Agency/ Centre National d'Etudes Spatiales/ ERS-1
Contractor:	Marconi Space Systems
Power/ Mass:	ND/ ND
Data Rate/ Duty Cycle:	105Mbps (image mode), 370kbps (wave mode)/ 79.5 minutes per orbit; ~10% image mode, 70% wave mode; max along-track coverage per orbit = 4000km
Antenna Description:	Wind scatterometer = 3 antennas (mid 0.35m x 2.3m; fore and aft 0.25m x 3.6m)
Swath (Scan Angle):	80.4km - 99km (20.1° - 25.9° θ_{inc} range) imaging and wave modes; 500km (scatterometer mode); FOR = 250km right side of nadir
Pulse Description/ Data	
Precision and Accuracies:	ND
Frequencies	5.3 GHz 5.66 cm, C-band V V polarization
Band-width	15.55 MHz
Radiometric Resolution	2.5dB at -18dB (scatterometer mode); 5 bit quantization (image mode) 8m-200m (processing dependent)
Spatial Resolution	nominally 30m for image and wave modes and 50 km for wind scatterometer; geolocation \pm 1km
Calibrations/ Corrections:	Wavelength accuracy of $\pm 25\%$ over 100m - 1000m Direction accuracy of $\pm 20^\circ$ for wave scatterometer. Wind scatterometer data can be analyzed with $\pm 20^\circ$ accuracy for wind vectors from 4m - 24ms ⁻¹ and 0° - 360° at incidence angles between 27 - 58°

minute orbit; 72 minutes are used for the "wind/wave" mode. The ERS-1 Help Desk, Frascati, Italy serves as the central user service facility. North American AMI-SAR image products are available through RADARSAT, Richmond, B.C. and through the University of Alaska SAR Facility at Fairbanks, AK.

The ERS SAR is a single frequency and polarization radar operating at C-band (5.3 GHz) and VV-polarization. The spatial resolution of the instrument is approximately 25m and the precision image data are delivered with a pixel size of 12.5m and the number of looks is three. The look angle of the instrument at the center of the swath is 23°.

Windscatterometer

The ERS Wind scatterometer (WSC) was designed to obtain information on wind speed and direction over the sea surface. It operates by measuring the variation in the radar reflectivity of the sea as a function of look angle due to the presence of small ripples made by the wind close to the water surface. The instrument consists of 3 antennas producing 3 beams looking 45° forward, sideways and 45° backwards with respect to the satellite's flight direction. These beams continuously illuminate a 500 km wide swath as the satellite moves along its orbit. Across the swath local incidence angles range from 18-47° for the mid beam and 25-59° for the forward and aft beams, and 19 measurements are made across the swath. Thus three backscatter measurements at each grid point are obtained at different viewing angles and separated by a short time delay. These triplets are then used routinely to extract wind speed and direction over sea surfaces through the use of mathematical models. Measurements are also made over land surfaces and these triplets can therefore be used to retrieve surface parameters over land.

The Wind Scatterometer has a spatial resolution of the order of 45 km along and across track with a radiometric stability of <0.57 dB, and a localisation accuracy of better than 5 km. The operating frequency is 5.3 GHz with vertical transmit and receive (VV) polarization (See Table B.1).

B.1.3 JERS

Japan Earth Resources Satellite (JERS) with the L-band Synthetic Aperture Radar (JERS-SAR) is developed and operated under auspices of the Japanese Space Agency (NASDA)

Mission Objectives:

The main purpose of JERS-1 is to observe Earth's entire land area, including Antarctica. It is expected to obtain data useful for land survey, agriculture, forestry, fisheries, environmental protection, disaster prevention, and coastal monitoring.

System Characteristics

JERS-1

Launch:	
Date:	1992
Vehicle:	H-1
Site:	Tanegashima
Orbit:	
Altitude:	568km
Type:	LEO, sun-synchronous
Inclination:	97.7°
Revisit:	44 days (659 revolutions)
Coverage:	Global
Equatorial crossing:	10:30 - 11:30 AM
Period:	96 minutes
Stabilization:	4 reaction wheels, magnetorquers, gyros for 0-momentum attitude control; Earth and sun sensors provide 0.3° accuracy
Dimensions:	
Mass:	1340kg bus: 840kg instruments: 500kg
Size:	0.93m x 1.83m x 3.16m (w/o SAR antenna & solar panel deployment) SAR antenna and panels: 11.9m x 2.4m
Instruments:	SAR, OPS (VNIR, SWIR)
Design lifetime:	2 years
Prime Contractors	Mitsubishi Electric w/ NEC, Toshiba; JAROS

B.1.4 JERS-1 SAR

Data Availability:

For information contact Remote Sensing Technology Center of Japan, Uni Roppongi Bldg., 1-9-9, Roppongi, Minato-ku, Tokyo 106, Japan. JERS-SAR data are

Table B.2: JERS-1SAR instrument characteristics

Dates of Operation:	1992 -
Primary Mission:	Geology
Owner/ Operator/ Platform:	Japan/ National Space Development Agency of Japan/JERS-1
Contractor/Prinicipal Participants:	JAROS; NASDA
Sensor Description	JERS-SAR is an L-band system
Power/ Mass:	1.3kW/ ND
Data Rate/ Duty Cycle	onboard storage = 72Gb/max along-track coverage per orbit = 9000km
Antenna Description	11.9m X 2.4m
Swath (Scan Angle):	75km (35° incidence angle)
Pulse Description/ Data	
Precision and Accuracies:	PPS = 1500
Frequencies	1.275 GHz L-band, HH polarization, SNR ~6dB
Band-width	15MHz
Radiometric Resolution	noise equivalent scattering coefficient -20.5dB
Spatial Resolution	Azimuth 18m (3 looks); Range 18m; geolocation 100m
Calibrations/ Corrections:	Radiometric calibration accuracy < 1dB

recorded onboard and transmitted via 8.15GHz and 8.35GHz to NASDA/EOC (Hofu, Japan), Tokai University (Kumamoto, Japan), National Institute of Polar Research (Syowa, Antarctica), Alaska SAR Facility (Fairbanks, Alaska), CCRS/Canada (Gatineau, Prince Albert), ESA (Kiruna, Sweden; Fucino, Italy; Mas Palomas, Gran Canaria), National Research Council of Thailand (Bangkok, Thailand), and Australian Center for Remote Sensing (Belconnen, Australia)

B.1.5 LANDSAT

System Characteristics

	Landsat-1, -2, -3	Landsat-4,-5	Landsat-7
Launch:			
Date:	1972, -75, -78	1982-84	1998
Vehicle:	Delta	Delta	Delta II
Site:	Vandenberg	Vandenberg	Vandenberg
Orbit:			
	L1 = 907 km		
Altitude:	L2 = 908 km	705km	705 km
	L3 = 915 km		
Type:	LEO, sun-synchronous	LEO, sun-synchronous	LEO, sun-synchronous
Inclination:	99°	98.2°	98°
	L1=18 days		
Revisit:	L2 < 12 day revisit	16 days	16 days
	L3 < 12 day revisit	(233 orbits)	(233 orbits)
Coverage:	Global	Global	Global
	(81° N & S latitude)		
Equatorial crossing:	L1 = 8:50 am		
	L2 = 9:08 am	9:45 am	10:00 am
	L3 = 9:31 am		
Period:	103 min	99 min	ND
	(14 orbits/day)	(14 orbits/day)	
Stabilization:	±1.0°,	Gyro	3-axis
	±1.0° orbital plane (yaw)	Earth oriented	to within 0.05°
Dimensions:			
Mass:	953kg	2200kg	2200kg
Size:	3m x 1.5m	2m x4m	2.8m x 4.3m
	with 4m solar paddles		
Instruments:	MSS, RBVGE	MSS, TM	ETM+
Design lifetime:	1 year minimum	3 years	5 years
Prime Contractors	Hughes, SBRC	GE,Hughes, SBRC	Lockheed/ Martin, Hughes, SBRC

Program Objectives

The Landsat (Originally Earth Resources Technology Satellite - ERTS, USA) program grew out of NASA's Earth Resources Survey Program with the collaboration and shared resources of other Federal agencies. First known as the Earth Resources Technology Satellite (ERTS-1), Landsat-1 was the "proof-of-concept" that Earth-orbiting satellites could effectively monitor natural and cultural resources. Subsequent Landsats have continued to define spectral and spatial requirements for next generation sensors and stimulated research to determine optimum data processing and interpretation. Quickly after launch of Landsat-1 in 1972, quasi-operational uses for synoptic Earth data began to emerge. To accommodate this "instant" success,

Congress moved the "ground segment" responsibility first to the USGS EROS Data Center in Sioux Falls, and shortly thereafter, to the Department of Commerce. In late 1985 Congress privatized both the "space" and "ground segments" by transferring responsibility to EOSAT Corporation; but in 1992 returned federal control to NASA and DOD. Landsat-6 failed to achieve orbit in 1993. Landsat-7 is a joint effort by NASA (provider), NOAA (operator) and USGS (archivist)

Instruments

MSS: The Multispectral Scanner is a 4-channel whisk-broom optical mechanical instrument that provides 80m ground resolution on a 16-18 day revisit cycle. Although based on 1960s technology, it provided humankind's first synoptic imagery of the globe from low Earth orbit.

RBV: The Return Beam Vidicon was a three-camera video system designed for what was then regarded as high accuracy cartographic mapping data. It was a successful proof-of-concept instrument, but one that was eclipsed in the science community by the more versatile and popular MSS.

TM: Thematic Mapper is a 7-channel whisk-broom scanner providing 30m ground resolution. It offers an order-of-magnitude improvement in spectral and spatial data collection for Earth resources.

ETM and ETM+: Enhanced Thematic Mapper was designed as a sensor improvement for Landsat-6, but never achieved orbit. Its conceptual successor, ETM+, is designed as a 4-channel VNIR and 2-channel SWIR sensor having 30m ground resolution; a panchromatic, 15m channel; and a 2-channel LWIR having 60m resolution.

Table B.3: LandsatTM sensor characteristics

Dates of Operation:	1982 –
Primary Mission:	Monitor Earth resources
Owner/ Operator/ Platform:	USA/ NASA, EOSAT Corp./ Landsat-4, -5
Contractor/ Principal Participants:	Hughes Santa Barbara Research Center
Power/ Mass/:	385W (peak)/ 258kg/
Data Rate/ Duty Cycle	85Mbps/ 100%
	Channel 1-5:16 detectors/channel = Si
Detector Technology:	Channel 6: 4 detectors = HgCdTe
	Channel 7: 16 detectors = InSb
Swath (Scan Angle):	FOV = 15.39°, 185km at 705km altitude

B.1.6 LANDSAT TM

Thematic Mapper (TM)Heritage = MSS

Sensor Description

TM is a 7-channel scanning radiometer. Scene energy is collected in both directions cross-track while spacecraft forward motion provides the scan along-track. Light reflected from the scan mirror is directed to a 40.6cm clear aperture Ritchey-Chretien telescope with $f_l = 243\text{cm}$. The variation in radiant flux passing through the field stop onto the detectors creates an electrical output that represents the radiant history of the line.

Detectivity/ Accuracy/ Precision/Stability

Table B.4: Radiometric Performance of the Landsat TM sensor

Spec.			Meas.	
			L-4	L-5
NE $\Delta\rho$	1.	0.8%	0.16	0.16
	2.	0.5%	0.18	0.21
	3.	0.5%	0.20	0.23
	4.	0.5%	0.19	0.22
	5.	1.0%	0.23	0.25
	7.	2.4%	0.41	0.37
NE ΔT	6.	0.5°C (300-320K)	0.12	0.13

Calibrations/ Corrections:

Three radiance controlled tungsten filament lamps are used for the reflective channels, and a blackbody, controllable to three known temperatures, is used for the thermal band. A black surface of known temperature provides the source for a dc-restoration of all bands. The calibrator is an oscillating shutter mechanism that is synchronized with the scan mirror to bring the calibration sources sequentially into view of the detectors during each scan-mirror turnaround.

Table B.5: Landsat-TM instruments channel characteristics				
Channel	Spectral Channels/ Frequencies	Band-width	Radiometric Resolution	Spatial Resolution
1	0.45μm - 0.52μm	70nm	8 bit quantization	30m
2	0.52μm - 0.60μm	80nm		30m
3	0.63μm - 0.69μm	60nm		30m
4	0.76μm - 0.90μm	140nm		30m
5	1.55μm - 1.75μm	200nm		30m
6	10.40μm - 12.50μm	2.10μm		120m
7	2.08μm - 2.35μm	270nm		30m
Interband registration				= 0.1 IFOV

Data Availability:

EOSAT, 4300 Forbes Blvd., Lanham, MD 20706-9954, (301) 552-0537; USGS EROS Data Center, Sioux Falls, SD 57198, (605) 594-6099,

DAAC URL: <http://sun1.cr.usgs.gov/landdaac/landdaac.html>

B.1.7 Space Shuttle

Program Objectives

NASA's Space Shuttle system remains the most technologically advanced and complex machine on Earth. Its major components are: the orbiter spacecraft; the three main engines; the external tank that feeds the main engines; and the two solid rocket boosters. The orbiter is the heart of the Space Transportation System. About the same size and weight as a DC-9 aircraft, the orbiter contains the pressurized crew compartment which can carry up to seven crew members, the cargo bay, and the three main engines mounted aft. The Space Shuttle's cargo bay is designed for versatility. Large enough to accommodate a tour bus 18.28m x 4.57m, the cargo bay carries satellites, spacecraft, and Spacelab scientific laboratories to and from Earth orbit. Although there are numerous Shuttle missions and a variety of Earth observation experiments, data are not necessarily gathered continuously over every orbit, throughout each mission, or throughout the life of the phenomenon being recorded.

System Characteristics

Launch:

Date: various
Vehicle: Orbiters Discovery, Challenger, Endeavor, Atlantis, Columbia
Site: Cape Canaveral

Orbit:

Altitude: ca. 300km
Type: LEO, equatorial
Inclination: $\pm 57^\circ$
Revisit: NA
Coverage: Global
57° N & S latitude

Equatorial crossing: Instruments:

Period: 90 minutes

Stabilization: ND

Dimensions:

Mass: 98,500kg (variable)
Size: 17.2m x 40m w/23.6m wingspan
Instruments: Variable (mission specific)
Design lifetime: Reusable (mission life 1 - 3 weeks)

B.1.8 SIR-C

Shuttle Imaging Radar-C (SIR-C/X-SAR)(aka SRL-1, -2)

Sensor Description

SIR-C/X-SAR operates simultaneously at three frequencies. The antenna design is a new generation that allows the radar beams to be steered electronically without physically moving the antenna. The footprint remains illuminated for up to 0.5 seconds

during which time it is irradiated with 600-900 pulses. The "synthetic" length of the antenna is the distance traveled by the spacecraft during the period of illumination. The longer the synthetic antenna (aperture), the better the ground resolution after data processing. The two missions in 1994 (SRL-1, -2) were designed to collect seasonal data over the same sites for discipline oriented research.

Dates of Operation:	1994
Primary Mission:	Provide calibrated data to compare with ERS-1, JERS-1, and RADARSAT to obtain time series data of geophysical attributes; provide multifrequency radar images
Owner/ Operator/ Platform:	USA/ NASA/ Space Shuttle Endeavor (STS-59, STS-68)
Contractor/ Principal Participants:	Jet Propulsion Laboratory (SIR-C); Div. (Antenna); Ball Aerospace Communications Systems; Deutsche Agentur für Raumfahrtangelegenheiten; Agenzia Spaziale Italiana (X-SAR)
Power/ Mass	2kW/ 5600kg
Data Rate/ Duty Cycle	90Mbps via TDRSS (each for K- and C-bands)/ ND
Antenna Description	C-band microstrip panel = 12m x 0.75m L-band microstrip panel = 12m x 2.95m X-band slotted waveguide panel = 12m x 0.4m
Swath (Scan Angle):	L- & C-band = 70km (incidence 15° - 60°) X-band = 15km - 45km (35° - 70°)
Pulse Description/ Data Precision and Accuracies:	PRF = 1200-1800pps
Frequencies	1.25GHz, 23cm L-band HH, HV, VV, VH pols. 5.3GHz, 6cm C-band HH, HV, VV, VH pols. 9.6GHz, 3cm X-band V V polarization
Band-width	ND
Radiometric Resolution	ND
Spatial Resolution	L- & C-band = 30m (azimuth); 10-20m (range) X-band = 30m (azimuth); 10- 20m (range)
Calibrations/ Corrections:	ND

Data Availability

(1) Data are digitally coded and recorded onboard. Only one SAR data stream at a time is possible; Ku-band via TDRSS. Image size is 100km x 50km. Public Affairs Office, Jet Propulsion Laboratory, 4800 Oak Grove Drive, Pasadena, CA, (818) 354-4321, fax (818) 354-3437, URL: <http://www.jpl.nasa.gov/> (2) for SIR-C data via ftp, contact Customer Services, EROS Data Center, Sioux Falls, SD 57198, (605) 594-6511, fax (605) 594-6589,

URL: <http://sun1.cr.usgs.gov/landdaac/landdaac.html>

B.1.9 SPOT

Satellite Pour l'Observation de la Terre (SPOT) (originally named Systeme Probe-troire d'Observation del la Terre) - France

Mission Objectives

The SPOT program is committed to commercial remote sensing on an international scale and has established a global network of control centers, receiving stations, processing centers and data distributors. The SPOT satellite is owned and operated by the Centre National d'Etudes Spatiales (CNES), the French space agency. Worldwide commercial operations are anchored by private companies: SPOT Image Corporation in the U.S.; SPOT Image in France; SATIMAGE in Sweden; and distributors in over 70 other countries. Central to SPOT's commercial approach is the commitment to launch a minimum of five satellites. This ensures a continuous source of image data into the 21st century and a strong foundation for continued industry growth.

System Characteristics SPOT (1-5)

Launch:

Date: 1986, 1990, 1993, 1994, 1998

Vehicle: Ariane V16; Ariane V34

Site: Kourou, French Guiana

Orbit:

Altitude: 832km

Type: LEO, sunsynchronous

Inclination: 98.7°

Revisit: 26 days (satellite ground track); 1-3 days (off nadir mode)

Coverage: Global

Equatorial crossing: 10:30

Period: 101 minutes

Stabilization: 3-axis pointing accuracy 0.1°
maintained by 3 momentum wheels

Dimensions:

Mass: 1750 kg

Size: 2m x 2m x 2.5m

Instruments: HRV (2 each on SPOT-1, -2, -3); POAM-II, (SPOT-3);
HRVIR (SPOT-4); VMI (SPOT-4)

Design lifetime: 3 years (SPOT-1 thru 4); 5 years (SPOT-4, -5)

Prime Contractors Matra Marconi with Aerospatiale, Sodern

B.1.10 High Resolution Visible Sensor (HRV)

Sensor Description

HRV sensor operates in two modes: Multispectral Mode and Panchromatic Mode. Each SPOT payload consists of two identical HRV imaging instruments that are

Table B.6: SPOT HRV instrument characteristics

Dates of Operation:	1986-
Primary Mission:	Obtain Earth imagery for land use, agriculture, forestry, geology, cartography, regional planning, and water resources
Owner/Operator/Platform:	France, Sweden, Belgium/ Centre National d'Etudes Spatiales/ SPOT-1, -2, -3
Contractor:	Matra Marconi Space
Power/ Mass/:	170W direct transmission; 270W recorder playback/ one HRV = 250kg
Data Rate/ Duty Cycle	25Mbps, each mode/ 100%
Detector Technology:	On SPOT-1 each spectral band uses Fairchild's 122 DC detectors; SPOT-2,-3 use four Thompson-CF TH 7801A 1728-element CCD arrays. All are pushbroom linear CCD arrays. Each linear CCD consists of 6000 detectors.
Swath (Scan Angle):	FOV = $\pm 2.08^\circ$; 117km with 3km overlap with up to 27° off-nadir viewing to create 970km swath via a tilting mirror that permits viewing on 7 successive passes at 0° lat. and 11 passes at 45° lat

pointable in the cross-track direction up to 27° from nadir. The viewing mirror is operated by a stepping motor that can tilt the mirror in 0.3° steps ($= 0.6^\circ$ change in the line-of-sight or about 8.7km on the ground). This enables the HRV to image a swath up to 475km off nadir (~ 4.5 ground tracks). The telescope is a modified Schmidt with a focal length of 108.2cm and aperture of 33cm.

Detectivity/ Accuracy/ Precision/Stability

MTF at Nyquist Frequency	SNR	RMS Location Accuracy
row 0.23	Pan 290	300m
column 0.17	1 380	
	2 390	
	3 400	

Calibrations/ Corrections:

Calibration is performed weekly by taking each unit temporarily out of service. The procedure is performed by closing the mirror over the aperture during the nighttime ascending node. A tungsten-filament halogen lamp illuminates the detectors. The irradiance varies over the focal plane but the pattern is known and correctable. There is also a solar calibration, and interband, absolute, and multirate calibrations.

Table B.7: SPOT instrument spectral band characteristics

Channel	Spectral Channels	Band -width	Radiometric Resolution	Spatial Resolution
1	50 μ m - .59 μ m	90nm	8 bit quantization	multispectral mode = 20m
2	61 μ m - .68 μ m	70nm	..	(image area = 60km x 60km)
3	79 μ m - .89 μ m	100nm	..	3000 pixels/ line
4	51 μ m - .73 μ m (panchromatic)	220nm	6 bit quantization	panchromatic mode = 10m (image area = 60km x 60km) 6000 pixels/ line

Data Availability

Commercial data distributed by SPOT Image SA, 5 rue des Satellites, BP 4359, F-31030, Toulouse Cedex, 6219 4040, fax 6219 4011; and SPOT Image Corp., 1897 Preston White Drive, Reston, VA 22091-4368, (703) 620-2200, fax (703) 648-1813.

B.2 Airborne sensors

B.2.1 EMISAR

Electromagnetics Institute Synthetic Aperture Radar (EMISAR)

Sensor Description

EMISAR began as a single polarization C-band SAR but has been upgraded to a dual frequency polarimetric (C- and L-band) instrument and C-band interferometric SAR.

Dates of Operation:	1989, 1993, upgraded to interferometer 1994			
Primary Mission:	ND			
Owner/ Operator/ Platform:	Denmark/ Electromagnetics Institute/ Gulfstream G-3			
Contractor/ Principal Participants:	Electromagnetics Institute, Technical University of Denmark			
Power/ Mass/ Data Rate:	C-band = 2kW, L-band = 6kW/ ND/ 107Mbps			
Antenna Description:		Gain	3dB beamwidth	
			azimuth	elevation
	C-band	27dB, 25dB	2.7°, 2.5°	30°
	L-band	15dB est.	12°	55°
Swath (Scan Angle):	System records 8192 range samples so swath = 8192 × the programmable range pixel spacing; Depression ∠ = 20° - 80°			
Pulse Description/ Data Precision and Accuracies:	Pulse length = 20μs; PRF = ND			
Spectral Channels/ Frequencies	5.3 GHz 5.6cm C-band VV polarization C-band HH, HV, VV, VH polarizations 1.25 GHz L-band HH, HV, VV, VH polarizations			
Band-width	100MHz (for L-band TBD)			
Radiometric Resolution	8 bit quantization Inflight programmable			
Spatial Resolution	C-band = 2m x 2m best possible = 1.5m			
Calibrations/ Corrections:	System includes motion compensation			

Data Availability

Contact EMI, Technical University of Denmark, Lyngby, Denmark

B.2.2 EMIRAD

Electromagnetics Institute Radiometer (EMIRAD)

Sensor Description

EMIRAD is a passive multifrequency radiometer. The antenna and receivers are mounted on a cargo pallet located on the platform loading ramp. The ramp is lowered during data collection to provide unobstructed viewing.

Dates of Operation:	1980-
Primary Mission:	Monitor sea ice conditions in the high Arctic and oil films on sea surfaces
Owner/ Operator/ Platform:	Denmark/ Electromagnetics Institute/ Hercules C-130
Contractor/ Principal Participants:	Electromagnetics Institute, Technical University of Denmark
Power/ Mass/ Data Rate:	ND/ ND/ ND
Antenna Description:	Offset 1m aperture parabolic reflector with sinusoidal scan around the vertical axis and viewed by 3 horns
Swath (Scan Angle):	Scan angle = $\pm 12.5^\circ$ at 1000m altitude; $\pm 25^\circ$ at 2000m altitude; Swath = 500m at 1000m altitude 2km at 2000m altitude Incidence angle = 41° at (5GHz), 54° at (17GHz), 50° at (34GHz) $\pm 20^\circ$
Pulse Description/ Data Precision and Accuracies:	Beam efficiency 95%
Frequencies:	5GHz H, V polarizations; 17GHz H, V polarizations; 1 34GHz H, V polarizations
Band-width:	500MHz, 1GHz, 1GHz
Radiometric Resolution:	ND
Spatial Resolution:	footprint at 1000m altitude = 160m x 248m (5GHz) 47m x 73m (17GHz) 24m x 37m (34GHz)
Calibrations/ Corrections:	Inertial navigation data are recorded onto the CCT data tape along with radiometry data.

Data Availability

Contact EMI, Technical University of Denmark, Lyngby, Denmark

B.2.3 ESTAR

The ESTAR (Electronically Steered Thinned Array Radiometer) is a synthetic aperture radiometer operating at L-band. (Jackson *et al.*, 1995).

Sensor Description

ESTAR is an experimental airborne, passive microwave, synthetic aperture, radiometer. It uses Fourier synthesis to create images from antenna elements. The real aperture stick antennas produce a fan beam that is narrow along-track and broad across-track. The beam is swept along-track to provide azimuth resolution while the cross-track resolution is achieved by aperture synthesis. Images are generated indirectly by measuring the Fourier transform of the brightness temperature over the FOV (called the visibility function) and then inverse transformed to form an image.

Dates of Operation:	1988(prototype)
Primary Mission:	Apply microwave interferometry to soil moisture and ocean salinity measurements
Owner/ Operator/ Platform:	USA/ NASA-Goddard Space Flight Center/ P-3, C-130
Contractor/ Principal Participants:	NASA-Goddard Space Flight Center, University of Massachusetts
Power/ Mass/ Data Rate:	ND/ ND/ ND
Antenna Description:	Stick antennas
Swath (Scan Angle):	$\pm 45^\circ$
Pulse Description/ Data Precision and Accuracies:	ND
Spectral Channels/ Frequencies:	1.4GHz (L-band)H polarization ND
Band-width:	25MHz
Radiometric Resolution:	ND
Spatial Resolution:	Azimuth resolution $\pm 4^\circ$ Range resolution $\pm 3^\circ$
Calibrations/ Corrections:	ND

Data Availability

Contact Public Information Office, Goddard Space Flight Center, Greenbelt Road, Greenbelt, MD 20771, (301) 286-2000, fax (301) 286-8142,

URL: http://www.gsfc.nasa.gov/GSFC_homepage.html

B.2.4 JPL-AIRSAR

The JPL-AIRSAR

Airborne Synthetic Aperture Radar (AIRSAR)

Dates of Operation:	1987 -
Primary Mission:	Various measurement assignments, surface wind velocity, topographic mapping
Owner/ Operator/ Platform:	USA/ NASA-Ames Research Center/ DC-8
Contractor/ Princ.Participants:	Jet Propulsion Laboratory
Power/ Mass/ Data Rate:	ND/ ND/ 10Mbps
Antenna Description:	3 aft of port wing for dual polarized data collection, 1 (L-band) forward of port wing 2 (C-band) antennas in parallel forward of the polarimetric antennas Look angle = 70°
Swath (Scan Angle):	
Detectivity/ Accuracy/ Precision/ Stability:	ND
Spectral Channels/ Frequencies:	C-band/ 5.298 GHz Full. polarimetric/ $\lambda = 5.65\text{cm}$ L-band/ 1.248 GHz Full. polarimetric/ $\lambda = 24\text{cm}$ P-band/ 0.438 GHz Full. polarimetric/ $\lambda = 67\text{cm}-70\text{cm}$
Band-width:	20 MHz
Radiometric Resolution:	8 bit video data
Spatial Resolution:	7km x 12km; 1 280 (range) x 1024 (azimuth) pixels
Calibrations/ Corrections:	ND

Sensor Description

AIRSAR has a stable local oscillator (STALO) clock and a single digital chirp generator to generate an L-band wave form. This signal can then be converted to C-band and P-band, and all three transmitted by dual polarized microstrip patch array antennas. Antennas are mounted on the fuselage of the DC-8 aft of the port wing. Return from all three frequencies and both polarizations are multiplexed, combined with navigational data, and stored in-flight on high density recorders. The system is capable of operating in both along-track and cross-track interferometry modes (ATI and XTI). For the XTI mode, two C-band vertically polarized antennas are mounted in parallel to measure topography. The signal is transmitted from the bottom antenna and signals are received at both. For the ATI mode, the aft L- and C-band antennas are combined with the forward L-band and bottom XTI antennas to measure surface wind velocities.

Data Availability

Contact Public Affairs Office, Jet Propulsion Laboratory, 4800 Oak Grove Drive, Pasadena, CA 91109, (818) 354-4321, fax (818) 354-3437, URL: <http://www.jpl.nasa.gov/>

B.2.5 NS001

Sensor Description

This instrument simulates TM on Landsat-4 and -5 by collecting multispectral data in the seven TM bands. It also collects data in the $1.13\mu\text{m}$ - $1.35\mu\text{m}$ range.

Dates of Operation:	ND
Primary Mission:	Earth science applications in support of Thematic Mapper satellite measurements
Owner/ Operator/ Platform:	USA/ NASA-Ames Research Center/ C-130B
Designer/Builder:	Stennis Space Center
Power/ Mass/ Data Rate:	ND/ ND/ ND
Detector technology:	ND
Swath (Scan Angle):	FOV = 100° ; 7.26km at 3000m
Detectivity/ Accuracy/ Precision/ Stability:	ND
Spectral Channels/Band-width:	$458\mu\text{m}$ - $.519\mu\text{m}$ / 61nm $529\mu\text{m}$ - $.603\mu\text{m}$ / 74nm $633\mu\text{m}$ - $.697\mu\text{m}$ / 64nm $767\mu\text{m}$ - $.910\mu\text{m}$ / 43nm $1.13\mu\text{m}$ - $1.35\mu\text{m}$ / 22nm $1.57\mu\text{m}$ - $1.71\mu\text{m}$ / 14nm $2.10\mu\text{m}$ - $2.38\mu\text{m}$ / 28nm $10.9\mu\text{m}$ - $12.3\mu\text{m}$ / $1.4\mu\text{m}$
Radiometric Resolution:	8 bit quantization (838 words/frame)
Spatial Resolution:	IFOV = 2.5mrad, 7.6m at 3000m; 699 pixels/line
Calibrations/ Corrections:	Onboard blackbody sources and a calibration lamp are carried for thermal calibration.

Data Availability

Customer Services, EROS Data Center, Sioux Falls, SD 57198 in the form of computer compatible tapes (605) 594-6151, URL: <http://sun1.cr.usgs.gov/eros-home.html> Areas of coverage, flight documentation and sensor calibration data are available from the Aircraft Data Facility, Ames Research Center, Mail Stop 240-6, Moffett Field, CA 94035-1000, (415) 604-6252. Information on investigator-sponsored sensors and experiments may be obtained from the Medium Altitude Missions Branch, Ames Research Center, Mail Stop 211-12, Moffett Field, CA 94035-1000, (415) 604-5336, URL: <http://www.arc.nasa.gov/>

B.2.6 PBMR

Table B.8: PBMR instrument characteristics

Platform	NASA C-130
Principal operator	NASA
Number of bands	1
Center frequency	1.42 GHz
Polarization	H
Antenna	Real aperture, 4 beams pointing at $\pm 8^\circ$ and $\pm 24^\circ$ from nadir
Resolution	0.3 aircraft altitude
Swath width	1.2 · aircraft altitude

Data acquisition description

The Push Broom Microwave Radiometer (PBMR) data are recorded directly from the instrument onto a floppy disk on board the aircraft. These data are then calibrated as a function of time using a second software package. The C-130 flights are typically plotted using video tapes of the flight on copies of high-altitude photos obtained by NASA. These flight lines are then digitized directly into UTM coordinates using easily identified landmarks. This produces maps of aircraft position in UTM coordinates as a function of time for each flight line. Before creating the final images with these data, the outer beams are corrected for incidence angle effects (limb darkening) by multiplying them by the ratio of the average of the center beam to the outer beam on each side. This darkening is due to the decrease in emissivity with angle for horizontal polarizations.

Appendix C

Description of the electromagnetic field

C.1 Introduction

The electromagnetic energy is the means by which information can be transmitted from one place to another (e.g. from an object to a sensor). This information can be encoded in the frequency content, intensity or polarization (Elachi, 1987). The electromagnetic radiation can be described by two different approaches; the wave approach and the quantum approach. The quantum approach describes the electromagnetic energy by means of particles called photons. This description is especially useful for the interaction between matter and electromagnetic energy with very short wavelengths. In most other cases, the wave approach is more suitable. This approach is based upon the Maxwell equations. This theory describes the propagation of electromagnetic energy in the form of smooth waves, resulting from two forces which are always perpendicular to each other namely the electric force (field) and the magnetic force (field) (Fig. C.1). Thus, in any region where an electric field exists, there is also a magnetic counterpart. And as we will see in paragraph C.2 if one of the fields is described automatically the other field is also described.

C.2 Theory of the electromagnetic field

C.2.1 The Maxwell equations

The fundamentals of the theory considering electromagnetism are contained in the Maxwell equations. These equations are based upon experimental observations done by Maxwell in the late 19th century. They give the relationships between the electric field strength $\mathbf{E} = \mathbf{E}(\mathbf{r}, t)$ and the magnetic field strength $\mathbf{H} = \mathbf{H}(\mathbf{r}, t)$ as a function of time t and place \mathbf{r} (with $-\infty < \mathbf{r} < \infty$, and $0 < t < \infty$).

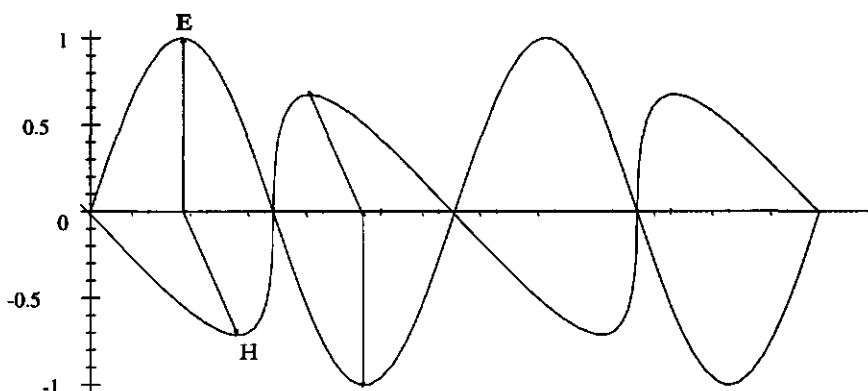


Figure C.1: The electric and magnetic force field.

In vacuum these equations can be written in their most simplified form as:

$$\nabla \times \mathbf{H} = \epsilon_0 \mu_0 \frac{\partial \mathbf{E}}{\partial t} \quad (\text{C.1})$$

$$\nabla \times \mathbf{E} = -\frac{\partial \mathbf{H}}{\partial t} \quad (\text{C.2})$$

$$\nabla \cdot \mathbf{E} = 0 \quad (\text{C.3})$$

$$\nabla \cdot \mathbf{H} = 0 \quad (\text{C.4})$$

in which the permittivity of vacuum, ϵ_0 is defined as:

$$\epsilon_0 = (\mu_0 c_0^2)^{-1} \quad (\text{C.5})$$

in which the permeability of vacuum $\mu_0 = 4\pi \cdot 10^{-7} \text{ H m}^{-1}$ and the speed of light in vacuum $c_0 = 2.9979 \cdot 10^8 \text{ m s}^{-1}$, giving $\epsilon_0 \approx 8.8544 \cdot 10^{-12} \text{ F m}^{-1}$.

For the propagation of the fields in a medium the above equations have to be adjusted for the interaction of the electromagnetic energy with matter. In their most general form, valid for both electromagnetic, electrostatic and magnetostatic fields in a given medium, they can be written as (de Hoop, 1975; Tsang *et al.*, 1985):

$$\nabla \times \mathbf{H} = \mathbf{J} + \epsilon_0 \frac{\partial \mathbf{E}}{\partial t} + \frac{\partial \mathbf{P}}{\partial t} \quad (\text{C.6})$$

$$\nabla \times \mathbf{E} = -\mu_0 \frac{\partial \mathbf{H}}{\partial t} - \mu_0 \frac{\partial \mathbf{M}}{\partial t} \quad (\text{C.7})$$

$$\nabla \cdot (\epsilon_0 \mathbf{E} + \mathbf{P}) = \rho \quad (\text{C.8})$$

$$\nabla \cdot (\mu_0 \mathbf{H} + \mu_0 \mathbf{P}) = 0 \quad (\text{C.9})$$

The interaction with the medium is accounted for by magnetization $\mathbf{M} = \mathbf{M}(\mathbf{r}, t)$ (section 2.2.2) and polarization $\mathbf{P} = \mathbf{P}(\mathbf{r}, t)$ (section 2.2.2) and electric current density $\mathbf{J} = \mathbf{J}(\mathbf{r}, t)$ (section 2.2.2). In Eq. C.8 the ρ represents the electric charge density. A very important aspect of electric currents is that electric charge is conserved:

$$\nabla \cdot \mathbf{J} = -\frac{\partial \rho}{\partial t} \quad (\text{C.10})$$

Eq. C.6 is also referred to as the first equation of Maxwell in a medium and Eq. C.7 as the second equation of Maxwell in a medium. To simplify these equations two new properties can be defined, $\mathbf{D} = \mathbf{D}(\mathbf{r}, t)$ which is the electric flux density or dielectric displacement

$$\mathbf{D} \stackrel{\text{def}}{=} \epsilon_0 \mathbf{E} + \mathbf{P} = \epsilon' \mathbf{E} \quad (\text{C.11})$$

and $\mathbf{B} = \mathbf{B}(\mathbf{r}, t)$ the magnetic flux density:

$$\mathbf{B} \stackrel{\text{def}}{=} \mu_0 (\mathbf{H} + \mathbf{M}) = \mu' \mathbf{H} \quad (\text{C.12})$$

Along with,

$$\mathbf{J} = \sigma \mathbf{E} \quad (\text{C.13})$$

these equations are called constitutive relations and describe the interaction of the electromagnetic field with matter. The definition and physical meaning of the real part of the permittivity ϵ' and permeability μ' will be treated in section 2.2.1 Using Eqs. C.11 and C.12 the Eqs. C.6 until C.9 can be transformed into:

$$\nabla \times \mathbf{H} = \mathbf{J} + \frac{\partial \mathbf{D}}{\partial t} \quad (\text{C.14})$$

$$\nabla \times \mathbf{E} = -\frac{\partial \mathbf{B}}{\partial t} \quad (\text{C.15})$$

$$\nabla \cdot \mathbf{D} = \rho \quad (\text{C.16})$$

$$\nabla \cdot \mathbf{B} = 0 \quad (\text{C.17})$$

C.3 Wave equation

In homogeneous, isotropic and non magnetic media, the Maxwell's equations can be combined to derive the wave equation. The wave equation describes the propagation of the electric (and magnetic) field in space and time. For the simplest case, i.e. the

Maxwell equations in vacuum, Eqs. C.1-C.4, the wave equations can be derived, for instance, by eliminating the magnetic flux density \mathbf{B} from Eqs. C.1-C.2 by taking the curl of both sides of Eq.C.1 and the time derivative of both sides of Eq.C.2 (Arfken, 1985; Borisenko & Tarapov, 1979 (original 1968)). Since time and space derivatives commute :

$$\frac{\partial}{\partial t} (\nabla \times \mathbf{B}) = \nabla \times \frac{\partial \mathbf{B}}{\partial t} \quad (\text{C.18})$$

thus giving

$$\nabla \times (\nabla \times \mathbf{E}) = -\varepsilon_0 \mu_0 \frac{\partial^2 \mathbf{E}}{\partial t^2} \quad (\text{C.19})$$

Using Eqs. C.3 and C.4 yields the three-dimensional wave equation for the electric field:

$$\nabla \cdot \nabla \mathbf{E} = \varepsilon_0 \mu_0 \frac{\partial^2 \mathbf{E}}{\partial t^2} \quad (\text{C.20})$$

$$\nabla^2 \mathbf{E} - \varepsilon_0 \mu_0 \frac{\partial^2 \mathbf{E}}{\partial t^2} = 0 \quad (\text{C.21})$$

A solution for Eq. C.21 is (Borisenko & Tarapov, 1979 (original 1968); ?; ?):

$$\mathbf{E} = \mathbf{A} e^{j(\omega t - \mathbf{k} \cdot \mathbf{r} + \phi)} \quad (\text{C.22})$$

with

$$\mathbf{k} \cdot \mathbf{r} = kr \cos \alpha \quad (\text{C.23})$$

where, ω is the angular frequency, \mathbf{A} is the amplitude of the wave, α the angle between \mathbf{k} and \mathbf{r} , ϕ is the phase, k is the wave number ($k = \frac{2\pi}{\lambda}$) and r is the spatial coordinate. The wave vector, \mathbf{k} describes the direction of propagation of the wave. This formula describes a (transverse) harmonic plane wave. Similarly, the wave equations can be derived for electromagnetic fields in media with permittivity ε , permeability μ and conductivity σ (Borisenko & Tarapov, 1979 (original 1968)) which results in a complex \mathbf{k} (with $\mathbf{k} = \mathbf{k}_1 + j\mathbf{k}_2$) giving:

$$\mathbf{E} = \mathbf{A} e^{\mathbf{k}_2 \cdot \mathbf{r}} e^{j(\omega t - \mathbf{k}_1 \cdot \mathbf{r} + \phi)} \quad (\text{C.24})$$

The general wave equation in free space in Cartesian coordinates, for the electric field can be given as (Groot, 1991):

$$\mathbf{E}(x, y, z, t) = \mathbf{i}_x E_x(x, y, z, t) + \mathbf{i}_y E_y(x, y, z, t) + \mathbf{i}_z E_z(x, y, z, t) \quad (\text{C.25})$$

The general form of the (transverse) harmonic plane wave, propagating in the $+\mathbf{i}_z$ direction can be given as (Groot, 1991; Ulaby *et al.*, 1981):

$$\mathbf{E}(z, t) = \mathbf{i}_x E_x(z, t) + \mathbf{i}_y E_y(z, t) \quad (\text{C.26})$$

As can be seen from Eq. C.26 the electric field propagating in the direction $+\mathbf{i}_z$ has two components $E_x(z, t)$ and $E_y(z, t)$ which can be rewritten as:

$$E_x(z, t) = A_x \cos(\omega t - kz + \phi_x) = A_x e^{j(\omega t - kz + \phi_x)} \quad (\text{C.27})$$

$$E_y(z, t) = A_y \cos(\omega t - kz + \phi_y) = A_y e^{j(\omega t - kz + \phi_y)} \quad (\text{C.28})$$

where, A_x and A_y are the amplitudes of the electric field components in the x - and y -directions respectively, and ϕ_x and ϕ_y are the phases of the field components in the x - and y -directions.

The intensity of an electromagnetic wave, an harmonically oscillating wave, is given by the vector product of the electric and magnetic field strengths:

$$I = \frac{1}{2} \mathbf{E} \times \mathbf{H}^* \quad (\text{C.29})$$

and can be defined as the average rate of energy flow per unit area. Since, \mathbf{E} and \mathbf{H} are perpendicular Eq. C.29 can be rewritten as:

$$I = \frac{1}{2} \mathbf{E} \mathbf{H}^* \quad (\text{C.30})$$

The ratio between the electric and magnetic fields is always constant for a given medium:

$$\frac{E}{H} = \sqrt{\frac{\mu}{\epsilon}} = \eta \quad (\text{C.31})$$

where η is called the wave impedance of the medium the wave is travelling in. Thus we can define the intensity in an isotropic medium as:

$$I = \frac{1}{2} \frac{E^2}{\eta} = \frac{E^2}{2\sqrt{\frac{\mu}{\epsilon}}} \quad (\text{C.32})$$

or written in some different forms:

$$I = c\epsilon_o \langle \mathbf{E}^2 \rangle = c\epsilon_o \mathbf{E} \mathbf{E}^* = \frac{1}{2} c\epsilon_o (E_x^2 + E_y^2) \quad (\text{C.33})$$

C.4 Polarization of electromagnetic radiation

From Eqs. C.26-C.28 can be seen that the electric field can be described by two vectors one in the x -direction and one in the y -direction. The orientation of the electric field vector in a reference plane perpendicular to the direction of propagation is called polarization¹ (see Fig. C.2). If the wave linearly oscillates only in the x -direction, the wave is called *horizontally polarized*. If the wave is linearly oscillating in the y -direction the wave is said to be *vertically polarized*. All other polarization types are called *elliptical polarization* of which the circular polarization is a special case in

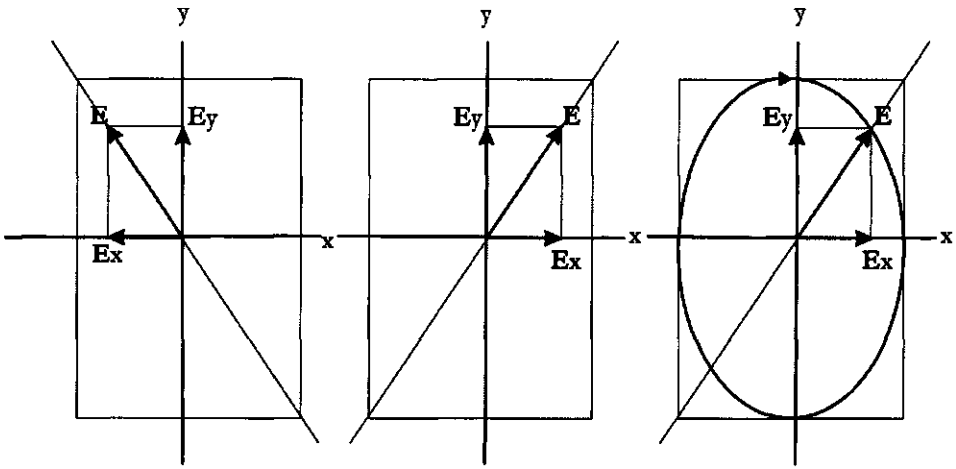


Figure C.2: The wave polarizations as a result of the phase differences between the component waves E_x and E_y . The tip of the field vector runs along the bold lines. Adapted from (Schanda, 1986)

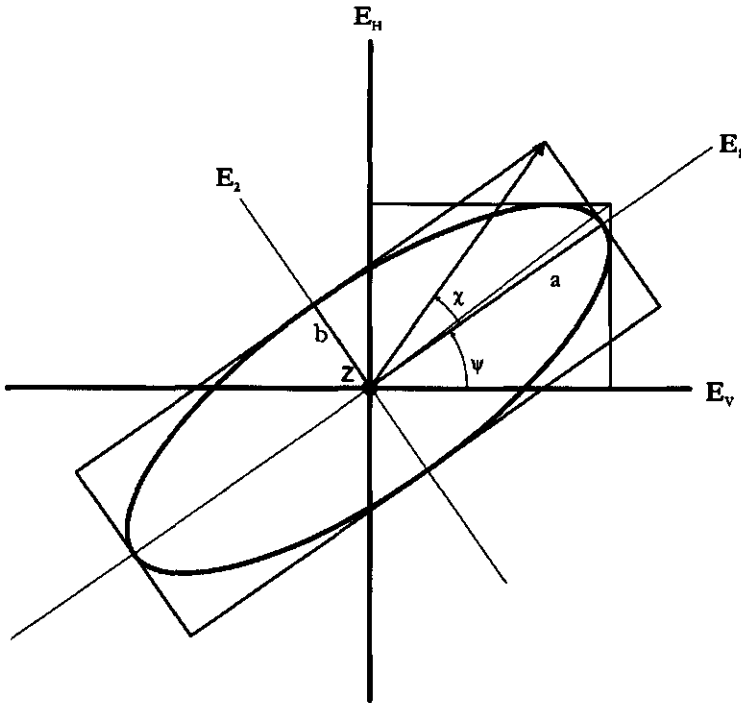


Figure C.3: The polarization ellipse.

which the oscillations in both x - and y -directions are equal. The polarization states can be easily visualised by means of the polarization ellipse (see Fig. C.3). The general equation for an ellipse is of the form:

$$\frac{E_1^2}{a^2} + \frac{E_2^2}{b^2} = 1 \quad (\text{C.34})$$

where a and b are the semi axes of the ellipse and E_1 and E_2 are the coordinate system axes. The ellipse in Fig. C.3 can be described by the following equation, resulting from adding Eqs. C.26-C.28 and eliminating the dependence on (z, t) (Ulaby & Elachi, 1990; Born & Wolf, 1975):

$$\left(\frac{E_2}{|E_v|} \right)^2 + \left(\frac{E_1}{|E_h|} \right)^2 - \frac{2E_1E_2}{|E_v||E_h|} \cos \delta = \sin^2 \delta \quad (\text{C.35})$$

with $\delta = \phi_y - \phi_x$. However, it is more convenient (for reasons which will become clear in the next paragraph) to describe the ellipse as a function of the polarization angles, namely rotation angle ψ ($-\frac{\pi}{2} < \psi < \frac{\pi}{2}$) and ellipticity angle χ ($-\frac{\pi}{4} < \chi < \frac{\pi}{4}$) (see Fig. C.3). The rotation angle is defined as the angle between the major axis of the ellipse and the x -, or E_h -direction. The ellipticity angle is defined as the ratio between the two axes of the ellipse:

$$\tan \chi = \pm \frac{a}{b} \quad (\text{C.36})$$

The direction of rotation of the E -vector in the reference plane is called *sense of polarization* or *handedness*. There are two conventions, the IEEE definition (IEEE, 1983) looks at the wave in the direction of propagation, if in that case the field vector turns clockwise (counter-clockwise) the sense is called right-handed (left-handed). The sense of polarization can also be deduced from χ if $\chi < 0$ the rotation is right-handed otherwise, i.e. $\chi > 0$ the rotation is left-handed.

In the backscatter direction the scattering matrix S and the Stokes scattering operator M are symmetrical, the Mueller (or Stokes) matrix L in general is non-symmetrical. Since $M_{11} = M_{22} + M_{33} + M_{44}$ the 4×4 real matrix M (and also L) can be fully characterized by 9 independent numbers for the backscatter direction. Pixels of multi-look polarimetric SAR images, therefore, usually contain these 9 numbers, which fully describe the backscatter properties of extended targets and can be averaged over certain image areas, with the objective for example to reduce speckle. Single-look SAR images can also be expressed in terms of scattering matrices. The scattering matrix in the backscatter direction is fully characterized by 5 independent numbers (if the absolute phase is omitted). The Stokes scattering operator follows from the scattering matrix and therefore can also be characterized by 5 numbers for a single observation. After ensemble averaging 9 numbers are needed in general and inversion to a unique (averaged) scattering matrix is not possible. In comparison to the scattering matrix the Stokes scattering operator contains additional information describing the physical process of depolarization of the wave by the target.

1. This polarization is not to be confused with the alignment of molecules/electrons under influence of an electric field as described in section 2.2.2

Appendix D

Mathematical description and measurement of surface roughness

A rough surface has a strong impact on the scattering and emission of microwave radiation. It acts as a diffuse reflector and scatters radiation in every direction and thus a significant part will be reflected towards the sensor. The surface roughness can be defined as the variation of surface height within a image resolution cell (Henderson & Lewis, 1998). The transition of the surface from smooth to rough is qualitative and is also a function of wavelength and incidence angle. Roughness in general decreases with increasing wavelength or decreasing incidence angle. There have been various criteria developed to discriminate between a rough and a smooth surface. The Rayleigh criterion is used most often but various others are also possible (Ulaby et al., 1982).

- Rayleigh criterion:

$$R_a < \frac{\pi}{4}$$

$$R_a = k\sigma \cos \theta_{inc}$$

where R_a is known as the Rayleigh parameter, k is the wave number ($=\frac{2\pi}{\lambda}$), σ is the root mean square deviation from a reference plane and θ_{inc} is the angle of incidence of the plane wave. The criterion is developed for a plane monochromatic wave incident on a sinusoidal surface.

- Modified Rayleigh criterion by Peake and Oliver (1971):

$$\sigma < \frac{\lambda}{25} \cos \theta_{inc}$$

is for a smooth surface and for a rough surface:

$$\sigma > \frac{\lambda}{4.4} \cos \theta_{inc}$$

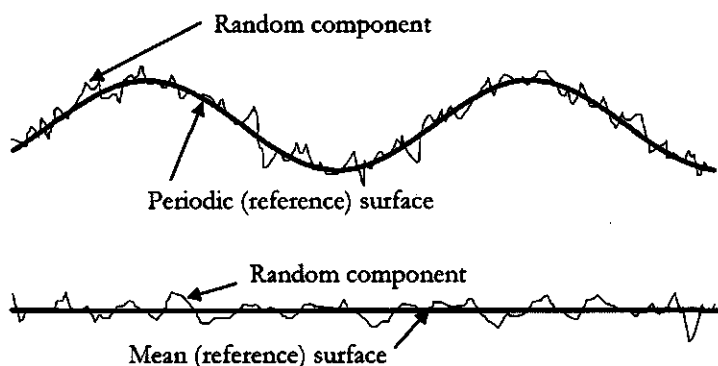


Figure D.1: Surface roughness configurations. a) Random height variations superimposed on a periodic surface and b) random height variations superimposed on a flat surface (adapted from Ulaby *et al.*, 1982, Henderson and Lewis, 1998)

- The Fraunhofer criterion:

$$\sigma < \frac{\lambda}{32 \cos \theta_{\text{inc}}}$$

This criterion is proposed by Ulaby *et al.*, 1982 because it is more stringent than the Rayleigh criterion and better suited for natural surfaces where λ is of the order of σ .

The surface roughness can be described in various ways which will be highlighted in the next paragraphs.

D.1 Statistical descriptions

Most surfaces can be described by a surface height profile consisting of two variables; a random component with certain statistical properties and a deterministic component. The statistical variation is often characterized by its RMS height, σ and its correlation function, C . These are defined relative to a reference surface which can be a mean surface or a periodic surface (Figure D.1). Estimations of root mean square height or σ can be determined directly from samples of $h(\mathbf{x})$ and $h(\mathbf{y})$ (see Section D.3), yielding σ_y and σ_x . Likewise estimations of the autocorrelation functions $C(\mathbf{x})$ and $C(\mathbf{y})$, in x - and y -directions respectively, follow. Because of the assumed independence between the two directions, $C(\mathbf{r}) = C(\mathbf{x})C(\mathbf{y})$. The autocorrelation lengths l_x and l_y are defined as the distance at which the normalised autocorrelation functions (for which $C(0) = 1$) fall off to a value of $1/e$.

The power spectral density function (or power spectrum) is usually defined as the Fourier transform of the unnormalised autocorrelation function:

$$W(\bar{\mathbf{k}}) = \frac{\sigma^2}{(2\pi)^2} \int_{-\infty}^{\infty} C(\mathbf{r}) \exp(j\bar{\mathbf{k}}\mathbf{r}) d\mathbf{r}$$

and is also called the surface roughness spectrum. Here \bar{k} is the spatial wave number of the surface ($k = 2\pi/\lambda$), which in this case is related to the electromagnetic wave number k by the expression:

$$\bar{k} = 2k \sin \theta_i$$

Also from the power spectral density (PSD) function the autocorrelation lengths l_x and l_y can be derived from the points where the normalised PSD function falls off to the value $1/e$ as $l_{x,y} = \frac{2}{k_{x,y}}$. Using the theorems of Wiener-Khintchine and Parseval (Press *et al.*, 1992) it can easily be shown that the total area under the power spectrum gives the variance, or 'power' of the surface:

$$\int_{-\infty}^{\infty} W(\bar{k}) d\bar{k} = \sigma^2$$

The theory of wave scattering from rough surfaces often assumes that surface autocorrelation functions are Gaussian and may be given as:

$$C(\mathbf{r}) = \exp\left(\frac{-\mathbf{r}^2}{l^2}\right)$$

Then, the surface roughness spectrum $W(\bar{k})$ follows as:

$$W(\bar{k}) = \frac{\sigma^2 l^2}{4\pi} \exp\left(\frac{\bar{k}^2 l^2}{4}\right)$$

or in the direction of the wave:

$$W(2k \sin \theta_i, 0) = \frac{\sigma^2 l^2}{4\pi} \exp\left(\bar{k}^2 l^2 \sin^2 \theta_i\right)$$

The power spectral density describes both the spread of heights about the mean plane and the height variation along the surface.

Alternative forms of the correlation function can also be given. The exponential form seems to fit measured surface roughness data better. The exponential correlation function can be written as:

$$C(\mathbf{r}) = \exp\left(\frac{-|\mathbf{r}|}{l}\right)$$

For higher order surface properties, such as surface gradients, this function poses problems because of the discontinuity at the origin. The surface spectrum for the exponential function becomes:

$$W(\bar{k}) = \frac{\sigma^2}{l^2 \pi^2} \frac{1}{\left(\frac{1}{l^2} + \bar{k}^2\right)}$$

Various other correlation function have been suggested. Furthermore it should be noted that surfaces may be described by more than one correlation function. This can be the case, for instance, for surface with roughness caused by different types of processes. More correlation functions can be found in Appendix 2B of Fung, (1994).

D.2 Other descriptions

D.2.1 Fractal geometry

The concept of fractal surfaces has been extensively described since the late 70's (Mandelbrot, 1977). Fractals surface can be describe as surface which have a structure on all scales and that structure has a similar form (self-similarity) at those scales (Ogilvy, 1990). Fractal surfaces therefore enclose a finite volume with an infinite area. The fractal dimension D is defined as the dimension of the fractal surface when cut by a plane. For non-fractal surface $D = 1$ and for fractal surfaces $1 < D < 2$. Statistics as RMS height and autocorrelation length is for such surfaces therefore non-existent. Fractal surfaces and fractal like surfaces can be described through the use of the power spectrum (Ogilvy, 1990; Davidson *et al.*, 2000):

$$P(f) \sim \frac{1}{f^\nu}$$

with ν related to D through:

$$D = \frac{(5 - \nu)}{2}$$

such that $1 < f < 3$ because for this range the Fourier transform of $P(f)$ is infinite.

The surface roughness, $S(x, y)$ can be modelled by:

$$S(x, y) = Z(x, y) + F(x, y)$$

where $Z(x, y)$ represents the single scale process and $F(x, y)$ the fractal random process. Davidson *et al.*, 2000 show that for longer profiles for smooth agricultural surfaces the fractal description is appropriate (roughness caused be multi-scale processes). For the rougher agricultural surfaces the single scale process is dominant. They expect that for natural formed surfaces, which are caused by natural processes the surface roughness needs to be differently modelled.

D.2.2 Discrete random process

Most models describe the surface roughness as a continuous process rather than a discrete process. The theory of Markov chains can be used to describe this discrete random process (Beckmann & Spizzichino, 1963; van Kampen, 1992; Vanmarcke, 1983). The surface height correlation function from a discrete measurement process (such as "needle board") can be calculated from:

$$C_j = C(j\Delta x) = \frac{N}{N-j} \frac{\sum_{i=1}^{N-j} h_i h_{i+j}}{\sum_{i=1}^N h_i^2}$$

where Δx is the measurement interval, N is the number of points, h is the surface height.

D.3 Measurement of surface roughness

Measurement of surface roughness is a difficult procedure because rough surfaces exhibit roughness at various scales and can be discrete of nature (at the atomic scale). The surface profile retrieved is often dependent upon the type of measurement, instrument resolutions, sampling interval, measurement length, sample shape and size (Ogilvy, 1990). Measurements are usually performed using a discrete method while the surface roughness in many (descriptive) models is supposed to be continuous of nature. Therefore depending upon the application the appropriate measurement technique needs to be utilized. The measurements methods of surface roughness can be distinguished in contact and non-contact methods. A few examples are illustrated in the next two sections.

D.3.1 Contact methods

Contact methods use devices that come in direct physical contact with the soil surface and therefore the risk exists that the measurements are disturbed. In practice however depending upon the method these disturbances can be neglected.

Needle board or stylus instrument

This is one of the most common contact methods. This method measures an effective surface profile because it involves needles or styli with tip radii varying between 4 and 12 μm which lead to a horizontal resolution of approximately twice this value. The method is easy to use, and by digitising the profile the RMS and correlation lengths can easily be retrieved. These days, with the availability of digital cameras the whole process can be automated from image to retrievals. Besides the limited and fixed horizontal resolution the tips of the needles can distort the roughness by penetrating the surface. Another disadvantage is the limited length of the instrument which might be too short to effectively calculate the roughness correlation length. Surface roughness measurements

The soil surface roughness that is used in this thesis is most of the times determined using a needle board from Wageningen University (see Fig D.2). The needle board consists of two aligned areas with different density of needles by which the measurements can be made. Macro roughness can be measured with low density sampling (1 needle per cm) and micro roughness can be measured with high density sampling (3 needles per cm). Each measurement gives 151 samples in both high and low density, where the high density is measured over 50 cm and the low density over 150 cm (Visser & Hoekman, 1991). The needle board has to be placed level over the surface, the needles can then be lowered such that the top of the needles just hit the surface and altogether give a profile of the soil surface. Of the whole board a photograph is taken

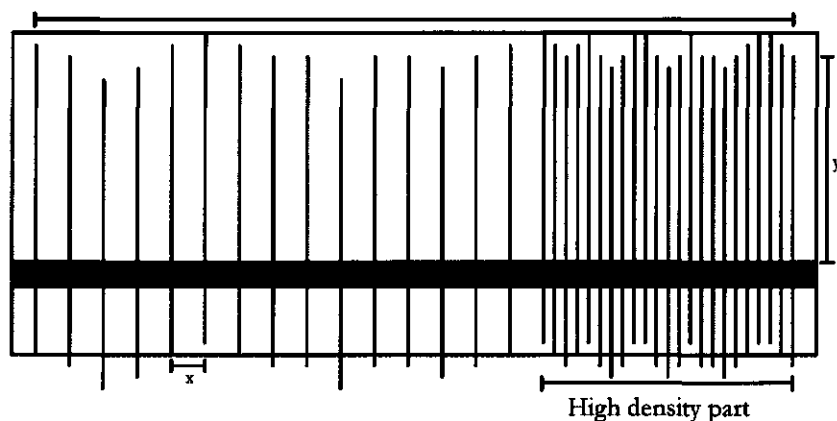


Figure D.2: Soil profile meter or "needle board"

and the profile can then be digitised. In this way two sets of x, z coordinates is given for each pair of needles, where " x " stands for the distance between the needles and " z " is the height of the needles.

The number of measurements made is limited to those surfaces that were distinct and representative for the area. For each measurement location two pairs of measurements are made, resulting in one perpendicular to the row direction (the " y " direction) and one parallel to it (the " x " direction). Since we assume that the physical processes that cause surface roughness are uncorrelated for both directions, measurements restricted to these two directions are sufficient. The root mean square (RMS) (mm) of the height differences, σ , of the needles, and the autocorrelation length (cm), l , can be calculated as a measure of surface roughness. With these values the power density spectrum using the fast Fourier Transform (FFT), and the Autocorrelation function using an inverse FFT can be calculated using the algorithms from Press *et al.* (1992) (see also Section D.1).

Contact spray

The contact spray method uses a sheet of paper which is put in the ground and with quick drying spray paint the surface contours is sprayed on the paper. Afterwards this profile can be easily digitized to retrieve the required roughness parameters. Disadvantages of this method are the paint residues on the soil, not very accurate due to disturbing of profile by pushing the board into the ground, wind effects and spraying "around" or behind the profile and this method is more difficult to use in vegetated areas.

Gridded pane

This method uses a gridded pane that is put into the ground and photographed to again digitise the surface roughness profiles. Disadvantages are that the pane can distort the profile, and is hampered by shade effects and is difficult to use in vegetated

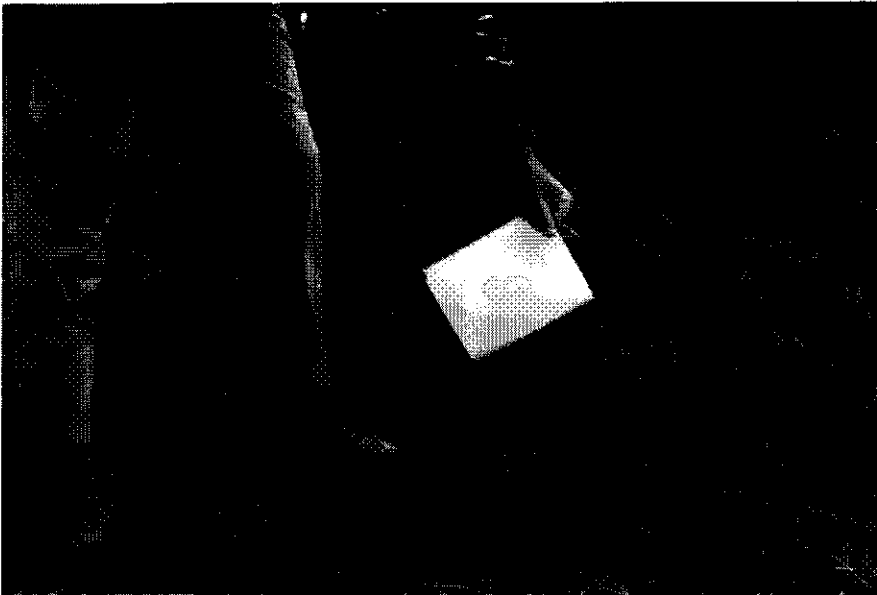


Figure D.3: Photograph demonstrating the use of the transparent 1 cm gridded pane in a pea field.

areas. Actually this method is better suited to described vegetation structure than surface roughness especially when a transparent gridded pane is used (Figure D.3).

D.3.2 Non-contact methods

There are various devices that can be used to determine the surface roughness without coming into direct physical contact with the surface. Of the various devices or methods available only the ones using electromagnetic radiation will be considered here, since they are more accurate and widely used for remote sensing purposes.

Laser profiler

The laser profiler uses coherent radiation to illuminate the surface. By moving the beam over the surface the phase differences, and thus the distance can be measured. This method is highly accurate because of the very small beam resolutions possible and high spatial sampling rates. One of the disadvantages is the need for high tech equipment and batteries in the field to operate such a system. Another disadvantage is that depending upon the wavelength of the laser different results can be obtained because of the scattering and absorption characteristics of the surface that is illuminated. These effects however are negligible for most purposes. The possibility of the laser profiler to measure longer lines, e.g. CESBIO-ESA laser profiler which can measure up to 25 m, is essential to obtain correct surface correlation lengths (Davidson *et al.*, 2000).

Laser altimetry

The laser altimeter is a laser profiler mounted on an airborne platform. The laser altimeter data therefore needs to be corrected for platform motion in all directions. The instrument is because of its lower spatial sampling rate compared to the ground-based laser profiler better suited to measure the mesoscale roughness features. The instrument is therefore often used to derive aerodynamic roughness lengths (Ritchie & Jackson, 1989; Menenti *et al.*, 1996).

Interferometry

Interferometry is a technique which illuminates the scene at least twice from a slightly different position or angle. From the relative changes between points of the two data sets the height differences can be calculated from the phase difference of the received electromagnetic radiation when the sensor height/position relative to the surface is known. This technique can be done at all different kind of resolutions, e.g. using microscopic photographic data to data from space-borne platforms such as ERS-1. Depending upon the sensor very high resolution are possible, however this technique is not practical for field survey due to the complex instrumentation and set-up involved.

Appendix E

The inversion of the Fresnel equations

E.1 Fresnel equation for a horizontally polarized wave

The Fresnel equation for a horizontally polarized wave can be written as:

$$\rho_h(\theta_{\text{inc}}, \varepsilon) = \left| \frac{\cos \theta_{\text{inc}} - \sqrt{\varepsilon - \sin^2 \theta_{\text{inc}}}}{\cos \theta_{\text{inc}} + \sqrt{\varepsilon - \sin^2 \theta_{\text{inc}}}} \right|^2 \quad (\text{E.1})$$

with the Fresnel reflection coefficient for horizontal polarization ρ_h and the dielectric constant ε as complex numbers, and θ_{inc} is the incidence angle relative to nadir. We can rewrite this equation by taking the square root on both sides. By doing that we have to make sure that we keep all possible solutions. This means that there are two solutions, with opposite signs, which have to be taken into account:

$$\sqrt{\rho_h(\theta_{\text{inc}}, \varepsilon)} = \pm \frac{\cos \theta_{\text{inc}} - \sqrt{\varepsilon - \sin^2 \theta_{\text{inc}}}}{\cos \theta_{\text{inc}} + \sqrt{\varepsilon - \sin^2 \theta_{\text{inc}}}} \quad (\text{E.2})$$

$$\left(\cos \theta_{\text{inc}} - \sqrt{\varepsilon - \sin^2 \theta_{\text{inc}}} \right) \sqrt{\rho_h} = \pm \left(\cos \theta_{\text{inc}} + \sqrt{\varepsilon - \sin^2 \theta_{\text{inc}}} \right) \quad (\text{E.3})$$

$$(\cos \theta_{\text{inc}}) \sqrt{\rho_h} - \left(\sqrt{\varepsilon - \sin^2 \theta_{\text{inc}}} \right) \sqrt{\rho_h} = \pm \left(\cos \theta_{\text{inc}} + \sqrt{\varepsilon - \sin^2 \theta_{\text{inc}}} \right) \quad (\text{E.4})$$

$$\begin{aligned} (\cos \theta_{\text{inc}}) \sqrt{\rho_h} - \left(\sqrt{\varepsilon - \sin^2 \theta_{\text{inc}}} \right) \sqrt{\rho_h} &= \cos \theta_{\text{inc}} - \sqrt{\varepsilon - \sin^2 \theta_{\text{inc}}} \\ (\cos \theta_{\text{inc}}) \sqrt{\rho_h} - \left(\sqrt{\varepsilon - \sin^2 \theta_{\text{inc}}} \right) \sqrt{\rho_h} &= -\cos \theta_{\text{inc}} + \sqrt{\varepsilon - \sin^2 \theta_{\text{inc}}} \end{aligned} \quad (\text{E.5})$$

$$\begin{aligned} (\cos \theta_{\text{inc}}) \sqrt{\rho_h} - \cos \theta_{\text{inc}} &= - \left(\sqrt{\varepsilon - \sin^2 \theta_{\text{inc}}} \right) \sqrt{\rho_h} - \sqrt{\varepsilon - \sin^2 \theta_{\text{inc}}} \\ (\cos \theta_{\text{inc}}) \sqrt{\rho_h} + \cos \theta_{\text{inc}} &= - \left(\sqrt{\varepsilon - \sin^2 \theta_{\text{inc}}} \right) \sqrt{\rho_h} + \sqrt{\varepsilon - \sin^2 \theta_{\text{inc}}} \end{aligned} \quad (\text{E.6})$$

$$\begin{aligned} \cos \theta_{\text{inc}} (\sqrt{\rho_h} - 1) &= \sqrt{\varepsilon - \sin^2 \theta_{\text{inc}}} (-\sqrt{\rho_h} - 1) \\ \cos \theta_{\text{inc}} (\sqrt{\rho_h} + 1) &= \sqrt{\varepsilon - \sin^2 \theta_{\text{inc}}} (-\sqrt{\rho_h} + 1) \end{aligned} \quad (\text{E.7})$$

$$\begin{aligned} \frac{\cos \theta_{\text{inc}} (\sqrt{\rho_h} - 1)}{(-\sqrt{\rho_h} - 1)} &= \sqrt{\varepsilon - \sin^2 \theta_{\text{inc}}} \\ \frac{\cos \theta_{\text{inc}} (\sqrt{\rho_h} + 1)}{(-\sqrt{\rho_h} + 1)} &= \sqrt{\varepsilon - \sin^2 \theta_{\text{inc}}} \end{aligned} \quad (\text{E.8})$$

If we take the square again of both sides, we again have to incorporate the two solutions with opposite signs, thus resulting in a total of four solutions:

$$\begin{aligned} \varepsilon - \sin^2 \theta_{\text{inc}} &= \pm \left[\frac{\cos \theta_{\text{inc}} (\sqrt{\rho_h} - 1)}{(-\sqrt{\rho_h} - 1)} \right]^2 \\ \varepsilon - \sin^2 \theta_{\text{inc}} &= \pm \left[\frac{\cos \theta_{\text{inc}} (\sqrt{\rho_h} + 1)}{(-\sqrt{\rho_h} + 1)} \right]^2 \end{aligned} \quad (\text{E.9})$$

Of the possible four different solutions only one is physically correct.

$$\varepsilon_1 = \sin^2 \theta_{\text{inc}} + \left[\frac{\cos \theta_{\text{inc}} (\sqrt{\rho_h} - 1)}{(-\sqrt{\rho_h} - 1)} \right]^2 \quad (\text{E.10})$$

$$\varepsilon_2 = \sin^2 \theta_{\text{inc}} - \left[\frac{\cos \theta_{\text{inc}} (\sqrt{\rho_h} - 1)}{(-\sqrt{\rho_h} - 1)} \right]^2 \quad (\text{E.11})$$

$$\varepsilon_3 = \sin^2 \theta_{\text{inc}} + \left[\frac{\cos \theta_{\text{inc}} (\sqrt{\rho_h} + 1)}{(-\sqrt{\rho_h} + 1)} \right]^2 \quad (\text{E.12})$$

$$\varepsilon_4 = \sin^2 \theta_{\text{inc}} - \left[\frac{\cos \theta_{\text{inc}} (\sqrt{\rho_h} + 1)}{(-\sqrt{\rho_h} + 1)} \right]^2 \quad (\text{E.13})$$

In our case the solution of ε_3 gives the right result. When $\rho'_h \geq 0$, $\wedge \rho''_h < 0$ will result in correct values for both the real and the imaginary part of the dielectric constant with $\varepsilon' \geq 0$, $\wedge \varepsilon'' < 0$.

E.2 The Fresnel equation for a vertically polarized wave

The Fresnel equation for a vertically polarized wave can be written as:

$$\rho_v(\theta_{\text{inc}}, \varepsilon) = \left| \frac{\varepsilon \cos \theta_{\text{inc}} - \sqrt{\varepsilon - \sin^2 \theta_{\text{inc}}}}{\varepsilon \cos \theta_{\text{inc}} + \sqrt{\varepsilon - \sin^2 \theta_{\text{inc}}}} \right|^2 \quad (\text{E.14})$$

with the Fresnel reflection coefficient for vertical polarization ρ_v and the dielectric constant ε as complex numbers, and θ_{inc} is the incidence angle relative to nadir. As in the previous section we take the square root on both sides and performing the same steps:

$$\sqrt{\rho_v(\theta_{\text{inc}}, \varepsilon)} = \pm \frac{\varepsilon \cos \theta_{\text{inc}} - \sqrt{\varepsilon - \sin^2 \theta_{\text{inc}}}}{\varepsilon \cos \theta_{\text{inc}} + \sqrt{\varepsilon - \sin^2 \theta_{\text{inc}}}} \quad (\text{E.15})$$

$$\left(\varepsilon \cos \theta_{\text{inc}} - \sqrt{\varepsilon - \sin^2 \theta_{\text{inc}}} \right) \sqrt{\rho_v} = \pm \left(\varepsilon \cos \theta_{\text{inc}} + \sqrt{\varepsilon - \sin^2 \theta_{\text{inc}}} \right) \quad (\text{E.16})$$

$$\begin{aligned} \frac{\varepsilon \cos \theta_{\text{inc}} (\sqrt{\rho_v} - 1)}{(-\sqrt{\rho_v} - 1)} &= \sqrt{\varepsilon - \sin^2 \theta_{\text{inc}}} \\ \frac{\varepsilon \cos \theta_{\text{inc}} (\sqrt{\rho_v} + 1)}{(-\sqrt{\rho_v} + 1)} &= \sqrt{\varepsilon - \sin^2 \theta_{\text{inc}}} \end{aligned} \quad (\text{E.17})$$

We end up with a quadratic form of the equation:

$$\begin{aligned} \pm \varepsilon^2 \left[\frac{\cos \theta_{\text{inc}} (\sqrt{\rho_v} - 1)}{(-\sqrt{\rho_v} - 1)} \right]^2 - \varepsilon + \sin^2 \theta_{\text{inc}} &= 0 \\ \pm \varepsilon^2 \left[\frac{\cos \theta_{\text{inc}} (\sqrt{\rho_v} + 1)}{(-\sqrt{\rho_v} + 1)} \right]^2 - \varepsilon - \sin^2 \theta_{\text{inc}} &= 0 \end{aligned} \quad (\text{E.18})$$

Using the quadratic formula to solve the problem:

$$\varepsilon_{1,2} = \frac{-b \pm \sqrt{b^2 - 4ac}}{2a} \quad (\text{E.19})$$

$$\begin{aligned} a &= \pm \left[\frac{\cos \theta_{\text{inc}} (\sqrt{\rho_v} - 1)}{(-\sqrt{\rho_v} - 1)} \right]^2, \quad \vee, \quad \pm \left[\frac{\cos \theta_{\text{inc}} (\sqrt{\rho_v} + 1)}{(-\sqrt{\rho_v} + 1)} \right]^2 \\ b &= -1 \\ c &= \sin^2 \theta_{\text{inc}}, \quad \vee, \quad -\sin^2 \theta_{\text{inc}} \end{aligned} \quad (\text{E.20})$$

will give eight possible solutions with the following solution as the only one physical correct:

$$\varepsilon_1 = \frac{1 + \sqrt{1^2 - 4 \left[\frac{\cos \theta_{\text{inc}} (\sqrt{\rho_v} - 1)}{(-\sqrt{\rho_v} - 1)} \right]^2 \sin^2 \theta_{\text{inc}}}}{2 \left[\frac{\cos \theta_{\text{inc}} (\sqrt{\rho_v} - 1)}{(-\sqrt{\rho_v} - 1)} \right]^2} \quad (\text{E.21})$$

When $\rho'_v \geq 0$, \wedge $\rho''_v < 0$ will result in correct values for both the real and the imaginary part of the dielectric constant with $\varepsilon' \geq 0$, \wedge $\varepsilon'' < 0$.

Appendix F

The inverse Dubois model

A more recent more empirical model is that of Dubois *et al.* (1995) hereafter referred to as the "Dubois model".. For a more detailed description, the boundary conditions and validity of this model see section 3.5.4. The forward solutions of the Dubois model are given by:

$$\sigma_{hh}^o = 10^{-2.75} \frac{\cos^{1.5}(\theta_{inc})}{\sin^5(\theta_{inc})} 10^{0.028\epsilon_r' \tan \theta_{inc}} (k\sigma \sin \theta_{inc})^{1.4} \lambda^{0.7} \quad (F.1)$$

$$\sigma_{vv}^o = 10^{-2.35} \frac{\cos^3(\theta_{inc})}{\sin^3(\theta_{inc})} 10^{0.046\epsilon_r' \tan \theta_{inc}} (k\sigma \sin \theta_{inc})^{1.1} \lambda^{0.7} \quad (F.2)$$

which are valid for a frequency range of 1.5 - 11 GHz. Note that the backscatter coefficient is not expressed in dB! The Dubois model can be inverted in various ways. For the use with ERS windscatterometer data the model can be inverted using two look angles and one polarization in Eq.F.2:

$$\theta_1 \wedge \theta_2 \implies \sigma_{vv1}^o \wedge \sigma_{vv2}^o \quad (F.3)$$

This will give a backscatter coefficient for each incidence/look angle:

$$\sigma_{vv1}^o = A \frac{1}{\tan(\theta_{inc1})} 10^{0.046\epsilon_r' \tan \theta_1} (h \sin \theta_{inc1})^{1.1} \quad (F.4)$$

$$\sigma_{vv2}^o = A \frac{1}{\tan(\theta_{inc2})} 10^{0.046\epsilon_r' \tan \theta_2} (h \sin \theta_{inc2})^{1.1} \quad (F.5)$$

with

$$A = 10^{-2.35} k^{1.1} \lambda^{0.7} \quad (F.6)$$

After some straightforward mathematics the real part of the dielectric constant ε' can be found as:

$$\varepsilon' = \frac{\log \frac{\sigma_{vv1}^o}{\sigma_{vv2}^o} - \log \frac{\tan(\theta_{inc2})}{\tan(\theta_{inc1})} + 1.1 \log \left(\frac{\sin \theta_{inc1}}{\sin \theta_{inc2}} \right)}{0.046 (\tan \theta_{inc1} - \tan \theta_{inc2})} \quad (F.7)$$

Another possible inversion is using the two polarizations (Eqs. F.1 and F.2). To simplify Eq. F.1 constants A and B are introduced:

$$A = 10^{-2.75} \frac{\cos^{1.5}(\theta_{inc})}{\sin^5(\theta_{inc})} \lambda^{0.7} \quad (F.8)$$

$$B = (k \sin \theta_{inc})^{1.4} \quad (F.9)$$

From above it follows that Eq.F.1 becomes:

$$\sigma_{hh}^o = A B 10^{0.028\varepsilon \tan \theta} (h)^{1.4} \quad (F.10)$$

or

$$h = \left(\frac{\sigma_{hh}^o}{A B 10^{0.028\varepsilon \tan \theta_{inc}}} \right)^{1/1.4} \quad (F.11)$$

To simplify Eq. F.2 the constants C and D are introduced:

$$C = 10^{-2.35} \frac{\cos^3(\theta_{inc})}{\sin^3(\theta_{inc})} \lambda^{0.7} \quad (F.12)$$

$$D = (k \sin \theta_{inc})^{1.1} \quad (F.13)$$

which yields:

$$\sigma_{vv}^o = C \cdot D \cdot 10^{0.046\varepsilon \tan \theta} (h)^{1.1} \quad (F.14)$$

Inserting Eq. F.11 into Eq. F.14 gives:

$$\sigma_{vv}^o = C \cdot D \cdot 10^{0.046\varepsilon \tan \theta} \left[\left(\frac{\sigma_{hh}^o}{A \cdot B \cdot 10^{0.028\varepsilon \tan \theta}} \right)^{1/1.4} \right]^{1.1} \quad (F.15)$$

By some straightforward mathematics the real part of the dielectric constant, ε' can be written explicitly as:

$$\frac{1}{0.024 \tan \theta} \log \left[\frac{\sigma_{vv}^o (A \cdot B)^{1.1/1.4}}{C \cdot D \cdot (\sigma_{hh}^o)^{1.1/1.4}} \right] = \varepsilon' \quad (F.16)$$

By inserting ε' in Eq. F.11 the roughness parameter h can be found.

References

- Altese, E., Bolognani, O., Mancini, M., & Troch, P.A. 1996. Retrieving soil moisture over bare soil from ERS-1 synthetic aperture radar data: sensitivity analysis based on a theoretical surface scattering model and field data. *Water Resources Research*, **32**(3), 653-661.
- Ansault, M., DeBacker, L.W., & Declercq, M. 1984. Statistical relationship between apparent dielectric constant and water content in porous media. *Soil Sci. Soc. Am. J.*, **48**, 47-50.
- Arfken, G. 1985. *Mathematical methods for physicists*. Third edn. San Diego: Academic Press.
- Attema, E.P.W., & Ulaby, F.T. 1978. Vegetation modelled as a water cloud. *Radio Science*, **13**, 357-364.
- Bastiaanssen, W.G.M., Menenti, M., Oevelen, P.J. Van, Hoekman, D.H., & Feddes, R.A. 1994. Spatial Variability and Accuracy of Remote Sensing Estimates of Evaporation and Soil Moisture Within EFEDA'91. Pages 175-192 of: *Proceedings Conference Trinity College Dublin, Sept. 7-9, 1994*
- Bastiaanssen, W.M.G., Hoekman, D.H., & Roebeling, R.A. 1993. A methodology for the assessment of surface resistance and soil water storage variability at mesoscale based on remote sensing measurements. *IAHS Special publication*, **2**, 66.
- Beckmann, P., & Spizzichino, A. 1963. *The Scattering of Electromagnetic Waves from Rough Surfaces*. Oxford, UK: Pergamon. Reprint: 1987 by Artech House Inc., Norwood, Ma, USA.
- Birchak, J.R., Gardner, C.G., Hipp, J.E., & Victor, J.M. 1974. High dielectric constant microwave probes for sensing soil moisture. *Proc. IEEE*, **62**(1), 93-98.
- Bolle, H. J., Andre, J.C., Arrue, J. L., Barth, H. K., Bessemoulin, P., Brasa, A., de Bruin, H.A.R., Dugdale, G., Engman, E. T., Evans, D. L., Fantechi, R., Fiedler, F., de Griend, A. Van, Imeson, A. C., Jochum, A. M., Kabat, P., Kratzsch, T., Lagouarde, J. P., Langer, I., Llamas, R., Lopes-Baeza, E., Miralles, J. Melia, Mubox, L. S., Munniosguren, J., Nerry, F., Noilhan, J., Oliver, H. R., Roth, R., Diaz, J. Saqnchez, de Sante Ollala, M., Shuttleworth, W. J., Sogaard, H., Stricker, H., Thornes, J., Vauclin, M., & Wickland, D. 1993. EFEDA: European Field Experiments I a Desertification Threatened Area. *Annales Geophysica*, **11**, 173-189.
- Borgeaud, M., Attema, E., Salgado-Gispert, G., Bellini, A., & Noll, J. 1995. Analysis of Bare Soil Surface Roughness Parameters with ERS-1 Data. In: *Symposium Extraction of Bio and Geophysical Parameters from SAR Data for Land Applications*. ESA.

- Borisenko, A.I., & Tarapov, I.E. 1979 (original 1968). *Vector and tensor analysis*. Dover series on advanced mathematics. New York: Dover Publications Inc. Translated from the Russian by R.A. Silverman.
- Born, M., & Wolf, E. 1975. *Principles of optics*. Fifth edn. New York: Pergamon Press.
- Böttcher, C.J.F., & Borderwijk, P. 1978a. *Theory of electric polarization*. Vol. I (dielectrics in static fields). Elsevier Scientific Company, Amsterdam.
- Böttcher, C.J.F., & Borderwijk, P. 1978b. *Theory of electric polarization*. Vol. II (dielectrics in time-dependent fields). Elsevier Scientific Company, Amsterdam.
- Brunfeldt, D.R., & Ulaby, F.T. 1984. The Effect of Row Direction on the Microwave Emission from Vegetation Canopies. Pages 125–129 of: *Proc. IGARSS'84 Symp.* ESA SP-215.
- Brunfeldt, D.R., & Ulaby, F.T. 1986. Microwave Emission from Row Crops. *IEEE Trans. Geosci. and Remote Sensing*, **22**, 315–323.
- Burger, H.C. 1915. *Phys. Zs.*, 73–76.
- Burke, W.J., Schmugge, T., & Paris, J.F. 1979. Comparison of 2.8 and 21 Cm Microwave Observations over Soils with Emission Model Calculations. *J. Geophys. Res.*, **84**, 287–294.
- Chandrasekhar, S. 1960. *Radiative Transfer*. Dover, New York.
- Chanzy, A., Schmugge, T.J., Calvet, J.C., Kerr, Y.H., van Oevelen, P.J., Grosjean, O., & Wang, J.R. 1996. Airborne microwave radiometry on a semi arid area during HAPEX-Sahel. *J. Hydrology*.
- Chen, K.S., Yen, S.K., & Huang, W.P. 1995. A simple model for retrieving bare soil moisture from radar-scattering coefficients. *Remote Sens. Environ.*, **54**, 121–126.
- Choudhury, B.J., Schmugge, T.J., Newton, R.W., & Chang, A. 1979. Effect of surface roughness on the microwave emission from soils. *J. Geophys. Res.*, **84**, 5699–5706.
- Choudhury, B.J., Kerr, Y.H., Njoku, E.G., & Pampaloni, P. (eds). 1995. *Passive Microwave Remote Sensing of Land-Atmosphere Interactions*. VSP, Utrecht, The Netherlands. ESA/NASA International Workshop, January 11–15, St.Lary, France.
- Chukhlantsev, A. A., & Shutko, A. M. 1988. An Account of the Effect of Vegetation During Microwave Radiometric Sounding of Terrestrial Deposits. *Remote Sens. Earth Space*, **2**, 67–72. (Engl. transl.).
- Cox, P., & Best, M. 1999. Implementation of MOSES in the Mesoscale Model. *UK Met. Office NWP Gazette*, December, 10–13.
- Curlander, J.C., & McDonough, R.N. 1991. *Synthetic Aperture Radar. Systems and Signal Processing*. New York: John Wiley Sons, Inc.
- Dasberg, S., & Dalton, F.N. 1985. Time domain reflectometry field measurements on soil water content and electrical conductivity. *Soil Sci. Soc. Am. J.*, **49**, 293–297.
- Davidson, M.W.J., Le Toan, T., Mattia, F., Satalino, G., Manninen, T., & Borgeaud, M. 2000. On the Characterization of Agricultural Soil Roughness for Radar Remote Sensing Studies. *IEEE Trans. Geosci. and Remote Sens.*, **38**(2), 630–640.
- Dawson, M.S., Manry, M.T., & Fung, A.K. 1995. Information retrieval from remotely sensed data and a method to remove parameter estimator ambiguity. *Proc. IGARSS'95*, **I**, 691–693.

- de Hoop, A.T. 1975. *Theorie van het elektromagnetische veld*. Delftse Universitaire Pers, Delft.
- de Loor, G.P. 1956. *Dielectric properties of heterogenous mixtures*. Ph.D. thesis, University of Leiden.
- de Loor, G.P. 1983. The dielectric properties of wet materials. *IEEE Trans. Geosci. Remote Sensing*, 21(3), 364-369.
- de Loor, G.P. 1990. *The dielectric properties of wet soils*. Report 90-13. BCRS (Netherlands Board of Remote Sensing).
- de Vries, D.A. 1952. *Het warmtegeleidingsvermogen van grond (the thermal conductivity of soil)*. Mededeling van de Landbouwhogeschool Wageningen, Nederland, vol. 52(1).
- Deardorff, J.W. 1977. A parameterization of ground-surface moisture content for use in atmospheric prediction models. *J. Atmos. Sci.*, 16, 1182-1185.
- Debye, P. 1929. *Polar Molecules*. Dover, New York.
- Dirksen, C., & Dasberg, S. 1993. Improved calibration of time domain reflectometry soil water content measurements. *Soil Sci. Soc. Am. J.*, 57, 660-667.
- Dobson, M.C., & Ulaby, F.T. 1986. Preliminary evaluation of the SIR-B response to soil moisture, surface roughness and crop canopy cover. *IEEE Trans. Geosci. Remote Sensing*, 24(4), 517-526.
- Dobson, M.C., & Ulaby, F.T. 1998. Mapping Soil Moisture Distribution with Imaging Radar. Chap. 8, pages 407-433 of: Henderson, F.M., & Lewis, A.J. (eds), *Principles Applications of Imaging Radar, Manual of Remote Sensing, Third Edition, Volume2*. Wiley and Sons.
- Dobson, M.C., Ulaby, F.T., Hallikainen, M., & El-Rayes, M. 1985. Microwave dielectric behaviour of wet soil. Part II: dielectric mixing models. *IEEE Trans. Geosci. Remote Sensing*, 23(1), 35-46.
- Dubois, P.C., van Zyl, J.J., & Engman, E.T. 1995. Measuring soil moisture with imaging radars. *IEEE Trans. Geosci. Remote Sensing*, 33(4), 915-26. Corrections in: 33(6):1340, November, 1995.
- Elachi, C. 1987. *Introduction to the physics and techniques of remote sensing*. John Wiley and Sons, New York.
- Engelder, D.S., & Buffler, C.R. 1991. Measuring dielectric properties of food products at microwave frequencies. *Microwave World*, 12(2), 2-10.
- English, S., Eymard, L., Smith, E., & Burns, B. 1999. Assessment of Assimilation and Retrieval Methods. Pages 115-129 of: Oevelen, P.J. Van, Eymard, L., & English, S. (eds), *Microwave Radiometry for Atmospheric Research and Monitoring*. Noordwijk (ZH), The Netherlands: ESA-ESTEC, for EU COST 712 and ESA-ESTEC.
- Engman, E.T., & Chauhan, N. 1995. Status of microwave soil moisture measurements with remote sensing. *Remote Sens. Environ.*, 51, 189-198.
- Eyre, J.R. 1997. Variational Assimilation of Remotely-Sensed Observations of the Atmosphere. *Journal of the Meteorological Society of Japan*, 75(1B), 331-338.
- Feddes, R.A., & Koopmans, R.W.R. 1995. *Agrohydrology*. Department of Water Resources, Wageningen Agricultural University. Lecture notes, K150-305, 06141109.
- Feynman, R., Leighton, R., & Sands, M. 1979. *The Feynman lectures in physics*. 6th edn. Vol. II. Addison-Wesley Publishing.

- Frisch, V. 1968. *Wave propagation in random media: probabilistic methods in applied mathematics*. Vol. 1. Academic Press, New York. Pages 75–198.
- Fung, A.K. 1982. Review of volume scatter theories for modeling applications. *Radio Science*, **17**, 1007–1017.
- Fung, A.K. 1994. *Microwave scattering and emission models and their applications*. Artech House, Norwood.
- Fung, A.K., & Chen, K.S. 1995. A validation of the IEM surface scattering model. *Proceedings IGARSS'95*, **1**, 933–935.
- Fung, A.K., & Chen, M.F. 1985. Numerical simulation of scattering from simple and composite random surfaces. *J. Opt. Soc. Am.*, **A2**, 2274–2284.
- Fung, A.K., & Eom, H.J. 1981. Multiple scattering and depolarization by a randomly rough Kirchhoff surface. *IEEE Trans. Ant. Prop.*, **AP-29**(3), 463–471. Also appears as Technical Report TR 369-4, Remote Sensing Lab., Univ. of Kansas, Lawrence, MI.
- Fung, A.K., Li, Z., & Chen, K.S. 1992. Backscattering from a randomly rough dielectric surface. *IEEE Trans. Geosci. Remote Sensing*, **30**(2), 356–369.
- Fung, A.K., Dawson, M.S., Chen, K.S., Hsu, A.Y., Engman, E.T., O'Neill, P.E., & Wang, J. 1996. A modified IEM model for scattering from surfaces with application to soil moisture sensing. Pages 1297–1299 of: *Proceedings IGARSS'96*. IEEE.
- Gabriel, C., & Grant, E.H. 1989. Dielectric sensors for industrial microwave measurement and control. *Proc. of High-Frequency/Microwave Conference (KEMA, Arnhem, The Netherlands)*.
- Goutorbe, J.P., Lebel, T., Tinga, A., Bessemoulin, P., Brouwer, J., Dolman, A.J., Engman, E.T., Gash, J.H.C., Hoepffner, M., Kabat, P., Kerr, Y.H., Monteny, B., Prince, S., Said, F., Sellers, P., & Wallace, J.S. 1994. HAPEX-Sahel: a large scale study of land-atmosphere interactions in the semi-arid tropics. *Annales Geophysicae*, **12**, 53–64.
- Groot, J.S. 1991 (April). *Introduction to radar polarimetry*. TNO-report FEL-91-B122. TNO Physics and Electronics Laboratory, The Hague, The Netherlands.
- Halldin, S., Goyttschalk, L., de Griend, A.A. Van, Gryning, S-E., Heikonen, M., Höglström, U., Jochum, A., & Lundin, L-C. 1995. *Science Plan for NOPEX*. Technical report 12. NOPEX Central Office.
- Hallikainen, M.T., Ulaby, F.T., Dobson, M.C., El-Rayes, M.A., & Wu, L. 1985. Microwave dielectric behaviour of wet Soil. Part I: empirical models and experimental observations. *IEEE Trans. Geosci. Remote Sensing*, **23**(1), 25–34.
- Hasted, J.B. 1973. *Aqueous dielectrics*. Chapman and Hall, London.
- Heathman, G. 1995. Personal communication.
- Heimovaara, T.J. 1988 (November). *Time domain reflectometry, a method for measuring volumetric water content of soil*. Tech. rept. Fysicg Geografisch en Bodemkundig Laboratorium, University Of Amsterdam (FGBL-UVA).
- Heimovaara, T.J., & Bouten, W. 1990. A computer controlled 36-channel time domain reflectometry system for monitoring soil water contents. *Water Resources Research*, **26**(10), 2311–2316.
- Henderson, F. M., & Lewis, A.J. (eds). 1998. *Principles Applications of Imaging*

- Radars*. Third edn. Manual of Remote Sensing, vol. 2. New York: John Wiley and Sons.
- Hillel, D. 1980. *Fundamentals of soil physics*. Academic Press, Inc., San Diego, California.
- Hippel, A. Von. 1958. *Dielectrics*. In: *Handbook of Physics*. McGraw-Hill, New York.
- Hoekman, D.H. 1990. *Radar remote sensing data for applications in forestry*. Ph.D. thesis, Wageningen Agricultural University.
- Hoekman, D.H. 1991. Speckle ensemble statistics of logarithmically scaled data. *IEEE Trans. Geosci. Remote Sens.*, **29**(1), 180-182.
- Hoekstra, P., & Delaney, A. 1974. Dielectric properties of soils at UHF and microwave frequencies. *J. Geophys. Res.*, **79**(11), 1699-1708.
- Houser, P.R., Shuttleworth, W.J., Famiglietti, J.S., Gupta, H.V., Syed, K.H., & Goodrich, D.C. 1998. Integration of Soil Moisture Remote Sensing and Hydrologic Modeling Using Data Assimilation. *Water Resources Research*, **34**(12), 3405-3420.
- Huang, X., & Jin, Y.-Q. 1995. A simple method to estimate the soil wetness and surface roughness by using active/passive microwave data. *Remote Sens. Environ.*, **53**, 212-214.
- IDL-ENVI. 1999. *Manual IDL-ENVI*. Research Systems Inc. 4990 Pearl East Circle Boulder, CO. 80301, USA.
- IEEE. 1983. IEEE Standard definitions of terms for antennas. *IEEE Trans. on Antennas and Propagation*, **AP-31**(6).
- Ishimaru, A. 1978. *Wave propagation and scattering in random media*. Vol. 1 and 2. New York: Academic Press.
- Jackson, T. J., Schmugge, T. J., & Wang, J. R. 1982a. Passive Microwave Remote Sensing of Soil Moisture under Vegetation Canopies. *Water Resources Research*, **18**, 1137-1142.
- Jackson, T.J., & O'Neill, P.E. 1990. Attenuation of Soil Microwave Emission by Corn and Soybeans at 1.4 and 5 GHz. *IEEE Trans. Geosci. and Remote Sensing*, **28**(50), 978-980.
- Jackson, T.J., & Schiebe, F.R. 1993. *Hydrology Data Report Washita'92*. Tech. rept. NAWQL 93-1. National Agricultural Water Quality Laboratory, USDA-Agricultural Research Service, Durant, Oklahoma.
- Jackson, T.J., & Schmugge, T.J. 1991. Vegetation effects on the microwave emission of soils. *Remote Sens. Environ.*, **36**, 203-212.
- Jackson, T.J., Schmugge, T.J., & Wang, J.R. 1982b. Passive microwave sensing of soil moisture under vegetation canopies. *Water Resour. Res.*, **18**(4), 1137-1142.
- Jackson, T.J., Le Vine, D.M., Swift, C.T., Schmugge, T.J., & Schiebe, F.R. 1995. Large area mapping of soil moisture using the ESTAR passive microwave radiometer in Washita'92. *Remote Sens. Environ.*, **53**, 27-37.
- Kalma, J.D., Franks, S.W., van den Hurk, B.J.J.M., McCabe, M.F.M., & Feddes, R.A. 1999. *Estimation Large Scale Land Surface Fluxes: The Use of Remote Sensing Data with SVAT and NWP Models*. Technical report 90. Department of Environmental Sciences, Wageningen University.
- Karam, M.A., & Fung, A.K. 1987. An Investigation of the Forward Scattering Theorem. Pages 1007-1012 of: *Proc. IGARSS'87*. IEEE.

- Karam, M.A., Fung, A.K., Lang, R.H., & Chauhan, N.S. 1992a. A microwave scattering model for layered vegetation. *IEEE Trans. Geosci. Remote Sensing*, **30**(4), 767-784.
- Karam, M.A., Chen, K.S., & Fung, A.K. 1992b. Statistics of backscatter radar return from vegetation. *Proc. IGARSS'92*, **1**, 242-244.
- Karam, M.A., Amar, F., Fung, A.K., Mougin, E., Lopes, A., Le Vine, D.M., & Beaudoin, A. 1995. A microwave polarimetric scattering model for forest canopies based on vector radiative transfer theory. *Remote Sens. Environ.*, **53**, 16-30.
- Kerr, Y. H., & Wigneron, J.P. 1995. Vegetation models and observations - a review. Chap. *Vegetation*, pages 317-344 of: Choudhury, B.J., Kerr, Y.H., Njoku, E.G., & Pampaloni, P. (eds), *Passive Microwave Remote Sensing of Land-Atmosphere Interactions*. VSP, Utrecht, The Netherlands. ESA/NASA International Workshop, January 11-15, 1993, St. Lary, France.
- Kerr, Y.H. 1998. *MIRAS on RAMSES: Radiometry Applied to Soil Moisture and Salinity Measurements*. Full proposal, A.O. Earth Explorer Opportunity Missions, ESA.
- Kim, C.P. 1995. *The water budget of heterogeneous areas: impact of soil and rainfall variability*. Ph.D. thesis, Wageningen Agricultural University.
- Kirdiashev, K.P., Chukhlantsev, A.A., & Shutko, A.M. 1979. Microwave radiation of the earth's surface in the presence of vegetation cover. *Radio Eng. Electron. Phys. (Engl. translation)*, **24**, 256-264.
- Kramer, H.J. 1994. *Observation of the Earth and its Environment: Survey of Missions and Sensors*. 2nd edn. Berlin: Springer-Verlag.
- Kuga, Y., Whitt, M.W., McDonald, K.C., & Ulaby, F.T. 1990. Scattering models for distributed targets. Pages 111-190 of: Ulaby, F.T., & Elachi, C. (eds), *Radar polarimetry for geoscience applications*. Norwood, MA, USA: Artech House.
- Lane, J., & Saxton, J. 1952. Dielectric dispersion in pure polar liquids at very high frequencies, III. The effect of electrolytes in solution. *Proc. Roy. Soc.*, 531-545.
- Legger, D., & van der Aa, M. 1994. *Soils of the "West Central Site", Niger, HAPEX-Sahel 1992*. Departmental report. Dept. of Soil Science and Geology, Wageningen Agricultural University, Wageningen, The Netherlands.
- Lorentz, H.A. 1909. *The theory of electrons and its applications to the phenomena of light and radiant heat*. Teubner, Leipzig.
- Mandelbrot, B.B. 1977. *Fractals: Form, Chance and Dimension*. San Francisco: Freeman.
- Mätzler, C. 1990. Seasonable Evolution of Microwave Radiation from an Oat Field. *Remote Sens. Environ.*, **31**, 161-173.
- Mätzler, C. (ed). 2000. *Radiative Transfer Models for Microwave Radiometry*. COST 712, University of Bern, Switzerland.
- McDaniel, S.T., & Gorman, A.D. 1983. An examination of the composite-roughness scattering model. *J. Ac. Soc. Am.*, **87**, 1476-1486.
- Menenti, M., Ritchie, J.C., Humes, K.S., Parry, R., Pachepsky, Y., Gimenez, D., & Leguizamon, S. 1996. Estimation of Aerodynamic Roughness at Various Spatial Scales. Pages 40-58 of: Stewart, J.B., Engman, E.T., Feddes, R.A., & Kerr, Y. (eds), *Scaling Up in Hydrology Using Remote Sensing*. England: John Wiley Sons, for Institute of Hydrology, Wallingford, UK.

- Mitchell, J.K. 1976. *Fundamentals of soil behavior*. John Wiley and Sons, New York.
- Mo, T., Choudhury, B.J., Schmugge, T.J., & Jackson, T.J. 1982. A model for microwave emission from vegetation-covered fields. *J. Geophys. Res.*, **87**, 11229–11237.
- Morain, S. A., & Budge, A.M. 1997. *Manual of Remote Sensing: Earth Observing Platforms and Sensors*. 3rd edn. ASPRS. Published only as CD-ROM.
- Mudgett, R.E. 1986. *Electrical properties of food*. Marcel Dekker inc. Chap. 7, pages 329–390.
- Nitzsche, R.P. 1994. Personal Communication.
- Njoku, E.G., & Kong, J.A. 1977. Theory for passive microwave sensing of near surface soil moisture. *J. Geophys. Res.*, **82**(20), 3108–3118.
- Ogilvy, J.A. 1990. *Theory of wave scattering from random rough surfaces*. Redcliffe Way, Bristol, BS1 6NX: IOP Publishing Ltd.
- Oh, Y., Sarabandi, K., & Ulaby, F.T. 1992. An empirical model and an inversion technique for radar scattering from bare soil surfaces. *IEEE Trans. Geosci. Remote Sensing*, **30**(2), 370–381.
- P. Kabat, S.D. Prince, & (Eds.), L. Prihodko (eds). 1997. *Hydrologic Atmospheric Pilot Experiment in the Sahel (HAPEX-Sahel). Methods, Measurements and Selected Results from the West-Central Supersite*. Wageningen, The Netherlands: DLO Winand Staring Centre. Report 130.
- Pampaloni, P., & Paloscia, S. 1986. Microwave Emission and Plant Water Content: A Comparison Between Field Measurements and Theory. *IEEE Trans. Geosci. and Remote Sensing*, **24**, 900–905.
- Peake, W.H., & T.L.Oliver. 1971. *The Response of Terrestrial Surfaces at Microwave Frequencies*. Technical Report AFAL-TR-70-301. Ohio State University, Electroscience laboratory, Columbus, Ohio.
- Peplinski, N.R., Ulaby, F.T., & Dobson, M.C. 1995. Dielectric properties of soils in the 0.3-1.3 GHz range. *IEEE Trans. Geosci. Remote Sensing*, **33**(3), 803–807. Corrections in Vol. 33 p. 1340.
- Petty, G. W. 1999. Review of Retrieval and Analysis Methods for Passive Microwave Imagers. Pages 3–30 of: van Oevelen, P.J., Eymard, L., & English, S. (eds), *Microwave Radiometry for Atmospheric Research and Monitoring* Noordwijk (ZH), The Netherlands: ESA-ESTEC, for EU COST 712 and ESA-ESTEC.
- Polder, D., & van Santen, J.H. 1946. The effective permeability of mixtures of solids. *Physica*, **12**(5), 257–271.
- Press, W.H., Teukolsky, S.A., Vetterlin, W.T., & Flannery, B.P. 1992. *Numerical recipes in FORTRAN. The art of scientific computing*. 2nd edn. Cambridge University Press.
- Raju, S., Chanzy, A., Wigneron, J-P., Calvet, J-C., Kerr, Y.H., & Laguerre, L. 1995. Soil moisture and temperature profile effects on microwave emission at low frequencies. *Remote Sens. Environ.*, **54**, 85–97.
- Rijckenberg, G.J. 1997 (January 24). *Inversion techniques in radar remote sensing of agricultural fields; case studies on sugar beet and winter wheat*. Ph.D. thesis, Wageningen Agricultural University, Wageningen, The Netherlands.
- Ritchie, J.C., & Jackson, T.J. 1989. Airborne Laser Measurements of the Surface

- Topography of Simulated Concentrated Flow Gullies. *Trans. Amer. Soc. Agr. Eng.*, **32**, 645-648.
- Rodgers, C. D. 1976. Retrieval of Atmospheric Temperature and Composition from Remote Measurements of Thermal Radiation. *Rev. Geophys. Space. Phys.*, **14**, 609-624.
- Saatchi, S.S., Evans, D.L., Dubois, P.C., & van Zyl, J.J. 1993. *SAR experiment in desertification-threatened area: EFEDA-Spain*. Report JPL D-10283. Jet Propulsion Laboratory, CA.
- Schanda, E. 1986. *Physical fundamentals of remote sensing*. Springer-Verlag, Berlin Heidelberg.
- Schmugge, T., & Jackson, T.J. 1991. Vegetation Effects on the Microwave Emission of Soils. *Remote Sensing of Environment*, **35**, 203-212.
- Schmugge, T.J. 1983. Remote sensing of soil moisture: recent advances. *IEEE Trans. Geosci. Remote Sensing*, **GE-21**(3), 336-344.
- Schmugge, T.J., & Choudhury, B.J. 1981. A comparison of radiative transfer for predicting emission from soils. *Radio Sci.*, **16**(5), 927-938.
- Schmugge, T.J., & Jackson, T.J. 1992. A dielectric model of the vegetation effects on the microwave emission from soils. *IEEE Trans. Geosci. Remote Sensing*, **30**(4), 757-760.
- Schmugge, T.J., & Jackson, T.J. 1996. Soil moisture variability. Chap. 12, pages 183-192 of: Stewart, J.B., Engman, E.T., Feddes, R.A., & Kerr, Y. (eds), *Scaling up in hydrology using remote sensing*. John Wiley and Sons, for Institute of Hydrology.
- Schmugge, T.J., Jackson, T.J., & McKim, H.L. 1980. Survey of methods for soil moisture determination. *Water Resources Research*, **16**(6), 961-979.
- Schmugge, T.J., Jackson, T.J., Kustas, W.P., & Wang, J.R. 1992. Passive Microwave Remote Sensing of Soil Moisture: Results from HAPEX, FIFE, and MONSOON 90. *ISPRS Journal of Photogrammetry and Remote Sensing*, **47**, 127-143.
- Schmugge, T.J., Chanzy, A., Kerr, Y., & Oevelen, P.J. Van. 1994. Microwave Radiometer Observations of Soil Moisture in HAPEX-Sahel. In: *Proceedings SPIE Conference SPIE*, for SPIE Conference. Rome, September 26-30, 1994.
- Shutko, A.M. 1986. *Microwave Radiometry of Water Surfaces and Grounds*. Moscow: Nauka. (Engl. transl.).
- Smith, M.W., & Tice, A.R. 1988. *Measurement of the unfrozen water content of soils; comparison of NMR and TDR methods*. Report.
- Soil Survey Staff. 1975. *Soil Taxonomy: A Basic System for Making and Interpreting Soil Surveys*. SCS, USDA: US Governm. printing office. Agric. handbook no. 436.
- Stafford, J.V. 1987. *Remote measurement of soil moisture content - a review*. Divisional note DN 1411. AFRC Engineering.
- Starks, P., & Humes, K. 1996. *WASHITA'94 Experiment Data Report*. Technical report NAWQL 96-1. USDA-ARS.
- Stauffer, D.R., & Seaman, N.L. 1990. Use of Four-Dimensional Data Assimilation in a Limited Area Mesoscale Model, I, Experiments with Synoptic-Scale Data. *Monthly Weather Review*, 1250-1277.
- Stogryn, A. 1970. The brightness temperature of a vertically structured medium. *Radio Sci.*, **5**, 1397-1406.

- Stratton, J.A. 1941. *Electromagnetic theory*. McGraw-Hill, New York.
- Tinga, W.R., & Nelson, S. O. 1973. Dielectric properties of materials for microwave processing - tabulated. *J. Microwave Power*, 8(1), 24-65.
- Tinga, W.R., Voss, W.A.G., & Blosssey, D.F. 1973. Generalized approach to multi-phase dielectric mixture theory. *J. Appl. Phys.*, 44(9), 3897-3902.
- Topp, G.C., Davis, J.L., & Annan, A.P. 1980. Electromagnetic determination of soil water content: measurement in coaxial transmission lines. *Water Resources Research*, 16(3), 574-582.
- Tsang, L., Njoku, E., & Kong, J.A. 1975. Microwave thermal emission from a stratified medium with non-uniform temperature distribution. *J. Appl. Phys.*, 46, 5127-5133.
- Tsang, L., Kong, J.A., & Shin, R.T. 1985. *Theory of microwave remote sensing*. Wiley and Sons, New York.
- Ulaby, F. T., Ranzani, M., & Dobson, M.C. 1983. Effects of Vegetation Cover on the Microwave Radiometric Sensitivity to Soil Moisture. *IEEE Trans. Geosci. and Remote Sensing*, 21, 51-61.
- Ulaby, F.T., & Elachi, C. (eds). 1990. *Radar polarimetry for geoscience applications*. Artech House, Dedham, MA.
- Ulaby, F.T., & Wilson, E.W. 1985. Microwave Attenuation Properties of Vegetation Canopies. *IEEE Trans. Geosci. and Remote Sensing*, 23, 746-753.
- Ulaby, F.T., Moore, R.K., & Fung, A.K. 1981. *Microwave remote sensing: active and passive*. Vol. I Microwave remote sensing: fundamentals and radiometry. Artech House, Norwood.
- Ulaby, F.T., Moore, R.K., & Fung, A.K. 1982. *Microwave remote sensing: active and passive*. Vol. II Radar remote sensing and surface scattering and emission theory. Artech House, Norwood.
- Ulaby, F.T., Moore, R.K., & Fung, A.K. 1986. *Microwave Remote Sensing: active and passive*. Vol. III From theory to applications. Artech House, Norwood.
- Ulaby, F.T., Sarabandi, K., McDonald, K., Whitt, M., & Dobson, M.C. 1990. Michigan Microwave Canopy Scattering Model. *Int. J. Remote Sensing*, 11(7), 1223-1253.
- van Beek, L.K.H. 1967. *Dielectric behavior of heterogeneous systems*. In: *Progress in Dielectrics*. Vol. 7. Heywood Books, London.
- van de Griend, A.A., Owe, M., & Chang, A.T.C. 1991. *Botswana water and surface energy balance research program Part 2: Large scale soil moisture and passive microwaves*. Project report 91-38B. Netherlands Remote Sensing Board (BCRS).
- van der Sanden, J.J. 1997 (December). *Radar Remote Sensing to Support Tropical Forest Management*. Ph.D. thesis, Wageningen Agricultural University.
- van Kampen, N.G. 1992. *Stochastic Processes in Physics and Chemistry*. Amsterdam: North-Holland.
- van Oevelen, P.J. 1998. Soil Moisture Variability: A Comparison Between Detailed Field Measurements and Remote Sensing Measurement Techniques. *Hydrological Sciences*, 43(4), 511-520.
- van Oevelen, P.J., & Hoekman, D.H. 1994. Estimation of areal soil water content during HAPEX-Sahel and EFEDA-Spain. *Proc. IGARSS'94*, 1591-1592.

- van Oevelen, P.J., & Hoekman, D.H. 1999. Radar backscatter inversion techniques for estimation of surface soil moisture: EFEDA-Spain and HAPEX-Sahel case studies. *IEEE Trans. Geosci. Remote Sensing*, 37(1), 113–123.
- van Oevelen, P.J., & Schmugge, T. J. 1997. Remote Sensing of Soil Moisture and Temperature. Pages 74–85 of: P. Kabat, S.D. Prince, & Prihodko, L. (eds), *Hydrologic Atmospheric Pilot Experiment in the Sahel (HAPEX-Sahel), Methods, Measurements and Selected Results from the West Central Supersite* Wageningen, The Netherlands: DLO Winand Staring Centre. Report 130.
- van Oevelen, P.J., & Woodhouse, I.H. 1996. *NOPEX/Forest-Dynamo Ground Data Collection and Data Analysis Report*. Technical Report 70. Dept. of Water Resources, Wageningen University.
- van Oevelen, P.J., Hoekman, D.H., & Vissers, M.A.M. 1993. *Soil moisture and surface roughness measurements during HAPEX-Sahel 1992. Ground data collection report*. Tech. rept. Department of Water Resources, Wageningen Agricultural University, Wageningen, The Netherlands. Report.
- van Oevelen, P.J., Hoekman, D.H., & Feddes, R.A. 1996. Errors in estimation of areal soil water content from SAR data. Chap. 14, pages 207–220 of: Stewart, J.B., Engman, E.T., Feddes, R.A., & Kerr, Y. (eds), *Scaling Up in Hydrology Using Remote Sensing* Wiley and Sons Ltd, West Sussex, England, for Institute of Hydrology, Wallingford, England.
- van Oevelen, P.J., Eymard, L., & English, S. (eds). 1998. *Microwave Radiometry to Atmospheric Research and Monitoring: 1. Retrieval, Analysis and Assimilation Methods; 2. Assessment of Methods* ESA, for ESA/EU COST 712.
- van Olphen, H. 1963. *An introduction to clay colloid chemistry*. Wiley and Sons, New York.
- van Zyl, J.J., Zebker, H.A., & Elachi, C. 1987. Imaging radar polarization signatures: theory and observation. *Radio Science*, 22, 529–543.
- Van Zyl, J.J., Chpman, B., Dubois, P., & Freeman, A. 1992. *POLCAL User's Manual: 4.0 upgrade edn*. Jet Propulsion Laboratory. JPL D-7715.
- Vanmarcke, E. 1983. *Random Fields: Analysis and Synthesis*. The Massachusetts Institute of Technology. Reprint: 1988.
- Vissers, M.A.M., & Hoekman, D.H. 1991. *Groundtruth Data Collection Report: HAPEX-EFEDA'91*. Tech. rept. Wageningen University. Unpublished.
- Vissers, M.A.M., & Hoekman, D.H. 1992. *EFEDA-Spain: a ground truth data collection report*. Internal Report. Department of Water Resources, Wageningen Agricultural University.
- Vyas, A. D., Trivedi, A. J., Calla, O. P. N., Rana, S. S., S., B. Sharma, & Vora, A. B. 1990. Experimental Data for Separation of Vegetation and Soil and Estimation of Soil Moisture Using Passive Microwaves. *Int. J. Remote Sens.*, 11(8), 1421–1438.
- Wang, J., Shiue, J., Engman, E., et al. 1980. *Remote Measurements of Soil Moisture by Microwave Radiometers at BARC Test Site*. Tech. Memorandum 80720. NASA.
- Wang, J., O'Neill, P., Engman, E., et al. 1982. *Remote Measurements of Soil Moisture by Microwave Radiometers at BARC Test Site*. Tech. Memorandum 83954. NASA.
- Wang, J. R., Schmugge, T. J., Shiue, J. C., & Engman, E. T. 1990. The L-Band

- PBMR Measurements of Surface Soil Moisture in FIFE. *IEEE Trans. Geosci. and Remote Sensing*, **28**, 906-914.
- Wang, J.R. 1980. The dielectric properties of soil-water mixtures at microwave frequencies. *Radio Sci.*, 977-985.
- Wang, J.R. 1983. Passive microwave sensing of soil moisture content: the effects of soil bulk density and surface roughness. *Remote Sens. Environ.*, **13**, 329-344.
- Wang, J.R. 1987. Microwave emission from smooth bare fields and soil moisture sampling depth. *IEEE Trans. Geosci. Remote Sensing*, **25**(5), 616-622.
- Wang, J.R., & Choudhury, B.J. 1981. Remote sensing of soil moisture content over bare field at 1.4 GHz frequency. *J. Geophys. Res.*, **86**(C6), 5277-5282.
- Wang, J.R., & Choudhury, B.J. 1995. Passive microwave radiation from soil: example of emission models and observations. Chap. *Soil moisture*, pages 423-460 of: Choudhury, B.J., Kerr, Y.H., Njoku, E.G., & Pampaloni, P. (eds), *Passive Microwave Remote Sensing of Land-Atmosphere Interactions*. VSP, Utrecht, The Netherlands.
- Wang, J.R., & Schmugge, T.J. 1980. An empirical model for the complex dielectric permittivity of soils as a function of water content. *IEEE Trans. Geosci. Remote Sensing*, **18**(4), 288-295.
- Wang, J.R., O'Neill, P.E., Jackson, T.J., & Engman, E.T. 1983. Multifrequency measurements of the effects of soil moisture, soil texture, and surface roughness. *IEEE Trans. Geosci. Remote Sensing*, **GE-12**(1), 44-51.
- Warrilow, D.A. 1986. Indications of the sensitivity of European climate to land use variation using a one-dimensional model. *Proc. ISLSCP Conference, Rome, Italy*, 156-159.
- Warrilow, D.A., & Buckley, E. 1989. The Impact of Land Surface Processes on the Moisture Budget of a Climate Model. *Annales Geophys.*, **7**, 439-450.
- Wigneron, J.-P., Waldteufel, P., Chanzy, A., Calvet, J.-C., Marloie, O., Hanocq, J.-F., & Kerr, Y. 2000. *Retrieval Capabilities of L-Band 2-D Interferometric Radiometry over Land Surfaces (SMOS Mission)*. VSP Press. In Press.
- Wilheit, T.T. 1978. Radiative transfer in a plane stratified dielectric. *IEEE Trans. Geosci. Electron.*, **16**, 138-143.
- Wobschall, D. 1977. A theory of the complex dielectric permittivity of soil containing water, the semidisperse model. *IEEE Trans. Geosci. Electron.*, **15**(1), 49-58.

Curriculum Vitae

Petrus Johannes van Oevelen werd geboren op 19 januari 1967 te Oudenbosch. In juni 1985 haalde hij zijn Atheneum diploma aan het Thomas More college in Oudenbosch. Hierna begon hij aan zijn studie cultuurtechniek aan de Landbouwniversiteit Wageningen waarin hij afstudeerde in augustus 1991, met als specialisatie, hydrologie. Direct na zijn afstuderen heeft hij een kortdurend project voor de FAO uitgevoerd, waarna hij in februari 1992 als assistent in opleiding (AIO) aan zijn promotieonderzoek begon. Van september 1994 tot en met oktober 1995 was hij werkzaam als gastmedewerker bij het Department of Environmental and Civil Engineering, University of California at Davis. Na de vierjarige periode als AIO is hij nu in deeltijd werkzaam als toegevoegd wetenschappelijk medewerker bij de vakgroep Waterhuishouding. Sinds 1999 is hij medeoprichter en werkzaam bij SarVision, een bedrijf wat zich specialiseert in het ontwikkelen van radartoepassingen voor met name bos-, natuur- en milieubeheer.

Nawoord

Een nawoord is de plek in het proefschrift waar je het gevoel wat je hebt en hebt gehad bij de totstandkoming van het werk kunt aangeven. Tijdens het lezen van een novelle stuitte ik op een zin die voor mij dat gevoel niet beter had kunnen weergeven:

"I think of it as it should have been, with its proxilities docked, its dullnesses enlivened, its fads eliminated, its truths multiplied" (Henry Fowler in Fowler's Modern English Usage).

Hoewel dit boekje onder mijn naam wordt gepubliceerd en alle verantwoordelijkheid dan ook bij mij ligt is dit proefschrift tot stand gekomen dankzij de bijdragen van een groot aantal mensen. Een woord van dank is dan ook op zijn plaats aan al degenen die de afgelopen jaren direct of indirect een bijdrage hebben geleverd!

Een aantal mensen in het bijzonder wil ik bij naam noemen. Allereerst Dirk Hoekman die als mijn directe begeleider en co-promotor in staat is geweest mij te sturen en bij te staan met zijn heldere kijk op zaken en analytische vermogen. Daarnaast heeft hij mij de vrijheid gegeven waardoor ik een enorme hoeveelheid ervaring en kennis heb kunnen opdoen met microgolf remote sensing, ook buiten de context van dit proefschrift.

Ik dank mijn promotor, Prof. Reinder Feddes voor zijn vertrouwen en zijn kritische houding ten aanzien van mijn werk. De wijze waarop hij de hier en daar toch complexe materie weet te gronden heeft mijn diepe respect!

Massimo Menenti die als projectleider van het zogenaamde BCRS-EOS project een belangrijke rol heeft gespeeld in de totstandkoming van dit proefschrift. Sinds die tijd heb ik regelmatig met Massimo samengewerkt en ik heb grote bewondering voor zijn visie en wijze waarop hij dit werkelijkheid probeert te laten worden.

In 1994 I had the opportunity to work at the University of California at Davis with Prof. Levent Kavvas who I had met the previous year in Wageningen. He has taught me the essence of stochastics, something I wished I had used more in my work. Thank you Lev for being a friend and tutor in the best possible way!

Somebody whom I shared the office with for several years and whose comments and friendship are greatly appreciated is Iain Woodhouse. Thank you Iain!

En, last but not least, mijn ouders en mijn gezin. Suzanne, die mij alert hield door haar kinderlijke wijsheid en vrolijkheid; Teun, die mij door zijn puberteitsperikelen de relativiteit van het bestaan, dus ook van mijn proefschrift, keer op keer liet zien;

Anna, die mij betrok bij haar muzikale aspiraties en daarin zorgde voor ontspanning; Nelleke, die in eerste instantie puur door haar aanwezigheid het proefschrift met een jaar vertraagde, maar die mij ook op vele manieren steunde. En die tegelijkertijd voorkwam dat ik mij met mijn proefschrift afsloot van de wereld door mij te stimuleren ook aan het dagelijks leven met al haar facetten, van verdriet tot grote uitbundigheid, van afwas tot opera, te blijven deelnemen.